DIRECT NUMERICAL SIMULATIONS OF BUBBLY FLOWS

Jian Zhai

Submitted in accordance with the requirements for the
degree of Doctor of Philosophy

The University of Leeds

School of Chemical and Process Engineering

September 2020

The candidate confirms that the work submitted is his own, except where work which has formed part of jointly-authored publications has been included. The contribution of the candidate and the other authors to this work has been explicitly indicated below. The candidate confirms that appropriate credit has been given within the thesis where reference has been made to the work of others.

In this thesis, work from jointly authored publications have been used in Chapters 3 and 4. The candidate performed all simulation works, data acquisition, result analysis and original draft writing and revision. The contribution from other authors were manuscript writing and project supervision. The citations for these publications are as follows.

1. Zhai J., Fairweather M., and Colombo M. 2020. *Simulation of microbubble dynamics in turbulent channel flows*. Flow, Turbulence and Combustion. 2020, **105**, pp.1303-1324.
2. Zhai J., Fairweather M., and Colombo M. 2019. Direct numerical simulation of microbubble dynamics in turbulent channel flow. In: *the 10th International Conference on Multiphase Flow 19-24 May 2019, Rio de Janeiro, Brazil.* 2019.

Acknowledgements

I would like to thank many people who gave help and guidance during this PhD project. I wish to thank, first and foremost, my supervisor Professor Michael Fairweather, who offered me this opportunity, and whose support and advice have been invaluable.

I am indebted to the insights, the support and the guidance from my colleagues. I would like to thank Dr Marco Colombo for helping to fill in the many gaps in knowledge of bubbly flows and his continued support throughout this project. My coding ability and getting started of Nek5000 over the early stage of this process would not have been same without Dr Lee Mortimer and Mr David Rupp. I must also thank Dr Bashar Mohamoud, whose friendship and mental support are very impressive. The same must also be paid to the other unmentioned members in Nuclear Group that deserve acknowledgements here.

The PhD project would not have been possible without the support from my friends who made my time at Leeds so wonderful.

I would also thank the University of Leeds for the Leeds Anniversary Research Scholarships and for the Advanced Research Computing (ARC) facility through which all the computational simulations of this project were performed.

Finally, I would like to thank my dearest mother Gao Shujuan and father Zhai Lishen for their unconditional love before and throughout my PhD.

Abstract

The work presented considers direct numerical simulation (DNS) based studies of bubbly flows in turbulent channel and pipe flows. A variety of bubble sizes are simulated by means of Lagrangian tracking (LPT) and the volume of fluid (VOF) approaches to gain an in-depth knowledge of the physical phenomena involved in, and provide a predictive capability for, turbulent bubbly flows.

DNS coupled with LPT is used to investigate microbubble dynamics in four-way coupled channel and pipe flows. Microbubbles, assumed to be non-deformable and spherical, in channel flows show that one- and two-way coupled predictions demonstrate different trends, with microbubbles pushed by the lift force towards the channel wall in upflow and towards its centre in downflow. Analysis of bubble collision behaviour highlights that binary collisions most frequently occur at very small approach angles and with low relative approach velocities. This trend is confirmed in pipe flows, with bubble coalescence in both geometries predicted using film drainage and energy-based models.

DNS of turbulent channel flow with large deformable bubbles is studied using the VOF method. The motion of single bubbles is considered, with 8 mm bubbles travelling in roughly rectilinear paths in upflow owing to their higher deformability than smaller bubbles which move towards the walls. A method for estimating the drag coefficient is proposed, with good agreement found with experimental data. Time-averaged liquid turbulence statistics are evaluated to quantify bubble-induced turbulence, and bubble clustering is analysed by simulating bubble swarms with a horizontal alignment of colliding bubbles found.

The work reported contributes new understanding of the phenomena involved in bubbly flows down to the smallest scales, with the VOF method, in particular, allowing highly accurate results to be generated that improve understanding. The DNS-LPT technique, for the foreseeable future, will remain the main predictive tool for modelling practically relevant bubbly flows.

Table of Contents

List of Tables

List of Figures

Nomenclature

Latin formula characters

A	Projected area of the bubble
C_C	Calibration constant in contact time model
C_{D}	Drag coefficient
C_{L}	Lift coefficient
C_{VM}	Virtual mass coefficient
C_0	Initial bubble concentration
D	Pipe diameter
d_b	Bubble diameter
d_{eq}	Equivalent bubble diameter
E	Aspect ratio
E_{kin}	Kinetic collision energy
Eo	Eötvös number
Eo_{H}	Modified Eötvös number
E_{s}	Surface energy
f	Volume fraction
f_x, f_y, f_z	Bubble force in x, y, and z directions
F	Compression force in film drainage time model
$\boldsymbol{F}_D$	Drag force vector

$\boldsymbol{F}_G$	Gravity/buoyancy force vector
$\boldsymbol{F}_L$	Lift force vector
$\boldsymbol{F}_m$	Virtual added mass force vector
$\boldsymbol{F}_n$	Total bubble force vector
$\boldsymbol{F}_p$	Pressure gradient force vector
F_r	Froude number
$\boldsymbol{g}$	Gravity acceleration vector
G	Bubble pair correlation function
h_0	Initial film thickness in film drainage time model
h_f	Critical film thickness in film drainage time model
H	Channel height
L_x, L_y, L_z	Channel length scales in *x*, *y*, and *z* directions
Mo	Morton number
N_b	Number of bubbles
$N_{collision}$	Number of bubble collisions
N_x, N_y, N_z	Numbers of mesh elements in *x*, *y*, and *z* directions
p	Pressure
q	Quantity of interest in averaging routine
r_b	Bubble radius
r_{eq}	Equivalent bubble radius of two colliding bubbles
R	Pipe radius
Re	Reynolds number
Re_τ	Shear Reynolds number
Re_b	Bulk Reynolds number

Re_B	Bubble Reynolds number
t	Time
$t_{contact}$	Contact time in film drainage model
$t_{drainage}$	Film drainage time in film drainage model
$\boldsymbol{u_b}$	Bubble velocity vector
$\boldsymbol{u_{b,rel}}$	Relative bubble velocity vector
$u'_{br,rms}$, $u'_{b\theta,rms}$	Radial and azimuthal rms of bubble velocity fluctuations
$u'_{bx,rms}$, $u'_{by,rms}$, $u'_{bz,rms}$	Streamwise, wall-normal, and spanwise rms of bubble velocity fluctuations
$u'_{bx}u'_{by}$	Bubble shear stress
$\boldsymbol{u_f}$	Fluid velocity vector
u_{n}	Normal component of the relative impact velocity
$\boldsymbol{u_{rel}}$	Relative fluid velocity vector
$u'_{r,rms}$, $u'_{\theta,rms}$	Radial and azimuthal rms of fluid velocity fluctuations
u_τ	Fluid shear velocity
$u'_{x,rms}$, $u'_{y,rms}$, $u'_{z,rms}$	Streamwise, wall-normal, and spanwise rms of fluid velocity fluctuations
$u'_x u'_y$	Fluid shear stress
U_B	Bulk velocity
V_b	Bubble volume
$\boldsymbol{\omega_f}$	Fluid vorticity vector
We	Weber number
$\boldsymbol{x_b}$	Bubble position
$\boldsymbol{x}_{b,rel}$	Relative bubble position vector

Δr, $\Delta(R\theta)$	Cylindrical grid spacings
Δx, Δy, Δz	Grid spacings in *x*, *y*, and *z* directions

Greek formula characters

α	Void fraction
δ	Half channel height
ε	Turbulence kinetic energy dissipation rate
η	Kolmogorov length scale
θ_c	Bubbles collision angle
κ	von Karman constant
μ_f	Dynamic viscosity of the fluid phase
μ_d	Dynamic viscosity of the dispersed phase
ν	Fluid kinematic viscosity
ρ_b	Bubble density
ρ_f	Fluid density
σ	Surface tension
τ_w	Wall shear stress

Acronyms

BIT	Bubble-induced turbulence
BWR	Boiling water reactor
CFD	Computational fluid dynamic
DNS	Direct numerical simulation
E-E	Eulerian-Eulerian

E-L	Eulerian-Lagrangian
FT	Front tracking
GL	Gauss-Legendre
GLL	Gauss-Lobatto-Legendre
HFA	Hot film anemometry
HPC	High performance computing
IT	Interface tracking
k-ε	Epsilon turbulence model
LDV	Laser Doppler velocimetry
LES	Large eddy simulation
LPT	Lagrangian particle tracking
LS	Level set
LWR	Light water reactor
MAC	Marker-and-cell
MPI	Message-passing interface
MRV	Magnetic resonance velocimetry
PDA	Phase Doppler analysis
PIV	Particle image velocimetry
PTV	Particle tracking velocimetry
PWR	Pressurized water reactor
RANS	Reynolds-Averaged Navier-Stokes
rms	Root mean squared
SEM	Spectral element method
SGS	Subgrid-scale

TKE	Turbulence kinetic energy
VLSM	Very large-scale turbulent motions
VOF	Volume of fluid

Chapter 1 Introduction

1.1 Overview of turbulent bubbly flows

The study of two-phase flows is of fundamental importance due to their ubiquitous nature and relevance to many natural and engineering systems, including nuclear energy applications, chemical and pharmaceuticals industry, oil and gas operations, minerals processing and similar [1]. Two-phase flows can be divided into two categories: continuous two-phase flows and dispersed two-phase flows. In the first category, both phases can be treated as a continuous medium. In contrast, one of the phases is continuous and the other one is composed of a number of discrete elements (i.e. solid particles, drops or bubbles) dispersed in the continuous phase in the second group. Depending on the nature of the phases involved, dispersed two-phase flows in industrial processes can be classified as gas-solid flows, liquid-solid flows, gas-droplet flows, and liquid-liquid (immiscible) flows.

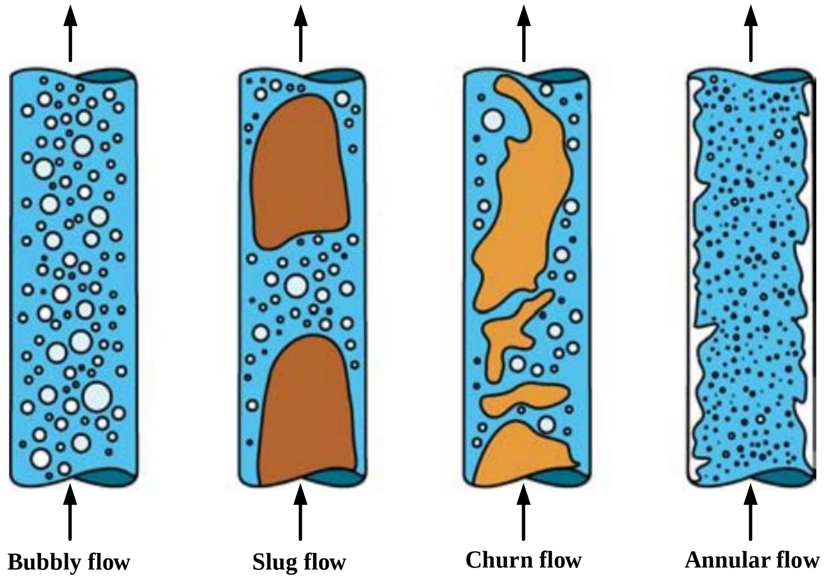

Figure 1.1 Flow patterns for a gas-liquid flow in a vertical pipe [2].

The flow patterns of a gas-liquid flow in vertical pipes are shown in Figure 1.1. At low gas volume fraction (void fraction), small bubbles of gas flow in the continuous liquid.

With the increase of vapour flow rate, bubble coalescence occurs, and mean bubble sizes increase until the flow now contains large gas slugs. In slug flows, the bullet-shaped Taylor bubbles [3, 4] are often surrounded by a dispersion of small bubbles. Further increases result in churn flow [5], which is a highly disturbed flow of gas and liquid, characterised by the presence of a very thick and unstable liquid film that is frequently oscillating. With a further increase in vapour flow rate, an annular flow ultimately occurs, where the liquid and gas phases occupy the wall and the core regions of the pipe, respectively. The focus of this thesis is dispersed air-water bubbly flows in vertical pipes and channels (as shown schematically in Figure 1.1), where a population of gas bubbles is immersed in a liquid continuum water flow. Bubbly flows in vertical channels or pipes vary due to differences in bubble size and shape. Various types of bubbly flows are involved in a number of natural phenomena, and are also widely used in engineering applications such as power generation and, for example, bubble columns in chemical and petroleum engineering.

In nuclear power plants, the study of bubbly flows is critical for nuclear reactor design, where boiling phenomena usually occurs with a large amount of bubbles being generated in large channels [6]. Light water reactors (LWR) are by far the most widely known and used type of nuclear power plant, and they can be generally classified as pressurized water reactors (PWR) and boiling water reactors (BWR) [7]. In BWRs, the water boils in the reactor core and the steam generated in the core is sent directly to a turbine to generate electricity. On the other hand, in PWRs boiling often occurs during transients and accidents, such as a loss of coolant accident, which are of extreme concern for the safety of the reactor. For this reason, detailed understanding of the physical mechanisms that govern bubbly flows is of utmost importance to ensure the safety and efficient operations of reactors in nuclear power generation plant.

Equipment where the injection of bubbles is used to promote mixing and mass transfer, such as in bubble columns, is applied extensively in chemical and petrochemical processes. Bubble columns are cylindrical vessels with a gas inlet at the bottom. As bubbles travel vertically through the liquid phase, they can dissolve in the liquid and/or react. The benefits of such equipment are due to their simple structure, having no moving parts, and since they provide good hydrodynamic and mass/heat transfer characteristics, such as in the Fischer-Tropsch synthesis reactor [8, 9]. Similar applications exist in oxidation, hydrogenation and fermentation processes [10]. In particular, intensification of mass transfer in such bubble columns can be brought about by the use of microbubbles, which are bubbles with diameters in the range 1-1000 µm. Due to the superior characteristics of microbubbles in terms their enhancement of, for example, chemical reactions due to size effects, higher gas hold-up and interfacial area concentration, high gas-liquid heat and mass transfer rates can be obtained [11]. However, back-mixing in such columns is still a drawback in their operation. Such back-mixing is affected by the bubble size distribution and gas hold-up, often resulting in poor column performance [12, 13]. Although previous studies have concerned the flow of microbubbles in a wide range of geometries, considered further in the flowing literature review, to the best of the author's knowledge, microbubble hydrodynamics in a turbulent bubbly pipe flow have as yet not been reported in the literature.

Various other applications of bubbly flows can also be found in the pharmaceutical, food, waste water treatment and biochemical industries [14], which makes it is vitally important to accurately predict and clarify the behaviour of the bubbles and their interactions with the carrier flow. However, the complexity of such flows, which may include heat and mass transfer, bubble-bubble interaction, bubble-fluid interaction, bubble coalescence and break-up makes their research challenging. For example, literature studies have revealed that bubble interaction becomes significant when the void fraction is greater than 10^{-3}, with bubble coalescence and break-up playing an important role when the void fraction is greater than 3% [15].

These complexities significantly limit the use of analytical theory in predicting such flow. To this end, both experimental and numerical investigations of bubbly flow behaviour have been carried out and reported in the literature. Experimental studies do, however, often suffer from contaminants [16], except when specially designed to examine the effect of surfactants. The effect of contaminants results in a change of the slip condition at the bubble surface, from free-slip to non-slip, and reduces the bubbles' rising velocity with an increase of the drag force. Additionally, they also have a remarkable influence on the lift force, confirmed by both experimental and numerical evidence [17, 18], and dramatically change the bubble spatial distribution. Therefore, a difficulty for experiments is the production of turbulent clean air-water bubbly flows. Furthermore, experiments often fail to obtain all the desired information simultaneously, such as the area of the bubble interface and bubble clustering, as well as data on the continuous flow field. Due to the interface between the gas and liquid phases, it is therefore difficult to simultaneously measure the bubble shape, for example, and the surrounding fluid in experiments. When clusters of bubbles in a turbulent flow are formed, the visualization of all the bubbles also becomes problematic. Moreover, experiments are generally limited to short time and length scales, the latter in terms of the flow geometry at least. Due to these issues, numerical simulations of bubbly flows have been used to elucidate these complex flow mechanics that are difficult to measure experimentally in detail. This is particularly thanks to the high development of high performance computing (HPC) platforms in recent decades.

1.2 Numerical simulation of bubbly flows

To better simulate the dynamics of the carrier fluid turbulence, a number of computational fluid dynamic (CFD) approaches with their own advantages and disadvantages have been developed. The most widely used approach is based on the Reynolds-Averaged Navier-Stokes (RANS) equations. Reynolds- or ensemble-averaged forms of the Navier-Stokes equations are generally solved [19], with the fluid turbulence predicted using a suitable turbulence model. RANS approaches have been extensively used to study bubbly flows in recent years [20]. Compared to RANS, large eddy simulation (LES) resolves the largest and most energetic turbulent eddies within a flow, while only the smallest scales are modelled by means of a subgrid-scale (SGS) model. Although LES has been successfully used to predict many single-phase turbulent flows, the treatment of the dispersed phase in turbulence still remains a challenge. In contrast, in direct numerical simulation (DNS) all the length and time scales in the flow are resolved down to the Kolmogorov scale without any modelling assumptions. DNS has been proven of value as a research tool in gaining a deep understanding of complex phenomena down to the smallest scales, and its predictions are used to underpin improve closure models in more macroscopic approaches. With the development of more powerful computers, DNS has become more and more affordable and is now used in an increasingly large number of studies of bubbly flows. In the last decade, therefore, the number of DNS studies of bubbly flows has grown enormously, with the technique used to predict a single or a few bubbles, up to large numbers of deformable bubbles, frequently at relatively high Reynolds numbers. Predicting the complexity of bubbly flows requires accurate resolution of both the continuous and the dispersed phase, and all bubble-bubble and bubble-liquid interactions. Hence DNS, with numerical resolution of all the turbulent scales, is used in this work as an effective tool to advance current knowledge of the fluid dynamics of two-phase bubbly flows.

With knowledge of the flow field obtained using DNS, three kinds of approaches for computation of the dispersed bubbles can be employed, coupling the dispersed phase with carrier phase, i.e. Eulerian-Eulerian (E-E), Eulerian-Lagrangian (E-L) and interface tracking to predict bubble behaviour in turbulent flows at the smallest scales and in the greatest detail. The E-E method is also known as the two-fluid method, such that the dispersed phase is averaged resulting in two sets of equations for both the carrier and dispersed phases. This method requires the least computational cost among the three approaches. But a major difficulty of this method is that it is not straightforward to implement complex phenomena, such as bubble coalescence and break-up. In contrast, the E-L method, also known as Lagrangian particle/bubble tracking, tracks the bubbles individually by solving Newton's second law of motion in an accurate manner, making bubble coalescence and break-up easy to implement in the model. However, the bubbles are considered as points, and closure relations for the interphase forces are needed which are usually obtained from empirical relations derived from experiments, or more accurate numerical simulations. Hence, a disadvantage here is that the bubbles should be smaller than the resolved scales of turbulence. For large and deformable bubbles, an interface tracking method, such as the volume of fluid (VOF) approach, is able to provide more insight into bubbly dynamics, including bubble-induced turbulence, bubble shape deformation, and bubble clustering effects. Due to the need to reconstruct the bubble interface, however, this approach requires extremely high computational mesh resolutions, and associated high computational costs. As a consequence, this highest accuracy method is usually used to deal with only small numbers of bubbles and low Reynolds numbers. Due to their usefulness and accuracy, and ability to provide flow details that cannot be obtained from E-E approaches, both the E-L and interface tracking techniques are used in the current work. A more detailed overview and comparison amongst all computational methods used in literature studies is addressed in Section 2.1.

1.3 Research motivation, aims and objectives

In the literature, for very dilute flows (void fraction $\alpha \leq 10^{-4}$), the bubbles are treated as having no obvious effect on the carrier phase, so that interactions from the bubbles to the fluid are neglected (one-way coupling). When the void fraction is increased ($10^{-4} \leq \alpha \leq 10^{-3}$), the bubbles transfer a significant amount of momentum to the fluid so that the bubbles alter the fluid flow properties (two-way coupling), although at such concentrations the bubbles are not considered to interact with each other. However, in reality, most bubbly flows are very dense and at high void fractions, and bubble interactions, including coalescence and break-up, play very important roles in determining the bubble size distribution and turbulence modulation. Accounting for these bubble-fluid and bubble-bubble interactions is generally referred to as four-way coupling. With the aid of the E-L method, many studies of microbubble flows have been carried out using one-way and two-way coupling. However, there still remains many challenges in describing the flow of microbubbles to a high accuracy. This is because DNS studies of microbubble flows under four-way coupling with coalescence are rarely seen in the literature. In the present work, therefore, the first aspect of interest is turbulent bubbly flow with microbubbles at a high void fraction and with consideration of hydrodynamic interactions.

It is also well known that large and deformable bubbles travel completely differently compared to small and non-deformable, spherical bubbles. The dramatic difference in their trajectories derives from the drag and lift forces acting on the bubbles. Also, previous simulations are generally limited to low mass density ratios between the carrier and dispersed phases. Although recent simulation work has progressed rapidly, results for realistic mass density ratios are still rare. Accordingly, the physics underpinning many real bubble flow phenomena is still not fully clear. A more detailed knowledge is therefore required of bubble trajectory, bubble-bubble interaction mechanisms, bubble interfacial force closures and bubble-induced turbulence.

To address these gaps, the present research uses DNS coupled with Lagrangian bubble tracking, in an E-L approach, to investigate and clarify four-way coupled microbubble flows, with bubble coalescence considered. For large and deformable bubbles, a higher mass density ratio closer to real air bubbles in water is investigated by means of DNS coupled with the VOF method. This approach allows a detailed description of the motion of realistic large and deformable air bubbles in turbulent water flows.

1.4 Outline of the thesis

The thesis is structured as follows. A literature review of computational DNS studies with Eulerian-Eulerian, Eulerian-Lagrangian and interface tracking approaches, and experimental measurements of bubbly flows, is introduced in Chapter 2. In Chapter 3, the numerical methodologies employed are described. Chapter 4 presents results and analyses DNS of turbulent microbubble-laden channel flows in upward and downward flow directions, in which the bubble dynamics in one-way, two-way and four-way coupling with coalescence are reported. The DNS simulation of turbulent pipe flows with microbubbles is considered in Chapter 5, in which bubble behaviour in a wall bounded geometry with curvature is considered. Lastly, the application of interface tracking of spherical and deformable bubbles, predicted using the volume of fluid method, is discussed in Chapter 6, again for the case of channel flows. Finally, a summary of the thesis results and future developments is presented in Chapter 7.

Chapter 2 Literature Review

Bubbly flows in vertical or horizontal pipes and channels are commonly used in industrial applications. Tryggvason and co-workers have published many books and review papers on numerical methods and models for general multiphase flows [21-26], a review of experimental studies can be found in Joshi et al. [27], and a summary of different DNS investigations on particle/bubble-laden turbulent flow is available in [28]. However, there still exists only a few reviews that are specific to the DNS and experimental study of bubbly flows in different geometries. In addition, the topic of turbulent bubbly flow numerical simulation is broad, and investigations continue on various fronts. Hence, this literature review aims to cover previous studies relevant to the present work through an in-depth, critical review of DNS and experimental works focused on bubbly flows. The validation of computational models against detailed experimental data for simplified flow configurations is a basic requirement for the accurate prediction of more complex flows. Therefore, part of the literature review identifies existing experimental databases on bubbly flows obtained using high-fidelity measurement methods, such as hot film anemometry (HFA), particle image velocimetry (PIV), magnetic resonance velocimetry (MRV), laser Doppler velocimetry (LDV), particle tracking velocimetry (PTV) and phase Doppler analysis (PDA).

The chapter is organized as follows. Firstly, a brief overview of numerical methods and models that have been used for the simulation of bubbly flows is presented. Furthermore, the application of these methods using DNS is reviewed. Finally, existing experimental works are discussed and experimental databases for bubbly flows in different geometries identified.

2.1 Computational two-phase fluid dynamics of bubbly flows

2.1.1 Overview and challenges

Early simulations mainly researched the flow of only one or a few bubbles. For example, Ryskin and Leal [29] examined one deformable rising bubble in an unbounded, quiescent fluid, studying the shape change mechanics of buoyancy-driven rising bubbles. Also, research by Taeibi-Rahni et al. [30] investigated the impact of large bubbles on shear flow structure, with bubbles entering either into the centre of vortices or just above the braid region (i.e. the gap region between coherent turbulent rolls). Several similar studies can also be found in the literature [31, 32]. Although these studies give some useful information regarding bubble dynamics, with the rapid development of computer science, the interest of investigators in recent times has turned to understanding more complex systems with more bubbles, including larger numbers of deformable bubbles.

In order to study the complexity of such flows, three methods are generally used to model and simulate two-phase bubbly flows, i.e. the Eulerian-Eulerian approach (E-E approach), the Eulerian-Lagrangian approach (E-L approach) and the interface tracking (IT) technique. The E-E approach is also referred to as the two-fluid model, in which the continuous and dispersed phases are treated as inter-penetrating continua and described using Eulerian conservation equations. The dispersed phase may also be described in a dynamic (Lagrangian) reference frame leading to the E-L approach. The IT method is a one-fluid model since one set of mass and momentum equations is solved for the whole domain. The bubble interface is explicitly resolved, giving specific information on the flow field around bubbles without using any empirical constitutive laws. Bubbles of different shape can be simulated (e.g. spherical, ellipsoidal, skirted and spherical cap), and even bubble-bubble and bubble-liquid interactions can be accounted for. However, due to the extremely large computational requirements of solving for all the turbulence and interface details, the IT approach is often limited to a few hundred bubbles. As such, for large time and length scale systems, the E-L approach is preferred to study the effect of bubble-bubble interactions. In this method, the bubbles are treated as points in which closure laws for bubble-liquid interactions are provided, but the flow field at the scale of each individual bubble is not solved for, as in the IT method. For systems of even larger time and length scales, the E-E approach is most appropriate in view of its relatively low computational cost. A detailed review on the application and comparison of these three main approaches used in the literature is presented in the following.

For the simulation of bubbly flows there are four main configurations investigated in the literature, namely the fully periodic domain, the channel, the duct and the pipe. In the first configuration, researchers have investigated the behaviour of bubble swarms in an unbounded infinite domain. The other three geometrical wall-bounded configurations have been mainly employed to simulate industry relevant situations where the two-phase flow is geometrically confined between walls. The difference between these three simple geometries exists not only in the presence of wall curvature in a pipe, but also in the turbulence scales within the flows. Hence, the review of experimental studies is carried out in terms of these different geometries.

2.1.2 Eulerian-Eulerian approach

The Eulerian-Eulerian approach is also referred to as the two-fluid model, in which the continuous and dispersed phases are treated as inter-penetrating continua and described using Eulerian conservation equations. In this approach both phases are present at the same place at the same time. The two-fluid model provides an averaged description of the two-phase system using time-averaged, volume-averaged, or ensemble-averaged mass and momentum equations solved for each phase, similarly to the RANS equations for the single-phase flow. One major advantage of this approach is its low computational cost, particularly for systems with high dispersed void fractions, which makes the simulation of industrial-scale systems much easier. Another advantage is that four-way coupling between the phases is implicitly taken into account. However, the details of the bubble interface are lost in the averaging procedure, and interfacial transfers of mass, momentum and energy are entirely modelled through specific closure relations.

A number of authors have developed Eulerian-Eulerian models of bubbly flows. Antal et al. [33] developed a two-fluid model of a multidimensional laminar bubbly two-phase flow in a circular pipe, showing good agreement with existing experimental data. The predictions showed that the balance between the lift and the wall lubrication force determines the gas volume fraction profile. Lopez de Bertodano et al. [34] confirmed computational predictions by comparison with experimental data on pipe flows in the literature, and predicted the lateral phase distribution in bubbly flows in vertical triangular ducts, with data including local measurements of phase distribution and liquid-phase velocity. Similarly, Pan et al. [35] investigated two-dimensional bubble columns using E-E dynamic simulations and provided satisfactory results for the bubbly flows at low gas superficial velocities. Druzhinin and Elghobashi [36] employed the two-fluid approach and DNS to perform dilute bubble-laden homogeneous isotropic turbulence simulations, neglecting the forces on the bubbles with diameters smaller than the Kolmogorov length scale. Both one-way and two-way coupling were considered. Results showed that the two-fluid model could be successfully employed for the DNS of turbulent microbubble flows.

Zhou et al. [37] used the two-phase model and found that bubbles at a low void fraction and inlet velocities could enhance the liquid phase turbulence, in contrast to results at high void fraction and high inlet velocities. Ferrante and Elghobashi [38] examined application of the E-E model in a DNS study of a microbubble-laden, spatially developing turbulent boundary layer by comparing results with those obtained using the E-L apporach [39, 40]. It was demonstrated that the E-E model was unable to produce the drag reduction observed in predictions of the E-L model due to the absence of accurate bubble concentration predictions in the E-E model. Finally, a Knudsen number was proposed as a criterion for the validity of the E-E model in the DNS of bubbly flows with strong unsteady preferential concentration.

More results obtained using the E-E approach can be found in recent papers in terms of its application to bubble-induced turbulence [41, 42] and lateral void fraction distribution [43].

2.1.3 Eulerian-Lagrangian approach

In the E-L approach, the continuous phase is treated in an Eulerian framework, whereas the motion of individual or groups of bubbles is simulated to move across the Eulerian domain by solving Newton’s second law of motion, accounting for the forces acting on the bubbles, such as the drag, lift, pressure gradient, virtual mass, gravity/buoyancy and inertial forces. Because in the Lagrangian tracking method each bubble trajectory is calculated, the E-L method is able to provide more detailed information for each bubble when compared to the E-E method, and phase interactions can be simulated with a much higher spatial resolution than in the E-E approach. Also, the size of each particle or bubble is independent from other particles, and thus poly-dispersity can be managed easily. However, the bubbles are considered as points so that the bubbles should be smaller than the smallest resolved carrier phase scales. Furthermore, closure relations for interphase forces are needed, which are usually taken from empirical relations derived from experiments or higher-level simulations (e.g. using the IT method). In addition, the accurate calculation of each bubble path can become computationally expensive in large systems with a large number of bubbles.

Over recent decades, the E-L approach has been frequently applied to the simulation of bubbly flows. The models currently available in literature can be classified into three categories. The first is the E-L approach where the continuous phase flow is resolved by

DNS, and that is what is reviewed below. Alternatively, in other work the continuous phase turbulent flow is resolved by means of RANS or LES approaches. Of these, the latter has already been reviewed in literature [44] and hence will not be presented in detail here.

Early E-L studies [45-48] were carried out mainly in two-dimensional domains. The main differences between the works are in the bubble dynamics description, and the coupling mechanism between the phases. For example, Laín et al. [49, 50] proposed a numerical model of turbulent bubbly flow using a two-dimensional E-L approach. They used the k-ε turbulence model, with the dispersed bubble motion simulated within a Lagrangian framework. This coupled methodology was applied to a simple pipe flow with reasonable agreement with experimental data obtained. Although these numerical studies suggested the feasibility of performing simulations of large systems of dispersed bubbles that would complement experiments and assist new model development, the two-dimensional approach was usually successfully applied to dilute bubbly flows only without bubble-bubble interaction considered. With the later development of computer power, three-dimensional predictions of bubbly flows were easily obtained with excellent agreement compared to experimental data, e.g. [51]. More phenomena started to be accounted for, and predicted via DNS and the three-dimensional E-L approach, including bubble spatial distribution, bubble size distribution, local void fraction profile, bubble-bubble interactions, and bubble-induced turbulence in the fluid phase, with some of these studies explained in detail below.

Among the forces that act on a bubble, the lift force plays a decisive role in its lateral movement [52]. Since Mazzitelli et al. [53, 54], more evidence of the importance of the lift force acting on the bubbles in driving both the bubbles’ dispersion and turbulence modification of the fluid induced by the bubbles has been provided. Giusti et al. [55] reported the mutual interactions between microbubbles and turbulence in a vertical channel flow and confirmed previous findings that indicated that gravity and the lift force determine the microbubbles’ distribution in the wall region. Results for a downward flow show that the bubbles are segregated in high streamwise velocity regions due to the lift force, while non-preferential distribution was observed in upward flow, which was perhaps the main finding of their study. The results of Pang et al. [56] also predicted a similar trend in the bubble distribution in a vertical channel, showing that bubbles tend to migrate to the wall region resulting in peak-wall void fraction distributions due to the action of the lift force. Also, both these investigations confirmed the important role played by interphase forces in the motion of bubbles, where the drag force balances the buoyancy force in the direction of the flow, while the shear lift force balances the virtual mass force in the direction perpendicular to the main flow when the bubbles are at steady-state. Although these studies were insightful, they were limited in considering small non-deformable bubbles in very dilute conditions (void fraction is less than 10^{-3}) at a relative low shear Reynolds number ($Re_\tau = 150$), and bubble-bubble interaction was neglected. Due to the limitation of the point approximation in the model, the bubbles need to be smaller than the smallest resolved scale. Hence, most of these studies focused on the flow of microbubbles, as opposed to larger bubble sizes, and studies of their behaviour in turbulence [53, 54, 57-59]. On the other hand, for larger bubbles and larger bubble number densities, the lateral bubble distribution might be altered by the flow induced in the wake of large bubbles, while the same effect is not obvious if the void fraction is significantly lower [60]. The movement of large and deformable bubbles is more effectively simulated using interface tracking techniques that will be considered in Section 2.1.4.1.

Due to the effect of not only the lift force but also the added mass and drag forces, bubble movement can result in preferential accumulation. In a very dilute situation, bubble-bubble interaction and the momentum-exchange between the fluid and the bubbles can be neglected, such that bubble clustering can be expected, as observed numerically in core vortex regions by the Lagrangian particle tracking method [61, 62]. For example, Shams et al. [63] demonstrated a spiral bubble trajectory drawing bubbles toward the vortex centre. However, the underlying physics of preferential concentration in bubbly flows still holds, although it was noted that the lift force effect needed further consideration, particularly in terms of its modelling [1].

Bubbles have a non-negligible effect on the fluid phase when the void fraction becomes greater than 10^{-3}. This effect on the fluid can be accounted for by taking momentum coupling into account in the so-called two-way coupling mechanism. Pang et al. [56] and Molin et al. [64] tested a two-way coupled model to explain and predict bubble effects on liquid-phase turbulence in a vertical channel. Their results showed that the streamwise mean liquid velocity in the central region was enhanced in upflow and decreased in downflow due to the presence of the bubbles. Also, in an upward flow channel, the wall-normal and spanwise turbulence intensities and Reynolds shear stresses were found to be reduced. The study by Liu et al. [65] gives an insight into bubble-fluid interactions and buoyancy effects induced by the bubble phase that enhances/suppresses turbulence fluctuations across the channel in upflow/downflow. Their study was carried out in a vertical channel flow at $Re_\tau = 194$ and switched from upflow to downflow by changing gravitational acceleration from -0.5 to 0.5. They found the effect of the bubble phase to be more obvious when the gravitational acceleration increases.

When the void fraction increases, bubble-bubble interactions (i.e. collisions, coalescence and break-up) play an important role and these are usually implemented via four-way coupling to study bubble dynamics. In the E-L approach, these are implemented with appropriate collision detection, coalescence and break-up models. Most of the studies of these phenomena have focused on the alterations induced by these interactions on the bubble size distribution. The studies by Sungkorn et al. [66, 67] tracked the bubble size distribution by using a lattice-Boltzmann method coupled to a Lagrangian particle tracker with bubble collision, coalescence and break-up considered. In these studies, stochastic inter-particle collisions were detected and the coalescence model of Prince and Blanch [68] was used to compare two characteristic times that govern coalescence, i.e. film drainage time and contact time. The break-up of bubbles was accounted for via a theoretical model derived from the theory of isotropic turbulence form Luo [69]. On the other hand, Darmana et al. [70] implemented Sommerfeld et al.'s coalescence model [71] in a so called PETSc (portable, extensible, toolkit for scientific computation) library. They verified the new model and obtained good validation against data. The proposed model was used to study the effect of coalescence on the hydrodynamics of a bubble column. Results showed that the flow structure, mean velocity and root mean squared (rms) velocities of both phases were altered considerably by bubble coalescence. However, bubble break-up was neglected in their model so that the prediction of the bubble size distribution was overestimated. Based on the model of Darmana et al., Lau et al. [72] accounted for break-up with the model of Martínez-Bazán et al. [73, 74] and obtained different qualitative shapes of the bubble size distribution.

Turbulent drag reduction by bubbles can also be investigated through the Eulerian-Lagrangian approach [75]. Ferrante and Elghobashi [39, 40] used DNS results to explain the physical mechanisms behind reduced skin friction in a microbubble-laden spatially developing turbulent boundary layer with volume fractions ranging from 0.001 to 0.02 and different Reynolds numbers. A decrease of the drag reduction percentage was found with increasing Reynolds number. Also, the microbubble concentration gradient was found to bring about a local positive velocity divergence which creates a displacement of streamwise vortical structures. Pang et al. [76] studied drag reduction by microbubbles in a horizontal channel with DNS. The bubbles' shape was assumed to be spherical at all times because of their small size. Results showed the liquid phase velocity was enhanced by the microbubbles in regions were the bubbles gathered. However, a significant limitation in this work was that bubble coalescence and break-up were neglected, largely due to the low bubble void fraction and the low shear Reynolds number considered.

2.1.4 Interface tracking approach

The interface tracking approach solves the instantaneous Navier-Stokes equations so that the gas and liquid phases are simulated with a very high spatial resolution with no empirical constitutive assumptions. According to how the different phases are identified, the interface tracking approach can be divided into two groups. The first is the marker-and-cell (MAC) method which uses colour functions (or a phase-indicating scalar) with different values in the different fluids. Examples of this method are the volume of fluid (VOF) [77], the level set (LS) [78, 79], the phase-field and cubic-interpolated propagation (CIP) approaches. In the second group, marker points are used to track the interface between the two fluids, and the colour function is reconstructed from the location of the interface. This kind of method using marker points is generally referred to as the front tracking (FT) method. A front tracking algorithm that uses unstructured triangular moving grids to mark the boundary between the two fluids [80], which is an attractive computational method for the simulation of multiphase bubbly flows, has been well validated by Esmaeeli and Tryggvason [81], and Bunner and Tryggvason [82]. The difference between the MAC and FT methods exists in the description of the bubble/liquid phase boundaries. Traditional MAC methods capture the interface on a fixed grid while a Lagrangian surface mesh is generally used for the FT method. Front tracking methods improve the accuracy of the surface tension calculation [83], and have been well validated, improved and used to examine a large number of multiphase bubbly flow problems, see, for example, [81, 82, 84-93], however, it is also the most complex method to implement. On overview of different techniques can be found in [94].

Overall, DNS studies coupled with IT approaches can elucidate the bubble dynamics more deeply with respect to the other methods presented before in this literature review. Here, studies of bubble lateral migration, interfacial force closures and wall effects, and bubble-induced turbulence, for spherical and deformable bubbles using IT methods, are noted and reviewed.

2.1.4.1 Bubble lateral migration

For a single spherical bubble, it is well known that the bubble moves differently in upflow and downflow because the lift force pushes bubble in different directions depending on the flow. In downflow, the weight of the bubble and fluid mixture in the centre of the flow will be high so that the imposed pressure gradient pushes the bubble in the downflow direction. When the bubble moves to the centre, the density of the core region is decreased until the weight of the mixture and the imposed pressure gradient reach a balance. Then, the bubble stops moving and stays in the centre of the flow. The contrary is observed in upflow. When the imposed pressure gradient and the weight of the bubble and fluid mixture are balanced, the bubble will move towards the wall so that the density in the centre is sufficiently enough. For multiple bubbles, this lateral migration results in two bubble distribution trends, i.e. a bubble-free wall layer in downflow and a bubble-rich wall layer in upflow. This has been confirmed in many studies by Tryggvason and co-workers. For example, Lu et al. [92] studied a bubbly flow of buoyancy-driven spherical bubbles in a laminar flow at relatively modest Reynolds number using the FT method. A difference between the void fraction distribution in a channel for the upward and downward flow was found, and it was confirmed that near spherical bubbles were pushed to the wall and away from it depending on the flow direction. Later, these authors extended their DNS study to turbulent downflow in a vertical channel with buoyant bubbles using the same method [95]. Three mean void fractions were examined with the same Reynolds number to study the effect of the mean void fraction on bubble migration and the liquid-phase velocity profile, which indicated that the flow has a particularly simple structure, as in laminar downflow. The main difference was that the boundary between the bubble-layer and wall-layer in turbulent downflow was not as sharp as in laminar flow. Later, DNS of turbulent bubbly downflows were conducted by Lu and Tryggvason [96] with a parallelized FT approach to establish the effect of bubble size on flow properties. Two different bubble sizes with diameters of 31.8 and 38.2 wall units were introduced into the flow. The results indicate that the bubble size has little effect on the bubble distribution and the average vertical velocity profile. The same authors extended this study to two large channel downflows at $Re_\tau = 250$, one with 140 spherical bubbles and another with 119 small bubbles and 1 large bubble. The void fraction was kept fixed to establish whether the simple behaviour observed previously applied to larger systems with higher Reynolds numbers [97]. A minor difference between the overall void fraction profiles was observed, except in the central region of the flow where the large bubble was predicted to move to. This difference between the lateral movement of small and large spherical bubbles was confirmed by Santarelli and Fröhlich [98]. In upflow, small bubbles were observed to move to the near-wall region, while large bubbles remained in the centre of the channel resulting in a bubble-free layer at the wall.

When the bubble becomes deformable, Lu and Tryggvason [99] showed that the reason for the different void fraction distribution observed in [96] was the bubble deformability that reversed the sign of the lift force. However, the results were obtained in a relatively small system with only 21 bubbles and a friction Reynolds number of 127. Similarly, the impact of the deformability of viscous bubbles on the upward bubbly flow rate in a vertical channel was observed using the FT approach and DNS in [100], where a bubble distribution transition was examined by varying the Eötvös number (Eo). Here, the Eötvös number is a dimensionless number and the ratio between the buoyancy and surface tension forces [16], as shown in Eq. (2.1), which means that large bubble deformability is characterized by a large value of Eo. Results showed that a critical Eo exists below which the bubble's deformability has little effect on any bubble transition so that the bubbles remain near channel walls, while for higher Eo values the bubbles are concentrated in the central regions of the channel core.

$$Eo = \frac{g(\rho_f - \rho_d)d_b^2}{\sigma} \tag{2.1}$$

where, ρ_f and ρ_d are the continuous and dispersed phase densities, respectively, d_b is the bubble diameter, and σ is the surface tension.

Apart from the DNS-based work discussed above, a DNS investigation based on stabilized finite elements and an LS approach used to track the air-water interface was carried out by Bolotnov et al. [101]. This study was performed using the Parallel, Hierarchic, higher-order, Adaptive, Stabilized Transient Analysis flow solver (PHASTA). A turbulent bubbly flow with a higher friction Reynolds number of 180 in a vertical channel containing several bubbles was simulated and analysed. As expected, the void fraction distribution of two test cases were found to be consistent with previous pioneering works.

For bubbly flows with high void fractions, bubble clustering has been found to be different from that with a few single bubbles. Early studies by Bunner and Tryggvason showed that spherical bubbles tend to form a horizontal alignment, while a vertical stream was found for deformable bubbles [89, 90]. More precisely, Tagawa et al. [102] demonstrated that the bubble aspect ratio is a key factor in determining bubble clustering phenomenon which is related to the amount of vorticity generated by the bubbles.

2.1.4.2 Interfacial force closures

In both the E-E and E-L approaches, the momentum exchange between the gas and liquid phases requires all empirical force terms to be specified, so that the accuracy of the interfacial force closures is crucial to such numerical simulations of bubbly flows. Typically, the interfacial forces include the lift, drag, virtual mass and turbulent dispersion forces. Amongst these, studies of lift and drag are of great interest due to the fact that the lift force determines the bubbles lateral segregation and the drag force dominates the terminal rise velocity of the bubbles.

Interfacial force closures have been investigated experimentally or via simplified analytical solutions in the literature. This has helped to clarify that the bubble spatial distribution depends on bubble deformability. Less deformable bubbles (i.e. small bubbles) have a lift force towards the walls in an upward channel flow, while large deformable bubbles are concentrated in the channel centre because of their lift forces are close to zero or directed away from the walls. However, bubble size and shape depend on the turbulence level of the carrier phase. Naturally, the problem gets more complicated when the bubble interacts with a turbulent fluid. From the point of view of the drag force, according to the diagram of Grace [103], see Fig. 2.1, the drag on spherical and ellipsoidal bubbles is mainly determined by the viscous drag (low *Re* and *Eo*), whereas large bubbles are complicated as they are wobbling or spherically capped in form. Additionally, the complexity of studying bubble interfacial forces increases with the relative velocity or with the proximity of a wall. Thus far, most of the experimental studies in the literature have focused on air bubbles in water with low *Re* or low *Eo*, that is, mainly on spherical and ellipsoidal bubbles. However, in practice most bubbles will be large and deformable, with high values of *Re* and *Eo*. DNS coupled with IT methods require no assumptions, so that this technique has been used as an important way to establish interfacial force closures for deformable bubbles, and to give insight into the physics behind real bubble behaviour that can be applied in more engineering CFD approaches.

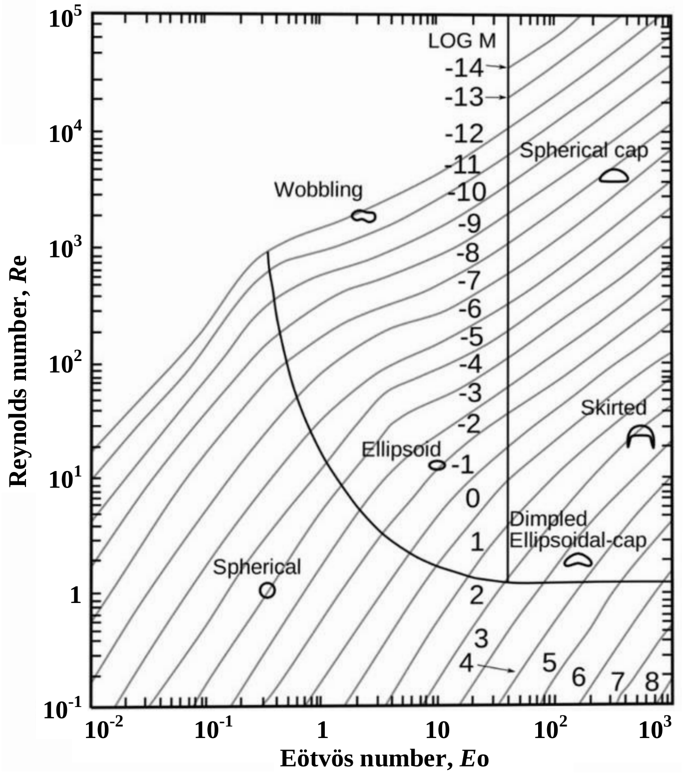

Figure 2.1 Different regimes of bubble shape in the diagram by Grace [103].

Drag force closure: The drag force is the resistance force caused by the motion of the bubble through a liquid. This force can be calculated based on the drag coefficient (C_D) as:

$$\overrightarrow{F_D} = -\frac{1}{2} C_\mathrm{D} A \rho_f \left|\overrightarrow{u_g} - \overrightarrow{u_f}\right| \left(\overrightarrow{u_g} - \overrightarrow{u_f}\right) \tag{2.2}$$

The drag force plays a dominant role in determining the bubble rise velocity, momentum transfer to the liquid phase and bubble clustering phenomenon. The IT method has been used to derive or improve closures for the drag coefficient in various systems from a single bubble [93, 104] to multiple bubble systems [105, 106] in periodic domains, and also for flows with the segregation of small and large bubbles.

Noteworthy, Roghair et al. [106] defined the drag coefficient in a mono-disperse bubble swarm using the local gas fraction and the *Eo* number:

$$\frac{C_\mathrm{D}}{C_{\mathrm{D},\infty}(1-\alpha)} = 1 + \left(\frac{18}{Eo}\right)\alpha \tag{2.3}$$

This drag coefficient model was validated in an Eulerian-Lagrangian framework [107] where good predictions with respect to experimental results were obtained [108]. Furthermore, a refined model was developed for a range of bubble diameters from 1.0 mm to 6.0 mm, accommodating the effect of the liquid phase viscosity:

$$\frac{C_\mathrm{D}}{C_{\mathrm{D},\infty}(1-\alpha)} = \begin{cases} 1+\left(\dfrac{22}{Eo+0.4}\right)\alpha\ (\text{low}-\text{viscosity liquid}) \\ 1+\left(\dfrac{6.612Eo+2.023}{Eo}\right)\alpha\ (\text{high}-\text{viscosity liquid}) \end{cases} \tag{2.4}$$

Moreover, the correlation was further tested in a dense bi-disperse bubble swarm with 8 small bubbles (3.5 mm in diameter) and 8 large bubbles (4.4 mm in diameter), and varying gas fractions from 5% to 50%, in [109]. The results agreed with previous findings with good accuracy.

Lift force closure: The lift force is referred to as the force transverse to the direction of flow when the bubble travels in a shear flow (such as a boundary layer). This force can be calculated from the mean velocity gradient of the carrier phase, the slip velocity and the lift coefficient (C_L) as:

$$\overrightarrow{F_\mathrm{L}} = -C_\mathrm{L}\rho_f\left(\overrightarrow{u_g}-\overrightarrow{u_f}\right)\left(\nabla\times\overrightarrow{u_f}\right) \tag{2.5}$$

Most lift force investigations have been carried out to establish which parameters determine the lift coefficient. For spherical bubbles, the study by Legendre and Magnaudet [110] clearly demonstrated that although the lift force is different at low and high Reynolds numbers, the following equation was valid over the entire range of Reynolds numbers studied (see details in Section 3.2.1):

$$C_\mathrm{L} = \sqrt{\left[C_\mathrm{L}^{\text{low }Re}(Re_B, Sr_B)\right]^2 + \left[C_\mathrm{L}^{\text{high }Re}(Re_B)\right]^2} \tag{2.6}$$

The numerical study of Bothe et al. [111] using the VOF method related the lift coefficient to a modified Eo_H number based on the bubble horizontal diameter. The authors tested different values of the bubble diameter, as well as the liquid phase viscosity, surface tension, grid resolution, shear rate and gravity force. A value $C_\mathrm{L} \sim 0.5$ was found appropriate at low Eo, in agreement with analytical studies [112]. The lift force was found to change for deformable bubbles, with the lift force being negative for large bubbles with asymmetric deformations. The numerical results of Adoua et al. [113] also revealed that due to the vorticity generated at the bubble surface, the sign of the lift force may change, although this effect only happens when the bubble aspect ratio is greater than 2, the Reynolds number is larger than 100 and the dimensionless shear rate is less than 0.1. Later the results of Dijkhuizen et al. [114] were used to extend the model of Legendre and Magnaudet [110] incorporating the effect of deformability. The proposed equation not only cover spherical bubbles, but also large deformable bubbles:

$$C_{\mathrm{L}} = \min\left(\sqrt{\left[C_{\mathrm{L}}^{\mathrm{low}\,Re}(Re_B, Sr_B)\right]^2 + \left[C_{\mathrm{L}}^{\mathrm{high}\,Re}(Re_B)\right]^2}, 0.5 - 0.11 Eo_{\mathrm{H}} + 0.002 Eo_{\mathrm{H}}^2\right) \tag{2.7}$$

2.1.4.3 Bubble-induced turbulence

Bubble-induced turbulence (BIT) refers to the effect a bubble has on the carrier phase due to interactions between the gas and liquid phases which affect the level of turbulence in the carrier fluid. Accurate BIT prediction is dependent on the lateral phase distribution. More specifically, the fluid mean velocity gradient depends on the fluid turbulence so that the lift force is also affected. In bubbly flow, the bubble generated vorticity is normally proportional to the local bubble interface curvature and, accordingly, deformable bubbles produce more turbulent vorticity than spherical bubbles. The mechanism of BIT generation can be described in terms of time-averaged phase velocities and rms of the fluctuating velocities, in addition to the turbulence kinetic energy (TKE) and the energy dissipation rate of the carrier phase. So far, most studies that used IT methods to study this phenomenon dealt with small numbers of bubbles, up to thousands of deformable bubbles in laminar flow, although few papers considering a turbulent carrier phase have been published.

For spherical bubbles, apart from the reviewed studies on BIT using the E-E approach discussed in Section 2.1.2, and the E-L approach in Section 2.1.3, IT methods have also been used. For example, Bolotnov et al. [101] clearly showed that the carrier phase turbulence was altered by additional velocity fluctuations induced by near-spherical bubbles (d_b = 0.9 mm, Eo = 0.11) in a fully periodic domain. The BIT phenomenon enhances the liquid phase mean velocity, TKE and turbulence energy dissipation rate compared to the single-phase flow. In an upward channel flow, Lu and Tryggvason [97] considered one large bubble in a small bubble swarm. The results obtained explained the increase of TKE in the channel centre due to the generated vorticity in the bubble wake region. Another noteworthy study with large numbers of bubbles was by Santarelli and

Fröhlich [115], again in an upward flow channel configuration. In the paper, both dilute and dense bubble swarms with spherical bubbles (d_b = 1 mm, Eo = 0.3) were considered by means of an immersed boundary method. The geometry dimensions were selected to be larger than those commonly used in other literature studies so that large-scale flow features introduced by the presence of bubbles could be addressed. The velocity fluctuations in the continuous phase were found to be enhanced considerably by the bubbles, and to a larger extent in bubbly flows with higher void fractions. Furthermore, extension of this work by Santarelli and Fröhlich [98] addressed the influence of spherical bubble size and bidispersity on the continuous liquid phase. It was found that liquid phase elongated flow structures were enhanced by large bubbles, and to a lesser extent by small bubbles, at the same void fraction, while the bidisperse bubble swarm case intemediate between the two. Also, the increase in turbulence in the liquid phase was greater for the large bubbles.

Previous studies of deformable bubbles suggest that these alter the liquid phase turbulence more than spherical bubbles. In laminar flows, for example, Bunner and Tryggvason [90] analysed the kinetic energy spectra and concluded that ellipsoidal bubbles provided a much stronger contribution to the velocity fluctuations in the liquid phase than spherical bubbles at a Reynolds number of 26. Similarly, in a laminar flow at a higher Reynolds number of 127, Lu and Tryggvason [99] demonstrated differences in fluid mean and rms velocities for different levels of bubble deformation. In the recent decades, simulations have also been conducted with high Reynolds numbers and larger geometry in order to consider differences with respect to the smaller systems considered previously. A turbulent example can be found in [101], where a large deformable bubble was injected into a turbulent channel flow at a shear Reynolds number of 180. The comparison between cases with nearly spherical bubbles and a large deformable bubble demonstrated that the large deformable bubble introduced stronger turbulence in the surrounding liquid. More recently, Feng and Bolotnov [116] studied different bubble surface tensions, so different Weber numbers (*We*) that quantifies bubble deformability. Not surprisingly, the BIT generated by the most highly deformable bubble of the cases studied, with a *We* of 3.39, gave the greatest enhancement in fluid turbulence.

2.1.5 Bubbles collision and coalescence

Bubble collision and the processes of bubbles coalescence and break-up govern the bubble size distribution and the interface density in bubbly flows. Because of their importance, modelling methods for collision, coalescence and break-up are reviewed in this section, specifically in the context of the Eulerian-Lagrangian approach.

Most studies have considered only bubble collisions induced by fluid turbulence, neglecting those due to global velocity-gradients, eddy-capture, buoyancy and wake effects. In general, models for collisions between bubbles can be classified as: (i) direct collision, e.g., soft sphere collision [117] and hard sphere collision [118]; and (ii) statistics-based collision, e.g. stochastic, inter-particle collision models introduced by Sommerfeld [119]. The soft sphere collision model is solved by numerical integration of the bubble motion equations, including all forces from other bubbles, which accounts for all collision possibilities. In contrast, the hard sphere collision model assumes only binary collisions of rigid bubbles and the post-collision velocities and positions are determined by the momentum conservation law. Due to their physics, the computational time needed to detect soft sphere collisions is much greater than that for the hard sphere model. However, for dispersed bubbly flows, the assumption of only binary collisions is normally sufficient [120]. In addition to collision detection, the modelling of bubble coalescence requires determination of whether a collision results in a coalescence, or in the two bubbles bouncing off each other after the collision [121]. Numerous models are available to model coalescence that have been recently summarized in the comprehensive work of Liao and Lucas [122]. A variety of mechanisms have been identified in the literature for bubble coalescence, including the film drainage model, the kinetic collision model and the critical approaching velocity model, which were summarized below.

2.1.5.1 Film drainage model

The most widely used model is the film drainage model, which predicts the coalescence efficiency from two characteristic time scales, i.e. the film drainage time that should be longer than the collision contact time for coalescence to happen [121]. In this model, the coalescence process can be described as follows: (i) the bubbles collide; (ii) draining of a thin liquid film trapped between the colliding bubbles occurs; and (iii) film rupture occurs when the film thickness becomes lower than a critical value [121, 123, 124].

Contact time. Many attempts have been made to model the film drainage mathematically [68, 71, 125]. According to Chesters [121, 126], the contact time can be written in terms of the viscous or the inertial collision contact time depending on whether the bubble Reynolds number is much smaller or much larger than unity, respectively. In laminar flow, the collisions are usually considered as viscous. The contact time is expected to be inversely proportional to the characteristic rate of strain in the smallest eddies:

$$t_{contact} \sim \left(\frac{\varepsilon}{\nu}\right)^{-\frac{1}{2}} \tag{2.8}$$

For inertial collision, in contrast, the bubbles are brought together by the flow, and separate from each other after collision if coalescence does not occur. The collision time, however, is normally less than the time for two bubbles to pass one another. Chesters [121] gave the interaction time from the onset of bubble flattening due to collision up to the point at which the bubble motion is arrested:

$$t_{contact} \cong \left[\frac{\left(\frac{4\rho_d}{3\rho_f}+1\right)\rho_f r^3}{2\sigma}\right]^{\frac{1}{2}} \tag{2.9}$$

Kamp et al. [125] proposed a model of the coalescence probability of equal to unequal bubbles, taking bubble-turbulence and bubble-bubble interactions into account. Model predictions were validated against experimental results for cases where bubble collisions were only induced by turbulence. They gave the contact time by assuming a balance between the increasing surface free energy and the corresponding reduction in the kinetic energy of the system:

$$t_{contact} = \frac{\pi}{4}\left(\frac{8\rho_f C_{\mathrm{VM}} r_{eq}^3}{3\sigma}\right)^{\frac{1}{2}} \tag{2.10}$$

$$r_{eq} = 2.0\left(\frac{1}{r_i}+\frac{1}{r_j}\right)^{-1} \tag{2.11}$$

Here, r_{eq} is an equivalent bubble radius of two colliding unequal sizes bubbles of r_i and r_j, and C_{VM} is the virtual mass coefficient.

Other researchers proposed simplified models of bubble interaction time which are also popular in the literature. For example, in the framework of Sommerfeld et al.'s [71] work, which has been widely used [70, 72, 127-132] together with the drainage model of Prince and Blanch [68], the bubble contact time is considered to be directly proportional to a deformation distance divided by the normal component of the collision velocity:

$$t_{contact} = \frac{C_c r_{eq}}{u_{\mathrm{n}}} \tag{2.12}$$

Here, C_c is a calibration constant which determines the deformation distance as a fraction of the effective bubble radius, and u_{n} is the normal component of the relative impact velocity.

Film drainage time. In the film drainage model, the film drainage time quantifies the time that is required for the fluid trapped between the bubbles to drain enough for film to rupture to occur. In Chesters' studies [121, 126], the film drainage time was derived in terms of different rigidity and mobility of the interfaces. With regards to the concept of interface mobility, the surface of clean bubbles is usually considered to be fully mobile, while that of contaminated bubbles is fully immobile. In their assumptions, for two non-deformable colliding bubbles, the drainage time can be expressed as:

$$t_{drainage} = \frac{3\pi\mu_f}{2F} r_{eq}^2 \ln\left(\frac{h_0}{h_f}\right) \tag{2.13}$$

Here, μ_f is the dynamic viscosity of the continuous phase, h_0 and h_f are the initial and critical film thickness, and F is the compression force between bubbles ($F \sim 2^{8/3}\rho_f\varepsilon^{2/3}(r_1+r_2)^{2/3}r_{eq}^{2}$). However, this model works only for very small bubbles (bubble diameter < 1 mm). They also extended the model to the collision of two deformable bubbles with immobile interfaces. In these systems, such as those with extremely high dispersed-phase viscosities or a surfactant soluble in the continuous phase, the drainage time can be specified from the parallel-film model on the basis proposed by Mackay and Mason [133]. If F is constant, then:

$$t_{drainage} = \frac{3\mu_f F}{4\pi\sigma^2} r_{eq}^2 \left(\frac{1}{h_f^2} - \frac{1}{h_0^2}\right) \tag{2.14}$$

For deformable bubbles with partially-mobile interfaces, the drainage time can be related by assuming a quasi-steady creeping flow approximation and a constant F:

$$t_{drainage} = \frac{\pi\mu_d F^{\frac{1}{2}} r^{\frac{3}{2}}}{2(2\pi\sigma)^{\frac{3}{2}}} \left(\frac{1}{h_f} - \frac{1}{h_0}\right) \tag{2.15}$$

Here, μ_d is the dynamic viscosity of the dispersed phase.

In a fully-mobile interface system, the viscosity of the dispersed phase is small enough so that the drainage time can be assumed to not be controlled by the dispersed phase. For such complicated systems, the drainage regime includes both viscous and inertial control terms [134]. Two limits have been considered in the literature, i.e. only viscous control and only inertial control, which can be specified as below:

$$t_{drainage} = \frac{3\mu_f r}{2\sigma} \ln\left(\frac{h_0}{h_f}\right) \tag{2.16}$$

$$t_{drainage} = \frac{\rho_f u_{rel} r^2}{8\sigma} \ln\left(\frac{h_0}{h_f}\right) \tag{2.17}$$

$$u_{rel} = \sqrt{u_i^2 + u_j^2} \tag{2.18}$$

Here, u_{rel} is the relative velocity calculated from the centres of colliding bubbles. To apply the above drainage time equation to bubbles in turbulent flows, the drainage regime is given as:

$$t_{drainage} = \frac{\rho_f u_{rel} r^2}{2\sigma} \tag{2.19}$$

Numerous studies have been based on the mechanisms proposed by Chesters. However, only inertial collisions by turbulent fluctuations were generally considered, based on classical theories of isotropic turbulence. Luo et al. [69] proposed a model similar to the equation above for bubbles of different sizes r_i and r_j in turbulent flows. The model shows that the drainage time is shorter if the approaching velocity is low:

$$t_{drainage} = \frac{2\rho_f u_{rel} r^2}{\left(1 + \frac{r_i}{r_j}\right)^2 \sigma} \tag{2.20}$$

Other than Chesters [121], the model by Prince and Blanch [68] is one of most widely used in the literature. Prince and Blanch considered bubble collisions due to turbulence, buoyancy, and laminar shear, and neglecting the influence of the viscosity obtained the drainage equation below (Eq. (2.21)). This model, however, is limited to the coalescence of clean bubbles with the diameter of the contact surface equal to the bubble diameter, which could be an overestimation.

$$t_{drainage} = \sqrt{\frac{r_{eq}^3 \rho_f}{16\sigma}} \ln\left(\frac{h_0}{h_f}\right) \tag{2.21}$$

2.1.5.2 Kinetic collision model

The kinetic collision model was firstly developed by Howarth [135, 136]. In this ‘energy model’, the occurrence of coalescence only depends on the impact of the colliding bubbles, i.e. the relative velocity along the line connecting the centres of two colliding bubbles that should be over a critical value. Based on this hypothesis, Sovová [137] proposed a model where coalescence only occurs when the kinetic collision energy E_{kin} exceeds the surface energy E_{s}.

The surface energy of the bubble is proportional to the interfacial tension and the bubble surface area:

$$E_{\mathrm{s}} = 4\sigma \left(\frac{\pi}{6}\right)^{\frac{2}{3}} \left(r_i^2 + r_j^2\right) \tag{2.22}$$

The kinetic collision energy E_{kin} is obtained from the momentum balance during collision [138], being proportional to the average volume $\overline{V}$ ($\overline{V} = V_i V_j / (V_i + V_j)$) and the relative velocity of two colliding bubbles u_{rel}:

$$E_{\mathrm{kin}} = \frac{2\pi}{3} \rho_d u_{rel}^2 \frac{r_i^3 r_j^3}{r_i^3 + r_j^3} \tag{2.23}$$

2.1.5.3 Critical approaching velocity model

Another coalescence model is the critical approaching velocity model, according to which the approach velocity between the bubbles must be small enough to lead to a coalescence [139]. This critical velocity for coalescence can be obtained experimentally.

2.2 Experimental research on bubbly flows and validation datasets

2.2.1 Pipe flows

In this section, a review of experimental measurements of bubbly flows in pipes will be presented, starting from 1975 when detailed measurements started to be gathered. Table 2.1 summarizes the experimental databases and the ranges of parameters investigated.

Table 2.1 Summary of experimental studies of bubbly flows in pipes.

Reference	Pipe diameter (mm)	Pipe length (mm)	Bubble diameter (mm)
Serizawa et al. [140]	60	2,100	3.5–4
Serizawa et al. [141]	60	2,100	3.5–4
Serizawa et al. [142]	60	2,100	3.5–4
Sato and Sekoguchi [143]	34.8	3,000	0.3
Theofanous and Sullivan [144]	60	1,960	3.6
Van Der Welle [145]	100	3,000	1–10
Wang et al. [146]	57.15	Not explicitly given	Not explicitly given
Hesketh et al. [147]	38	6,000	2–7
Liu and Bankoff [148]	38	2,800	2–4
Liu and Bankoff [149]	38	2,800	2–4
Ohnuki and Akimoto [150]	48	2,000	Not explicitly given
Nakoryakov et al. [151]	14.8; 42.3	6,500; 5,000	2.2–2.4
Kashinsky and Randin [152]	42.3	4,800	0–1.71
Yoneda et al. [153]	155.2	1,200	Not explicitly given
Guet et al. [154]	72	18,000	4–10
Guet et al. [155]	72	18,000	4–10
Fujiwara et al. [156]	44	1,500	0–2
Shen et al. [157]	20	24,000	Not explicitly given
Descamps et al. [158]	50	7,000	3–25
Shawkat et al. [159]	200	9,560	1–6
Shawkat et al. [160]	200	9,560	1–6
Nakagawa et al. [161]	44	1,500	1.7; 2.6
Shawkat and Ching [162]	200	9,560	3–6
Lelouvetel et al. [163]	44	2,200	1–3.38
Smith et al. [164]	102; 152	3,060; 2,736	Not explicitly given
Lelouvetel et al. [165]	44	2,200	1

Serizawa et al. [140, 141] firstly performed experimentally studies of bubbly flows in a vertical pipe of 60 mm diameter and 2100 mm length at atmospheric pressure. They measured the phase distribution and the velocities of the bubbles and water. The maximum void fraction was observed in the wall region, while the gas-phase distribution was nearly uniform in the central region. In the same year, an experimental study of turbulent bubbly flows with heat transfer was carried out by the same group. The results highlighted the remarkable impact of the turbulent velocity components of the liquid phase in the transport processes [142]. However, there were many limitations in the estimation of bubble size and velocity distributions due to uncertainties in gathering measurements using a resistivity probe. Van Der Welle [145] investigated vertical air-water upward flows for void fractions between 0.25 and 0.75, and found the void fraction profiles appeared to have a local maximum in the pipe centre region, whereas local maxima close to the wall were absent. Later, Wang et al. [146] measured air-water upflows and downflows in a circular pipe. The distinct peaks in void fraction in the centre region and wall region were observed for the downward and upward flows, respectively. After these studies, Liu and Bankoff [148, 149] experimentally studied an air-water bubbly upflow in a circular pipe of 38 mm diameter under a range of flow conditions and local void fractions. They used hot film anemometry (HFA) probes to measure liquid local velocities and turbulent stresses, and a miniature dual-sensor resistivity probe to obtain the gas parameters (e.g. radial profiles of void fraction, bubble velocity and bubbly size). Hot film anemometry is a technique commonly used the perform the velocity measurement in the fluid flows, based on the relation between the heat flux from an electrically heated sensing element placed in a flow and the local fluid velocity. The results showed that turbulence is increased by increasing the gas flow rate while keeping the liquid flow parameters constant, with turbulence also increased in the wall region but reduced in the core region by increasing the liquid flow rate at constant gas flow rate. The data obtained were also compared with the predictions of Wang et al. [146] and Sato and Sekoguchi [143] under the same flow conditions, and fairly good agreement between predictions and experiments was obtained. Ohnuki and Akimoto [150] investigated the two-phase flow along a vertical pipe of 48 mm diameter, with a ratio of pipe length to flow path of 4.2, mainly focusing on the effect of two air injection methods, namely porous sinter injection and nozzle injection. The flow pattern, axial distribution of differential pressure and radial distribution of local void fraction were measured in the tests. In 2000, the same authors investigated the dependency of gas-liquid two-phase flow on the pipe dimensions in an upward vertical pipe of 20 mm diameter and a ratio of pipe length to diameter of 61.5 [166].

Before the study of Nakoryakov et al. [151], most attention had been focused on the study of co-current upward gas-liquid flows. Nakoryakov and co-workers conducted both turbulent downward and upward flow experiments in 42.3 mm and 14.8 mm diameter pipes, respectively. In their work, the existence of a universal near-wall velocity distribution was found in the downward bubbly flow. In the downward flow, turbulent fluctuations were reduced when compared to a single-phase turbulent flow. Kashinsky and Randin [152] measured some local characteristics (i.e. wall shear stress, local void fractions, liquid velocity and velocity fluctuations) in a vertical 42.3 mm inner diameter pipe. They focused on a downward bubbly flow and parameters measurement in the near-wall region that had not been studied before. Their research found that the wall shear stress become larger for larger bubbles, and higher than in a single-phase flow with the same liquid velocity. A reduction in the velocity fluctuations in the carrier fluid was also observed with respect to the single-phase flow case. Guet et al. [154, 155] examined a vertical upward bubbly flow in a 72 mm diameter and 18 m length pipe to study the effect of bubble size on the gas-lift efficiency, and the radial void fraction and phase velocity profiles. The liquid flow rate was kept low, and various bubble diameters were tested during the experiment. Finally, drift-flux model parameters were developed and the model validated against the experimental data. Descamps et al. [158] investigated the influence of bubbles on the wall shear stress for bubbly flows in a vertical upward pipe. The bubbles travelling close to the wall were shown to have a zig-zag motion, which resulted in time and space oscillations of the thickness of the liquid layer between the wall and the nearest bubbles, this effect being most pronounced for smaller bubbles since in this case more bubbles were present in the near-wall region. Mendez-Diaz et al. [167] analysed a vast experimental database and proposed a criterion to predict the radial void fraction distribution in an upward bubbly pipe flow using critical values of the Reynolds and Weber numbers for the transition from wall to core peak in void fraction. The criterion proposed was also validated against literature data and their own experimental results.

A large number of experimental studies have focused on the liquid phase turbulence kinetic energy, and turbulent transfer between the liquid and the gas phase in bubbly flows. Fujiwara et al. [156] performed experiments in an upward pipe flow configuration and investigated the influence of bubbles on the fluid turbulence. In their study, the budget terms of the TKE were evaluated to investigate their influence on the total void fraction and the role of surfactants. An analysis of the mechanisms involved in turbulence modification in bubbly flows can be found in the work of Kataoka and Serizawa [168, 169] who proposed a transport equation for the TKE. Shawkat and Ching [160, 162] also investigated a 200 mm diameter upward bubbly pipe flows and the TKE transfer between the liquid and the gas phases. They proposed a model for the turbulence energy production spectra due to the bubbles. Similar analysis of the TKE in downward bubbly pipe flows can be found in the papers by Lelouvetel et al. [163, 165].

Although the results obtained by different researchers are slightly different due to the different bubble sizes and pipe parameters employed, it can be concluded that in vertical upward flows the bubble and pipe diameters determine the bubble distribution and its influence on the flow. In small or relatively small pipes (pipe diameter < 100 mm), small bubbles (bubble diameter < 5 mm) tend to migrate towards the pipe wall region, where a wall-peak in the void fraction is observed. In contrast, larger or deformable bubbles accumulate preferentially in the pipe centre and produce a core-peak of the void fraction. For upward flows in large pipes, the local void fraction profile is generally core-peaked because of the effect of the lift force and the turbulent dispersion force. In downward flows, small bubbles (bubble diameter < 5 mm) in small-diameter pipes (pipe diameter < 60 mm) tend to move to the central region of the pipe. The average liquid velocity in the pipe centre is reduced by the buoyant bubbles, with an average liquid velocity peak in the wall region where no or few bubbles are present. With regards to bubble coalescence and break-up, many experimental studies have been performed. Hesketh et al. [147], for example, conducted bubble and droplet breakage experiments in turbulent pipe flows, where they found that breakage to form equal-sizes bubbles has the lowest probability of occurrence.

2.2.2 Channel flows

A number of experimental studies have also been carried out for turbulent bubbly channel flows, and these are listed in the Table 2.2.

Table 2.2 Summary of experimental studies of bubbly flows in channels.

Reference	Channel size (mm × mm)	Channel length (mm)	Bubble diameter (mm)
Lance and Bataille [170]	450 × 450	2,000	5
Lunde and Perkins [171]	100 × 100	700	5
Deshpande et al. [172]	150 × 150	2,000	2–12
Murai et al. [173]	100 × 100	1,000	0.6–0.89
Ellingsen and Risso [174]	150 × 150	700	2.5
So et al. [175]	40 × 400	1,600	1
Wu and Gharib [176]	150 × 150	610	1–2
Zenit et al. [177]	20 × 200	2,000	1–2.5
Rensen et al. [178]	450 × 450	2,000	2–5
Luther et al. [179]	450 × 450	2,000	3–5
Martínez-Mercado et al. [180]	200 × 15	1,000	1.2–1.45
Riboux et al. [181]	150 × 150	1,000	1.6; 2.1; 2.5
Martínez Mercado et al. [182]	450 × 450	2,000	4–5
Bouche et al. [183]	1 × 400	800	3.9–4.6
Bouche et al. [184]	1×400	800	3.9–4.2
Sathe et al. [185]	200 × 15	1,000	5
Mendez-Diaz et al. [186]	100 × 50	2,000	1.97–3.7
Bouche et al. [187]	1 × 400	800	3.9–4.6

Lance and Bataille [170] experimentally studied the turbulence of bubbly flows at low void fraction. An analysis of the turbulence kinetic energy showed an increase of this parameter with the void traction. Liu [188] reported a study of the parametric effects of bubble size and the two-phase flow rate on the wall shear stress in a vertical channel. Different bubble sizes were studied, keeping fixed gas and liquid flow rates. It was found that the structure of the flow in the proximity of the wall had a significant effect on the wall shear stress. Deshpande et al. [172] also measured the properties of dilute bubbly flows, including the number size and size of the bubbles and slip velocity using LDV. A similar method for non-dilute flows was also proposed to estimate the local gas fraction and the phase velocities.

The study of Murai et al. [173] used PIV to investigate the inverse energy cascade in two-phase flows with rising buoyant bubbles in a rectangular tank. They compared their measurements with the DNS results of Esmaeeli and Tryggvason [189], finding good agreement and obtaining a relationship between the energy spectrum and the bubble-bubble separation distance.

So et al. [175] measured bubble size and liquid velocity for the flow of mono-dispersed bubbles (bubble diameter 1 mm) with image processing and LDV methods. Three-pentanol at 20 ppm was injected in to the flow to create mono-dispersed bubble distributions. Three bulk Reynolds numbers (i.e. 1350, 4100, and 8200) were tested with void fractions less than 1.2%. Results indicated that the bubbles tended to migrate to the wall region, where the mean velocity profile of the liquid phase became steeper because of the driving force of the bubbles. In addition, turbulence intensity was enhanced in the vicinity of the wall, and the liquid velocity profile flattened in the centre of the channel.

Zenit et al. [177] investigated a channel flow with a small inclination from the vertical (less than 10°). The main contribution of their work was to provide the laminar shear properties of a nearly homogeneous bubble suspension. Rensen et al. [178] examined a fully turbulent bubbly flow by employing the HFA technique proposed by Luther et al. [179] in a rectangular channel geometry. Bubble distribution probability, bubble structure functions and power spectral functions were measured with results showing that the bubbles enhanced the two-phase flow energy, especially at the small scales.

Riboux et al. [181] investigated the agitation caused by rising bubbles with high Reynolds numbers (ranging from 500 to 800 based on the bubble rise velocity) and moderate void fractions. Statistics were recorded by dual optical probe and laser Doppler anemometry techniques with the aim to provide a better description of bubble-induced turbulence. Martínez Mercado et al. [182] first used a three-dimensional PTV method to obtain data on pseudo-turbulence in bubbly flows, in order to study the bubble distribution behaviour and the energy spectra at low void fraction. The method was, however, only applicable to dilute situations.

Bouche et al. [183, 187] studied a homogeneous swarm of high Reynolds number bubbles within a thin channel, finding that bubble velocity is increased with increasing bubble void fraction for bubbles ranging from 3.9 to 4.6 mm. The authors also used this experimental setup to study the influence of liquid agitation on the mixing mechanism [184].

Mendez-Diaz et al. [186] used the HFA technique in a vertical channel to investigate the power spectral density in monodispersed bubbly flows. The setup adopted was similar to that used in the study of Martínez-Mercado et al. [180]. Sathe et al. [185] also carried out an experimental investigation using PIV to measure bubble motion, which was subsequently used to analyse structure functions and the energy spectrum and study bubble-induced turbulence.

Regarding experiments on bubble shape oscillations, Ellingsen and Risso [174] studied bubble and liquid behaviours in a vertical channel. Bubbly flows with fixed bubble diameters were investigated, and the bubbles showed a zigzag path firstly, which later turned into a helical path. Similarly, Wu and Gharib [176] studied bubble shape and path in vertical channel flows. Both spherical and ellipsoidal bubbles were found to maintain a constant shape. Bubbles with diameter less than 1.5 mm moved rectilinearly, while larger bubbles showed a zigzag and spiral trajectory for spherical and ellipsoidal shape, respectively.

2.3 Concluding remarks

The study of dispersed bubbly flows is far more complicated than that of single-phase flow, since the former involves both the microscopic physics of the bubbly phase and larger structures of the carrier phase turbulence.

On one hand, based on the above review of numerical and experimental studies, bubbles smaller than the Kolmogorov length scale (e.g. microbubbles) with a high void fraction are difficult to track properly in experiments. This is simply because current experimental techniques have difficulty in obtaining accurate local instantaneous measurements of the velocity fields of both the carrier and the dispersed phases. In contrast, microbubbles can be easily simulated by the means of DNS or LES, where they are treated as non-deformable spherical points using an Eulerian-Lagrangian approach. However, LES discards the small scales of the flow from the bubble dynamics, leading to an underestimation of the bubble acceleration. DNS of microbubble dynamics does not suffer from this problem. Therefore, DNS-based predictions of microbubble dynamics in different kinds of wall-bounded geometries, such as channels and pipes, are meaningful and allow in-depth understanding of the interaction mechanisms between bubbles and fluid, and bubbles and bubbles.

On the other hand, for large and deformable bubbles, the point particle/bubble assumption is no longer valid and well-established interface tracking methods, such as the volume of fluid technique or the level set method, must be used to predict the interface deformation between the bubble and continuous phases by considering the effects of surface tension and the different viscosities and densities of the two phases. They are therefore able to simulate gas and fluid phases with a very high spatial resolution with no empirical constitutive assumptions. Recent and ongoing developments in computer power make these methods affordable over a significant range of bubble numbers and void fractions. Hence, the use of such techniques to provide first principle computations is expected to grow in future, and to provide ever improving detail of the physical mechanisms at play in bubbly flows that can be used to improve more engineering orientated, and computationally less expensive, predictive techniques.

With the aim of contributing to the gaps in the literature outlined above, the first stage of the work considered in this thesis is devoted to the DNS of microbubble-laden channel and pipe flows coupled to the Lagrangian particle tracking approach. This work considers coupling between the bubbles and the fluid flow up to the level of four-way coupling which has rarely been considered in the literature, and certainly not at the level of detail covered in the present work. In order to achieve this, previous studies are extended to high bubble void fractions with the additional consideration of bubble collision and coalescence. The understanding of microbubble coalescence generated through this work is as a novel addition to the existing literature. Later, the DNS of large and deformable bubbles is performed by means of the volume of fluid method, with a mass density ratio closer to real air bubbles in water, and which is higher, and hence more practically relevant, than alternative literature studies. Special attention is given to bubble lateral movement, the interfacial force coefficient, bubble-induced turbulence, and bubble clustering in bubble swarms. Overall, the present DNS-based studies provide a better understanding of the phenomena involved in bubbly flows down to the smallest scales, with that understanding being also of benefit to the formulation and validation of more pragmatic engineering approaches to predicting such flows.

Chapter 3 Methodology

This chapter is divided into three parts, reflecting the different techniques employed in the work described in this thesis. Firstly, direct numerical simulation (DNS) will be introduced in terms of the governing equations, the numerical solution method and the Nek5000 code employed. Subsequently, the Lagrangian bubble tracker and the modelling of bubble coalescence and break-up will be considered. The final part of the chapter discusses the TBFsolver, a DNS-based code that uses interface tracking based on the volume of fluid method.

3.1 Direct numerical simulation with Lagrangian particle/bubble tracking: Fluid phase

Turbulence is characterized by vortices or eddies with varying length and time scales. In DNS, the computational grid is refined enough to resolve the smallest turbulent scales in the flow, and to capture all the spectrum of turbulent scales, and turbulence energy, as a function of time and space without any assumptions [190]. This is obtained by solving the Navier-Stokes equations numerically. By its nature, DNS relies on accurate numerical methods with maximum efficiency and low numerical dissipation, as well as fine space and time discretisation.

Therefore, one difficulty in using this approach is to determine the DNS spatial mesh and temporal resolution that capture all the desired space and time scales. The computational scale of spatial resolution required is determined by flow physics. As the flow Reynolds number increases, the range of scales increases as well, which is generally expressed as $Re^{9/4}$ [191]. Likewise, the level of turbulent fluctuations within a flow also increases with Reynolds number, implying a requirement for increased temporal resolution as Reynolds number increases. So, fine temporal and spatial discretisation are needed for turbulent flows and, as a result, the computational cost of DNS for turbulent flows is generally expensive. The smallest scale needed to be solved is referred to as the Kolmogorov length scale, $\eta = (\nu^3 / \varepsilon)^{1/4}$ (for kinematic viscosity ν, and dissipation rate of turbulence kinetic energy ε). This scale, however, cannot be captured all the time because of the computational resource limit, particularly for high Reynolds number flow. Some DNS studies reported in the literature, [192, 193] for example, do not have sufficient resolution to capture the Kolmogorov scale, although the results do show good agreement with experimental data. It has been noted, however, that to obtain accurate first and second order statistics, the spatial resolution depends on the energy dissipation spectrum which is usually larger than the Kolmogorov length scale. Literature evidence suggests that resolution of O(η) [190, 194-196], rather than exactly η, is sufficient to obtained reliable statistics.

The spatial resolution is also affected by the numerical solution method employed which can be increased, in the case of spectral methods, by increasing the order of the polynomials used to approximate the unknowns. On the other hand, a good numerical method determines the fidelity of DNS. It is widely accepted that high-order methods are capable of resolving the smallest scales of turbulence. Several high-order methods have been used in the literature, e.g. spectral [197] and spectral element [198] methods, and such methods are undoubtedly those most frequently used as the basis of DNS. However, these methods restrict the type of geometry and grids that can be handled simply. Therefore, the spectral element method uses the division of complex geometries into small elements to overcome this problem.

In this thesis, the spectral element method used is embodied in the Nek5000 code [199]. The specific spatial discretisation of the different geometries employed will be discussed later in Sections 4.2.1, 5.2.1 and 6.2.1, with more details of Nek5000 given below in Section 3.1.2.

3.1.1 Governing equations

In this work, the high order spectral element Nek5000 code [199] is used to reproduce turbulence dynamics. Nek5000 is a Legendre polynomial-based code which solves the governing continuity and momentum balance equations for the fluid phase, written in non-dimensional form.

The non-dimensional continuity equation can be expressed as:

$$\nabla \cdot \boldsymbol{u}^* = 0 \tag{3.1}$$

and the non-dimensional momentum equation as:

$$\frac{\partial \boldsymbol{u}^*}{\partial t^*} + (\boldsymbol{u}^* \cdot \nabla)\boldsymbol{u}^* = -\nabla p^* + \frac{1}{Re_b}\nabla^2 \boldsymbol{u}^* + \boldsymbol{f}_i^* \tag{3.2}$$

Here, $\boldsymbol{u}^*$ is the velocity vector of the fluid flow field, and p^* is the pressure. Re_b is the bulk flow Reynolds number ($Re_b = U_b\,\delta\,/\,\nu$, with fluid kinematic viscosity ν). $\boldsymbol{f}_i^*$ is an arbitrary forcing term that incorporates the imposed pressure gradient used to drive the single-phase flow and feedback from the bubbles to the fluid phase (two-way coupling). All the parameters are normalized by bulk quantities, using the channel half-height δ as the reference length scale and the bulk velocity U_b as the reference velocity scale, which gives the reference time scale as $\delta\ /\ U_b$. The non-dimensional values of velocity, length, pressure, and time are therefore defined as follows:

$$\boldsymbol{u}^* = \frac{\boldsymbol{u}}{U_b} = \frac{1}{U_b}\begin{pmatrix} u \\ v \\ w \end{pmatrix},\quad \boldsymbol{x}^* = \frac{\boldsymbol{x}}{\delta} = \frac{1}{\delta}\begin{pmatrix} x \\ y \\ z \end{pmatrix},\quad \rho^* = \frac{\rho}{\rho_f},\quad t^* = \frac{tU_b}{\delta} \tag{3.3}$$

3.1.2 Nek5000 code overview

Nek5000 developed by Fisher et al. [199] at the Argonne National Laboratory is a computational fluid dynamics solver that solves the non-linear Navier-Stokes equations numerically. Based on its efficient parallelization via message-passing interface (MPI) platform, Nek5000 has been successfully employed for many turbulent problems [200-202], and two-phase particle-laden flows [203, 204], which has been proven to be scaling up to millions of processors. The code is based on the massively parallel spectral element method (SEM) [198], which is a subclass of Galerkin projection methods. Galerkin projection methods are commonly used for the numerical solution of partial differential equations, with other methods, such as finite element and spectral methods, belonging to this class of discretisation approaches. SEM simultaneously takes advantages of the geometrical flexibility characteristic of finite-element methods and the accuracy provided by spectral methods. Therefore, it is well known for its spectral accuracy, favourable dispersion properties and efficient parallelization in minimizing the error of the numerical computation in the energy norm over a chosen space of polynomials [199].

In Nek5000, the computational meshing is flexible and is able to build complex geometries. The domain is divided into a number of hexahedral local spectral elements. To obtain spectral accuracy, Gauss-Lobatto-Legendre (GLL) grid-points are distributed in each spectral element, and extended to 3D in a tensor-product formulation. A Legendre polynomial is employed to solve the incompressible Navier-Stokes equations. The basis chosen for velocity space is typically N^{th}-order Lagrange polynomial interpolants on GLL points, whereas for the pressure, Lagrangian interpolants of degree N-2 are used on Gauss-Legendre quadrature points. This is what is formally known as the P_N - P_{N-2} SEM discretisation of Maday and Patera [205]. This means the velocity field is calculated on the mesh of all GLL grid-points, whereas the pressure is interpolated on Gauss-Legendre (GL) points only (endpoints are excluded).

The time-stepping in Nek5000 is semi-implicit, with the viscous terms in the Navier-Stokes equations treated implicitly using third-order extrapolation (BDF), whereas the non-linear terms are treated by a third-order extrapolation (EXT3) scheme [206].

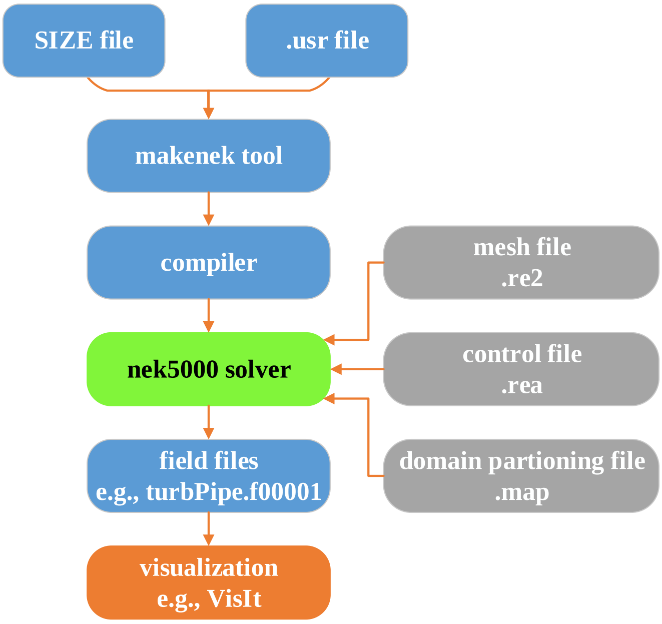

Figure 3.1 Nek5000 code overview.

In Nek5000, each simulation is defined by several files, i.e. .rea file, .usr file and the SIZE file. The setup case procedure is as shown in Figure 3.1. In the SIZE file, the polynomial degree and space dimensions (two- or three-dimensional) of the simulation are specified. The .rea file gives the ability to control runtime parameters, such as the flow Reynolds number, thermal conductivity, number of steps, time-steps, etc., and to specify the output format, namely parameter 66 with negative values for ASCII format (.fld output file) and positive values for binary format (.f%05d output file). Additionally, a .map file is generated by .rea file containing information on how the elements are split across parallel processors. The most important file is the .usr file which is of a set of Fortran subroutines. This allows direct access to all runtime variables, for example, the initial and boundary conditions are set via the subroutines *useric* and *userbc*. More information can be found in the Nek5000 user guide at https://nek5000.mcs.anl.gov/.

3.2 Direct numerical simulation with Lagrangian particle/bubble tracking: Bubble phase

In the Eulerian-Lagrangian method, the trajectory of each discrete dispersed phase element is individually tracked in a Lagrangian fashion. Therefore, as an integral part of this research, a Lagrangian particle tracking (LPT) routine has been developed and interfaced with the Nek5000 code to model the transport of the dispersed phase. An assumption here is that each bubble is spherical and represented by a Lagrangian point. The LPT routine solves the non-dimensional equations of motion for each bubble individually, using a time discretisation equal to that of the fluid solver.

3.2.1 Equations for the bubbles

The bubble motion in the turbulent flow is obtained by solving Newton's second law of motion for each individual bubble. Therefore, the force equation is as given in Eq. (3.4), where pressure gradient, gravity and buoyancy, drag, virtual added-mass and lift forces are chosen to act on the bubbles:

$$\sum \boldsymbol{F}_n = \boldsymbol{F}_p + \boldsymbol{F}_G + \boldsymbol{F}_D + \boldsymbol{F}_m + \boldsymbol{F}_L \tag{3.4}$$

In this force equation, $\boldsymbol{F}_n$ is the total force, $\boldsymbol{F}_p$ the pressure gradient force, $\boldsymbol{F}_G$ the gravity/buoyancy force, $\boldsymbol{F}_D$ is the interphase drag force, $\boldsymbol{F}_m$ is the virtual added mass force and $\boldsymbol{F}_L$ is the lift force. The non-dimensional motion equation of the bubble is therefore:

$$\begin{aligned} \rho_b^* \frac{d\boldsymbol{u}_b^*}{dt^*} = \frac{3C_D}{4d_b^*}\left|\boldsymbol{u}_f^* - \boldsymbol{u}_b^*\right|\left(\boldsymbol{u}_f^* - \boldsymbol{u}_b^*\right) + (1-\rho_b^*)\boldsymbol{g}^* + C_{VM}\left(\frac{D\boldsymbol{u}_f^*}{Dt^*} - \frac{d\boldsymbol{u}_b^*}{dt^*}\right) \\ + \frac{D\boldsymbol{u}_f^*}{Dt^*} + C_L\left(\boldsymbol{u}_f^* - \boldsymbol{u}_b^*\right) \times \boldsymbol{\omega}_f^* \end{aligned} \tag{3.5}$$

where ρ_b^* is the non-dimensional bubble density, $\boldsymbol{u}_f^*$ and $\boldsymbol{u}_b^*$ are the non-dimensional fluid and bubble velocity vectors, C_D is the drag coefficient, C_{VM} the virtual mass coefficient and C_L is the lift coefficient. The non-dimensional gravitational acceleration $\boldsymbol{g}^*$ is only set in the streamwise direction, given the Froude number *Fr*. $\boldsymbol{\omega}_f^*$ the fluid vorticity at bubble position and is given as $\boldsymbol{\omega}_f^* = \nabla \times \boldsymbol{u}_f^*$. The bubble position is obtained from:

$$\frac{d\boldsymbol{x}_b^*}{dt^*} = \boldsymbol{u}_b^* \tag{3.6}$$

where $\boldsymbol{x}_b^*$ represents the coordinates of the bubble position.

The first term on the right-hand side of Eq. (3.5) is the drag force, which is the force exerted by the continuous phase that opposes bubble movement. For rising bubbles at steady-state, the drag force is balanced by the buoyancy force and determines the relative velocity between the bubble and the continuous phase fluid. The drag coefficient C_{D} is obtained from the model of Naumann and Schiller [207], which provides a non-linear correction to the Stokesian drag force. The second term on the right-hand side of Eq. (3.5) combines the effects of gravity and buoyancy forces. The added-mass force characterizes the force acting on the bubbles because of the fluid displaced during the bubble motion. In Eq. (3.5), this is associated with the substantial derivative of the fluid velocity at the bubble position and the total derivative of the bubble velocity. In this thesis, the virtual mass coefficient C_{VM} is set at 0.5, which is a reasonable assumption for spherical bubbles [208]. The pressure gradient force arises because of the presence of pressure gradients in the fluid phase and is given by Maxey and Riley [209]. The lift force is the last term and accounts for the force acting on the bubble in the direction perpendicular to its motion due to the presence of shear in the fluid. The lift coefficient correlation is taken from Legendre and Magnaudet [110], which combines large and small Reynolds number formulations. All the models used are summarized in Table 3.1.

Table 3.1 Equations for force coefficients.

Coefficient	Formula	Reference
C_{D}	$C_{\mathrm{D}} = \frac{24}{Re_B}(1 + 0.15Re_B^{0.687})$ $Re_B = \frac{\lvert u_f - u_b \rvert d_b}{\nu}$	Naumann and Schiller [12]
C_{VM}	0.5	Brennen [13]
C_{L}	$C_{\mathrm{L}} = \sqrt{\left[C_{\mathrm{L}}^{\mathrm{low}\,Re}(Re_B, Sr_B)\right]^2 + \left[C_{\mathrm{L}}^{\mathrm{high}\,Re}(Re_B)\right]^2}$ $C_{\mathrm{L}}^{\mathrm{low}\,Re}(Re_B, Sr_B) = \frac{6}{\pi^2((Re_B Sr_B)^{0.5})}\left[\frac{2.255}{(1+0.2\zeta^2)}\right]$ $C_{\mathrm{L}}^{\mathrm{high}\,Re}(Re_B) = \frac{1}{2}\frac{Re_B+16}{Re_B+29}$ $Sr_B = \frac{\lvert \omega_b \rvert d_b}{2\lvert u_f - u_b \rvert}, \zeta = \left(\frac{Sr_B}{Re_B}\right)^{0.5}$	Legendre and Magnaudet [15]
Fr	$Fr = \frac{u_\tau^2}{g\delta}$	-

Here, Sr_B is the non-dimensional shear rate, and Re_B is the bubble Reynolds number.

3.2.2 Two-way coupling of continuous and dispersed phases

In the framework of two-way coupling, the intrinsic coupling between the motion of the bubbles and the continuous phase should be considered when the bubble volume fraction exceeds 10^{-6} [15]. Previous studies have revealed the nature of interaction between ensembles of bubbles and turbulence via two-way coupling [36]. This interaction is modelled as the momentum exchange between the continuous and the gas phases, and the contribution of the bubbles is applied via the forcing term $\boldsymbol{f}_i^*$ in the momentum equation Eq. (3.2). The backward force from the bubbles to the fluid is calculated as:

$$\boldsymbol{f}_i^* = -\frac{1}{V_b}\sum \boldsymbol{F}_{b,n} \tag{3.7}$$

Since the two phases are simulated in two different reference frames, i.e. the fluid in an Eulerian frame of reference and the bubbles in a Lagrangian frame, coupling is achieved using a mapping scheme which is necessary to correlate the two frames. This scheme allows interpolation of the continuous phase velocity determined on computational grid points close to the bubble centre onto that point. This so called ‘forward coupling’ is necessary to evaluate the forces acting on the bubbles and the bubble velocities. A spectral interpolation tool in Nek5000 was used to evaluate local instantaneous fluid velocities at each bubble position. This code has been validated with good accuracy for Eulerian solutions of Lagrangian particles [210]. In essence, the mapping from point to processor is first carried out. This is because the Nek5000 code runs on distributed memory computers with allocation of computational elements across a set of processors which have the information of local elements only. Then, searching from point to element can be performed in the local processor, with the concerned mesh cell finally mapped. Specifically, the subroutine *findpts* in Nek5000 performs mapping from the global physical position x to the processor via a rectangular mesh (global hash mesh) of the whole domain. The hash mesh is defined by processor numbers and ranges from x^{min} to x^{max}. Accordingly, the processor that potentially has the element inside is identified. After that, the point $x \rightarrow$ element mapping in the located processor is done similarly. The routine *findpts* also returns the result whether the point is found inside an element, on a border, or was not found within the mesh. More details of the interpolation algorithm and its operations can be found in [211].

At the same time, in two-way coupling the impact of bubble motion on the fluid is calculated and added to the continuous phase momentum via Eq. (3.2), this being known as ‘backward coupling’. In the literature, many studies [212, 213] have demonstrated the importance of point force smoothing in two-way coupling. Hence, depending on the Eulerian numerical grid resolution and the bubble diameter, when the bubble diameter is of the order of the spatial resolution, the effect of the bubble should be spread over the surrounded grid points rather than a single grid point, particularly close to wall boundaries. For this purpose, a distribution treatment of the ‘backward coupling’ force via a Gaussian function was adopted, as shown below:

$$g(\boldsymbol{x}) = (2\pi\Delta^2)^{-\frac{1}{2}} e^{-\frac{(\boldsymbol{x}-\boldsymbol{x}_b)^2}{2\Delta^2}} \tag{3.8}$$

$$\int_{-\infty}^{\infty} g(\boldsymbol{x}) = 1 \tag{3.9}$$

In Eq. (3.8), Δ is the standard deviation and $\boldsymbol{x}_b$ is the bubble position. The impact over several grids of one bubble provides a smooth interpolation kernel and makes this approach easily adaptable to arbitrarily shaped grids in Nek5000, which is illustrated in Figure 3.2. This Gaussian function treatment has been shown to behave well for the point force in two-way coupled simulations of polymer-laden turbulent flows [212].

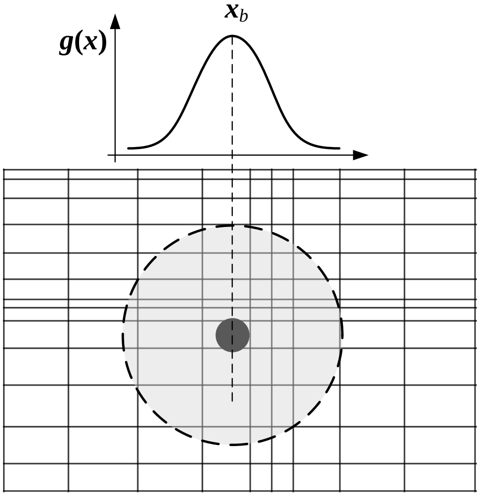

Figure 3.2 Force distribution treatment in two-dimensional Lagrangian and Eulerian two-way coupling by means of a Gaussian function.

3.2.3 Bubble-bubble interaction

When the bubble concentration is higher, bubble-bubble interactions become relevant and need to be taken into account, and this is achieved in four-way coupled simulations. In this E-L study, the deterministic hard sphere collision model was used in which deformation after collision is neglected. Only binary collisions were considered due to the low bubble concentrations examined, and bubble breakup was neglected because of the small bubble size and the low Reynolds numbers considered in this thesis which have been demonstrated to be incapable of breaking up bubbles of the sizes used.

3.2.3.1 Bubble-bubble collision detection

During the very short time steps used in this work, only collisions between neighbouring bubbles are possible and, in order to save computational costs, a three-step collision detection algorithm commonly used in simulating particle-laden flows [118, 215], is adopted in the present work.

Step 1: The geometry is divided into $n \times n \times n$ virtual slices as in Figure 3.3, to eliminate unnecessary checking for collisions between distant bubbles [118, 215]. In each slice, all potential bubble collisions are counted together and evaluated one by one. The slice number n is determined to keep the bubble number in every cell low enough to reduce the computational collision checking time from order $O(N_b^2)$ to $O(N_b)$. This computational time saving is extremely important for the work undertaken in this thesis where bubble numbers are of $O(10^8)$. Such domain decomposition is made possible by the short time step adopted in the DNS, during which bubbles are usually moving over distances of the order of one bubble diameter.

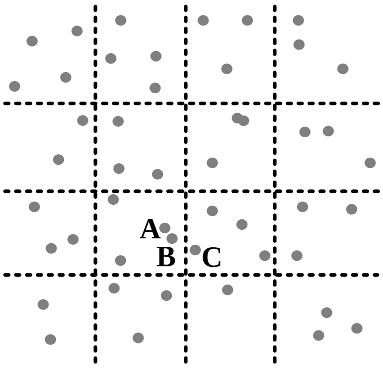

Figure 3.3 Collision searching in virtual slices.

Each bubble is counted and identified using the three Cartesian coordinates x, y and z according to Eq. (3.10). As a result, all bubbles in the same slice are charaterized by the value ($i_{b,x}$, $i_{b,y}$, $i_{b,z}$).

$$i_{b,x} = int\left(\frac{x_b + x_{max}}{\Delta x}\right) + 1$$
$$i_{b,y} = int\left(\frac{y_b + y_{max}}{\Delta y}\right) + 1 \qquad (3.10)$$
$$i_{b,z} = int\left(\frac{z_b + z_{max}}{\Delta z}\right) + 1$$

Here, Δx, Δy and Δz are the slice lengths in x, y and z directions and $x_{\max}$, $y_{\max}$, and $z_{\max}$ are the maximum values of the x, y and z coordinates.

Step 2: Collisions between bubbles in the same slice are checked. An essential precondition for bubble collision is that the two bubbles approach each other during the time step. Two kinds of bubble pair situation are presented in Figure 3.4. According to Yamamoto et al. [214], the bubble velocity in a time step could be seen as constant. Consequently, the possible collision for a pair of bubbles is described by the condition in Eq. (3.11) of the two bubbles approaching each other:

$$\boldsymbol{x}_{b,rel} \cdot \boldsymbol{u}_{b,rel} < 0 \qquad (3.11)$$

Here, $\boldsymbol{x}_{b,rel}$ is the relative distance and $\boldsymbol{u}_{b,rel}$ is the relative velocity between a pair of bubbles.

Only the pairs that satisfy this condition can go to step 3, further helping in reducing the computational time [118, 215]. For example, the left pair of bubbles in Figure 3.4 has the potential to collide, whilst the pair on the right will separate from one another and are not checked further.

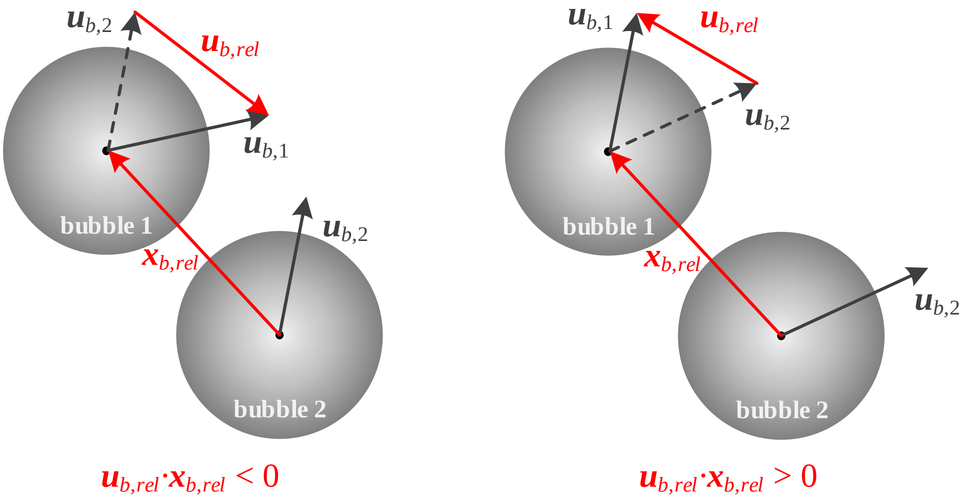

Figure 3.4 Schematic representation of two pairs of bubbles according to Breuer and Almohammed [215].

Step 3: According to Breuer and Alletto [118], once the bubbles are approaching one another, two situations may occur, i.e. the bubbles have already collided or are isolated from each other. For the isolated bubbles, there is a minimum bubble relative distance $\boldsymbol{x}_{b,relmin}$ which should be less than the sum of their radii (e.g. radii are R_i and R_j). The bubbles then need to travel towards one another and achieve the minimum relative distance within one time step for a collision to occur, otherwise collision is impossible. Hence, two further conditions are expressed as Eq. (3.14), with the minimum time Δt_{min} given in Eq. (3.12) and the minimum distance $\boldsymbol{x}_{b,relmin}$ in Eq. (3.13):

$$\Delta t_{min} = -\frac{\boldsymbol{x}_{b,rel} \cdot \boldsymbol{u}_{b,rel}}{|\boldsymbol{u}_{b,rel}|} \tag{3.12}$$

$$\boldsymbol{x}_{b,relmin} = \boldsymbol{x}_{b,rel} + \boldsymbol{u}_{b,rel} \Delta t_{min} \tag{3.13}$$

$$\begin{gathered} \Delta t_{min} < \Delta t \;\&\; |\boldsymbol{x}_{b,relmin}| \leq (R_i + R_j) \text{ (for isolated bubbles)} \\ |\boldsymbol{x}_{b,rel}| \leq (R_i + R_j) \text{ (for collided bubbles)} \end{gathered} \tag{3.14}$$

The collision time Δt_{coll} at which the bubble relative distance $\boldsymbol{x}_{b,rel}$ is equal to the sum of the bubble radii is then calculated if the condition required by Eq. (3.14) is met. The solution of these equations can be expressed as Eq. (3.15):

$$|\boldsymbol{x}_{b,rel} + \boldsymbol{u}_{b,rel} \Delta t_{coll}| = R_i + R_j \tag{3.15}$$

where
$$\Delta t_{coll} = \Delta t_{min}\left(1 - \sqrt{1 - K_1 K_2}\right) \tag{3.16}$$

and
$$K_1 = \frac{|\boldsymbol{x}_{b,rel}|^2 |\boldsymbol{u}_{b,rel}|^2}{(\boldsymbol{x}_{b,rel} \cdot \boldsymbol{u}_{b,rel})^2}, K_2 = 1 - \frac{(R_i + R_j)^2}{|\boldsymbol{x}_{b,rel}|^2} \tag{3.17}$$

Therefore, the normal vector for collision to occur can be written as:

$$\boldsymbol{x}_{b,relcoll} = \boldsymbol{x}_{b,rel} + \boldsymbol{u}_{b,rel} \Delta t_{coll} \tag{3.18}$$

3.2.3.2 Bubble-bubble collision with coalescence

When two bubbles collide, therefore, there are two possible outcomes, i.e. the two bubbles merge and coalesce or they bounce off each other after the collision. In the current Lagrangian particle tracking routine, the film drainage model proposed by Prince and Blanch [68] and the contact model of Sommerfeld et al. [71] were adopted to determine whether bubbles coalesce after they collide. In addition, a different contact time model from Kamp et al. [125] and the energy model from Sovová [137] were also evaluated.

According to the film drainage model, when two bubbles collide a thin liquid film remains trapped between them [121, 124]. In this model, the contact time is the time of interaction between the bubbles, while the drainage time quantifies the time required for the liquid film to drain down to a critical thickness at which film rupture can occur. The coalescence therefore happens only when the bubble contact time $t_{contact}$ is longer than the film drainage time $t_{drainage}$.

The contact time according to Sommerfeld et al. [71] can be written as:

$$t_{contact} = \frac{C_C R_{ij}}{u_n} \tag{3.19}$$

Here, C_C is a constant that determines the deformation distance as a fraction of the effective bubble radius, i.e. the distance that the two bubble centres move further towards each other when the bubbles deform, and can be considered to be 0.25 from comparison with experimental data [71]. u_n is the normal component of the relative impact velocity. The equivalent bubble radius R_{ij} of two different sized bubbles (for radii are R_i and R_j) was taken from Chester and Hoffman [126].

$$R_{ij} = 2.0\left(\frac{1}{R_i} + \frac{1}{R_j}\right)^{-1} \tag{3.20}$$

The contact time from Kamp et al. [125] was also tested. In their model, the contact time is expressed from a balance between the increasing surface free energy of a bubble and the corresponding reduction in the kinetic energy of the system:

$$t_{contact} = \frac{\pi}{4}\left(\frac{8\rho_f C_{VM} R_{ij}^3}{3\sigma}\right)^{\frac{1}{2}} \tag{3.21}$$

The drainage time of Prince and Blanch [68] can be described neglecting the effects due to surfactants and Hamaker forces as:

$$t_{drainage} = \sqrt{\frac{R_{ij}^3 \rho_f}{16\sigma}}\, ln\left(\frac{h_0}{h_f}\right) \tag{3.22}$$

For air-water systems, the initial film thickness h_0 and the final thickness before rupture h_f can be taken as 10^{-4} m and 10^{-8} m, respectively.

The energy model of Sovová [137] has been described in Section 2.1.5.2. This energy model assumes that coalescence only happens when the kinetic collision energy E_{kin}

exceeds the surface energy E_s. Therefore, the equations below were adopted to evaluate whether coalescence occurred:

$$E_s = 4\sigma \left(\frac{\pi}{6}\right)^{\frac{2}{3}} \left(R_i^2 + R_j^2\right) \tag{3.23}$$

$$E_{kin} = \frac{2\pi}{3} \rho_g u_{rel}^2 \frac{R_i^3 R_j^3}{R_i^3 + R_j^3} \tag{3.24}$$

Once coalescence occurs, the new bubble's radius and bubble velocity are calculated from mass and momentum balances:

$$R_{new} = \left({R_i}^3 + {R_j}^3\right)^{1/3} \tag{3.25}$$

$$\boldsymbol{u}_{b,new} = \frac{m_i \boldsymbol{u}_{b,i} + m_j \boldsymbol{u}_{b,j}}{m_i + m_j} \tag{3.26}$$

Here, m_i and m_j are the masses of bubble i and bubble j, respectively.

3.2.3.3 Bubble-bubble collision without coalescence

If the bubbles fail to coalesce, a fully-elastic collision model is adopted to determine bubble post-collision velocities and positions. First of all, the bubble velocities before collision in the direction normal (denoted by an overbar $\overline{}$) to collision are essential and calculated Eqs. (3.27) and (3.28):

$$\overline{u_{n,i}} = \frac{x_{b,relcoll}}{\left|\boldsymbol{x}_{b,relcoll}\right|} u_{b,i} + \frac{y_{b,relcoll}}{\left|\boldsymbol{x}_{b,relcoll}\right|} v_{b,i} + \frac{z_{b,relcoll}}{\left|\boldsymbol{x}_{b,relcoll}\right|} w_{b,i} \tag{3.27}$$

$$\overline{u_{n,j}} = \frac{x_{b,relcoll}}{\left|\boldsymbol{x}_{b,relcoll}\right|} u_{b,j} + \frac{y_{b,relcoll}}{\left|\boldsymbol{x}_{b,relcoll}\right|} v_{b,j} + \frac{z_{b,relcoll}}{\left|\boldsymbol{x}_{b,relcoll}\right|} w_{b,j} \tag{3.28}$$

Here, $u_{b,i}$, $v_{b,i}$ and $w_{b,i}$ are three Cartesian components of bubble i velocity $\boldsymbol{u}_{b,i}$ before collision in x, y and z direction, and similarly for bubble j in Eq. (3.28). $x_{b,relcoll}$, $y_{b,relcoll}$ and $z_{b,relcoll}$ are three Cartesian components of collision normal vector $\boldsymbol{x}_{b,relcoll}$.

According to the fully-elastic collision model [72], only the velocity component in collision-normal direction is changed after collision. Hence, the bubble velocities after collision in the direction normal (denoted by double overbars $\overline{\overline{}}$) to collision are expressed as follows:

$$\overline{\overline{u_{n,i}}} = \frac{\left(m_i - m_j\right)\overline{u_{n,i}} + 2m_j\overline{u_{n,j}}}{m_i + m_j} \tag{3.29}$$

$$\overline{\overline{u_{n,j}}} = \frac{\left(m_j - m_i\right)\overline{u_{n,j}} + 2m_i\overline{u_{n,i}}}{m_i + m_j} \tag{3.30}$$

The bubble post-collision velocities (denoted by superscript $^+$) are:

$$\boldsymbol{u}_{b,i}{}^{+} = \overline{\overline{u_{n,i}}}\frac{\boldsymbol{x}_{b,relcoll}}{\left|\boldsymbol{x}_{b,relcoll}\right|} \tag{3.31}$$

$$\boldsymbol{u}_{b,j}{}^{+} = \overline{\overline{u_{n,j}}}\frac{\boldsymbol{x}_{b,relcoll}}{\left|\boldsymbol{x}_{b,relcoll}\right|} \tag{3.32}$$

Within one time step, the bubble will keep moving after the collision. The updated bubble position (denoted by superscript $^+$) after collision could be calculated as follows:

$$\boldsymbol{x}_{b,i}{}^{+} = \boldsymbol{x}_{b,i} + \boldsymbol{u}_{b,i}(\Delta t - \Delta t_{coll}) \tag{3.33}$$

$$\boldsymbol{x}_{b,j}{}^{+} = \boldsymbol{x}_{b,j} + \boldsymbol{u}_{b,j}(\Delta t - \Delta t_{coll}) \tag{3.34}$$

3.2.4 Bubble-wall interaction

In the current Lagrangian particle tracking routine, if the distance between bubble centre and the wall boundary becomes less than the bubble radius, a bubble-wall interaction occurs during the time step. For bubble-wall interactions, the fully elastic collision model without friction is also applied. Accordingly, only the sign of the wall-normal direction velocity will be changed, whereas the other velocity components remain unchanged. Figure 3.5 shows a schematic representation of an interaction between a bubble and a flat wall. The bubble on the left is considered to hit the wall and the semi-transparent bubble, below the wall, shows the final position without accounting for wall-bubble interaction. In the framework of the fully elastic collision model, the bubble will rebound back into the computational domain at the same distance from the wall. After the collision, the wall-normal velocity component is reversed. Similarly, in pipe flow, when the bubble touches a curved wall, the velocity in the radial direction is reversed, while azimuthal and streamwise components remain unchanged.

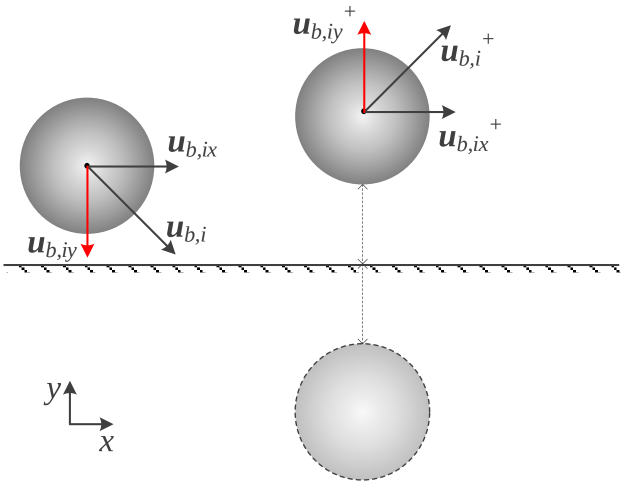

Figure 3.5 Schematic representation of the interaction between bubble and a flat wall.

3.3 Direct numerical simulation with volume of fluid method

In this thesis, large bubbles cannot be reliably predicted using the Lagrangian point particle assumption so that an interface tracking method, based on the VOF method, is employed to model with high resolution single and multiple deformable bubbles. Generally, in this “one-fluid” approach, the governing equations of the whole flow field are solved on fixed grids, while the material properties of the different fluids, on the other hand, are identified by a marker function, this being the indicator function of volume fraction [23]. Accordingly, the interface between two phases is reconstructed by the difference in indicator function values between each phase. The present DNS study of large deformable bubbles is based on a numerical VOF code “TBFsolver” by Cifani [216, 217], who have demonstrated excellent predictions by the code in both 2D and 3D advection simulations, with similar good agreement with the DNS results of turbulent channel downflows of Lu and Tryggvason [95].

In this section, the governing equations taking surface tension into account are introduced firstly. Then, the numerical solution for the governing equation discretisation is discussed. Subsequently, the advection of the fluid interface using the VOF method is given.

3.3.1 Governing equations

The non-dimensional incompressible governing equations written in Section 3.1.1 do not include interface effects, such as surface tension. The surface tension effect is concentrated at the bubble surface boundary only and can be included in the Navier-

Stokes equations using a single term involving a delta (δ) function [23]. Thus, the non-dimensional continuity and momentum equations are expressed as:

$$\nabla \cdot \boldsymbol{u}^* = 0 \tag{3.35}$$

$$\frac{\partial \boldsymbol{u}^*}{\partial t^*} + (\boldsymbol{u}^* \cdot \nabla)\boldsymbol{u}^* = -\nabla p^* + \frac{1}{Re_b}\nabla^2 \boldsymbol{u}^* + \frac{\boldsymbol{g}^*}{Fr} + \frac{1}{We} k \boldsymbol{n}^* \delta(n) \tag{3.36}$$

in which *We* is Weber number, as below, k is the curvature of the interface, $\boldsymbol{n}^*$ is the normal vector to the interface, and *Fr* is the Froude number ($Fr = U_B^2 / gL$, with L the characteristic length of the non-dimensional simulation):

$$We = \frac{\rho_f \delta U_B^2}{\sigma} \tag{3.37}$$

Similarly, all non-dimensional parameters here are based on bulk flow values, as in Section 3.1.2.

The flow field is discontinuous across the interface so that all properties should therefore be interpreted by a generalized indicator function $f(x, y, z, t)$. The indicator function f, in this study, represents the volume fraction of each phase, specifically being 1 if (x, y, z, t) is in the gas phase, and 0 elsewhere, except at the surface boundary which takes f values between (0, 1), as illustrated in Figure 3.6.

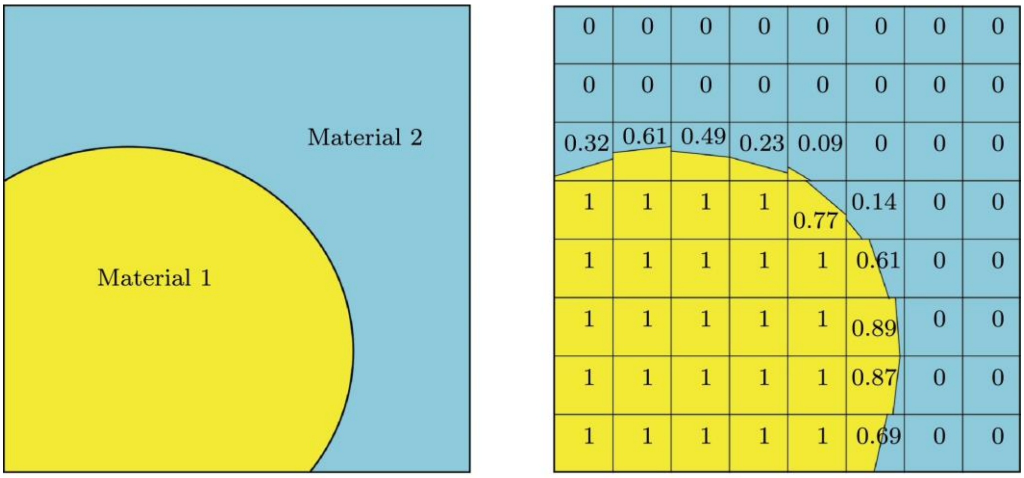

Figure 3.6 Interface between two materials, as demonstrated by Pathak and Raessi [218].

The present study concerns clean bubbles moving in water with the absence of phase change, corresponding to the indicator function f having a zero-material derivative. So, the advection equation can be expressed as:

$$\frac{Df}{Dt^*} = \frac{\partial f}{\partial t^*} + u^* \cdot \nabla f = 0 \tag{3.38}$$

As a result, the non-dimensional local mass density and dynamic viscosity of whole fluid are identified by a linear weighting with *f* as:

$$\rho^* = \frac{\rho_g}{\rho_f} f + (1 - f) \tag{3.39}$$

$$\mu^* = \frac{\mu_g}{\mu_f} f + (1 - f) \tag{3.40}$$

Overall, the Eqs. (3.35), (3.36), and (3.38) describe multiphase bubbly flows where the surface tension force appearing in the momentum Eq. (3.36) applies only in the vicinity of the bubble/water interface.

3.3.2 Discretisation of governing equations

In DNS studies, the continuous variables are represented as discrete and derivatives are approximated by relations between discrete values. To achieve spatial discretisation in the interface tracking scheme, a finite volume method is employed to discretize the governing equations. The finite volume method is successfully employed in many complex computational geometries because of its simplicity and suitability for any type of grid [219-221]. It casts the computational domain into small finite control volumes with a stationary structured mesh and discretizes the momentum and continuity equations in all grid cells. The computational channel geometry, used later, is discretised on a three-dimensional Cartesian grid. Specifically, the staggered grids along the streamwise (*x*) and spanwise (*z*) directions are uniformly spaced, while they are refined at the wall in wall-normal (*y*) direction according to the hyperbolic tangent profile used in [222]. The locations of the staggered grids $y_{s,i}$ and cell centres $y_{c,j}$ are defined by:

$$y_{s,i} = \frac{1}{2} L_y \left(1 + \frac{tanh\left(-\gamma + \frac{2\gamma i}{N}\right)}{tanh(\gamma)} \right), i = 0, \cdots, N \tag{3.41}$$

$$y_{c,i} = \frac{1}{2} L_y \left(1 + \frac{tanh\left(-\gamma + \frac{2\gamma (i-1/2)}{N}\right)}{tanh(\gamma)} \right), i = 0, \cdots, N+1 \tag{3.42}$$

where the locations in Eq. (3.41) at $i = 0, N$ denote the walls of the channel. The locations of $i = 1, \ldots, N$ in Eq. (3.42) refer to the cell centres in channel, and $i = 0$ and $N+1$ are the centres of a layer of ghost-cells outside the channel.

Accordingly, the grid spacing in the wall-normal direction is defined by:

$$h_{c,i} = y_{s,i} - y_{s,i-1}, i = 0, \cdots, N \quad (3.43)$$

$$h_{s,i} = y_{c,i+1} - y_{c,i}, i = 0, \cdots, N + 1 \quad (3.44)$$

3.3.2.1 Storage arrangement of variables

The first thing in discretising the governing equations is defining the storage arrangement of the field variables. For the finite volume method, two kinds of arrangements in the literature are typically used. The first is called the “collocated arrangement” which stores all variables in a cell at the centre of the control volume. This offers an advantage when the boundary conditions are discontinuous or have slope discontinuities [220]. Also, it minimises the number of coefficients because each of the governing equations is discretised in the same control volume. However, it causes difficulties in pressure-velocity coupling, although it satisfies continuity constraints, which can lead to the occurrence of oscillations in the pressure field [223]. To solve such problems, a specific scheme was proposed by Rhie and Chow [224]. The variables, on the other hand, can also be stored on the cell faces, this being known as the “staggered arrangement”.

In the present VOF code, a staggered arrangement is adopted for spatial discretisation in which the pressure p and phase indicator f are defined at the cell centres, while the velocity u is defined at the cell faces. Such a combination provides the convenience of a strong coupling between the velocities and the pressure. Also, the advection velocity of the volume fraction fluxes is easily available at cell faces without any further interpolation.

3.3.2.2 Discretisation of convective and diffusion terms.

In the finite volume approach, the convection term in momentum Eq. (3.36) is discretised in a momentum-conserving divergence form which requires velocities to be interpolated from one staggered location to the cell face of the same or another velocity components. In this study, to acquire velocities on cell faces, the interpolations average over two contiguous points. A simple weighted average with weight of 1/2 is used for the derivatives including $\partial(uu)/\partial x$, $\partial(vu)/\partial y$, $\partial(wu)/\partial z$, $\partial(uw)/\partial x$, $\partial(vw)/\partial y$, $\partial(ww)/\partial z$, and $\partial(vv)/\partial y$. For $\partial(uv)/\partial x$ and $\partial(wv)/\partial z$, the formulation of the interpolation is deduced from [225] which has been verified to be an energy-conserving convective scheme on the non-uniform grid in [222]. For example, the v in the discretisation of $\partial(uv)/\partial x$, is interpolated by a weighing of 1/2, however, the convective velocity u is interpolated by $(h_{c,j+1}u_j + h_{c,j}u_{j+1}) / 2\ h_{s,j}$. In two-phase simulations, as suggested by Lu and Tryggvason [95], the central differencing scheme usually results in an unphysical oscillatory behaviour or disastrous non-convergence in regions where advection strongly dominates diffusion with Reynolds number increasing. So, a third-order upwind scheme, i.e. quadratic upstream interpolation for convective kinematics (QUICK) [226] scheme, is implemented instead of the central differencing scheme to overcome such problems.

Turning to the discretisation of the diffusion term, a second-order central finite difference scheme for all derivatives is employed. The discrete pressure gradient and divergence operators are represented by $\boldsymbol{G} = (G_x, G_y, G_z)$ and $\boldsymbol{D} = (D_x, D_y, D_z)$. The discrete pressure gradient $\boldsymbol{G}$ is a central finite difference operator between adjacent grid points, and the discrete divergence operator $\boldsymbol{D}$ is the finite difference operator between the face values. This scheme results in a second-order accurate discretisation of a Poisson equation on a uniform grid. The discretisation of surface tension is detailed in Section 3.3.3.

3.3.2.3 Time-stepping scheme

To ensure the stability of explicit numerical integrations of the convective and diffusive terms, time-stepping should be performed first. In terms of the Courant-Friedrichs-Lewy (CFL) constraint of the convective term, the time step limits to $\Delta t_{u\nabla u} \propto \Delta x \,/\, u$. On the other hand, the diffusive term may cause a severe limitation on the time step. The viscous term needs a time step $\Delta t_v \propto Re\Delta x^2$. The smallest length scale, in this study, is referred to as the Kolmogorov scale $\Delta\eta \approx LRe^{-3/4}$. For bubbly flows, the stability of the bubble/water interface simulation with surface tension depends on the propagation of capillary waves on the interface. The phase velocity of capillary waves follows from the dispersion relation so that the capillary waves of short wavelength travel faster than ones of long wavelength [227]. This dispersive behaviour of capillary waves strictly limits the time step. Thus, a CFL time step also a plays significant role in the accurate advection of surface tension. According to explicit treatments of surface tension, the time step constraint is imposed as $\Delta t_s \propto \left[\frac{\langle\rho\rangle(\Delta x)^3}{2\pi\sigma}\right]^{1/2}$, with $\langle\rho\rangle = \frac{1}{2}(\rho_f + \rho_b)$. In the present VOF code "TBFsolver", a second-order Adams-Bashforth (AB2) [228] time integration scheme is implemented to ease the difficulty in obtaining Δt_s.

In present code, an implicit treatment of surface tension is also available where the surface tension term is not an explicit function of the fundamental variable $\boldsymbol{u}$ but only indirectly via the volume fraction field. So, that the above constraint is removed. As a result, the time step limitation is orders of magnitude higher than Δt_s [227]. The fractional-step method by Lee et al. [229] is used to integrate the governing equations of Eqs. (3.35) and (3.36) in time. For the convection and diffusion terms of Eq.(3.36), a three-stage Runge-Kutta time-stepping (RK3) scheme [228], is employed to advance the solution in several stages. Because of its stability and the advantage of requiring the minimum amount of computer run-time memory for this class of scheme, this time-stepping procedure has been the most popular explicit method used so far [230]. Each time step has three stages from time level t^n to t^{n+1} during which the index s = [0, 3] is used, corresponding to $s = 0$ for time level t^n, and $s = 3$ for t^{n+1}. The coefficients γ and ξ in the RK3 scheme are taken from [231] as:

$$\gamma_1 = \frac{8}{15},\ \gamma_2 = \frac{5}{12},\ \gamma_3 = \frac{3}{4} \tag{3.45}$$

$$\xi_1 = 0,\ \xi_2 = -\frac{17}{60},\ \xi_3 = -\frac{5}{12} \tag{3.46}$$

However, when $\Delta t < \Delta t_s$, the disadvantage of time consumption required by the RK3 scheme may far outweigh the advantage of an enlarged numerical stability region. For this reason, in this study, it is more efficient to use the AB2 scheme which does not advance the solution in several stages. The code developer has confirmed that using the AB2 scheme is sufficient to carry out the DNS of bubbly flows [216, 217]. This is simply implemented by using one stage with $\gamma = 1.5$ and $\xi = -0.5$. Therefore, all simulations in the present work were performed using a fully explicit AB2 scheme.

3.3.3 Fast Poisson solver

A traditional way to solve the incompressible Navier-Stokes equations is to use the projection method [232]. In the projection method, a Poisson equation for the pressure is solved at each time step. The solution of the Poisson equation occupies most of the computational time in the Navier-Stokes solver. Accordingly, fast Poisson solvers have been proposed in the literature.

Considering time marching from time t^n to t^{n+1} ($\Delta t = t^{n+1} - t^n$), the discrete Poisson equation is:

$$\nabla \cdot \left(\frac{1}{\rho^{n+1}} \nabla p^{n+1}\right) = \frac{1}{\Delta t} \nabla \cdot \boldsymbol{u}^{n+1} \tag{3.47}$$

where ρ is the density, p is the pressure, and superscripts of n and $n + 1$ denote time advancing. A constant coefficient on the left hand side of Eq. (3.47) is essential, however $1 / \rho^{n+1}$ varies in space and time. To this end, Dong and Shen [233] transformed Eq. (3.47) to a constant coefficient equation, and Dodd and Ferrante [234] extended it further to two-fluid Navier-Stokes equations. To facilitate, the equations are provided from [234]. The scheme used here is to split $\frac{1}{\rho^{n+1}}\nabla p^{n+1}$ into a constant term and a variable term:

$$\frac{1}{\rho^{n+1}}\nabla p^{n+1} = \frac{1}{\rho_0}\nabla p^{n+1} + \left(\frac{1}{\rho^{n+1}} - \frac{1}{\rho_0}\right)\nabla \hat{p} \tag{3.48}$$

where ρ_0 is a constant and $\hat{p}$ is an explicit approximation to p at time level $n + 1$ given by linear extrapolation as:

$$\hat{p} = 2p^n - p^{n-1} \tag{3.49}$$

So, a constant coefficient Poisson equation is obtained as:

$$\nabla^2 p^{n+1} = \nabla \cdot \left[\left(1 - \frac{\rho_0}{\rho^{n+1}}\right)\nabla \hat{p}\right] + \frac{\rho_0}{\Delta t}\nabla \cdot \boldsymbol{u}^{n+1} \tag{3.50}$$

so that the equation can be solved by a fast Poisson solver. This formulation significantly reduces the computational cost, and speeds up solution of the Navier-Stokes equations in this study.

3.3.4 Discretisation of surface tension

3.3.4.1 Surface tension model

In this work, the continuous surface force (CSF) model designed by Brackbill et al [235] is employed to estimate the force at the bubble surface. The surface tension force in Eq. (3.36) is described in dimensional form as:

$$\boldsymbol{f}_\sigma = \sigma k \delta \boldsymbol{n} \tag{3.51}$$

where, σ is the constant surface tension, and $\boldsymbol{n}$ is the interface unit normal. The interfacial curvature k is calculated as:

$$k = -\nabla \cdot \boldsymbol{n} \tag{3.52}$$

Eq. (3.51) can be rewritten with the gradient of the volume fraction by replacing the delta function and the unit normal as below. The estimated surface tension force is defined as non-zero only on the faces where the face gradient of the volume fraction $(\nabla f)_f$ is non-zero:

$$\boldsymbol{f}_{\sigma,f} = \sigma k (\nabla f)_f \tag{3.53}$$

3.3.4.2 Curvature model

The curvature k is firstly calculated at cell centres and then interpolated at the cell faces. However, the CSF model is widely known to generate unphysical flow, i.e. spurious currents, near the surface when surface tension forces are dominant [236]. The above problem arises from the numerical balance of the surface tension force and the associated pressure gradient. To reduce these spurious currents, improvements in the accuracy of the curvature computation are required [237]. Traditionally, the curvature k can be interpolated by a standard height function (HF) method [238]. The height function is reconstructed by estimating the interface location, this being the volume integral of the volume fraction. The following example illustrates how the HF method estimates curvature in three-dimensions. Given a case where the largest interface normal component is in the z-direction, i.e. $n_z > n_x, n_y$, a 3 × 3 stencil is constructed in the $x - y$ plane around the interface cell (i, j, k); for each cell in the stencil a height function can be calculated by summing the volume fractions in the z-direction:

$$H_{i,j,k} = \sum_{k-3}^{k+3} f_{i,j,k} \Delta z_k \tag{3.54}$$

Then the curvature is estimated from these nine height functions as:

$$k = \left(\frac{f_z}{|f_z|}\right) \cdot \frac{H_{xx}+H_{yy}+H_{xx}H_y^2+H_{yy}H_x^2-2H_{xy}H_xH_y}{\left(1+H_x^2+H_y^2\right)^{3/2}} \tag{3.55}$$

Here, the derivatives H_x, H_y, H_{xx}, H_{yy}, H_{xy} are calculated using a second-order finite-difference scheme.

The standard HF method, however, suffers from inconsistencies when the radius of curvature of the interface becomes comparable to the grid spacing [239]. So, if the resolution of the bubble shape is low, the HF method is not applicable. In the present study, a generalised height function (GHF) method [239] is used to deal with the case of under-resolved interfaces. The GHF includes a fully-adaptive quad/octree discretisation allowing refinement along the interface. The accuracy and robustness of this technique have been validated by the code developer [216].

3.3.5 Multiple-maker method

In the presence of more than one bubble, the traditional volume of fluid method is not capable of representing multiple interfaces. It results in a numerical coalescence happening once two bubbles collide. In order to handle bubble-bubble interaction properly, in the present code, an individual marker function [240] is assigned to each bubble. For each bubble (i = 1, …, N), the advection equation Eq. (3.38) is solved by a piecewise-linear geometric method using different marker functions. As a result, a collision is physically handled without coalescence. The volume fraction field is then built as below keeping the volume fraction within [0, 1]:

$$f = \max_{i=1,\cdots,N} f_i \tag{3.56}$$

However, the number of marker functions is proportional to the number of bubbles. So the computation is more complicated and expensive as the bubble number increases. Instead, an efficient multiple-marker model [241, 242] is adopted in this study. The improved multiple-marker function is defined locally only in a finite rectangular box which is able to capture a full bubble. This box moves simultaneously along with the bubble, and the box shape depends on the deformation of the bubble in time. This arrangement significantly reduces the computational overhead for multiple bubble cases with large numbers of bubbles.

3.3.6 VOF advection scheme

The volume fraction advection equation is solved by a VOF piecewise linear interface calculation (VOF-PLIC) scheme [243]. The VOF-PLIC algorithm classically includes two steps: interface reconstruction and geometric flux evaluation and interface advection [244].

The interface reconstruction is evaluated in each grid cell by:

$$\boldsymbol{n} \cdot \boldsymbol{x} = a \tag{3.57}$$

where $\boldsymbol{n}$ is the interface normal and $\boldsymbol{x}$ is the position vector. The normal vector to the interface is calculated by summing the volume fractions in the neighbourhood of the cell. Once the interface reconstruction has been evaluated, the geometric fluxes can be computed easily on the regular Cartesian grids.

This VOF advection scheme preserves sharp interfaces and has been demonstrated to have second-order accuracy [245]. However, it is not strictly mass conservative with an error usually less than 0.01% [246].

Chapter 4 DNS of Bubbly Channel Flows with Lagrangian Particle Tracking

4.1 Introduction

To simulate bubble swarms at a large-scale, the channel geometrical configuration is widely studied in the past. The vertical channel flow is confined between two vertical walls and is periodic in the streamwise and spanwise directions. This setup offers not only the possibility to collect statistics over long times and over the two periodic and wall-normal directions, but more closely resembles real industrial applications in terms of the number of particles that can be accommodated [115]. Of particular interest in this and the next chapter is the flow of microbubbles of hundreds of microns in diameter in clean water. Numerical studies of microbubble channel flow have been performed frequently over the last few decades. The following review briefly addresses only those papers that are closely related to the work described in the present chapter.

Early studies were carried out to investigate microbubble distribution in homogeneous turbulence [57] without momentum transfer to the flow, and the reduction by the presence of microbubbles on turbulent skin friction [39, 40, 247-249], demonstrating that microbubbles are preferentially concentrated in regions of low pressure and high vorticity. Other studies have also demonstrated the impact of microbubbles on the momentum transfer rate [76, 250]. Current evidence from DNS studies on the behaviour of microbubbles in turbulent flows generally describes the modulation of turbulence by the microbubbles [64, 251] and the lift force effect on the bubble spatial distribution [53-55]. However, in gas-liquid flows, bubbles also constantly colliding with each other. Depending on the size, velocity and interfacial chemistry of the colliding bubbles, the bubbles may breakup or coalesce [252], changing the total number of bubbles and the bubble size distribution within the flow. These changes often affect the fluid flow field and heat and mass transfer in the system. Hence, a sound understanding of the dynamics of microbubble collision and coalescence is essential to accurately predicting bubbly flows for practical applications. However, detailed knowledge and understanding of bubble collision and coalescence is still lacking. To the author’s knowledge, most research to date in this area has concerned the use of large eddy simulation to study microbubble flows under four-way coupling with coalescence, e.g. [127, 129, 253], with DNS-based investigations of clean bubbles notable scarce.

On the other hand, three methods are available to predict the coalescence probability of interacting bubbles in the literature [122]: the film drainage model [123, 254], the energy model [135] and the critical approach velocity model [139]. In the commonly used film drainage model, when two bubbles approach and touch one another a liquid film is trapped between their interfaces. If the bubbles remain in contact for enough time to allow the film to drain away to a critical rupture thickness, bubble coalescence occurs. Otherwise, the two bubbles bounce off each other. Clearly, this is a complex process to model and is greatly affected by the interface properties. Most numerical studies [127, 252, 255] of microbubble coalescence have focused on surfactant-laden flows and it is well known that tiny amounts of contaminants or surfactants can drastically modify the air-water interface behaviour [256]. Experimental results reveal that clean air bubbles coalesce within milliseconds, much faster than when contaminants are present. Most coalescence models used in simulations in the literature adopt a stochastic collision rate and coalescence efficiency to model the evolution of bubble size. The Eulerian-Lagrangian method tracks bubbles individually and can be used to determine the positions and velocities of bubbles explicitly, so that bubble-bubble collisions can be computed directly without any additional models to predict the bubble size distribution.

For the reasons outlined above, in this chapter effort is devoted to the DNS of microbubble-laden channel flows coupled to the Lagrangian particle tracking approach, where bubbles are assumed non-deformable and spherical. The simulations are first validated against the results of Giusti et al. [55] and Molin et al. [64], and the model is later extended to four-way coupling by accounting for bubble collision and coalescence.

This chapter is organised as follows. First the validation of single-phase channel flows and two-phase bubbly flows is performed by comparing statistical profiles from the DNS and bubble tracker to single-phase [64, 257] and two-phase flow [55, 64] literature results (Section 4.2). Section 4.3 focuses on the simulation of four-way coupling with bubble coalescence considered. In this work, bubble-bubble collisions impact on the simulation results, and the mechanisms of microbubble collision and coalescence at different Reynolds numbers and microbubble diameters are studied in detail.

4.2 Model validation

A validation against literature data is performed to confirm that the current DNS model can be used to obtain reliable turbulence statistics. In this section, the single-phase flow and the bubbly flow are examined in a vertical channel. The present DNS simulations were carried out using the spectral element code Nek5000. As outlined in Chapter 3, the computational domain is discretised into a number of hexahedral local elements on which the incompressible Navier-Stokes equations are solved by means of local approximations based on a high-order orthogonal polynomial basis on Gauss-Lobatto-Legendre (GLL) grid-points. The flow in Nek5000 is governed by dimensionless numbers such as the bulk Reynolds number Re_b and the non-dimensional channel half-width δ. The shear-related quantities, however, are often used in the literature so that the present results are presented in terms of such shear quantities.

Firstly, the computed turbulence statistics and validation of single-phase channel flows at $Re_\tau = 150$ and 395 are discussed, comparing the results with references in the literature. Furthermore, a two-phase channel flow at $Re_\tau = 150$ with microbubbles was simulated under the one-way coupling approximation and compared with the results of Giusti et al. [55] and Molin et al. [64]. Moreover, the two-way coupled model was also validated in the same channel flow against the results of Molin et al. [64].

4.2.1 Single-phase channel flows

The flow domain studied is a vertical channel, modelled with two parallel walls. Streamwise, wall-normal and spanwise directions are denoted by x, y and z, respectively. Periodic conditions were assumed in both the streamwise and spanwise directions. The non-slip condition was imposed at the walls and the flow was driven by an imposed pressure gradient in the streamwise direction determined from the bulk Reynolds number. For the case of $Re_\tau = 150$, the size of the computational domain is $14\delta \times 2\delta \times 6\delta$ ($L_x \times L_y \times L_z$), matching the benchmark simulation of Molin et al. [64]. The geometrical dimensions are also comparable with other literature works on turbulent bubble-laden channel flows [92, 101, 258]. The domain was discretised into $27 \times 18 \times 23$ ($N_x \times N_y \times N_z$) spectral elements and 3.8 M GLL grid-points as shown in Figure 4.1(a), using 7th order spectral elements such as that one shown in Figure 4.1(c). Due the fact that high Reynolds number flows need a higher resolution, a total of 11.2 M GLL grid-points were used to discretise the flow at $Re_\tau = 395$ (see Figure 4.1(b)).

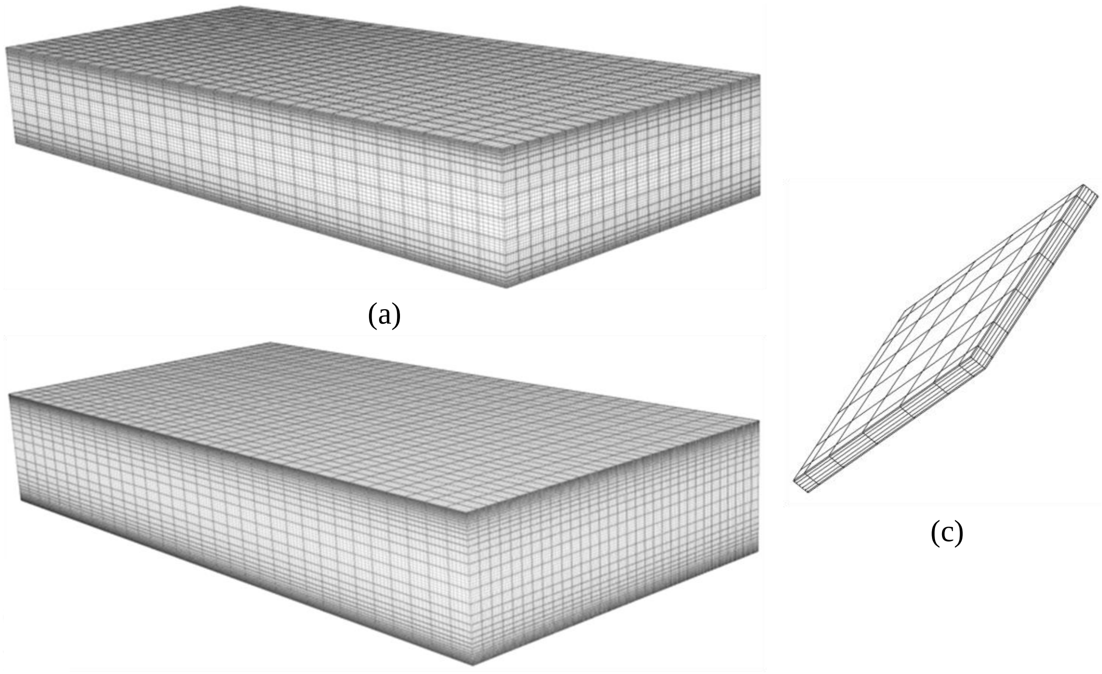

(a)

(b)

(c)

Figure 4.1 Computational grid points for DNS of channel flows at: (a) $Re_\tau = 150$ and (b) $Re_\tau = 395$; and (c) a spectral element in Nek5000.

Initially, the computational mesh resolution is assessed in order to ensure it captures the smallest length scales in the flow. For the flow case at $Re_\tau = 150$, the elements are uniformly distributed in the streamwise and spanwise directions, corresponding to grid spacings in the x direction of $\Delta x^+ = 11.1$ and in z direction of $\Delta z^+ = 5.6$ in wall units. To capture precisely the small-scale vortices in the near-wall region, grid points are clustered in the wall-normal direction, so that on average the largest grid spacing is equal to $\Delta y^+_{\mathrm{c}} = 6.5$, located in the channel centre, while the smallest is in the near-wall region with $\Delta y^+_{\mathrm{w}} = 0.6$ in wall units. Detailed characteristics of the computational grids are summarised in Table 4.1, being reported in non-dimensional units based on the half width δ and shear based units (these are specified with the superscript $^+$, while * is used for variables normalised with bulk quantities in relevant sections, such as in the description of the Nek5000 non-dimensional flow equations in Chapter 3). In order to make the comparisons consistent, all x, y and z values in Table 4.1 represent streamwise, wall-normal and spanwise directions, respectively. The grid resolution is comparable with, or higher than, other available literature studies of the same flow condition.

Table 4.1 Computational grid points of DNS and literature benchmarks for channel flows.

Re_τ	Re_b	References	$L_x \times L_y \times L_z$	$N_x \times N_y \times N_z$	Δx^+	Δy^+_c	Δz^+
150	≈ 2250	Molin et al. [259]	$4\pi\delta \times 2\delta \times 2\pi\delta$	128 × 129 × 128	14.7	3.7	7.4
		Present DNS	$14\delta \times 2\delta \times 6\delta$	216 × 144 × 184	11.1	6.5	5.6
395	≈ 6900	Moser et al. [257]	$2\pi\delta \times 2\delta \times 2\pi\delta$	256 × 193 × 192	10.0	6.5	6.5
		Present DNS	$12\delta \times 2\delta \times 6\delta$	256 × 256 × 256	21.2	10.4	10.6

In this work, the fluid is water with a density of 1,000 kg m^{-3} and a kinematic viscosity of 10^{-6} m^2 s^{-1}. The non-dimensional channel height δ equals 0.02 m, and the shear velocity is 7.5×10^{-3} m s^{-1} based on the shear Reynolds number $Re_\tau = 150$, corresponding to a mean velocity of 0.1125 m s^{-1}. Accordingly, the bulk Reynolds number is approximately 2,250. In contrast, the bulk Reynolds number is calculated as 6,900 for $Re_\tau = 395$.

Initially, single-phase flows were run until fully-developed conditions were reached. Once attained, the flow field was averaged until mean flow statistics independent of time were obtained. Mean values were obtained for the velocity and, to quantify turbulence velocity fluctuations and turbulent stresses, for the square of the velocity fluctuations:

$$\overline{\boldsymbol{u}} = \frac{1}{t_1 - t_0}\int_{t_0}^{t_1} \boldsymbol{u} dt \tag{4.1}$$

$$\overline{\boldsymbol{u}'}^2 = \frac{1}{t_1 - t_0}\int_{t_0}^{t_1} (\boldsymbol{u} - \overline{\boldsymbol{u}})^2 dt \tag{4.2}$$

where t_0 and t_1 are the start and end of the sampling interval.

Confidence in the grid resolution used is confirmed by comparisons with those used in the databases from the literature (see Table 4.1). Time- and space-averaged results normalized by the shear are compared with the DNS database of Molin et al. [64] at Reynolds number $Re_\tau = 150$ in Figure 4.2.

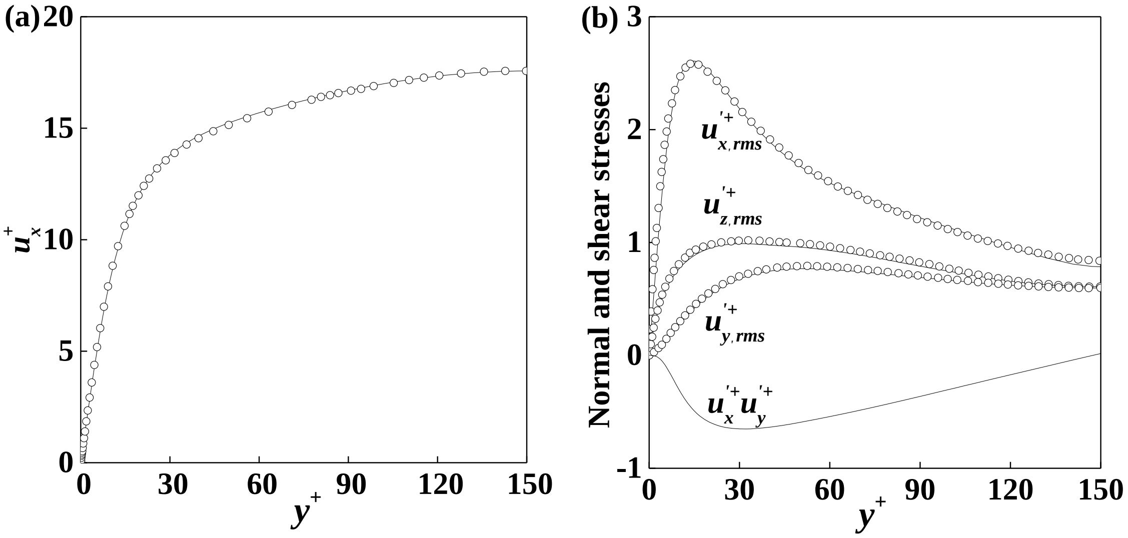

Figure 4.2 Comparison of single-phase fluid flow at Re_τ = 150 (—) with predictions of Molin et al. [64] (○). (a) Mean streamwise fluid velocity (u_x^+); (b) non-dimensional wall-normal ($u'^+_{y,rms}$), spanwise ($u'^+_{z,rms}$) and streamwise ($u'^+_{x,rms}$) rms of velocity fluctuations, and shear stress ($u'^+_x u'^+_y$).

The present results are plotted as solid lines in Figure 4.2, while the circles correspond to the predictions of Molin et al. [64]. Excellent agreement is obtained for the mean streamwise velocity in Figure 4.2(a) and the root mean square (rms) of the velocity fluctuations and the Reynolds shear stress in Figure 4.2(b). The instantaneous streamwise velocity in the channel is displayed in Figure 4.3, together with the GLL grid-points. The streamwise velocity is seen to be at a maximum in the centre of the channel and decreases to a minimum towards the walls due to the non-slip boundary conditions applied there.

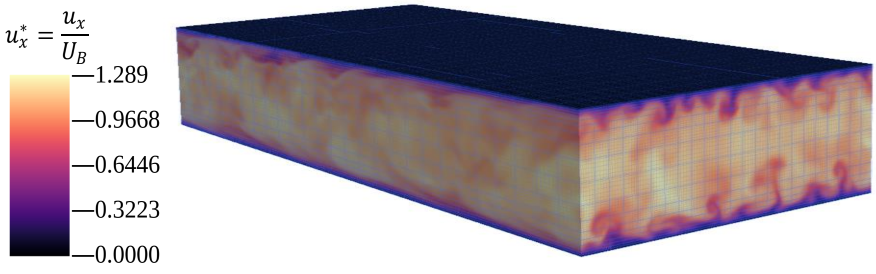

Figure 4.3 Computational mesh and non-dimensional instantaneous streamwise velocity in the channel for the single-phase flow at Re_τ = 150.

Good consistency is also observed for the case at Re_τ = 395. The results are very close to those of Moser et al. [257], with only a very slight deviation being for the spanwise rms of velocity fluctuations in Figure 4.4. The focus here is on the validation of the single-phase flow predictions and the excellent agreement with the literature results shown demonstrates that the employed numerical method is accurate and reliable and can be employed for the prediction of the continuous phase in the DNS of bubbly flows.

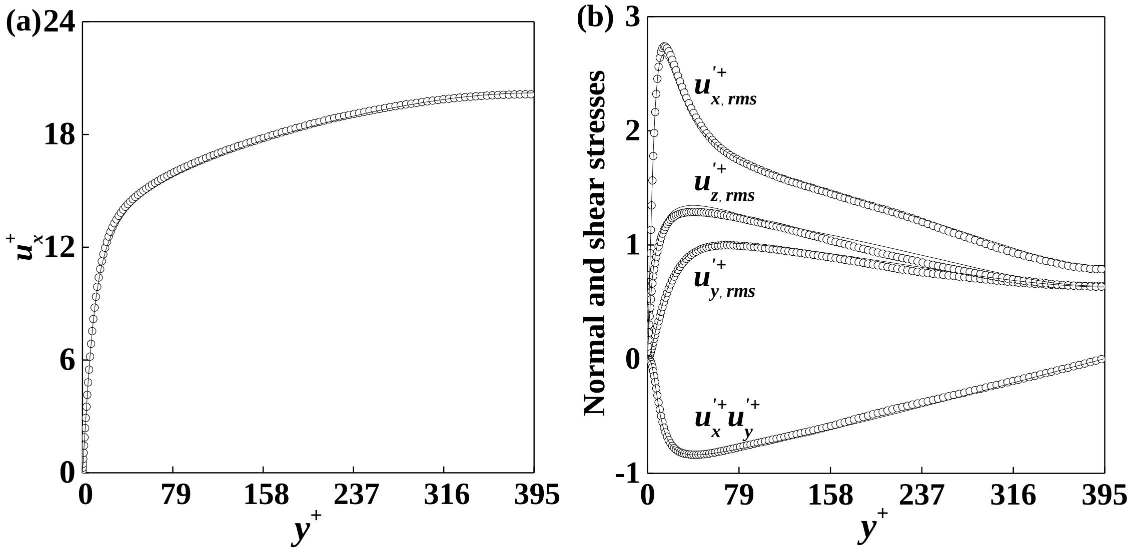

Figure 4.4 Comparison of single-phase fluid flow at Re_τ = 395 (—) with predictions of Moser et al. [257] (○). (a) Mean streamwise fluid velocity (u_x^+); (b) non-dimensional wall-normal ($u'^+_{y,rms}$), spanwise ($u'^+_{z,rms}$) and streamwise ($u'^+_{x,rms}$) rms of velocity fluctuations, and shear stress ($u'^+_x u'^+_y$).

4.2.2 Two-phase channel flows with one-way coupling

In this section, the DNS of bubbly flows for the two-phase channel flows with microbubbles of diameters d_b = 110 μm and 220 μm is considered, with the one-way coupling assumption, and results are compared with literature data sets. The bubble size range is of relevance to multiple engineering applications such as the treatment of waste water and sewage which uses microbubbles of 150 μm diameter to separate particulates from potable water, taking advantage of the high surface area to volume ratio of these bubbles [260]. A total of 181,340 and 22,659 bubbles of diameters d_b = 110 μm and 220 μm, respectively, were injected in fully-developed single-phase flow solutions. The number of bubbles corresponds to a void fraction of 0.01, which is low enough to keep the system dilute, which allows bubble-bubble interactions to be neglected.

The nondimensional Eötvös number ($Eo = \frac{(\rho_f - \rho_b) d_b^2 g}{\sigma}$) can be introduced to describe bubble deformability. The Eötvös number is proportional to the buoyancy force divided by the surface tension force. In this thesis, the surface tension is assumed to be 0.0728 N

m^{-1}, and the densities of the fluid and bubbles are 1000 kg m^{-3} and 1.3 kg m^{-3}, respectively, leading to $Eo \approx 1.63 \times 10^{-3}$ for 110 μm diameter bubbles, and $Eo \approx 6.51 \times 10^{-3}$ and 1.46×10^{-2} for 220 and 330 μm diameter bubbles. Considering that $Eo < 0.2$ for all bubble sizes, and the level of turbulence considered in this study, according to Grace [261], the Lagrangian-Eulerian method can be employed to treat microbubbles as non-deformable spheres subject to gravity, drag, added mass, pressure gradient, and lift forces, as outlined in Chapter 3.

For the simulations of bubbly flows reported in the present section, the following steps were adopted. Firstly, a single-phase flow at $Re_\tau = 150$ was simulated until a statistically steady-state solution was reached. The bubbles were injected with a random spatial distribution in the fully developed turbulent channel flow, with the initial bubble velocities matching those of the fluid at the bubble centre. When a bubble reached a periodic boundary, it was re-injected at the corresponding boundary, keeping the average void fraction of the bubbles constant. Both upflow and downflow flow conditions were studied and some results (see Sections 4.2.2.3 and 4.2.2.4) validated against the DNS predictions of Giusti et al. [55] and Molin et al. [64]. The gravity force is set to be positive in the streamwise direction for downflow and negative for upflow. The time-step advancement was set to be $\Delta t = 1.6 \times 10^{-4}$ s which is sufficient to provide a faithful reproduction of the bubble transient behaviour [262].

In the following sections, simulation results for different bubble diameters in up and downward channel flows are presented, including mean velocities and the normal and shear stresses of the fluid and the bubbles, forces acting on the bubbles, and bubble density profiles.

4.2.2.1 Downflow at $Re_\tau = 150$ with $d_b = 110$ μm

In Figure 4.5, the mean streamwise velocity and the normal and shear stresses of the continuous phase are compared to the results of Molin et al. [64]. It can be seen that the microbubbles do not have any significant effect on the fluid velocity field and the fluid statistics are unchanged from those given in Figure 4.2.

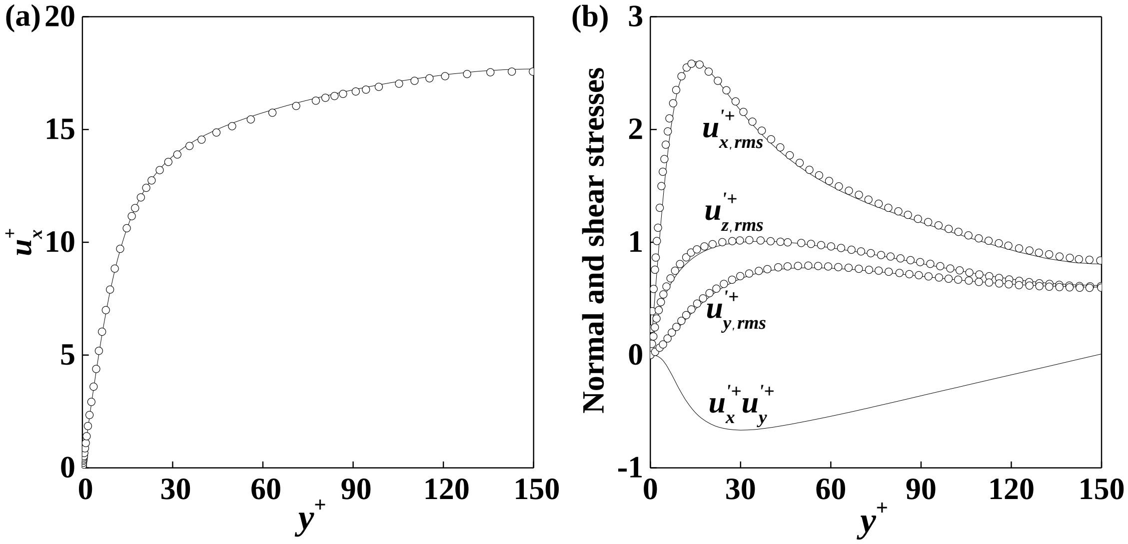

Figure 4.5 Comparison of continuous phase results in DNS of one-way coupled downflow at $Re_\tau = 150$ with $d_b = 110$ μm (—) with single-phase database (○). (a) Non-dimensional mean streamwise fluid velocity (u_x^+); (b) non-dimensional wall-normal ($u'^+_{y,rms}$), spanwise ($u'^+_{z,rms}$) and streamwise ($u'^+_{x,rms}$) rms of velocity fluctuations and shear stress ($u'^+_x u'^+_y$).

The bubble mean velocity profile, and the normal and shear stresses acting on the bubbles, for downflow with $d_b = 110$ μm are plotted in Figure 4.6. The bubbles move slightly slower than the carrier fluid in Figure 4.6(a), and the bubble velocity fluctuations are also lower in Figure 4.6(b). In the immediate vicinity of the wall ($y^+ < 10$), however, rms values tend to become higher. This is only a consequence of the small number of bubbles in the viscous sub-layer region that will be addressed when discussing the results given in Figure 4.7. Essentially, however, the small number of bubbles prevented statistically meaningful averages being obtained and, for this reason, additional results closer to the wall are not shown in Figure 4.6.

Figure 4.7 gives the instantaneous microbubble number density profile in the half channel at the end of the simulation normalised by the initial bubble concentration ($c_0 = N_b / V$, with V the volume of the channel domain). The channel was divided into 120 wall-parallel slabs across the wall-normal direction, and the bubble concentration in each slab computed as $c = N_{b,i} / V_i$, where $i = 1, \ldots, 120$. In downflow, the bubbles are pushed towards the channel centre due to the lift force, and a nearly uniform bubble distribution is observed away from the wall ($y^+ > 20$).

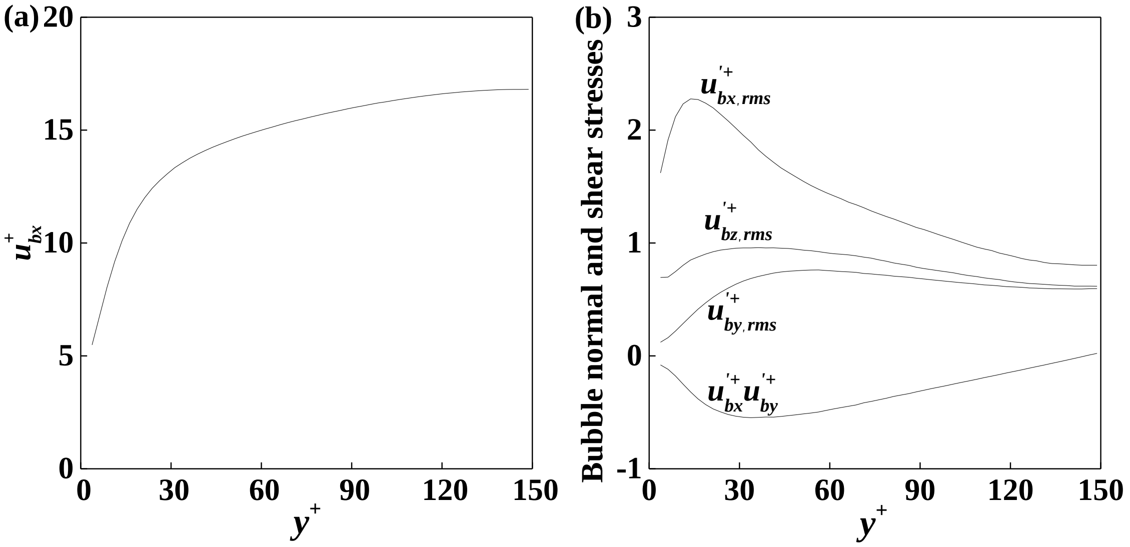

Figure 4.6 Bubble velocity statistics in the DNS of the one-way coupled downflow at Re_τ = 150 with d_b = 110 μm. (a) Non-dimensional mean streamwise microbubbles velocity (u^+_{bx}); (b) non-dimensional wall-normal ($u'^+_{by,rms}$), spanwise ($u'^+_{bz,rms}$), streamwise ($u'^+_{bx,rms}$) rms of microbubbles velocity fluctuations and shear stress ($u'^+_{bx}u'^+_{by}$).

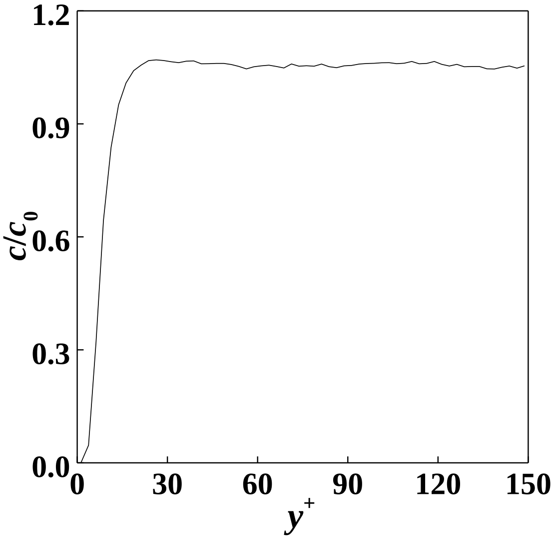

Figure 4.7 Microbubbles number density profile normalised by the initial bubble concentration for the DNS of the one-way coupled downflow at Re_τ = 150 with d_b = 110 μm.

Figure 4.8 shows the mean force components in the streamwise and wall-normal directions acting on the bubbles across the half channel width. It is worthwhile noting that the spanwise components are rather irrelevant to the macroscopic behaviour of the bubbles in the present geometry. In the streamwise direction (Figure 4.8(a)), the sign of the bubble buoyancy force is negative, and the buoyancy force is balanced by the drag force. In Figure 4.8(b), the components in the wall-normal direction demonstrate that the bubble lift force plays a significant role approaching the wall ($y^+ < 45$). The sign of the lift force is positive in downflow which advects bubbles towards the channel centre. This explains the dramatic decrease of the bubble density in the region $y^+ < 20$. Figure 4.8(b) also confirms that the lift force is counterbalanced by the drag force only. These trends are quantitatively consistent with those of Giusti et al. [55], where the region $y^+ < 40$ was observed to be dominated by the effect of the lift force in downflow.

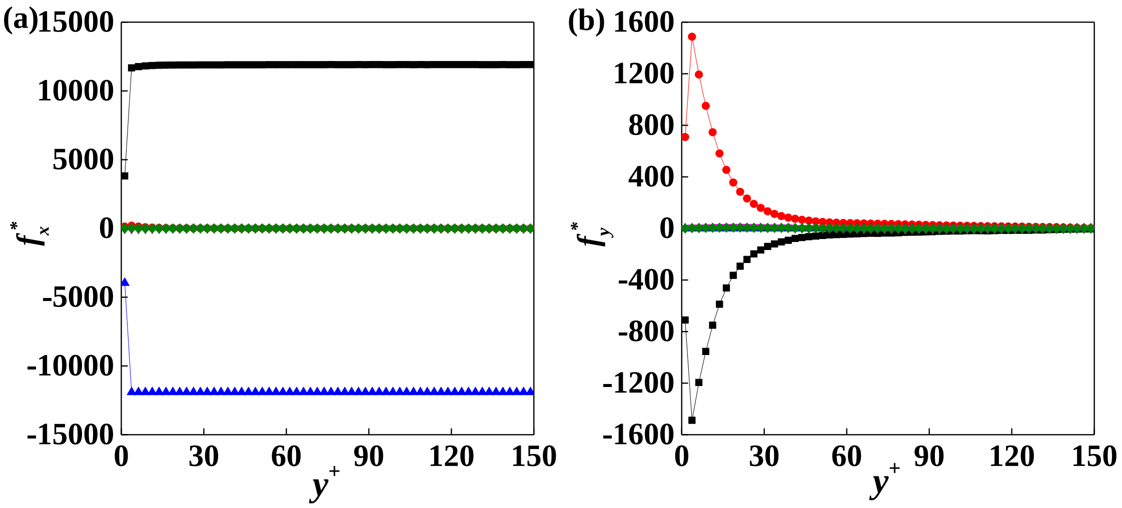

Figure 4.8 Forces acting on the bubbles in DNS of one-way coupled downflow at Re_τ = 150 with d_b = 110 μm. (a) Streamwise; (b) wall-normal components of the forces. Symbols: ■ drag force, ● lift force, ▲ gravity and buoyancy, ▼ pressure gradient force, and ♦ virtual mass force.

4.2.2.2 Upflow at Re_τ = 150 with d_b = 110 μm

Profiles for upflow with microbubbles of d_b = 110 μm are presented in Figure 4.9. As expected, bubbles again do not alter the mean quantities and turbulence intensities in the carrier phase. Figure 4.10 shows similar quantities for the microbubbles. Compared to Figure 4.9, the microbubbles move faster than the carrier phase due to their buoyancy.

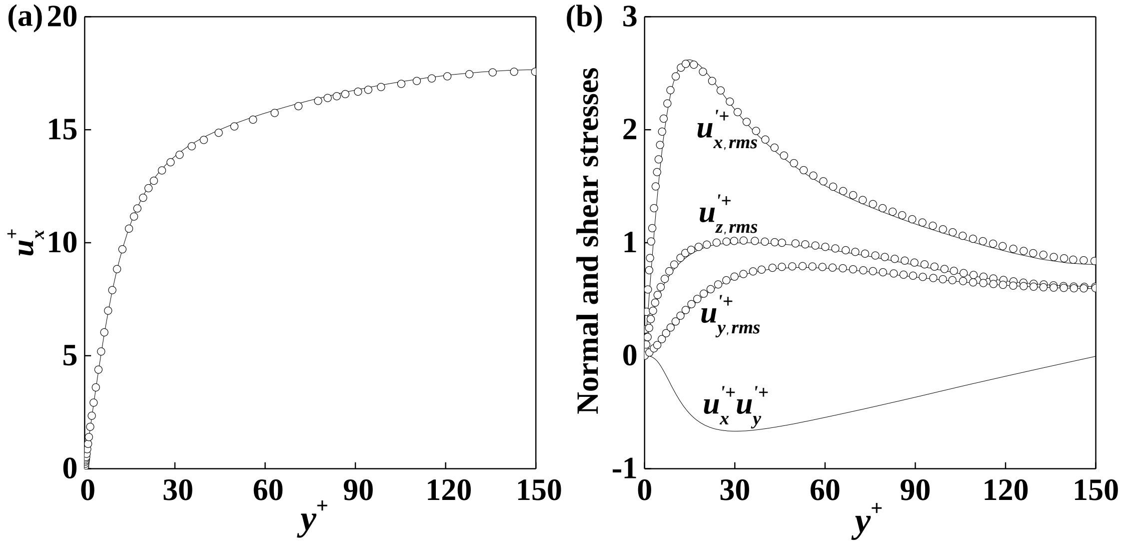

Figure 4.9 Comparison of continuous phase results in DNS of the one-way coupled upflow at Re_τ = 150 with d_b = 110 μm (—) with single-phase database (○). (a) Non-dimensional mean streamwise fluid velocity (u_x^+); (b) non-dimensional wall-normal ($u'^+_{y,rms}$), spanwise ($u'^+_{z,rms}$) and streamwise ($u'^+_{x,rms}$) rms of velocity fluctuations and shear stress ($u'^+_x u'^+_y$).

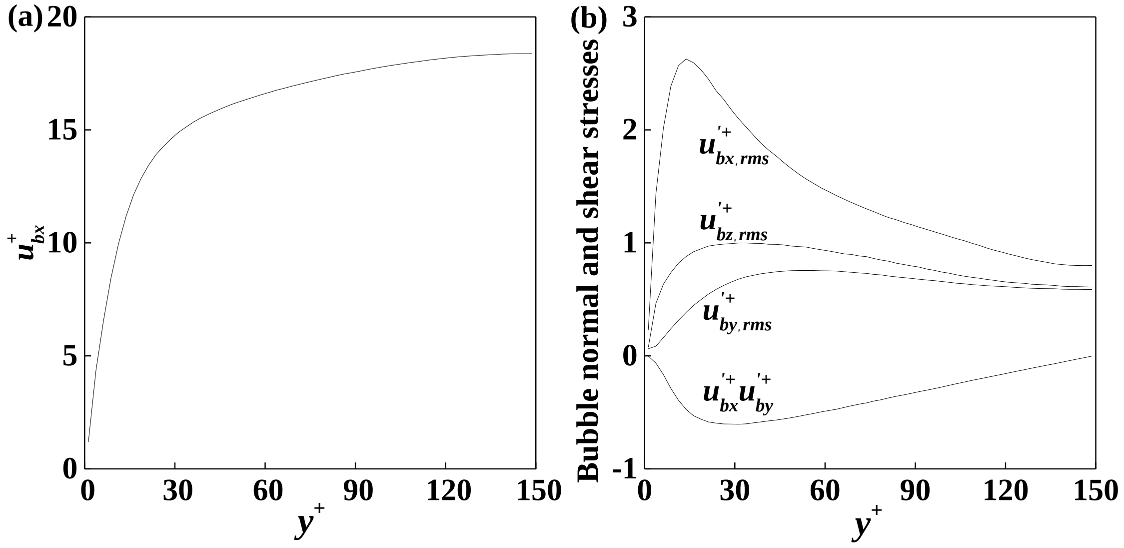

Figure 4.10 Bubble velocity statistics in DNS of one-way coupled upflow at Re_τ = 150 with d_b = 110 μm. (a) Non-dimensional mean streamwise microbubbles velocity (u_{bx}^+); (b) non-dimensional wall-normal ($u'^+_{by,rms}$), spanwise ($u'^+_{bz,rms}$), streamwise ($u'^+_{bx,rms}$) rms of microbubbles velocity fluctuations and shear stress ($u'^+_{bx} u'^+_{by}$).

The same analysis of bubble forces in Figure 4.11(a) quantitatively confirms that the two important forces acting on the bubbles in the vertical direction are the drag force, and gravity and buoyancy. The sign of the gravity and buoyancy force is positive in upflow and it is balanced by the drag force. In Figure 4.11(b), the impact of the lift force is directly responsible of the bubble lateral movement. The lift force value at different wall-normal positions reveals that the absolute value of the force increases toward the wall. It is also found that the sign of the lift force is negative so that the bubbles are pushed directly towards the wall. This finding is consistent with both numerical [55] and experimental [263] studies of turbulent microbubble dispersion. As a result, a wall accumulation of microbubbles was found in the upward channel flow due to the action of lift force, while the distribution remains uniform in the channel centre, as shown in Figure 4.12.

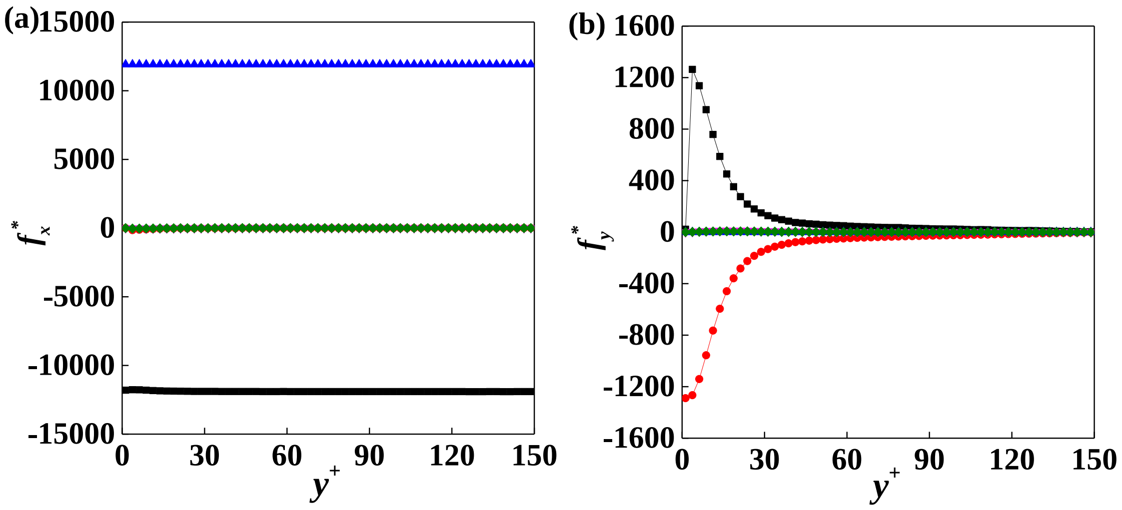

Figure 4.11 Forces acting on the bubbles in DNS of the one-way coupled upflow at Re_τ = 150 with d_b = 110 µm. (a) Streamwise and (b) wall-normal components of the forces. Symbols: ■ drag force, ● lift force, ▲ gravity and buoyancy, ▼ pressure gradient force, and ♦ virtual mass force.

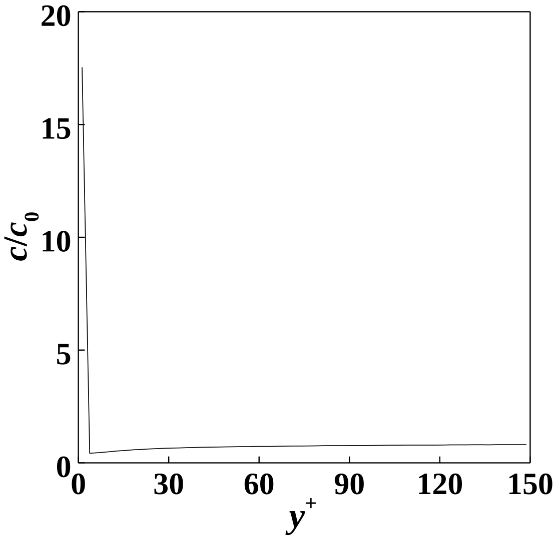

Figure 4.12 Microbubble number density profile normalised by the initial bubble concentration in DNS of one-way coupled upflow at Re_τ = 150 with d_b = 110 µm.

4.2.2.3 Downflow at Re_τ = 150 with d_b = 220 µm

In this section, microbubbles with a diameter of 220 µm are injected into the flow, and the fluid and bubble velocity fields are compared against the results of Giusti et al. [55]. Figure 4.13(a) provides the mean fluid phase velocity plotted across the half channel. A good agreement for the peak value is found in the channel centre, although there is some slight deviation in the log-law and the buffer regions. These differences can be explained by the less refined grid resolution of Giusti et al. [55], which divided the computational domain into 64 × 64 × 65 nodes. The higher mesh resolution employed in this work was validated earlier and demonstrated to be sufficient to obtain accurate predictions of the mean velocity and normal and shear stresses when compared to similar high resolution predictions. More pronounced are the difference in the results with respect to Giusti et al. [55] in the streamwise, spanwise and wall-normal rms values of velocity fluctuations (solid line) in Figure 4.13(b), with the present results being generally lower than those in the reference paper (circles) [55].

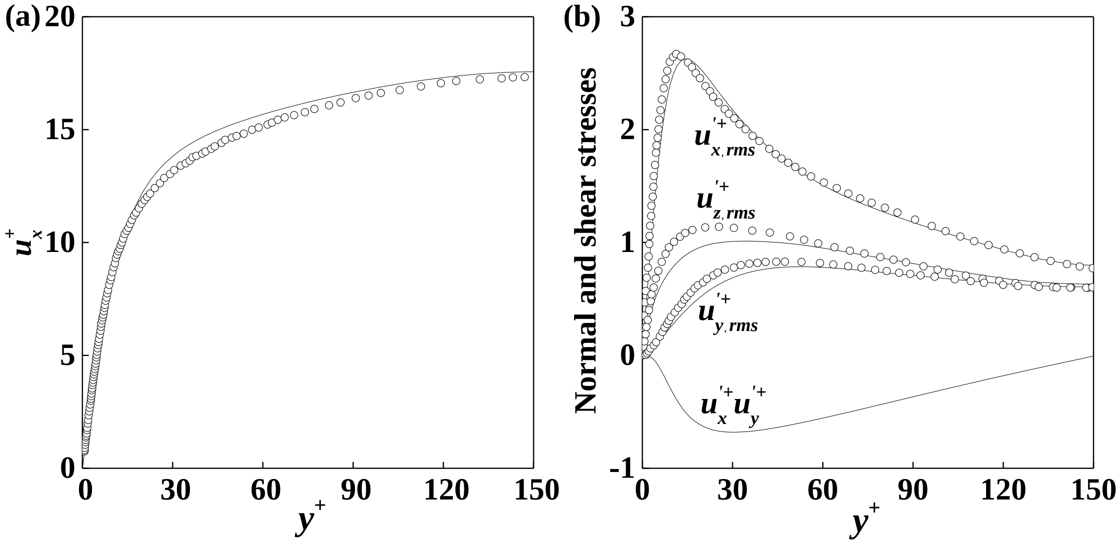

Figure 4.13 Comparison of continuous phase results in DNS of one-way coupled downflow at $Re_\tau = 150$ with $d_b = 220$ μm (—) with predictions of Giusti et al. [55] (○). (a) Mean streamwise fluid velocity (u_x^+); (b) wall-normal ($u'^+_{y,rms}$), spanwise ($u'^+_{z,rms}$) and streamwise ($u'^+_{x,rms}$) rms of velocity fluctuations, and shear stress ($u'^+_x u'^+_y$).

In agreement with the higher fluid mean velocity, the bubbles are also observed to flow faster than the reference predictions in the log-law and buffer regions, as shown in Figure 4.14(a). At the same time, the peak of the mean bubble velocity is lower than the peak in the fluid velocity, as expected in downflow. The normal and shear stresses, however, are not compared with the results of Giusti et al. [55] in Figure 4.14(b) because of the absence of these data in the reference paper. Analysis of the bubble force statistics (Figure 4.15) and microbubble concentration profile (Figure 4.16) is also provided, with a nearly bubble-free wall layer obtained as in the previous downflow case. Other observations are also in line with those made in Section 4.2.2.1.

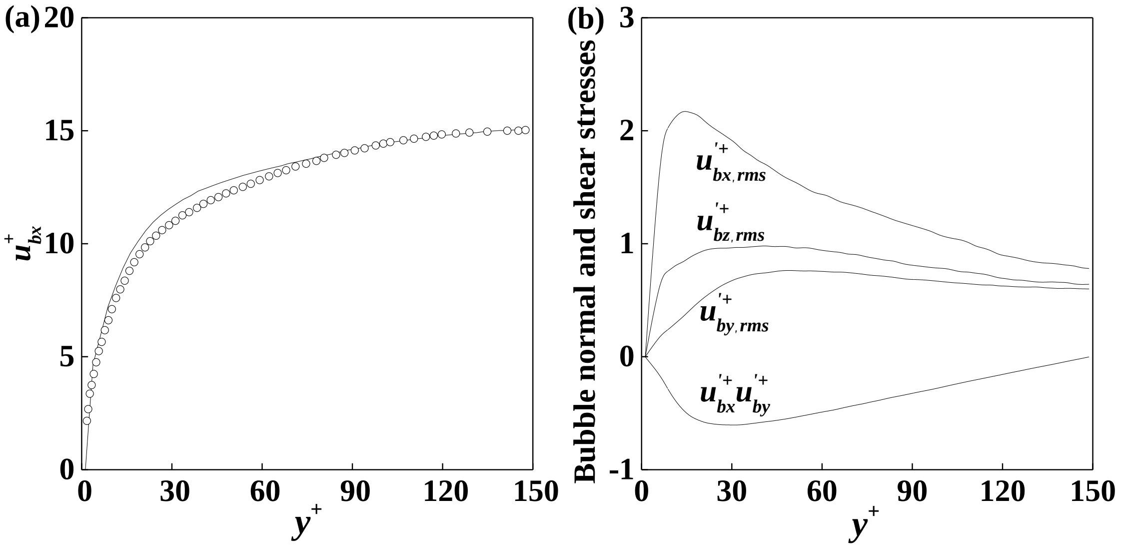

Figure 4.14 Comparison of bubble velocity statistics in DNS of one-way coupled downflow at Re_τ = 150 with d_b = 220 μm (—) with predictions of Giusti et al. [55] (○). (a) Mean streamwise bubble velocity (u^{+}_{bx}); (b) wall-normal ($u'^{+}_{by,rms}$), spanwise ($u'^{+}_{bz,rms}$) and streamwise ($u'^{+}_{bx,rms}$) rms of microbubbles velocity fluctuations, and shear stress ($u'^{+}_{bx}u'^{+}_{by}$).

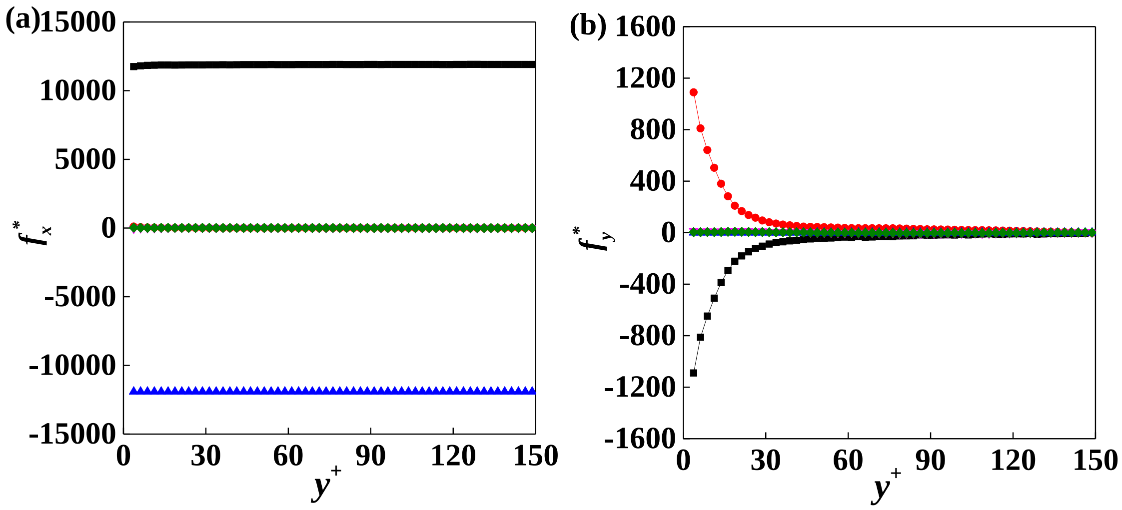

Figure 4.15 Forces properties acting on the bubbles in DNS of one-way coupled downflow at Re_τ = 150 with d_b = 220 μm. (a) Streamwise and (b) wall-normal components of the forces. Symbols: ■ drag force, ● lift force, ▲ gravity and buoyancy, ▼ pressure gradient force, and ♦ virtual mass force.

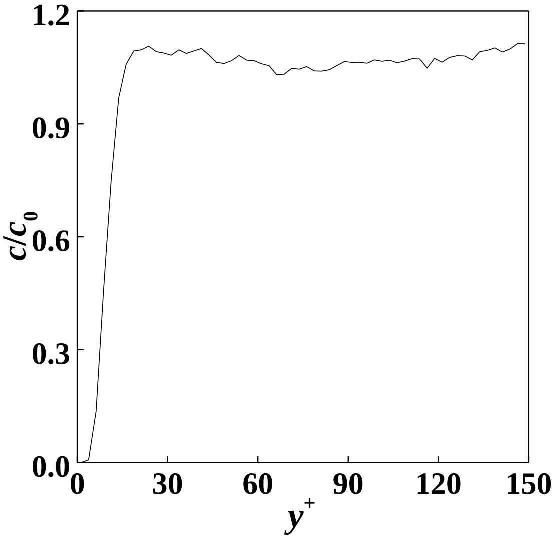

Figure 4.16 Microbubble number density profile normalised by the initial bubble concentration in DNS of one-way coupled downflow at $Re_\tau = 150$ with $d_b = 220$ µm.

4.2.2.4 Upflow at $Re_\tau = 150$ with $d_b = 220$ µm

In this section, results for the upward channel flow with bubbles of diameter of 220 µm are validated with the existing literature data from Molin et al. [64]. For this purpose, the same number of microbubbles was injected in the flow. The employed mesh resolution is more refined with respect to the work of Molin et al. [64], as already noted in Section 4.2.1. The mean streamwise velocity and rms of velocity fluctuations show a very good agreement with the predictions of Molin et al. [64] in Figure 4.17. In addition, validation of the bubble velocity predictions is also made by comparing the rms of the bubble velocity fluctuations in Figure 4.18(b). Good agreement is obtained except for the peak of the streamwise rms. It should be noted that mean velocity and shear stress predictions were not provided by Molin et al. [64]. Other statistical quantities, such as force properties and the bubble density profile, are also provided in Figure 4.19 and Figure 4.20, respectively. Again, the observations that can be made in relation to these results are again in line with those made in Section 4.2.2.1 for the upflow with $d_b = 220$ µm bubbles.

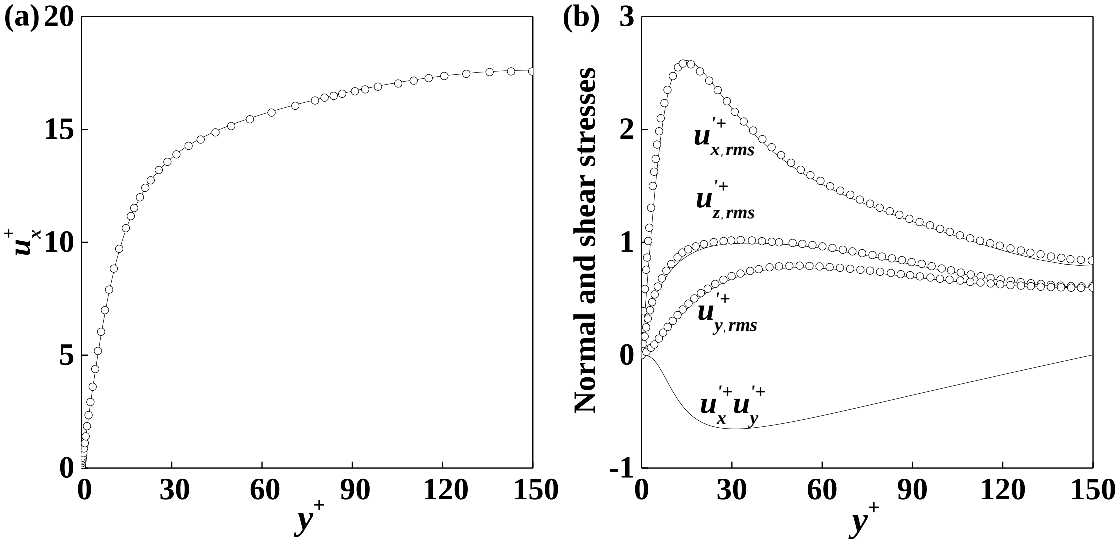

Figure 4.17 Comparison of continuous phase results in DNS of one-way coupled upflow at Re_τ = 150 with d_b = 220 μm (—) with literature data of Molin et al. [64] (○). (a) Non-dimensional mean streamwise fluid velocity (u_x^+); (b) non-dimensional wall-normal ($u'^+_{y,rms}$), spanwise ($u'^+_{z,rms}$) and streamwise ($u'^+_{x,rms}$) rms of velocity fluctuations and shear stress ($u'^+_x u'^+_y$).

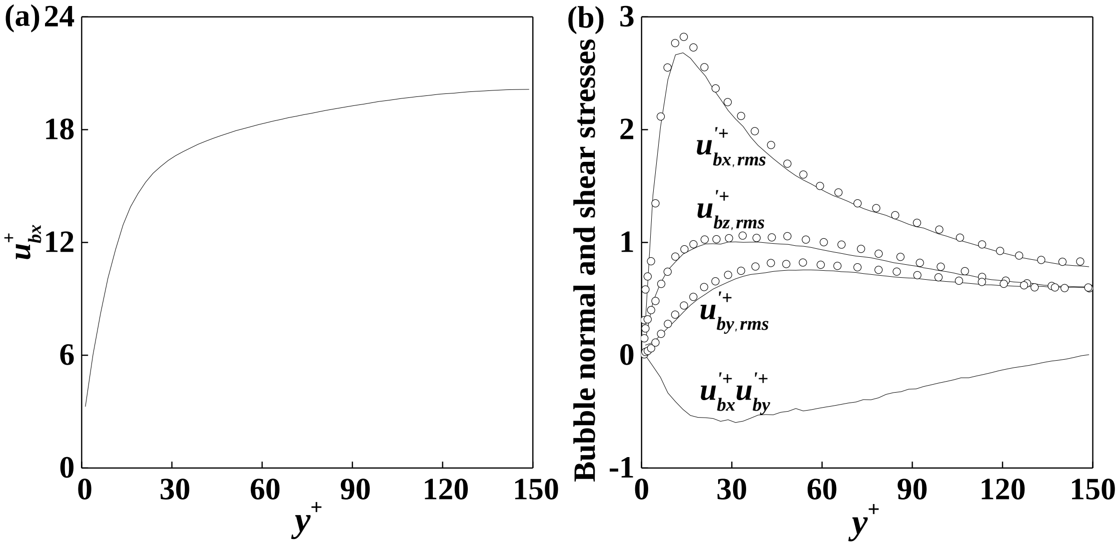

Figure 4.18 Comparison of bubble velocity statistics in DNS of one-way coupled upflow at Re_τ = 150 with d_b = 220 μm (—) with literature data of Molin et al. [64] (○). (a) Non-dimensional mean streamwise microbubbles velocity (u_{bx}^+); (b) non-dimensional wall-normal ($u'^+_{by,rms}$), spanwise ($u'^+_{bz,rms}$), streamwise ($u'^+_{bx,rms}$) rms of microbubbles velocity fluctuations and shear stress ($u'^+_{bx} u'^+_{by}$).

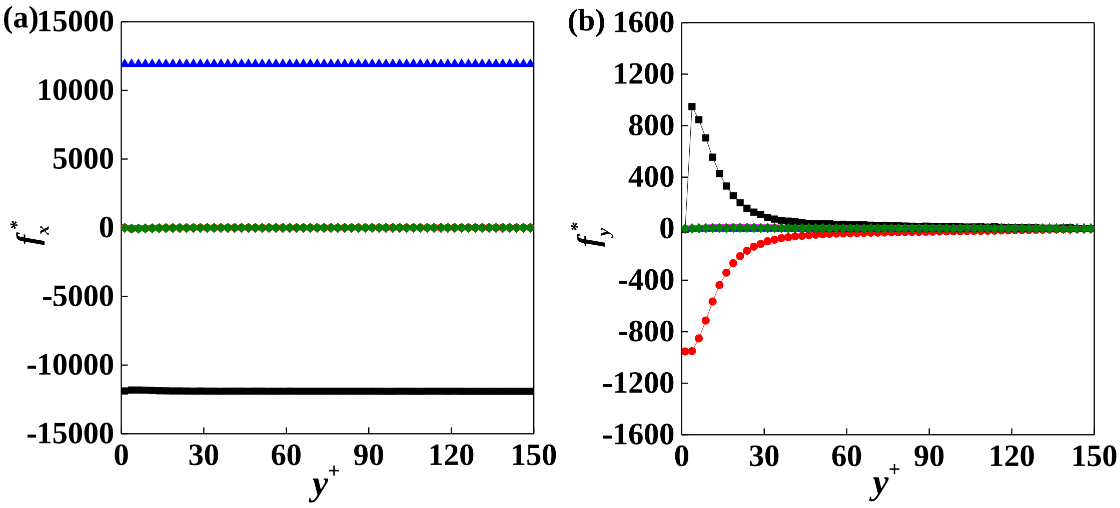

Figure 4.19 Forces properties acting on the bubbles in DNS of one-way coupled upflow at $Re_\tau = 150$ with $d_b = 220$ µm. (a) Streamwise and (b) wall-normal components of the forces. Symbols: ■ drag force, ● lift force, ▲ gravity and buoyancy, ▼ pressure gradient force, and ♦ virtual mass force.

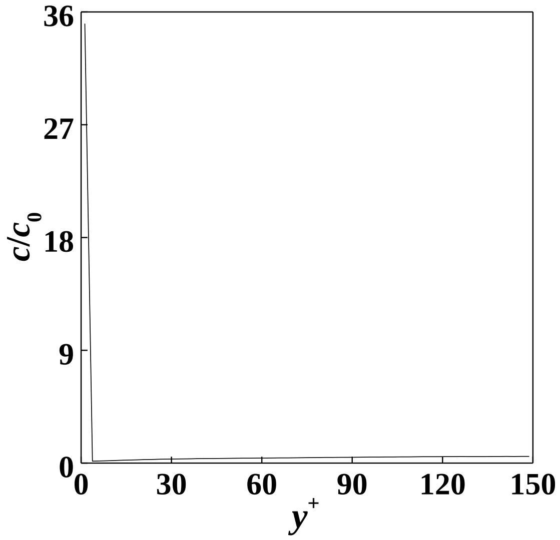

Figure 4.20 Microbubble number density profile normalised by the initial bubble concentration in DNS of one-way coupled upflow at $Re_\tau = 150$ with $d_b = 220$ µm.

It is also of importance to investigate the bubble spatial distribution in the channel. As described before, driven by the lift force, small spherical bubbles accumulate near the wall of the channel in upflow. Conversely, in downflow, since the bubbles travel more slowly than the fluid, the same lift force pushes the bubbles towards the centre of the channel. Special attention is given here to the case of upflow with $d_b = 220$ µm under one-way coupling.

Figure 4.21(b) depicts the bubble locations throughout the channel with values of bubble velocity presented, showing more bubbles are accumulated in the near-wall region. Figure 4.21(a) shows the bubble distribution close to the wall in the upward channel flow, superimposed on the streamwise fluid velocity field. It can be immediately seen that elongated streaks of relatively lower fluid velocity are generated by quasi-streamwise vortices that are orientated mainly in the streamwise direction. Clearly, the bubbles preferentially concentrate to form streaks in these low speed regions, while being dispersed in other regions. This elongated clustering is consistent with previous studies, e.g. Harleman et al. [264]. One explanation can be found through the lift force considerations of Thomas et al. [265] who noted that the bubbles are pushed to lower speed regions as the bubbles travel faster than the fluid due to the effects of buoyancy in upflow.

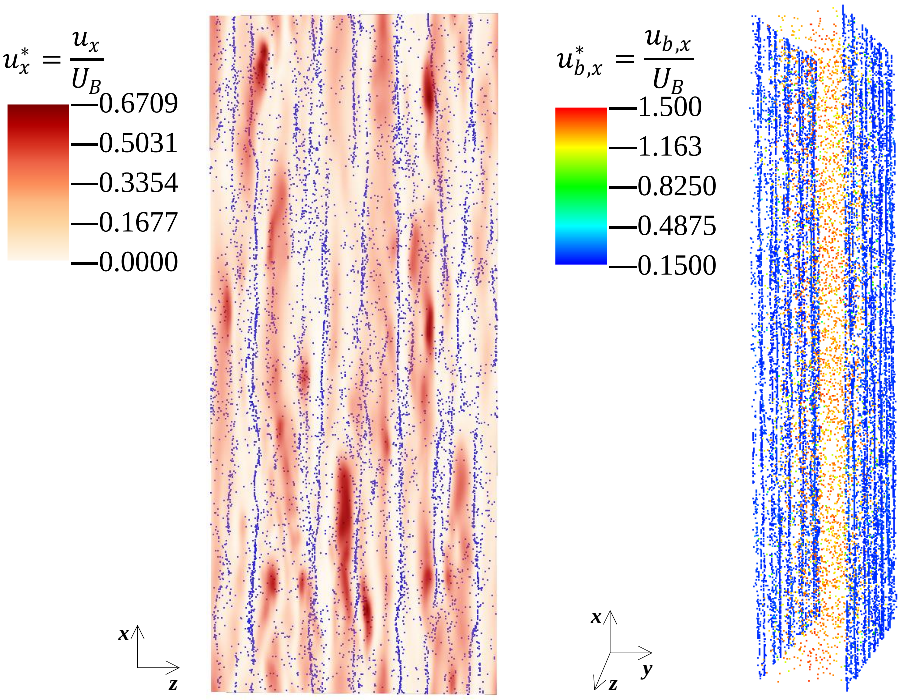

(a) (b)

Figure 4.21 Instantaneous bubbles distribution in the one-way coupled upflow at Re_τ = 150 with d_b = 220 μm. (a) Snapshot of the instantaneous bubble distribution in a thin slice of the viscous sub-layer region along the *x*-*z* plane with contour levels of the fluid streamwise velocity; (b) instantaneous bubble distribution with levels of bubble streamwise velocity in the whole channel.

4.2.3 Two-phase channel flows with two-way coupling

In this section, a further step forward towards four-way coupling with bubble coalescence is made with the validation of two-way coupled simulations, in which modifications of the turbulent flow by the bubbles are accounted for. Predictions are compared with the results of Molin et al. [64].

For the validation, the pressure gradient was modified in agreement with that used by Molin et al. [64] to include the reduced gravitational gain or loss that occurs as a consequence of the lighter mixture. As discussed in Molin et al. [64], this leads to a higher/lower wall shear, and mean velocity, in the upward/downward two-way coupled flows with respect to the single-phase flow. The prediction of the rescaling wall shear stress used by Molin et al. [64] is briefly summarised below for convenience.

Supposing each bubble causes a two-way force on the carrier phase as $f_{2w,i}$ ($i = 1, \ldots, N_b$), then the total contribution of all bubbles to the fluid is referred to as two-way coupling. In the vertical direction, the dominant forces are the drag force, gravity and buoyancy as discussed in Section 4.2.2, so that the two-way force can be described as:

$$f_{2w,i} = -F_D = F_G = (\rho_f - \rho_b) V_{b,i} g \tag{4.3}$$

Further, the bubbles are assumed to be uniformly distributed in the channel. Accordingly, the total two-way force is also uniformly distributed. Therefore, the modified pressure gradient can be computed as:

$$\Delta P_{2w} = \frac{\sum_{i=1}^{N_b} f_{2w,i} \, L_x}{V} = N_b (\rho_f - \rho_b) V_b g \frac{L_x}{V} \tag{4.4}$$

where V and V_b are the volume of the channel and bubbles, respectively. Based on the modified pressure gradient, the wall shear can be obtained depending on the flow direction as (+ sign refers to upflow and – sign refers to downflow):

$$\tau_{w,2w} = \frac{\Delta P \pm \Delta P_{2w}}{L_x} \frac{L_z}{2} \tag{4.5}$$

Therefore, the non-dimensional wall shear is calculated as:

$$\tau_{w,2w}^{+} = 1 \pm \frac{N_b V_b}{V} g^{+} \left(1 - \frac{\rho_b}{\rho_f}\right) Re_\tau \tag{4.6}$$

This change of the wall shear corresponds to the changes to the shear velocity and shear Reynolds number which are summarised in Table 4.2.

Table 4.2 Modified wall shear and shear Reynolds number

Single-phase flow	Upflow	Downflow
$\tau_w^+ = 1$	$\tau_{w,2\mathrm{w}}^+ = 1.35$	$\tau_{w,2\mathrm{w}}^+ = 0.65$
$Re_\tau = 150$	$Re_\tau = 174.2$	$Re_\tau = 121.1$

To keep the same average spatial concentration as in Molin et al. [64], the void fraction for both downflow and upflow was taken equal to 10^{-4}, corresponding to N_b = 181,340 bubbles. Each simulation was started from a fully developed single-phase turbulent velocity field, and kept running with bubbles present for enough time to reach statistically steady-state conditions and allow accurate sampling of the velocity field and bubble distribution.

4.2.3.1 Downflow at Re_τ = 150 with d_b = 110 µm

For the downward channel flow with two-way coupling, the comparison between simulated fluid velocity statistics and predictions of Molin et al. [64] is presented in Figure 4.22. As discussed by Molin et al. [64], compared to the single-phase profile in Figure 4.2, the mean fluid velocity is decreased due to the presence of the bubbles. In the two-way coupling of Molin et al. [64], the effect of microbubbles on the carrier fluid is taken into account by modifying the pressure gradient in the flow. This translates into the sum of the gravitational and frictional pressure losses being kept constant. In downflow, the gravitational pressure gain is reduced by the presence of bubbles so that the fluid flows slower. This observation is in agreement with the reference data [64]. The only difference is the shape of the mean fluid phase velocity which is found to be slightly different with respect to the reference data in Figure 4.22(a). Accordingly, the shape of the streamwise rms of velocity fluctuations is also over-predicted in Figure 4.22(b), while the normal and spanwise velocity fluctuations correspond quite consistently. This slight deviation in the fluid velocity leads to a small deviation in the time-averaged bubble velocity statistics. Figure 4.23 gives the bubbles mean and rms profiles for downflow compared with the predictions of Molin et al. [64]. The bubble velocity fluctuations are observed to be lower than the fluid turbulence intensities and this is in good agreement with literature data [64].

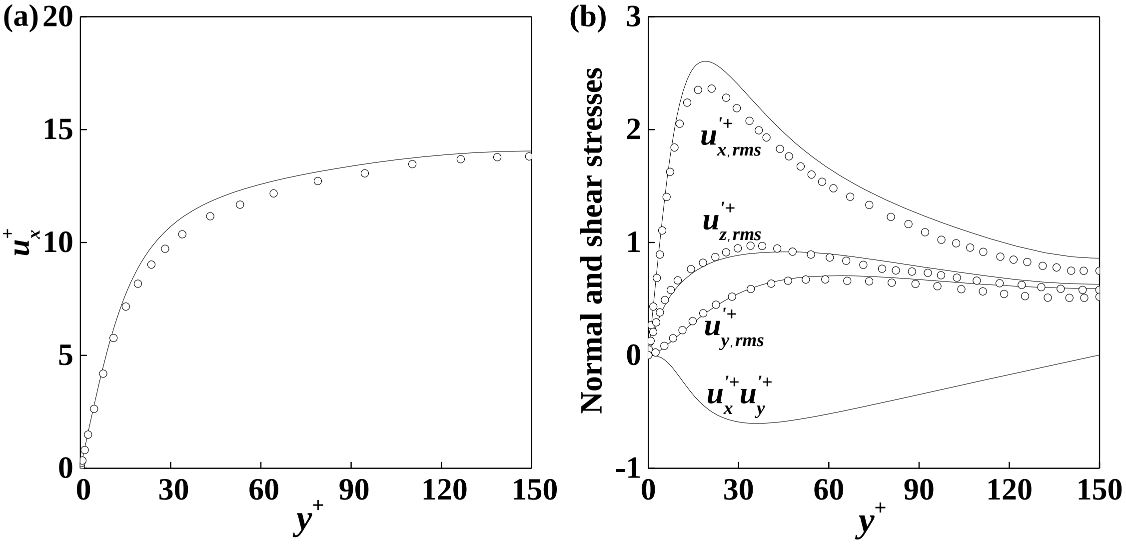

Figure 4.22 Comparison of continuous phase results in DNS of two-way coupled downflow at Re_τ = 150 with d_b = 110 μm (—) with literature data of Molin et al. [64] (○). (a) Non-dimensional mean streamwise fluid velocity (u_x^+); (b) non-dimensional wall-normal ($u'^+_{y,rms}$), spanwise ($u'^+_{z,rms}$) and streamwise ($u'^+_{x,rms}$) rms of velocity fluctuations and shear stress ($u'^+_x u'^+_y$).

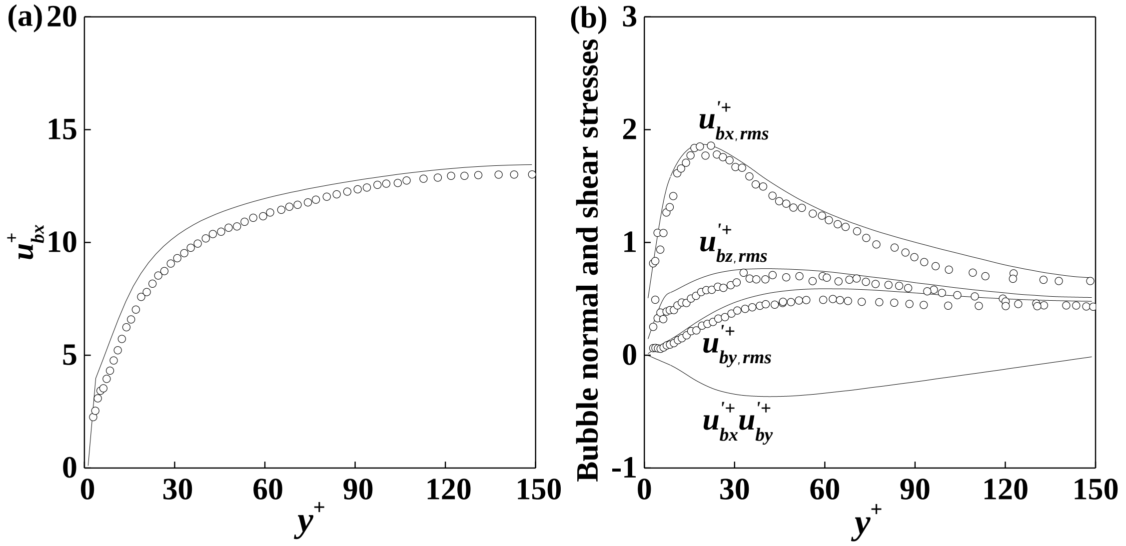

Figure 4.23 Comparison of bubble velocity statistics in DNS of two-way coupled downflow at Re_τ = 150 with d_b = 110 μm (—) with literature data of Molin et al. [64] (○). (a) Non-dimensional mean streamwise microbubbles velocity (u_{bx}^+); (b) non-dimensional wall-normal ($u'^+_{by,rms}$), spanwise ($u'^+_{bz,rms}$), streamwise ($u'^+_{bx,rms}$) rms of microbubbles velocity fluctuations and shear stress ($u'^+_{bx} u'^+_{by}$).

It has to be noted that small spikes in the predicted bubble rms values occur in the near-wall region that are not found in the results of Molin et al. [64]. This can be explained from results of Figure 4.24, where the normalised microbubble number density profile across the channel is presented. Figure 4.24 shows that nearly no bubbles are found in the very near-wall region ($y^+ < 3.75$), which makes the averaging in that region meaningless. This bubble free region is also observed in Molin et al. [64], where no bubbles were found at lower values than $y^+ \approx 3$. Therefore, results very close to the wall were not reported in Figure 4.23(b). In addition, Figure 4.24 clearly demonstrates and confirms that no preferential bubble distribution is found away from the channel wall where a uniform distribution is observed.

Differences between the present results and those of Molin et al. [64] shown in the above figures may be attributed to the higher gird resolution used in the present work, i.e. 3.8M computational nodes in this work as opposed to 2.1M in Molin et al. [64] (see Table 4.1).

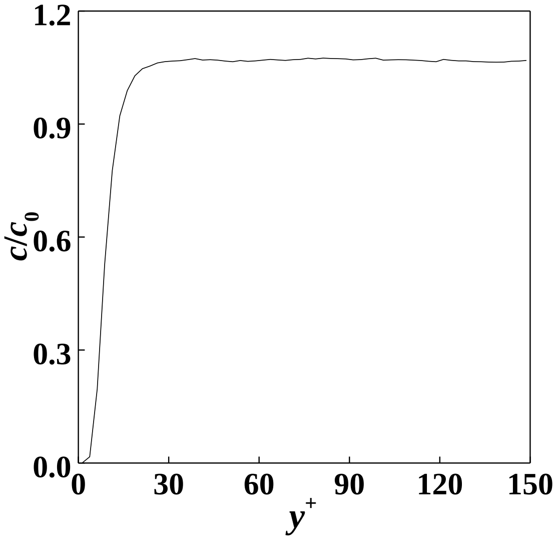

Figure 4.24 Microbubble number density profile normalised by the initial bubble concentration in DNS of two-way coupled downflow at $Re_\tau = 150$ with $d_b = 110$ µm.

The bubble forces are studied similarly to the one-way coupled case and plotted in Figure 4.25. The results confirm that in two-way coupled bubbly flows, gravity and buoyancy are perfectly balanced by the drag force in the streamwise direction. In the wall-normal direction, the lift force, being of positive sign, drives bubbles to the channel centre and is balanced by the drag force. These observations show good consistency with those of Molin et al. [64].

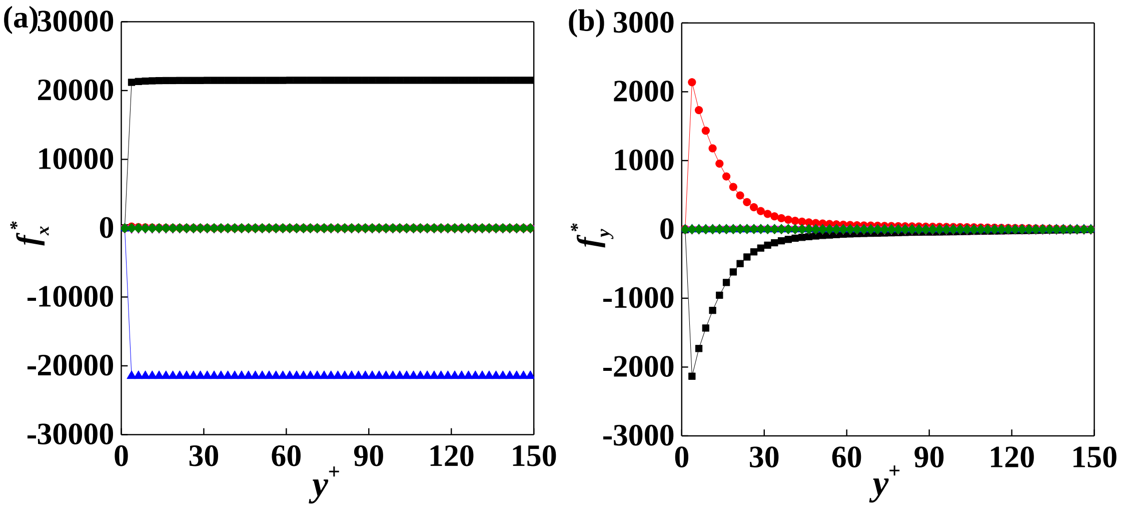

Figure 4.25 Forces acting on the bubbles in DNS of two-way coupled downflow at Re_τ = 150 with d_b = 110 μm. (a) Streamwise and (b) wall-normal components of the forces. Symbols: ■ drag force, ● lift force, ▲ gravity and buoyancy, ▼ pressure gradient force, and ♦ virtual mass force.

4.2.3.2 Upflow at Re_τ = 150 with d_b = 110 μm

In upflow, bubbles enhance the fluid turbulence intensity and, as expected, the introduction of bubbles results in a higher fluid mean velocity and increased normal and shear stresses (Figure 4.26) compared to the single-phase profiles in Figure 4.2. In the two-way coupling of Molin et al. [64] as discussed in downflow, the presence of the lighter mixture in upflow is expected to allow the fluid to flow faster. Figure 4.26 also shows, however, a higher mean fluid streamwise velocity and higher turbulence levels with respect to Molin et al. [64]. It was mentioned above that the imposed pressure gradient, and the wall shear stress, were modified to reproduce the results of Molin et al. [64]. In their work, the non-dimensional wall shear stress obtained from theoretical calculation was $\tau^+_{w,2w} = 1.35$. However, their results show that this theoretical value was not effectively reached in their DNS simulation. Therefore, the pressure gradient driving the flow was effectively lower and it is therefore not surprising that the mean fluid velocity predicted in this work, where the theoretical value was reached, is higher. Similarly, the bubble mean streamwise velocity and rms of the velocity fluctuations are also higher, as shown in Figure 4.27. Additionally, differences between the present results and those of Molin et al. [64] may also to some extent be attributed to the higher gird resolution used in the present work, as previously noted.

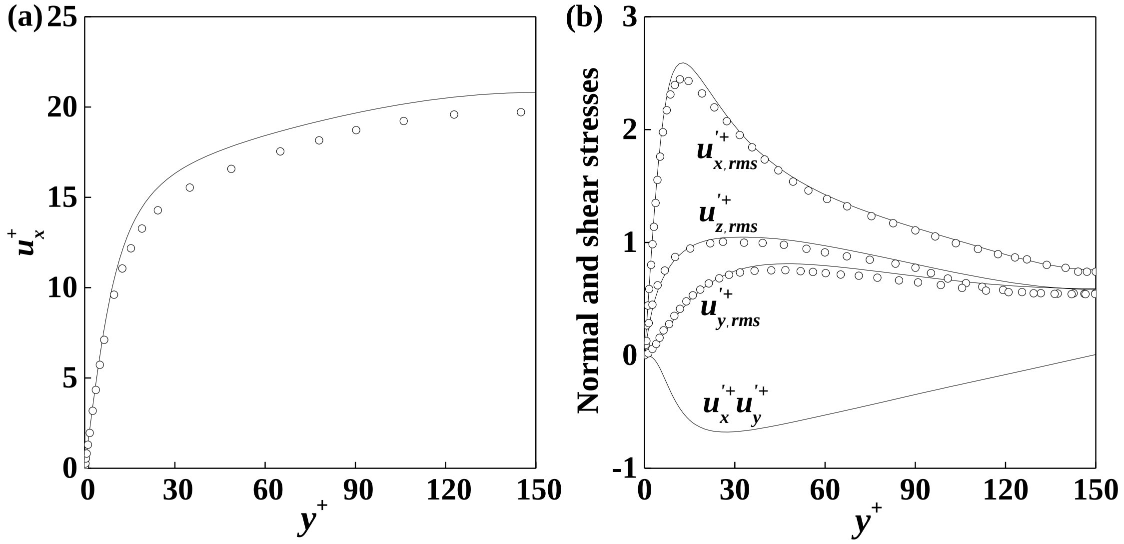

Figure 4.26 Comparison of continuous phase results in DNS of two-way coupled upflow at Re_τ = 150 with d_b = 110 μm (—) with literature data of Molin et al. [64] (○). (a) Non-dimensional mean streamwise fluid velocity (u_x^+); (b) non-dimensional wall-normal ($u'^+_{y,rms}$), spanwise ($u'^+_{z,rms}$) and streamwise ($u'^+_{x,rms}$) root mean square (rms) of velocity fluctuations and shear stress ($u'^+_x u'^+_y$).

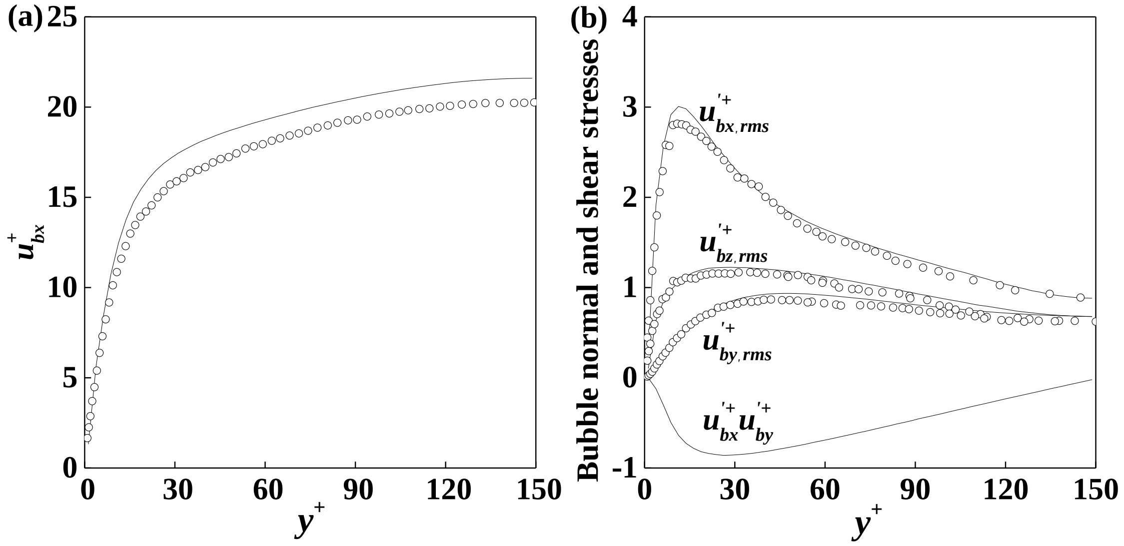

Figure 4.27 Comparison of bubble velocity statistics in DNS of two-way coupled upflow at Re_τ = 150 with d_b = 110 μm (—) with literature data of Molin et al. [64] (○). (a) Non-dimensional mean streamwise microbubbles velocity (u_{bx}^+); (b) non-dimensional wall-normal ($u'^+_{by,rms}$), spanwise ($u'^+_{bz,rms}$), streamwise ($u'^+_{bx,rms}$) rms of microbubbles velocity fluctuations and shear stress ($u'^+_{bx} u'^+_{by}$).

Figure 4.28 shows the normalised bubble number density profile. Compared to the one-way coupled case (see Figure 4.12), it can be seen that a greater accumulation of bubbles near the wall occurs with two-way coupling. In fact, Ounis et al. [266] and Chen and McLaughlin [267] have noted that particle accumulation in the wall region is due to wall coherent eddies. Due to the effect of two-way coupling, these turbulent eddies are enhanced and bubbles interact with the near-wall eddies more strongly. As a result, more bubbles appear in the wall region. Otherwise, the bubbles distribute nearly uniform away from the wall, although the bubble density is lower here.

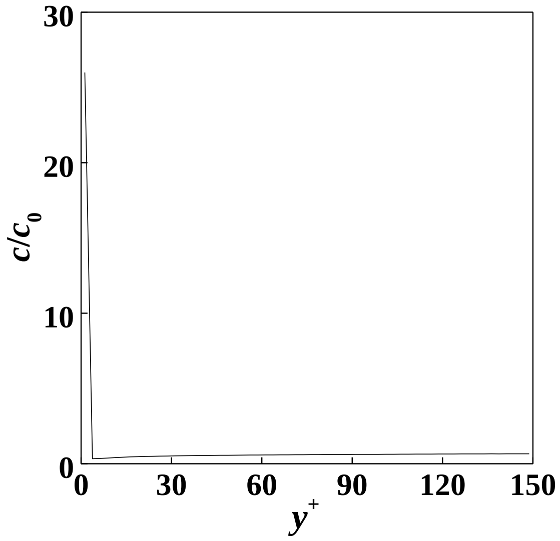

Figure 4.28 Microbubble number density profile normalised by the initial bubble concentration in DNS of two-way coupled upflow at $Re_\tau = 150$ with $d_b = 110$ µm.

Further validation of the present results can be gained by comparing the bubble forces. Figure 4.29 demonstrates a balance between the drag force and gravity and buoyancy in the streamwise direction, and a balance between the lift and drag forces in the wall-normal direction. However, Molin et al. [64] also examined an aerodynamic lift force by incorporating the wall-induced effect on the bubbles. As a result, their lift force profile gives a minimum value at $y^+ \approx 3$. This force, however, has not been considered in the present study, because its influence on bubbles of $d_b = 110$ µm is very small and the deviation of present results with respect to those of Molin et al. [64] is minimal.

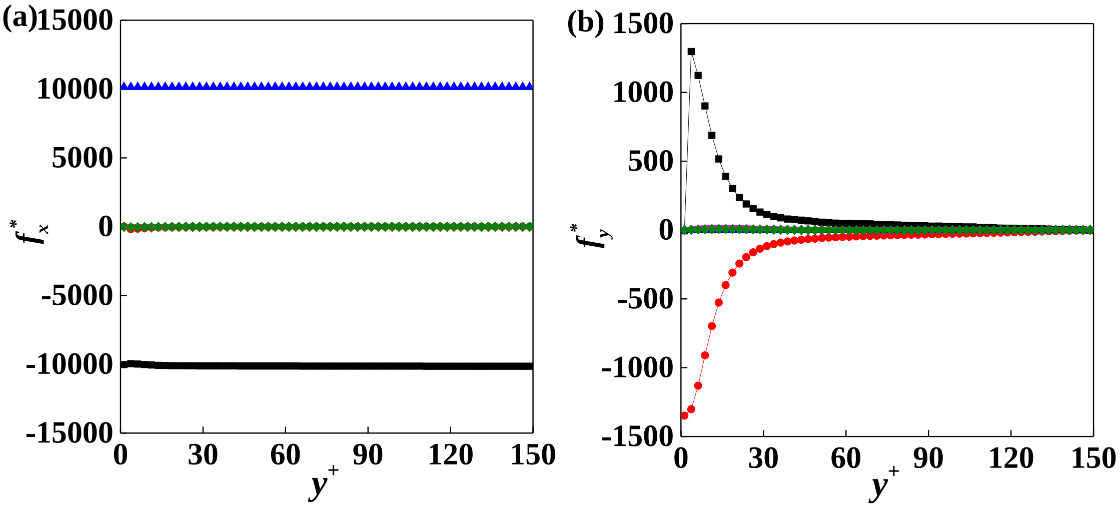

Figure 4.29 Forces acting on the bubbles in DNS of two-way coupled downflow at Re_τ = 150 with d_b = 110 µm. (a) Streamwise and (b) wall-normal components of the forces. Symbols: ■ drag force, ● lift force, ▲ gravity and buoyancy, ▼ pressure gradient force, and ♦ virtual mass force.

4.3 Two-phase channel flows with four-way coupling and coalescence

After successful validation, the four-way coupled model is first applied to upflow and downflow conditions at Re_τ = 150 with d_b = 110 µm bubbles, and a void fraction of 0.10%. With respect to the previous simulations, the void fraction is increased to enhance the number of collisions and coalescences, these being the main subject of the present section. The simulations are set up based on a fully developed single-phase channel flow, in which bubbles are injected with a random spatial distribution. To avoid bubbles overlapping, special attention is paid on checking the distance between the injected bubbles and already bubbles in the channel. Similarly with one-way and two-way coupling, the initial bubble velocities are assumed to be equal to the velocity of the fluid phase at the location of the bubbles. The collision algorithm outlined in Chapter 3 is employed. In this study, only binary collision is considered since multiple collisions are extremely rare under the present void fraction [120]. For simplification, bubble rotation is not considered. In the present section, DNS results for microbubble collision and coalescence are analysed. To further clarify the microbubble coalescence mechanism, additional simulations are also performed under different conditions either with a larger bubble dimeter or at a higher Reynolds number, and the results are compared with the cases of upflow and downflow at Re_τ = 150 with d_b = 110 µm bubbles.

4.3.1 Downflow at $Re_\tau = 150$ with $d_b = 110$ µm

The case of downflow at $Re_\tau = 150$ with $d_b = 110$ µm is examined first. Figure 4.30 shows the time evolution of the number of bubble collisions and bubbles of different sizes over the course of the simulation. In one-way and two-way coupled simulations, the void fraction was 0.01%. The four-way coupled DNS with that same void fraction was performed first, for which the number of bubble collisions is plotted as a dot line in Figure 4.30(a). The number of bubble collisions is too low to allow quantitative analysis, corresponding to a total of $O(10^3)$ collisions detected. Hence, as mentioned before, the void fractions of all four-way coupled cases was increased to 0.10%, which allows a sufficient number of bubble collisions to occur for coalescence events to take place. In Figure 4.30(a), the solid line represents the time evolution of collisions at the higher void fraction. It is easily seen that the number of bubble collisions increases dramatically after the injection of bubbles. It is observed that a total number of 10,012 collisions occurred up to $t^+ = 23.66$ due to the high number of bubbles at the start of the simulation. After that time, the number of collisions increases more and more slowly because of the significant reduction of the bubble concentration with the number of coalescence events. To quantify and discuss bubble coalescence properly, around 170,000 collisions were allowed to occur before terminating the simulation. The reason for not recording coalescences any further can be explained from the results of Figure 4.30(b). The bubbles are treated as spherical points throughout the simulation. This means that bubbles are supposed to be sufficiently small to allow a point particle approach. Since the volume of new bubbles after coalescence is the sum of the volumes of the colliding bubbles, increasingly larger bubbles appear with time. From Figure 4.30(b), the number of bubbles with 5 times the volume of the initial bubbles already exceeds 1,000 at the end of the simulation. Additional simulation time, therefore, would have resulted in even larger bubbles not compatible with the point particle approach. It is also found that the bubbles with 1, 2 and 3 times the volume of the original bubbles constitute the majority of bubbles in the system at the final time step.

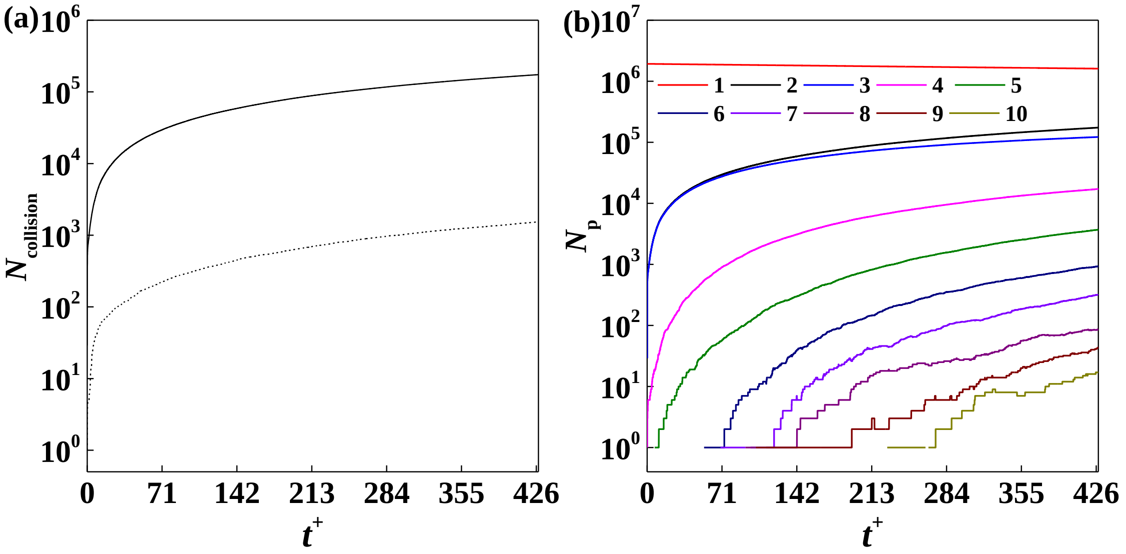

Figure 4.30 (a) Number of bubble collisions with void fraction of 0.01% (⋯) and 0.10% (—); (b) number of bubbles of different sizes as a function of the dimensionless time (by shear) in downflow at $Re_\tau = 150$ with $d_b = 110$ μm bubbles and void fraction 0.10%.

In channel flows, the flow statistics are a function of the wall-normal coordinate, which is the only inhomogeneous direction in such flows. In order to quantify the spatial character of bubble collisions, the computational domain is uniformly divided into 30 parallel slabs in the wall-normal direction. In each slab, the collision and coalescence statistics were collected, such as the number of collisions and coalescences, and the velocities and positions of each binary bubble collision. Firstly, collision and coalescence events were recorded and their distribution in the wall-normal direction is presented in Figure 4.31. Because of the symmetry in channel, Figure 4.31 presents the number of collision and coalescence events over the half channel. Due to the action of the lift force, the initial random bubble distribution is modified and more bubbles travel to the channel centre in downflow. It is seen in Figure 4.31, however, that more collisions are found near the channel walls than in the channel centre, despite the migration of bubbles towards the channel centre. However, the number of collisions in downflow decreases in the very near-wall region because of the very small number of bubbles that are found there. This occurs since, even if the concentration of bubbles is low near the wall, the near-wall region remains the area of the channel flow with the highest levels of turbulence and the largest velocity gradients, both of which promote collisions.

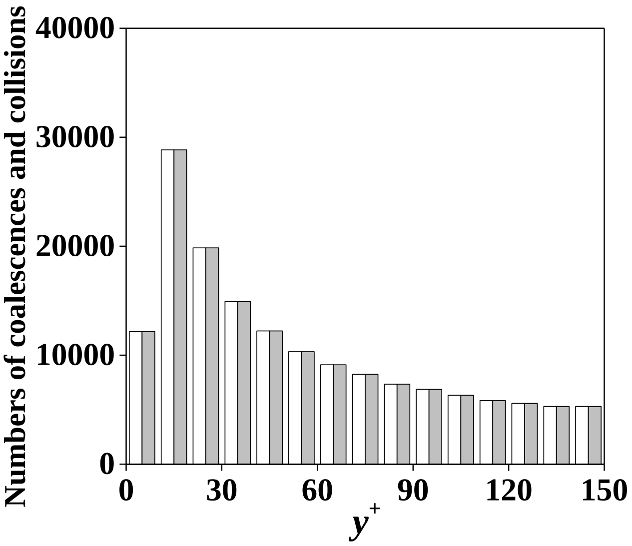

Figure 4.31 Numbers of bubble collisions (□) and coalescences (■) in the wall-normal direction in downflow at Re_τ = 150 with d_b = 110 μm bubbles.

One important aspect of the coalescence model is the coalescence efficiency. Based on the work of Coulaloglou and Tavlarides [268], most studies in the literature [68, 125, 269] consider two characteristic time scales, i.e. the film drainage time and the bubble contact time, leading to an exponential distribution of coalescence efficiency as $exp\ (- t_{drainage} / t_{contact})$. However, there is no satisfactory evidence so far to explain the exponential distribution of coalescence efficiency [270]. In this study, the coalescence efficiency is defined as the ratio between the numbers of coalescences and collisions. As seen in Figure 4.31, the coalescence efficiency is found to be 100%. This means that every collision in the channel results in a coalescence. These results were obtained using the contact time model of Sommerfeld et al. [71] and the film drainage time model of Prince and Blanch [68] (see Figure 4.32). Prince and Blanch [68] neglected the effect of surfactants and the Hamaker force, and proposed a simple drainage time relation as Eq. (3.22) (also shown in Figure 4.32) which better represents the present system. In Eq. (3.22), the initial film thickness h_0 and the final thickness h_f at which rupture occurs for the air-water system are taken from experiments [68, 271] as 10^{-4} m and 10^{-8} m, respectively. Sommerfeld et al. [71] estimated the bubble contact time by assuming that it is the time taken for a bubble to travel a deformation distance (a fraction of the bubble radius) with a certain relative collision velocity, given as Eq. (3.19). This contact model, however, suffers from the drawback of overestimation. On one hand, the coalescence calibration fraction (C_C) in Eq. (3.19) is defined as the ratio of the deformation distance and the effective bubble radius. Many studies [70, 127, 272] employed a value of 0.5 for this fraction. Given that a higher calibration fraction value results in longer contact times, it was arbitrarily set to 0.25 in present study which gives the best agreement with experimental result [71]. On the other hand, the deceleration of the bubbles during the collision process is neglected. As illustrated in Figure 4.31, results show that the bubble contact time of Sommerfeld et al. [71] is sufficiently long for all bubble collisions to result in coalescences.

Film drainage model:

- Contact time:
  - a. Sommerfeld et al. [71]:

$$t_{contact} = \frac{C_c r_{eq}}{u_n}$$

  - b. Kamp et al. [125]:

$$t_{contact} = \frac{\pi}{4}\left(\frac{8\rho_c C_{VM} r_{eq}^3}{3\sigma}\right)^{\frac{1}{2}}$$

- Drainage time: Prince and Blanch [68]:

$$t_{drainage} = \sqrt{\frac{{r_{eq}}^3\rho_C}{16\sigma}}\ln\left(\frac{h_0}{h_f}\right)$$

Energy model:
Sovová [137]

- Kinetic collision energy:

$$E_s = 4\sigma\left(\frac{\pi}{6}\right)^{2/3}(r_1^2 + r_2^2)$$

- Interfacial energy:

$$E_{kin} = \frac{2\pi}{3}\rho_g u_{rel}^2 \frac{r_1^3 r_2^3}{r_1^3 + r_2^3}$$

Figure 4.32 Selected coalescence models for evaluation of the coalescence efficiency.

To examine other coalescence modelling approaches in the literature for incorporation in the Lagrangian particle tracking routine, the contact time model of Kamp et al. [125] and the energy model of Sovová [137] (see Figure 4.32) were also tested for all collected collision data from the runs described without requiring extra extremely expensive computational runs. In the contact time model of Kamp et al. [125], the bubble contact time is obtained by considering the energy conservation equation for the initial kinetic energy for the bubbles at the moment that their surfaces first touch. The inertial effects accompanying film drainage are also considered in this model, which is usually neglected in most investigations [273, 274]. The results, however, showed the same 100% efficiency of coalescence, since the contact time between the bubbles was always sufficiently long to allow drainage of the liquid film trapped between them.

The energy model [137] determines coalescence efficiency by comparing the interfacial energy and the kinetic collision energy. From Eqs. (3.23) and (3.24) (also shown in Figure 4.32), it is easily seen that the surface energy is proportional to the interfacial tension and bubble surface area, whilst the kinetic collision energy is proportional to the average volume and relative velocity of the two colliding bubbles. This means that bubbles only coalesce when their approach velocity is less than a critical coalescence velocity [139, 275]. Results from this model, in contrast to previous findings, changed completely, with a 0% coalescence efficiency found.

An explanation for the 100% efficiency of the film drainage model (and 0% for the energy model) is found in the results of Figure 4.33 and Figure 4.34. In Figure 4.33, the relative bubble collision velocities in the streamwise direction, wall-normal direction, and spanwise direction are presented. In the wall-normal direction the turbulent channel flow can be characterised into four regions, in terms of the different dynamic mechanisms that dominate the turbulence kinetic energy balance, namely the viscous sub-layer ($y^+ < 5$), the buffer region ($5 < y^+ < 30$), the log-law region ($30 < y^+ < 50$), and the bulk flow region ($y^+ > 50$) [276, 277], and it is useful to understand the collision statistics in these different regions of the channel. In Figure 4.33, the relative bubble collision velocities are plotted in the four well-defined regions of the channel for downflow. The relative bubble collision velocities in the streamwise, wall-normal and spanwise directions are all found to be highest in the viscous sub-layer (Figure 4.33(a), (b) and (c)), where the largest mean velocity gradients, but the lowest turbulence levels, are found. Towards channel centre, the distributions of the PDFs of relative bubble collision velocities are observed to be more limited in range. The same is done for the bubble collision angles in Figure 4.34. Here, the distribution of the peak of collision angles is consistent with the collision velocities, being largest in the viscous sub-layer and decreasing away from the channel wall. These results show that the relative velocities, and angles, are always very small. At the shear Reynolds number considered, turbulence affects bubble motion mainly in the streamwise direction, resulting in collisions that are almost rectilinear and occurring mainly in the streamwise direction due to the small relative velocities and angles of colliding bubbles. As a consequence of the type of collision, the predicted contact time is always high, which explains the 100% coalescence efficiency returned by the film drainage model. Conversely, according to the energy model of Sovová [137], a high critical bubble velocity results in a rapid coalescence, otherwise coalescence is unlikely.

From the simulated results, the low relative velocity observed during collisions, which translates into low-energy collisions, explains the 0% efficiency of the energy model.

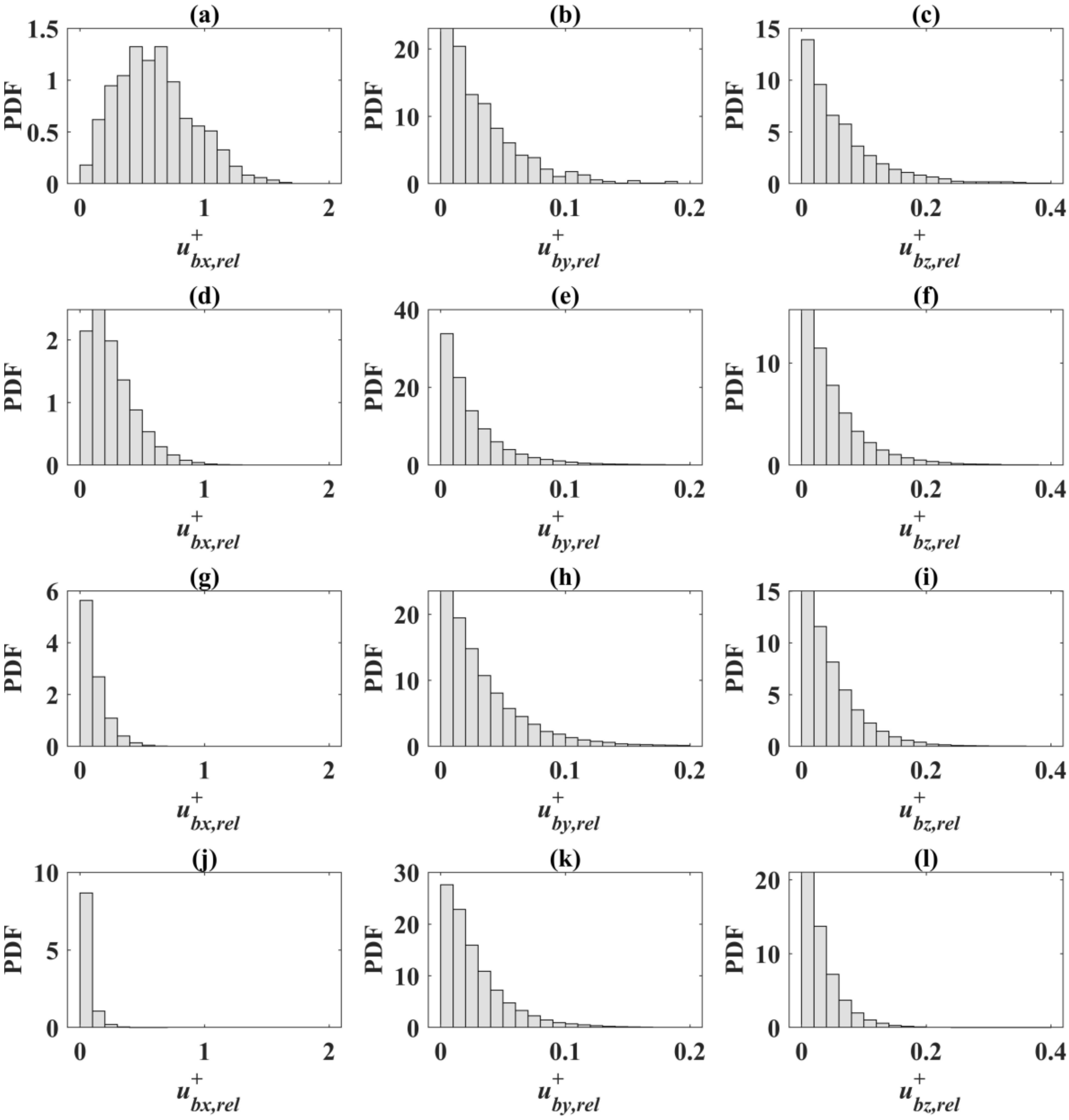

Figure 4.33 PDF of relative bubble collision velocities in *x*, *y*, and *z* direction and different regions of the channel in downflow at $Re_\tau = 150$ with $d_b = 110$ μm bubbles. (a), (b) and (c) Viscous sub-layer; (d), (e) and (f) buffer region; (g), (h) and (i) log-law region; (j), (k) and (l) bulk region.

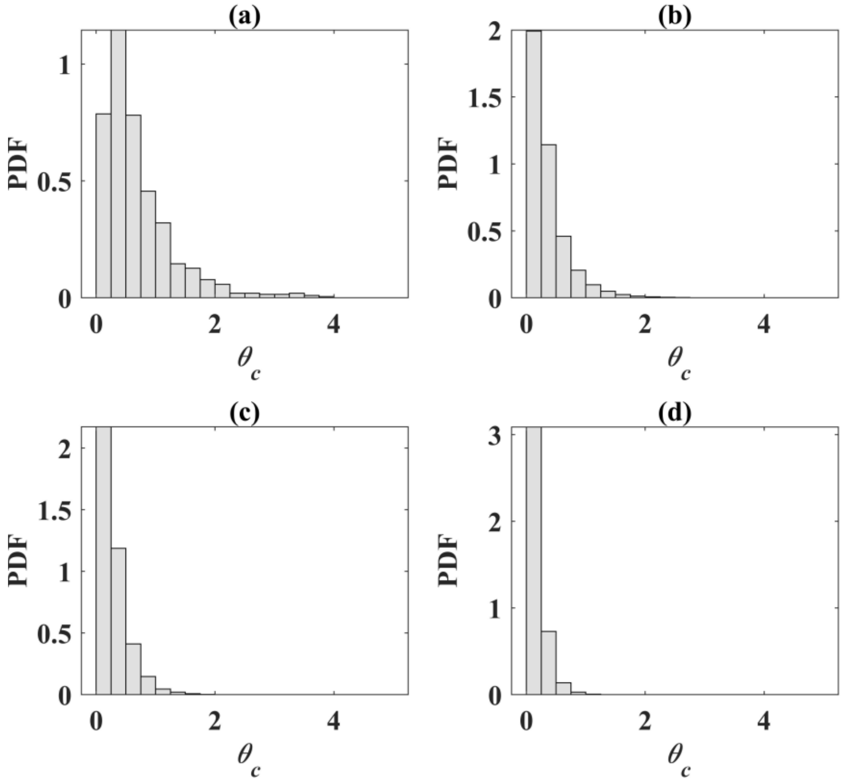

Figure 4.34 PDF of bubble collision angles in different regions of the channel in downflow at $Re_\tau = 150$ with $d_b = 110$ μm bubbles. (a) Viscous sub-layer; (b) buffer region; (c) log-law region; (d) bulk region.

4.3.2 Upflow at $Re_\tau = 150$ with $d_b = 110$ μm

Similar studies were performed for the case of upflow at $Re_\tau = 150$ with bubbles of d_b = 110 μm. The void fraction is again increased to 0.10%, because of the low number of collisions for the case of a low void fraction of 0.01%, shown as a dot line in Figure 4.35(a). The simulation was stopped as before when the number of bubbles with a volume of 4 times the original bubble size was about $O(10^3)$, see Figure 4.35(b), corresponding to a total of 210,000 collisions up to that time. As may be noted in the bubble size evolutions for both downflow in Figure 4.30(b) and upflow in Figure 4.35(b), bubbles with volumes of one, two and three times the original bubble size constitute the majority of bubbles in the system.

Bubble collision and coalescence events are plotted in the wall-normal direction in Figure 4.36. The results show that more collisions are found in the near-wall region, including in the viscous sub-layer. Besides the reasons discussed in Section 4.3.1, in upflow collisions are also promoted by the higher bubble concentration in the wall area driven by the lift force. Figure 4.36 also confirms that the coalescence efficiency is still 100%.

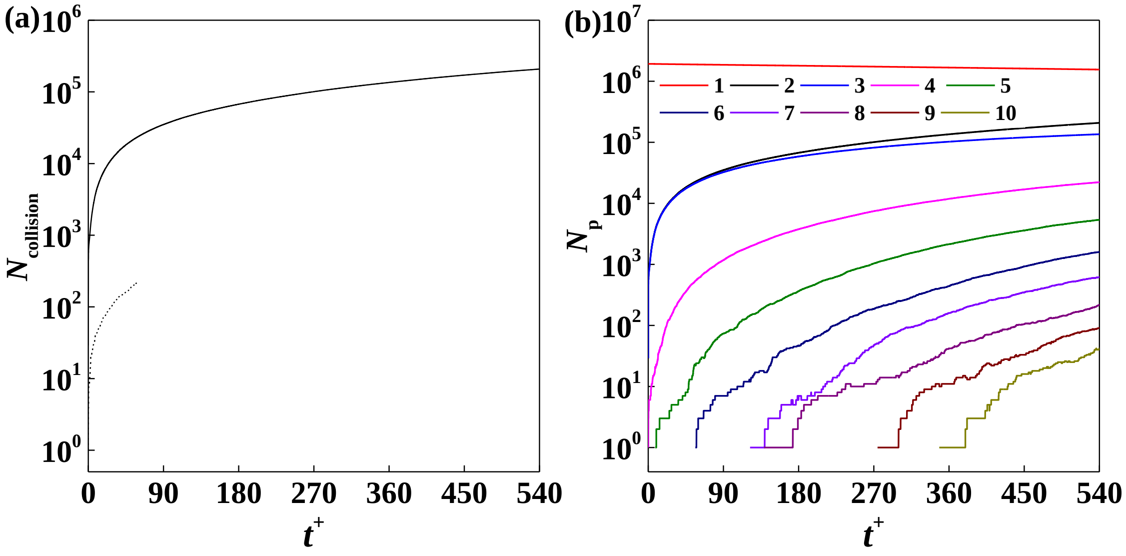

Figure 4.35 (a) Number of bubble collisions with void fraction of 0.01% (···) and 0.10% (—) and (b) evolution of the number of bubbles of different sizes as a function of the dimensionless time in upflow at $Re_\tau = 150$ with $d_b = 110$ μm bubbles.

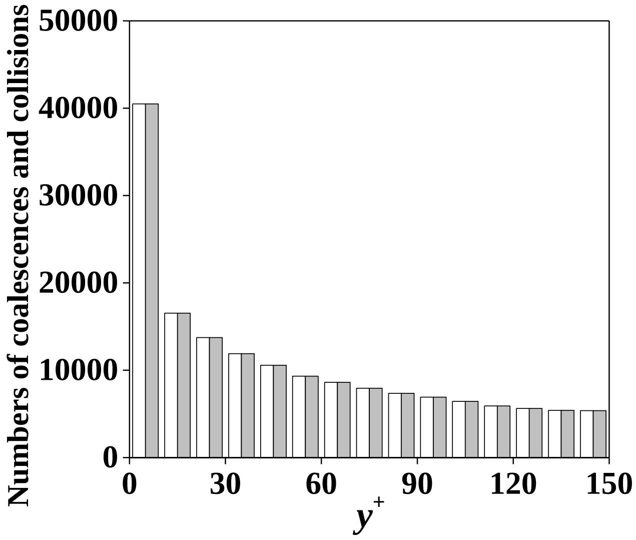

Figure 4.36 Numbers of bubble collisions (□) and coalescences (■) in the wall-normal direction in upflow at $Re_\tau = 150$ with $d_b = 110$ μm bubbles.

In Figure 4.37, the relative bubble collision velocities in the streamwise direction, wall-normal direction, and spanwise direction are plotted in different regions of the channel for upflow. It can be seen, compared with those of downflow in Figure 4.33, that the velocities in all direction are observed to be slightly larger in upflow, especially in the wall-normal and spanwise directions. Similarly, the collision angle distribution in all regions is shown in Figure 4.38. In Figure 4.36, more collisions are found in the viscous sub-layer. Due to the fact that the bubbles enhance fluid turbulence in upflow and that a large mean velocity gradient exists in viscous sub-layer, the peaks in the collision angle is larger in upflow compared to downflow. It may also be noted that the PDF in Figure 4.38(a) shows a lower probability at around 5º. Unfortunately, it is not possible to give a proper explanation for this distribution. In general, viscous effects are permitting more collisions in the viscous sub-layer than elsewhere. This increase in collision velocities and angles is not, however, enough to change the type of bubble collisions, with them again being substantially rectilinear, i.e. head on, which further confirms the reasons for the observed 100% coalescence efficiency.

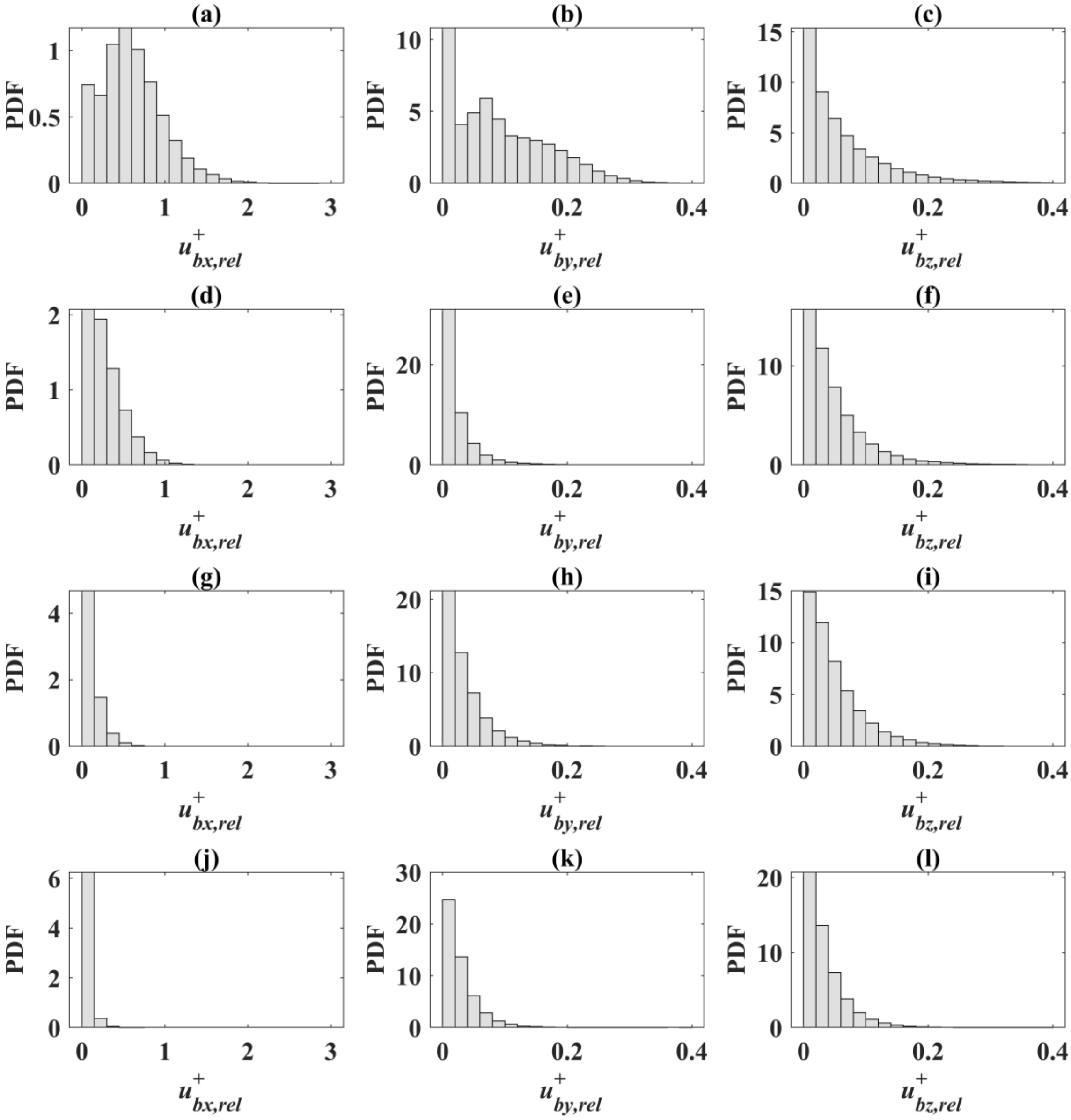

Figure 4.37 PDF of relative bubble collision velocities in *x*, *y*, and *z* direction and different regions of the channel in upflow at $Re_\tau = 150$ with $d_b = 110$ μm bubbles. (a), (b) and (c)

Viscous sub-layer; (d), (e) and (f) buffer region; (g), (h) and (i) log-law region; (j), (k) and (l) bulk region.

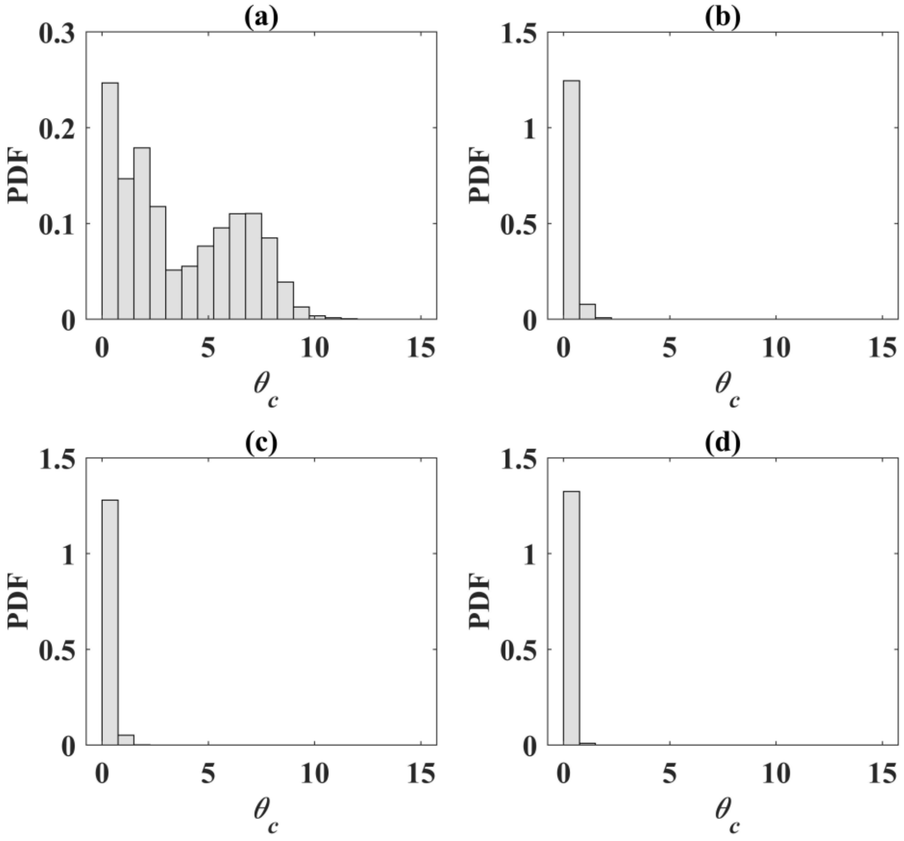

Figure 4.38 PDF of bubble collision angles in different regions of the channel in upflow at Re_τ = 150 with d_b = 110 µm bubbles. (a) Viscous sub-layer; (b) buffer region; (c) log-law region; (d) bulk region.

4.3.3 Downflow at Re_τ = 150 with d_b = 330 µm

To further understand microbubble dynamics in channel flows, the effect of bubble size is also considered because different bubble sizes have different rising velocities. An amount of 71,426 microbubbles with a larger diameter d_b = 330 µm were injected in downward channel flow corresponding to a void fraction of 0.10%. The simulation was performed for a void fraction of 0.10% only, simply due to the low number of collisions occurring for a void fraction of 0.01%, as discussed in Sections 4.3.1 and 4.3.2. The coalescence model was again taken from the contact time model of Sommerfeld et al. [71] and the film drainage time model of Prince and Blanch [68] to allow a comparison with small bubble results. The number of bubble collisions was counted until the number of bubbles with four times the original size reached $O(10^3)$, see Figure 4.39(b). As a result, a total of 32,293 collision were recorded. In this case, results for the downward flow in terms of the bubble number density profiles in Figure 4.39 were qualitatively similar to those given above for the smaller bubble diameter case in Figure 4.30. However, the similarity is lost in the bubble size distribution, where bubbles with one and two times the size of the original d_b = 330 μm bubble volume are observed to constitute the majority of bubbles at the final time-step. This is due to the low bubble density in the present case, with same volume fraction as the small bubble simulation, since large bubbles are more likely to contact with other large bubbles rather than d_b = 330 μm bubbles.

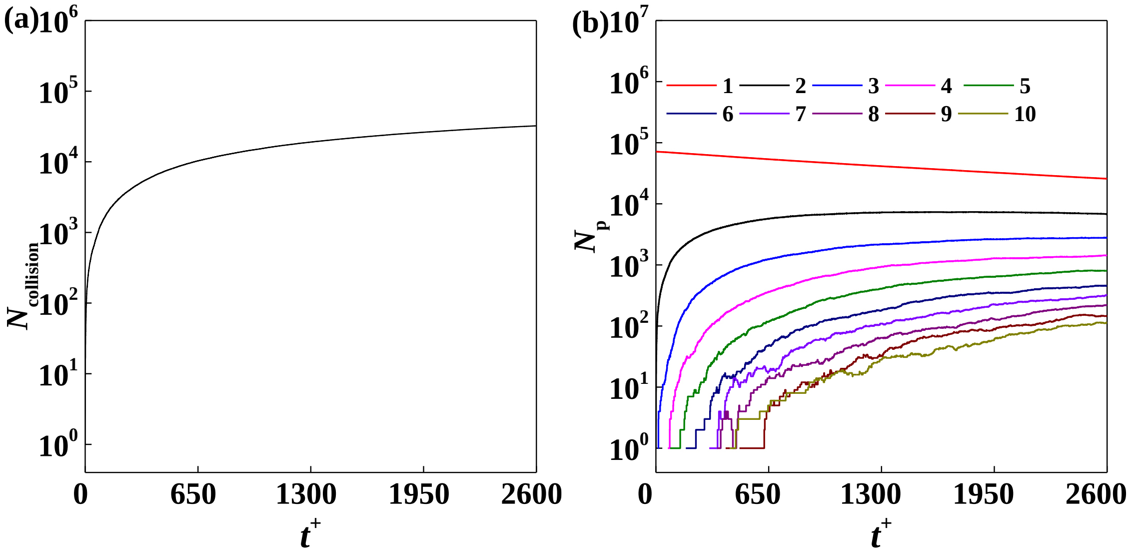

Figure 4.39 (a) Number of bubble collisions with void fraction of 0.10% and (b) evolution of number of bubbles of different sizes as a function of the dimensionless time in downflow at Re_τ = 150 with d_b = 330 μm bubbles.

Collision and coalescence events are presented in Figure 4.40, confirming that collisions are again favoured in regions with high levels of turbulence, i.e. towards the channel walls, with few collisions found in the very near-wall region due to the low bubble concentration there in downflow. This is in qualitative agreement with the small bubble case in Figure 4.31. On the other hand, the film drainage time given by the Prince and Blanch [40] model relates to the equivalent bubble diameter as ~ $r_{eq}^{3/2}$, while the contact time model of Sommerfeld et al. [71] relates as ~ r_{eq}. Accordingly, the increase of bubble diameter leads to a longer film drainage time and bubble collisions without coalescences are to be expected. However, the increase of bubble diameter, as seen in Figure 4.40, does not change the coalescence efficiency with every collision still resulting in a coalescence.

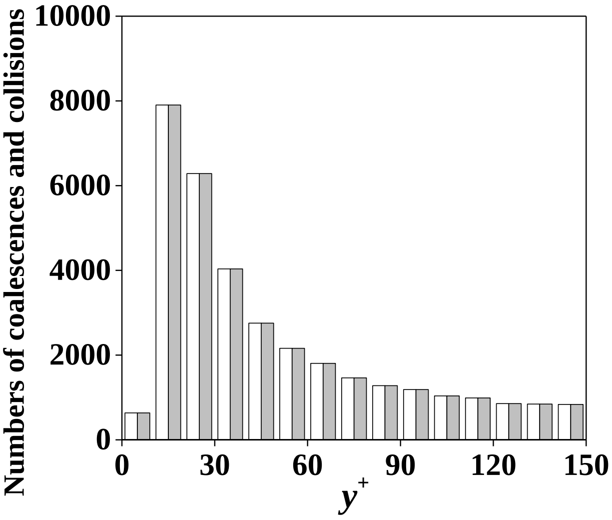

Figure 4.40 Numbers of bubble collisions (□) and coalescences (■) in the wall-normal direction in downflow at Re_τ = 150 with d_b = 330 μm bubbles.

Results for collision statistics are again plotted in different regions of the flow in the wall-normal direction, with PDFs of bubble collision velocities presented in Figure 4.41 and bubble collision angles in Figure 4.42. In both cases, results are compared with the case of downflow with bubbles of d_b = 110 μm in Figure 4.32. Due to the low bubble concentration in the channel wall area, few samples were found in the viscous sub-layer, which makes the PDF comparisons in Figure 4.41(a), (b) and (c) and Figure 4.42(a) unreliable, although it can be seen that some collisions show larger collision velocities and wider collision angles. The remaining plots in Figure 4.41 and Figure 4.42 show that, for the larger microbubbles, the ranges of both bubble velocities and collision angles tend to be slightly larger than in the case of the 110 μm bubbles. The cause of this is worthy of further consideration, since narrower ranges might have been expected given that the larger inertia of 330 μm bubbles should make them less prone to be affected by the fluid flow. Different phenomena may be responsible for the larger ranges, such as the higher shear across the bubble, and body forces, instantaneously experienced by the 330 μm bubbles in the most turbulent regions of the flow. At the same time, as soon as coalescence begins, larger more buoyant bubbles are formed. The increase in bubble size with coalescence, and the corresponding difference in velocity, can be expected to be much larger for coalescing 330 μm bubbles than for 110 μm bubbles. These bubble size broadening effects would cause the 110 μm bubbles to have smaller relative streamwise velocities and collision angles, with peak probability values at lower levels.

However, on one hand, in downflow larger bubbles can introduce more velocity fluctuations into the flow [96], leading to a fluid mean velocity profile, rms of velocity fluctuations and Reynolds shear stress, and vorticity increases with the bubble size, especially in the channel centre where more bubbles accumulate. On the other hand, the microbubbles are preferentially trapped in regions of high vorticity [57], which brings bubbles together and leads to collisions. Therefore, a wider range of collision velocities and angles is also expected.

Overall, the relative collision velocities and collision angles in Figure 4.41 and Figure 4.42 remain small in the remaining regions of the flow, which confirms that, for the microbubbles considered, both bubble sizes tend to move and collide in nearly rectilinear paths.

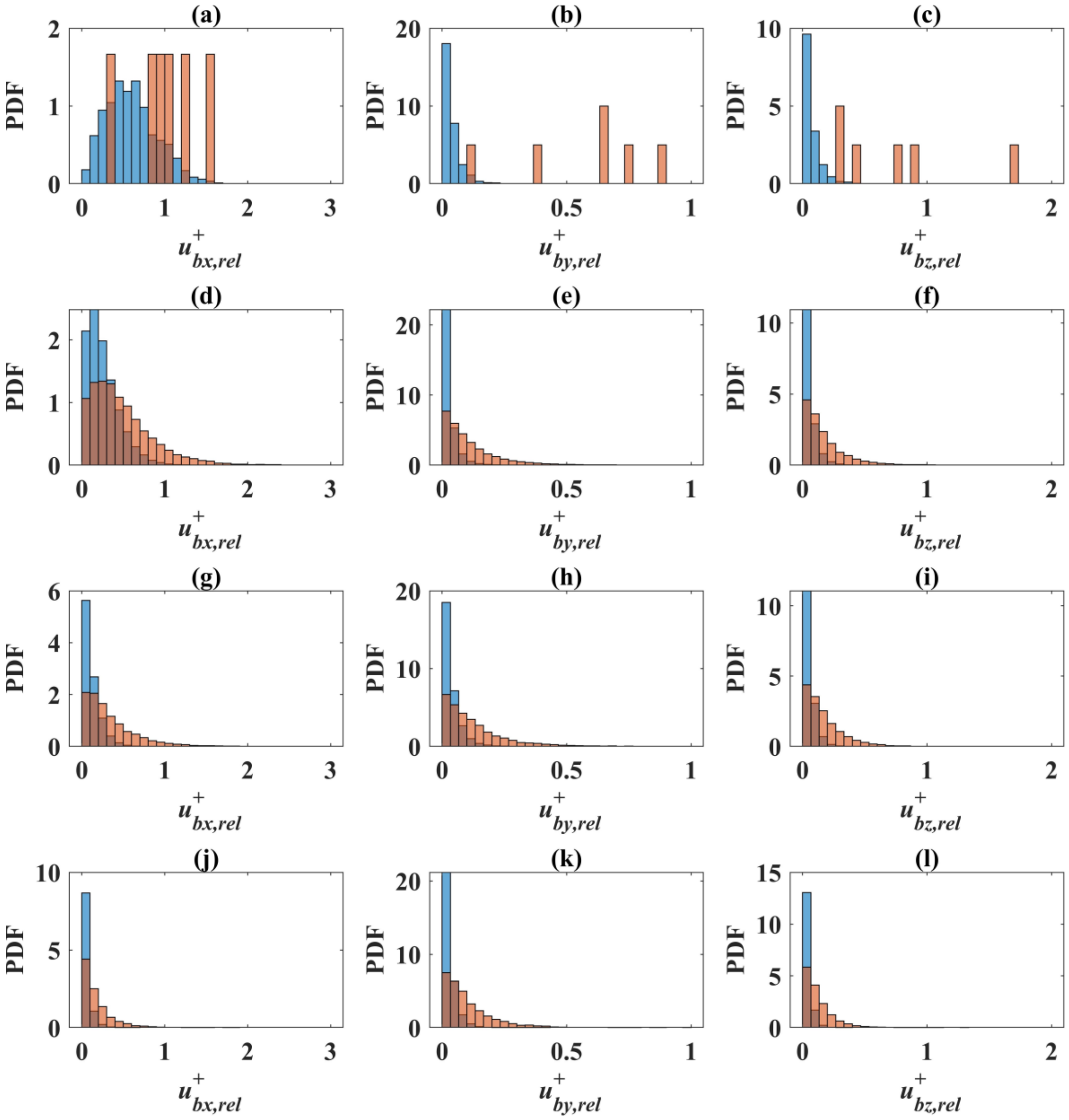

Figure 4.41 Comparison of PDF of relative bubble collision velocities in *x*, *y*, and *z* direction and different regions of the channel in downflow at $Re_\tau = 150$ with $d_b = 330$ μm (🟧) and 110 μm (🟦) bubbles. (a), (b) and (c) Viscous sub-layer; (d), (e) and (f) buffer region; (g), (h) and (i) log-law region; (j), (k) and (l) bulk region.

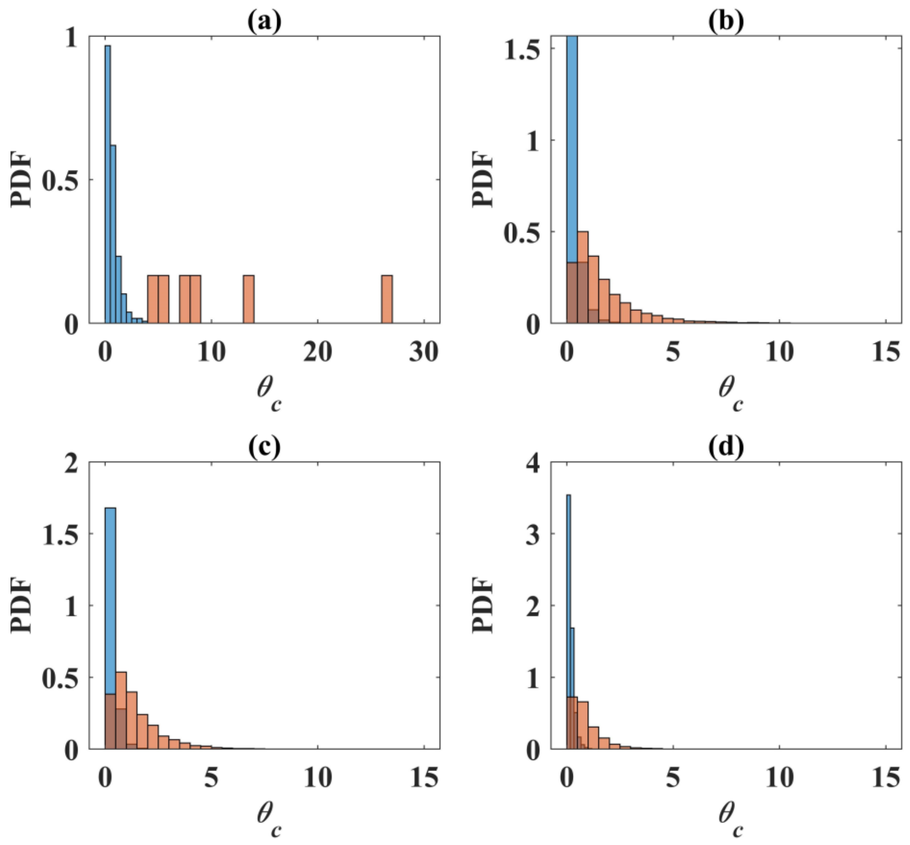

Figure 4.42 Comparison of PDF of bubble collision angles in different regions of the channel in downflow at Re_τ = 150 with d_b = 330 μm (🟧) and 110 μm (🟦) bubbles. (a) viscous sub-layer; (b) buffer region; (c) log-law region; (d) bulk region.

4.3.4 Upflow at Re_τ = 150 with d_b = 330 μm

A further investigation with large bubbles with diameters d_b = 330 μm is performed in upflow to confirm the above findings. The results are analysed using the 31,000 bubble collisions recorded (see Figure 4.43), counted similarly as in the previous simulations. Results for the number of bubble collisions and coalescences are shown in Figure 4.44. Interestingly, nearly 50% of collisions happened in the near wall region, which is the first slab on the channel wall. This is simply due to the higher concentration in this region than in the rest of channel, due to the effect of the lift force on the bubbles. However, in present study, there may have an over-estimation of the lift force on the d_b = 330 μm bubbles in upflow. Molin et al. [64] computed the lift coefficient for d_b = 330 μm bubbles as below:

$$C_L = \left[K_0\left(\frac{Sr_B}{2}\right)^{0.9} + K_1\left(\frac{Sr_B}{2}\right)^{1.1}\right]\frac{3}{4Sr_B} \tag{4.7}$$

where K_0 and K_1 are calculated as a function of non-dimensional the shear rate Sr_B from Kurose and Komori [278]. Additionally, a wall-induced aerodynamic lift force by

Takemura and Magnaudet [279] was also included to consider a repulsive contribution when the bubble approaches the wall. As a result, a positive lift force (away from the channel wall) was found in their study [64], which made the bubble concentration in the near-wall region in upflow lower than in the channel centre. This is, however, contrary to the present findings for this and the other upflows considered above. This concentration difference had no effect on the coalescence efficiency for the upflow case in the present study (see Figure 4.44) with 100% efficiency returned, even if the highest levels of turbulence and the largest velocity gradients are expected to give more possibilities of bubble collisions without coalescences. Asiagbe et al. [280] employed large eddy simulation (LES) to examine air bubble collision and coalescence in water flows at Re_τ = 150 with d_b = 220 μm bubbles using a similar film drainage coalescence model. In evaluating coalescence efficiency, the authors observed that, in the near-wall region, the bubbles experience shorter contact times. In these regions, this resulted in not all collisions leading to coalescence in both upward and downward flows, although towards the centre of the channel, where turbulence levels are lower, 100% or near-100% coalescence efficiency was achieved. Nevertheless, collisions efficiencies were always high (> 95%), even in the near-wall region, apart from in the upflow case where the efficiency was significantly reduced. Similarly, Asiagbe et al. [129], in considering a Re_τ = 150 horizontal channel flow with d_b = 110 μm bubbles, observed an effectively 100% coalescence efficiency throughout the flow, with this attributed to the low flow Reynolds number. The work of Asiagbe et al. [129, 280] used a high resolution LES with 2.1 M nodes although, clearly, not all the velocity scales were resolved, with the smallest scales modelled after filtering. The unresolved scales, particularly near the wall, will have some effect on the bubble motion, and may be responsible for the differences found between the present DNS- and LES-based simulations. Nevertheless, the differences between results based on the two simulation approaches are relatively small, particularly in view of the 100% efficiency returned by the film drainage model, and the 0% by the energy model, in the present work.

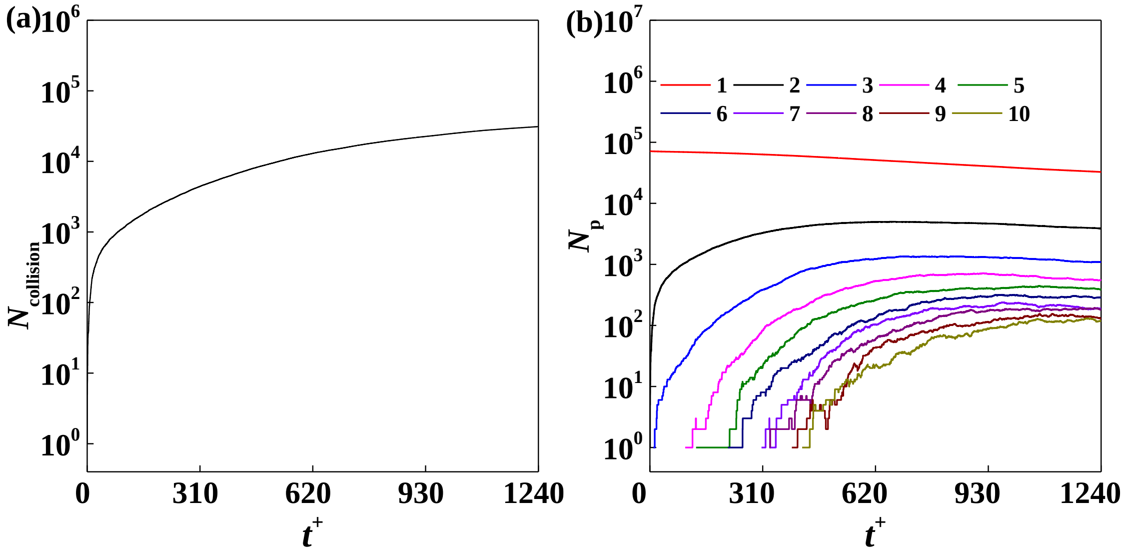

Figure 4.43 Number of bubble collisions (a) and number of bubbles of different sizes (b) evolution over time in upward channel flow at $Re_\tau = 150$ with $d_b = 330$ µm.

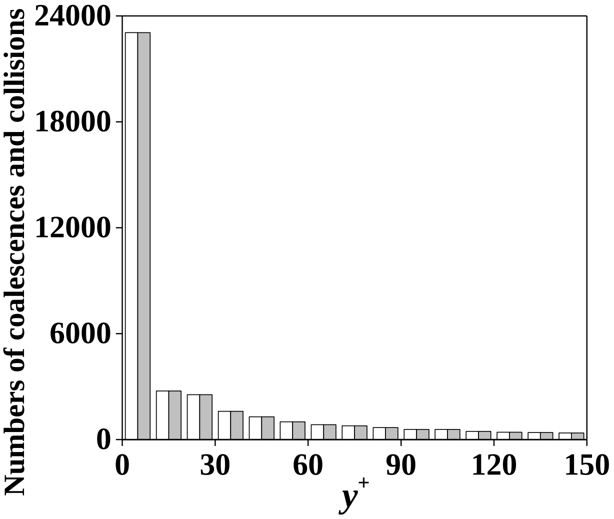

Figure 4.44 Numbers of bubble collisions and coalescences across the wall-normal direction in DNS of four-way coupled downflow at $Re_\tau = 150$ with $d_b = 330$ µm.

Compared to the downflow case, in upflow a generally similar range of relative velocities and collision angle magnitudes is found for both bubble sizes, as given in Figure 4.45 and Figure 4.46. This does not fully follow the difference between upward and downward flows with $d_b = 110$ µm as discussed above. The larger inertia of 330 µm bubbles makes them less prone to be affected by the fluid so that similar magnitudes of relative velocities and collision angles are observed in both flows, except in the viscous sub-layer where collisions are promoted by the large mean velocity gradient and higher bubble density ratio in upflow.

Qualitative differences in the PDFs between upflows with d_b = 110 μm and 330 μm are, however, apparent. In particular, coalescence leading to larger bubble sizes is found to give rise to the accumulation of large coalesced 330 μm bubbles in the viscous sub-layer, again with much larger sizes than for the 110 μm case. These large bubbles remain close to the wall, decreasing through buoyancy effects the streamwise relative velocity and collision angle, and also shifting the probability distributions to lower values.

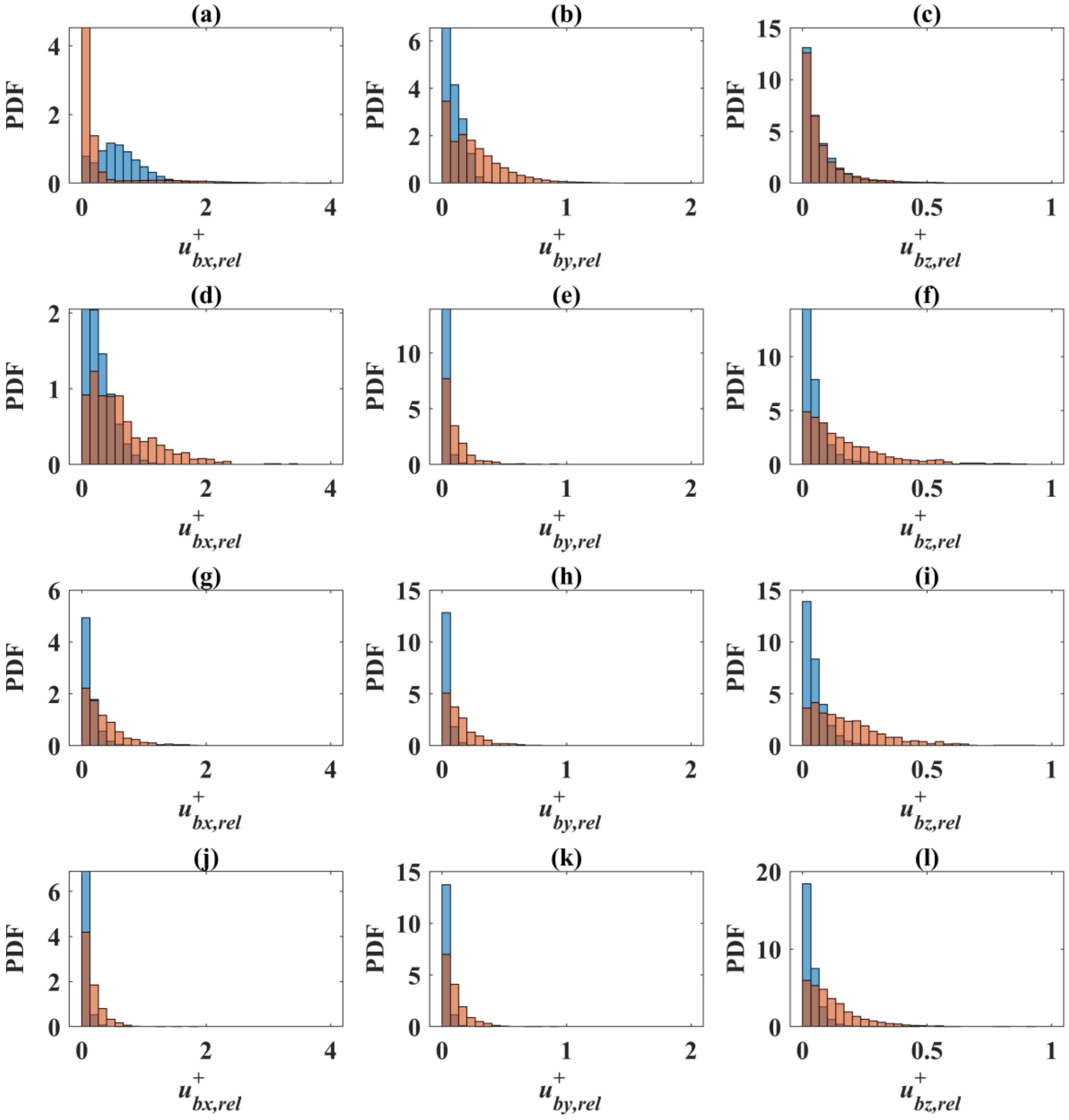

Figure 4.45 Comparison of PDF of relative bubble collision velocities in *x*, *y*, and *z* direction and different regions of the channel in upflow at Re_τ = 150 with d_b = 330 μm

(🟧) and 110 μm (🟦) bubbles. (a), (b) and (c) Viscous sub-layer; (d), (e) and (f) buffer region; (g), (h) and (i) log-law region; (j), (k) and (l) bulk region.

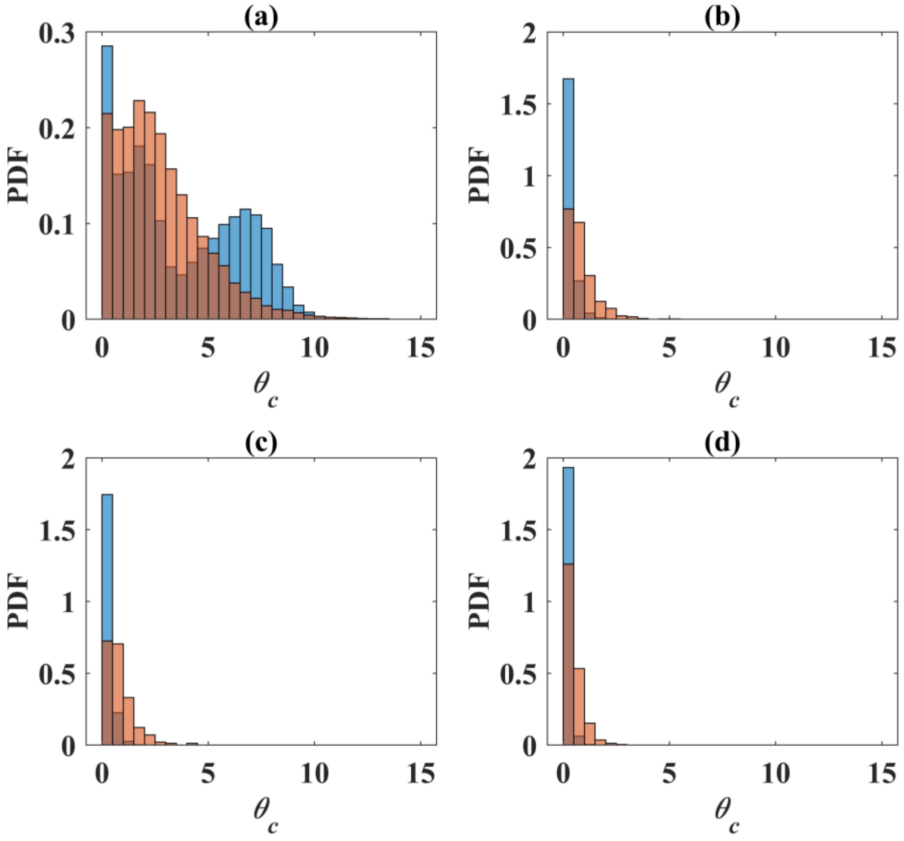

Figure 4.46 PDF of bubble collision angles in different regions of the channel in upflow at Re_τ = 150 with d_b = 330 μm bubbles. (a) Buffer region; (b) log-law region; (c) bulk region.

4.3.5 Downflow at Re_τ = 395 with d_b = 110 μm

In Sections 4.3.5 and 4.3.6, the effect of Reynolds number on the behaviour of bubble collisions is examined by moving from a Re_τ = 150 to a Re_τ = 395 flow with d_b = 110 μm bubbles under same void fraction in downflow and upflow. A single-phase channel flow at a moderate Reynolds number exhibits several different features compared to at a low Reynolds number, as previously noticed both experimentally and numerically [257]. For example, a wide log-law layer exists at high Reynolds number, which can reach to $y^+ \approx$ 200 for Re_τ = 395. Also, a high Reynolds number presents higher levels of velocity fluctuations. It has also been noted that, in bubbly flow with the same void fraction, the bubbles travel significantly differently under different levels of turbulence [129]. Therefore, the flow turbulence structure is an important factor determining bubble collisions and coalescences, and the effect of Reynolds number on bubble dynamics becomes of interest. Hence, the objective here is to check whether the collision type and the coalescence efficiency observed in Sections 4.3.1 and 4.3.2 remains the case in downflow and upflow at a moderate Reynolds number.

The simulation was started from an initially validated single-phase flow at $Re_\tau = 395$. The same void fraction of microbubbles of $d_b = 110$ µm were injected as in the previous four-way coupled simulations. To give a fair comparison with the lower Reynolds number case, the coalescence model is still taken from the contact time model of Sommerfeld et al. [71] and the film drainage time model of Prince and Blanch [68]. Results for downward flow in terms of bubble number density profiles were qualitatively similar to those given above for the lower Reynolds number, so are not reproduced here.

Comparisons between the current results and those of downflow at $Re_\tau = 150$ with $d_b =$ 110 µm bubbles are presented in Figure 4.47 and Figure 4.48. Recall that, in Figure 4.47, collision relative bubble velocities in the x, y and z directions are plotted in the viscous sub-layer, buffer region, log-law region, and bulk region, and the same is done for collision angles in Figure 4.48. The distributions in Figure 4.47 show a qualitatively similarity with the low Reynolds number case, except in the viscous sub-layer where a small amount of bubbles is found and the corresponding plots in Figure 4.47(a), (b) and (c) are lacking in data to be statistically meaningful. That said, nearly the same magnitude in the relative velocity in the streamwise direction is observed at the higher Reynolds number. However, slightly wider magnitudes of collision velocities in wall-normal and spanwise directions are returned in Figure 4.47 compared to the downflow at the lower Reynolds number. This is mainly due to the fact that, as the Reynolds number increases, the components of the rms velocities in the spanwise and wall-normal directions are more enhanced than in the streamwise direction. This enhancement also gives a slight increase in the collision angles which is shown in Figure 4.48. One potential reason for this is the vortical structures of channel flows at different Reynolds numbers. It is widely known that microbubbles in turbulent flow travel following the low-speed streaks close to the wall, and tend to accumulate in the cores of vortices. In the channel flow at $Re_\tau = 150$, quasi-streamwise vortices are dominant. With increases in the Reynolds number, the well-known hairpin vortex does not exist anymore. Instead, some single vortices are generated and dominate the flow structures. These vortical structures, including the streamwise vortices, are associated with the low-speed streaks. The microbubbles are preferentially accumulated in those low-speed streaks of the carrier phase and remain trapped there for a long time [281]. As a result, the microbubbles in different cores of the vortices exhibit a wider range of collision angles, especially in the viscous sub-layer and buffer region.

In contrast, away from the wall, the enhancements of both the relative velocities and collision angles in the log-law and bulk regions are very limited. This is simply because the rms profiles of the fluid velocity fluctuations in all three directions under Re_τ = 150 and Re_τ = 395 are the same in those two regions, more specifically, $u'^{+}_{x,rms}$, $u'^{+}_{y,rms}$, and $u'^{+}_{z,rms}$ collapse from y / δ = 0.4, 0.5 and 0.8, respectively. As a result, the microbubbles travel and collide with each other in the same way as in the lower Reynolds number flow.

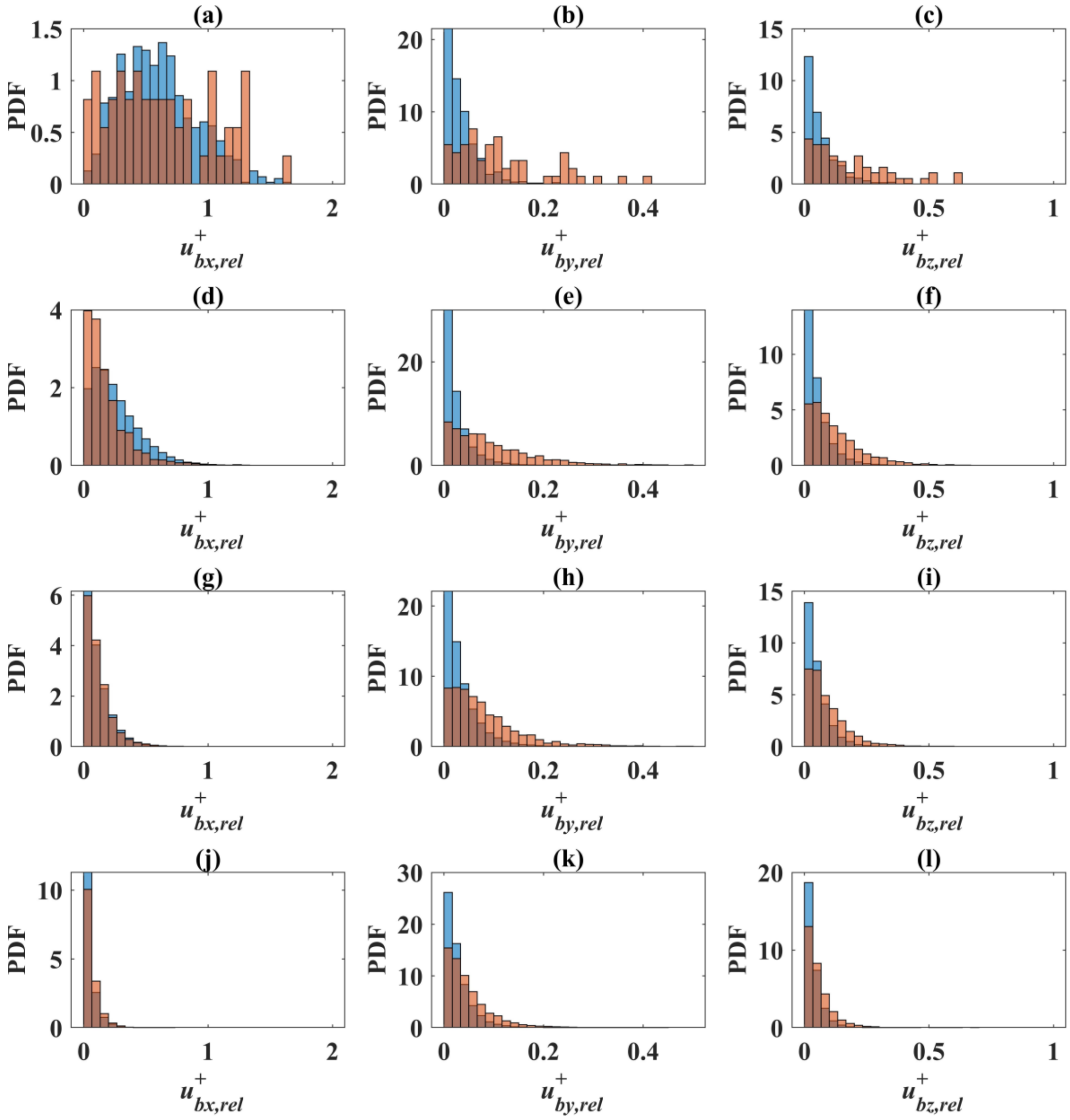

Figure 4.47 Comparison of PDF of relative bubble collision velocities in x, y, and z directions and different regions of the channel in downflow at Re_τ = 395 (🟧) and Re_τ =

150 (🟦) with d_b = 110 µm bubbles. (a), (b) and (c) Viscous sub-layer; (d), (e) and (f) buffer region; (g), (h) and (i) log-law region; (j), (k) and (l) bulk region.

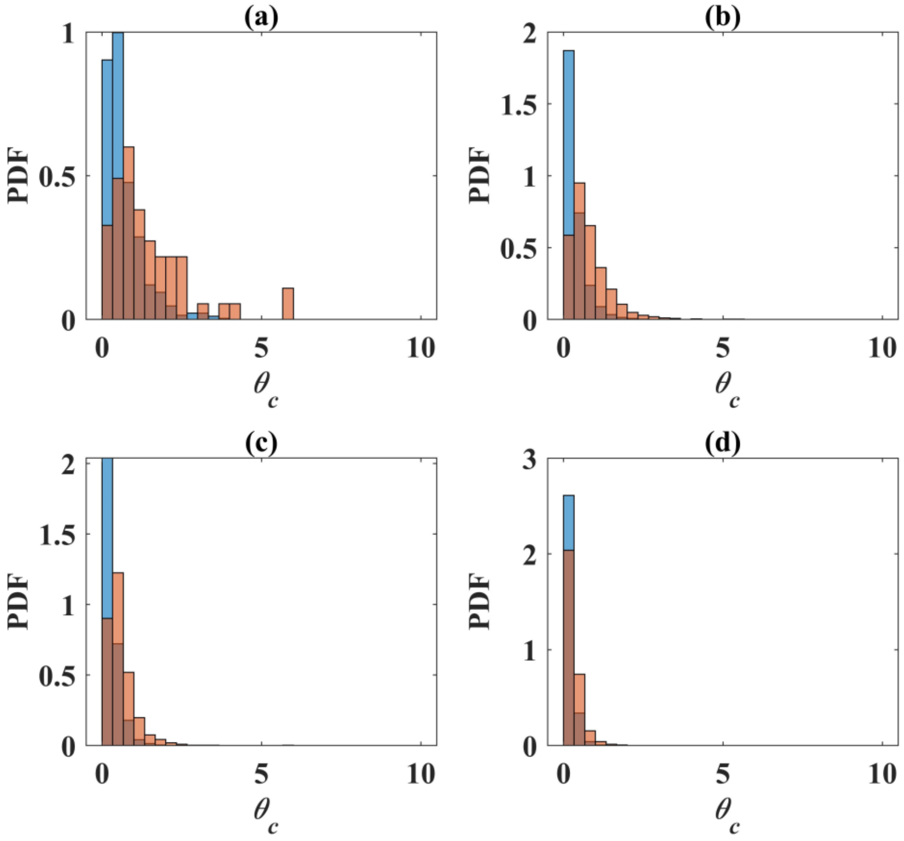

Figure 4.48 Comparison of PDF of bubble collision angles in different regions of the channel in downflow at Re_τ = 395 (🟧) and Re_τ = 150 (🟦) with d_b = 110 µm bubbles. (a) Viscous sub-layer; (b) buffer region; (c) log-law region; (d) bulk region.

4.3.6 Upflow at Re_τ = 395 with d_b = 110 µm

The case of upflow at Re_τ = 395 with the same bubble diameter under four-way coupling is simulated similarly, the results of which are compared in Figure 4.49 and Figure 4.50 with predictions of upflow at Re_τ = 150. Bubble collision velocities and angles in the four regions of the flow are again qualitatively similar although, in both figures, some slight enhancements are found in both the bubble collision velocities and angles.

Close to the wall region, there are obvious differences in both the viscous sub-layer and the buffer regions, where both velocities in the spanwise and wall-normal directions, and collision angles, generally become larger with increases in Reynolds number. This has been mentioned in Section 4.3.5, and is mainly due to the enhancement of fluid velocity fluctuations and vorticial structures at the higher Reynolds number. In the viscous sub-layer, larger rms fluid velocities fluctuations are found in the case of the $Re_\tau = 395$ flow which in turn enhances the streamwise relative velocity in Figure 4.49(a). However, the effect of Reynolds number does not change the magnitude of the collision angles, with a similar range of angles as for the $Re_\tau = 150$ flow observed. This may be due to the smaller bubble velocities and lower level of turbulence in the very near-wall region. Also, the PDF in Figure 4.50(a) shows that bubble collisions in the high Reynolds case preferentially occur at small angles. Away from the wall, the relative velocities in both the wall-normal and spanwise directions are larger for the higher Reynolds number, although trend decreases towards the channel centre, and is little different from the lower Reynolds number case in the bulk flow region.

However, the enhancements of both relative velocities and collision angles due to the increase in flow Reynolds number are limited. As a result, collisions between bubbles remain almost rectilinear, occurring mainly in the streamwise direction.

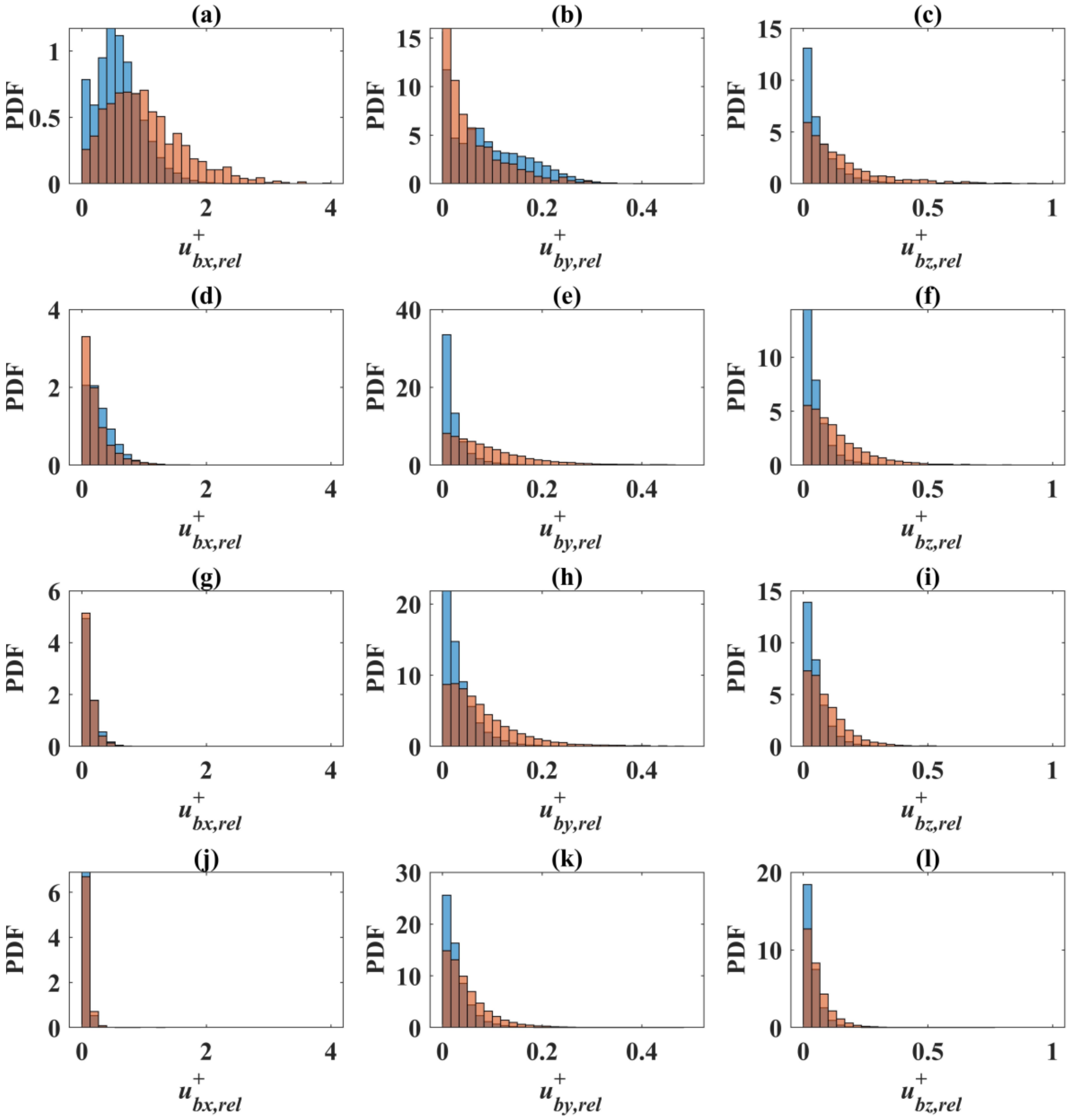

Figure 4.49 Comparison of PDF of relative bubble collision velocities in *x*, *y*, and *z* directions and different regions of the channel in upflow at $Re_\tau = 395$ (🟧) and $Re_\tau = 150$ (🟦) with $d_b = 110$ μm bubbles. (a), (b) and (c) Viscous sub-layer; (d), (e) and (f) buffer region; (g), (h) and (i) log-law region; (j), (k) and (l) bulk region.

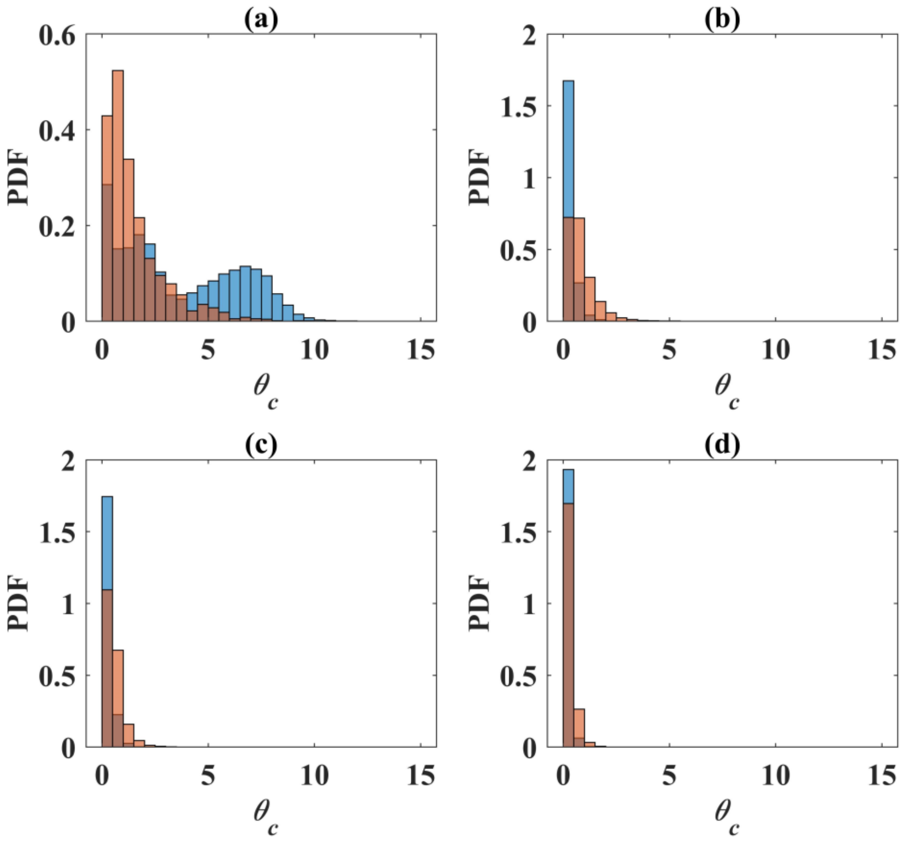

Figure 4.50 Comparison of PDF of bubble collision angles in different regions of the channel in upflow at Re_τ = 395 (🟧) and Re_τ = 150 (🟦) with d_b = 110 μm bubbles. (a) Viscous sub-layer; (b) buffer region; (c) log-law region; (d) bulk region.

4.4 Summary and conclusions

Turbulent upward and downward flows of microbubbles in a channel were studied using an Eulerian-Lagrangian approach under one-way, two-way and four-way couplings. The accuracy of the model was successfully validated against single-phase, one-way and two-way coupled two-phase flow literature results. The one-way coupled model gives a general impression of microbubble distributions in downward and upward channel flows. The effect of microbubbles on the fluid turbulence intensity was examined under two-way coupling. Due to the mechanism implemented in two-way coupling where the pressure gradient in the flow was modified, the fluid in upflow is expected to allow to flow faster than that for single-phase flow so that an enhancement of the fluid turbulence intensity is observed. In a similar way, suppression is found in downflow. The four-way coupled model provides a quantitative description of microbubble dynamics and clarifies the mechanisms of bubble collision and coalescence driven by the continuous fluid flow field. At the levels of turbulence investigated, collisions mainly occur on quasi-rectilinear bubble trajectories (see the example bubbles trajectories at $Re_\tau = 395$ in Figure 4.51). Therefore, the angle of collision between bubbles is usually very small and the relative approach velocity between the two colliding bubbles is generally low. These low-energy collisions favour the film drainage coalescence model over the energy model, but the contradictory predictions from these two approaches warrants further investigation. The development of more accurate and generally applicable coalescence models, possibly extended to cover recently observed behaviours specific to small microbubbles, such as clouding in vortices and low-speed streaks, should be pursued. The understanding generated on the dynamics of bubble-bubble interactions, which at the level of turbulence employed mainly occur on nearly rectilinear paths, is of value to the further development of coalescence models, and to the development of closure relations used in macroscopic Eulerian-Eulerian approaches.

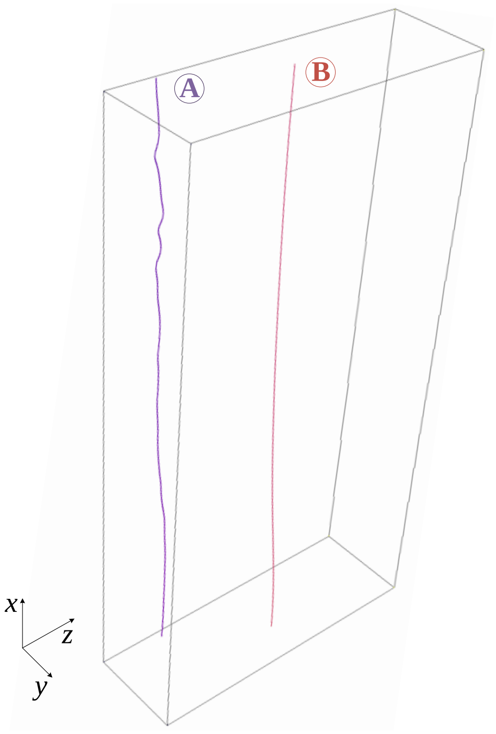

Figure 4.51 Trajectories of two moving bubbles in a channel upflow at $Re_\tau = 395$ with $d_b = 110$ µm. Symbols: Ⓐ in the wall area and Ⓑ in the channel centre.

Chapter 5 DNS of Bubbly Pipe Flows with Lagrangian Particle Tracking

5.1 Introduction

Practical engineering applications usually involve curved wall-bounded flows, e.g. bubble columns. In the literature, a straight circular pipe is one of the configurations most widely used to study fundamental problems in fluid mechanics, given that the pipe geometry is more practically relevant than a plane channel from an engineering viewpoint. In single-phase incompressible flows, a certain degree of universality exists between channel and pipe flows in the inner layer region, where mean statistics are unaffected by boundary effects and the logarithmic velocity profiles remain unchanged once scaled using shear quantities [282-284]. However, it is also known that pipe flows, due to the presence of curvature at the wall, are characterized by larger turbulence scales in the outer region of the pipe, as compared with channel flows. Such differences have been found and explained in terms of the mean streamwise velocity and the Reynolds stress budgets over a wide range of Reynolds numbers [283, 285-287].

The microbubbles, thanks to their large interfacial area and low buoyancy, are widely used in chemical plants to increase the efficiency of gas-liquid contact devices, as described in previous chapters. At the same time, the introduction of bubbles into a pipe leads to complex mechanisms of interactions between the single-phase turbulence structures and the dispersed gas phase. The understanding of these interactions in a curved wall-bounded flow such as in a pipe is therefore of great relevance for the accurate prediction of microbubble transport and dispersion. However, the large majority of available studies dealing with microbubble dynamics in turbulence are for channel flows, as outlined in Chapter 4, or turbulent boundary layers [39, 288]. In contrast, microbubble dynamics has rarely been studied in a straight pipe. Hence, the present chapter addresses the prediction of microbubble dispersion in a turbulent pipe flow using DNS-based modelling. A brief summary of numerical and experimental literature studies very closely related to the subject of the present chapter is provided first here below.

DNS has played an important role in understanding the physics of turbulence in single-phase pipe flows since the earliest work of Eggels et al. [289], in which a flow at Re_τ = 180, based on the pipe diameter and shear velocity, was computed. DNS has become more and more popular in the last decade, after studies such as that of Wu and Moin [290]. With the rapid increase of computing power, resolving all the turbulent scales in pipe flows, even at high Reynolds numbers (e.g. Re_τ = 3,008 by Ahn et al. [291]), has become affordable. Previous experiments [292] observed that very large-scale turbulent motions (VLSM) exist in the outer region of fully developed turbulent pipe flows, which largely contribute to the Reynolds shear stress [293]. In simulations, the streamwise length of the geometry limits the maximum length of the flow structures being captured, which, as a result, impacts the simulation accuracy. Therefore, a sufficient long pipe is essential to avoid any simulation being affected by periodicity. To capture VLSM, a range of axial lengths from 2.4R to 42R (where R is the pipe radius) [289-291, 293-301] have been used in the literature, depending on the Reynolds number considered. For example, Eggels et al. [289] employed a length of 10R for Re_τ = 180, and the results were compared with the channel flow results of Kim et al. [302], exactly matching for the same Reynolds number. However, non-zero, two-point velocity correlations were returned at distances of half the pipe length with no reasons provided for this discrepancy. Later, it was found by Chin et al. [296] that these were due to an insufficient pipe length being used. Chin et al. [296] also established that a length of $8\pi R$ is sufficient for all large scale structures and their associated statistics to be converged for Reynolds numbers up to Re_τ = 550, which was later employed by Klewicki et al. [298] for Reynolds numbers of Re_τ = 180 and 360, and El Khoury et al. [293] for moderately high Reynolds numbers ranging from Re_τ = 180 to 1,000. A length of 30R has also been used for analysing the VLSM structures in pipes with respect to turbulent boundary layers [291, 299]. More recently, Feldmann et al. [301] concluded that a minimum length of 42R is required for the VLSM to develop in pipe flows at high Reynolds numbers, up to Re_τ = 1,500.

For bubbly pipe flows, most of the reported studies considered upward flows, with particular attention paid to the gas phase distribution in the wall-normal direction and to the modulation of the liquid phase induced by the bubbles. Specifically, many previous studies [156, 303, 304] have focused on the bubble distribution in straight pipes. In particular, in upward flows, small bubbles preferentially travel to the pipe wall due to the effect of a positive lift force [156, 303, 304]. This leads to a peak in the bubble void fraction in the pipe wall area, where the fluid velocity profile is found to be flattened by the bubbles [156]. Furthermore, with the occurrence of bubble coalescence, larger more deformable bubbles are formed and these, in upward flows, experience a change in the direction of the lift force, induced by changes in the liquid flow structures around the bubbles, which tends to move the bubbles towards the pipe centre, generating a core-peaked void fraction distribution [159, 166]. In addition, random liquid turbulent motion causes additional effects on the bubble motion and this is known as turbulent dispersion [305]. Moreover, the presence of bubbles, depending on the flow conditions, can reduce or increase the turbulence intensity in the liquid phase and this needs to be properly accommodated if an accurate estimation of the turbulent stresses is to be made [156].

Experiments in downward flows [146, 152, 306, 307] show a different behaviour. Bubbles are slower than the fluid, and the same lift force pushes small bubbles to the pipe centre. Also, and as a consequence of drag from the slower bubbles, the fluid velocity is lower than that of the single-phase flow.

Many experiments on microbubbles in pipe flows studied pressure drop reduction [308] or drag reduction [309, 310], with only a few focused on microbubble coalescence. An example is the work of Yonemoto et al. [311] where the authors found coalescence to be favoured in ethanol with respect to tap or purified water. In addition, three types of outcome after bubble collision were detected, namely bouncing off, coalescence after a short duration of time and immediate coalescence. The potential reasons for these differences were further studied by calculation of the bubble contact time. The authors concluded that this might depend on mass transfer and thinning of the liquid film between bubbles, suggesting further investigation was desirable.

With the aim of contributing in the areas outlined above, in this chapter the DNS of microbubble-laden pipe flows is studied by means of the Eulerian-Lagrangian approach, with one-way, two-way and four-way coupling considered. The chapter is organised as follows. First, validation of the single-phase pipe flow is performed by comparing the present DNS results to single-phase literature data [293] (Section 5.2). Section 5.3 focuses on the simulation of one-way coupled flow in downward and upward pipe flows, demonstrating microbubble transport and dispersion phenomena. Turbulence suppression or enhancement in downflow or upflow is simulated with two-way coupling, and presented in Section 5.4. Further extension of the model to four-way coupling with the addition of bubble coalescence is considered in Section 5.5. Finally, conclusions are presented in Section 5.6.

5.2 Model validation

In this section, validation of fully resolved DNS of the single-phase pipe flow is carried out to lay the foundations for two-phase bubbly flow simulations. The single-phase flow is simulated at shear Reynolds numbers of $Re_\tau = 180$ and 361 in a vertical straight pipe. Results are compared with a literature database [293] at the same Reynolds numbers and pipe length scales. The present DNS is performed with the spectral element code Nek5000 [199], the main features of which have been presented in Chapter 3. Here, only specific features related to the pipe computational model and solution procedure are discussed.

5.2.1 Computational details

Details about the Nek5000 modelling of the channel flow were described in Section 4.2. Here, the differences between the channel and the pipe are presented. An incompressible flow of a viscous Newtonian fluid in a smooth straight pipe is considered and controlled by a nearly constant pressure gradient in the axial direction keeping a constant bulk velocity U_B. For the present pipe flows, two bulk Reynolds numbers ($Re_b = U_B\, D\, /\, \nu =$ 5,300 and 11,700, corresponding to shear Reynolds numbers $Re_\tau = u_\tau\, R\, /\, \nu = 180$ and 361, respectively) are examined. The computational domain is characterised with a pipe radius of R and a length of $25R$ ($\approx 8\pi R$), being long enough to capture VLSM-relevant turbulent scales at the current Reynolds numbers [283, 293, 296]. The pipe axis is aligned with the z-direction, where the boundary conditions are periodic inlet/outlet, while the non-slip condition is set at the wall.

The computational domain is divided into a number of hexahedral elements, where the solution of the discretised Navier-Stokes equations is obtained by means of the spectral element method. The domain size is equal to that of El Khoury et al. [293] and of Antoranz et al. [312] and is shown in Figure 5.1. Note that, considering the dramatic increase in computational memory required in the Lagrangian particle tracking simulations compared to that for a single-phase flow, the computational grid points are not changed between the two Reynolds numbers, different to what was used by El Khoury et al. [293] and Antoranz et al. [312]. Details of the meshes are provided in Table 4.1.

For both Reynolds numbers, the domain is discretised into 36,576 spectral elements, with 288 elements in the cross-section of the pipe and 127 elements in the streamwise direction. The nodes in each element are distributed with a polynomial of order 7, corresponding to a total of 12.54 M GLL grid-points, as shown in Figure 5.1(a). In the streamwise direction, the elements are uniformly distributed, while a non-uniform grid is employed in the radial direction, as shown in detail in Figure 5.1(b). Here, a total of 18 elements are used on the horizontal and vertical axis of the cross-section plane. The grid spacing in wall units is $\Delta r^+ \leq 4.77$, $\Delta(R\theta)^+ \leq 4.93$ and $\Delta z^+ \leq 7.42$ for $Re_\tau = 180$ as shown in Table 5.1. This is almost in line with El Khoury et al. [293], with slightly less-resolution in the radial direction and slightly more in the axial direction with respect to Antonoranz et al. [312]. For $Re_\tau = 361$, the present resolution is still comparable with that used by Antoranz et al. [312], but is less refined compared with El Khoury et al. [293].

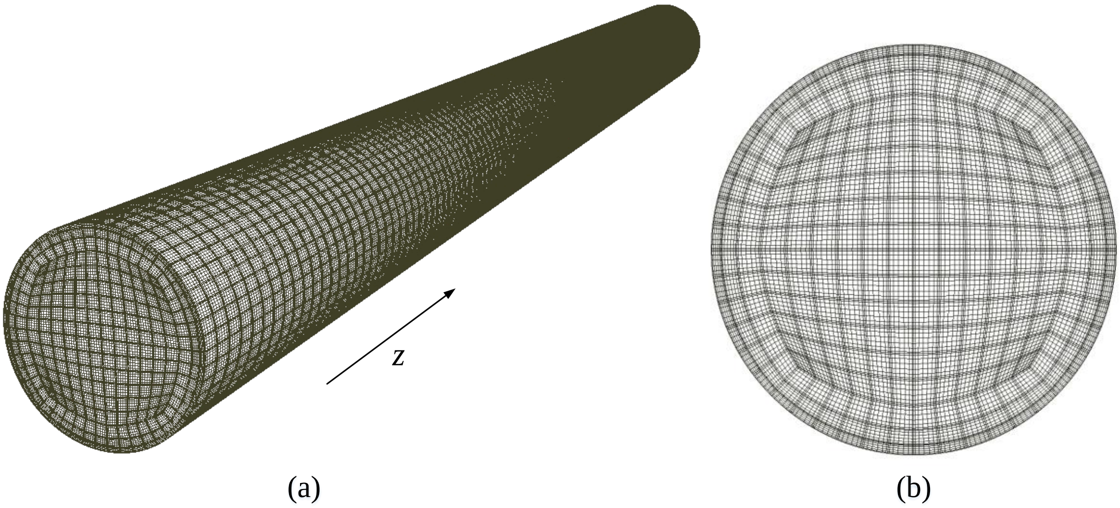

(a) (b)

Figure 5.1 (a) Overview and (b) cross-sectional view of the computational grid points with Gauss-Lobatto-Legendre quadrature points (7th order spectral elements) for both simulations at $Re_\tau = 180$ and $Re_\tau = 361$.

Table 5.1 Computational grid points of DNS and literature benchmarks for pipe flows.

Re_τ	Re_b	References	Elements	$\Delta r^+_{\max}$	$\Delta(R\theta)^+_{\max}$	$\Delta z^+_{\max}$
180	≈ 5,300	El Khoury et al. [293]	36,480	4.44	4.93	9.91
		Antoranz et al. [312]	55,440	3.50	3.50	9.00
		Present DNS	36,576	4.77	4.93	7.42
361	≈ 11,700	El Khoury et al. [293]	237,120	4.70	4.93	9.91
		Antoranz et al. [312]	55,440	7.00	7.00	18.00
		Present DNS	36,576	9.57	9.89	14.87

The solution of the Navier-Stokes equations provided by Nek5000 is represented in Cartesian coordinates, the origin of which is the zero-axial location of z. The velocity field (u, v, w) is solved by Nek5000 in Cartesian coordinates (x, y, z). Due to the singularity on the pipe axis, however, the velocity field is transformed from Cartesian (x, y, z) to cylindrical coordinates (r, θ, z) using tensor rotations after the simulation and before post-processing.

5.2.2 Instantaneous velocity

First, a general visual impression of the instantaneous streamwise velocity normalized by the bulk velocity is presented in Figure 5.2, for Reynolds numbers Re_τ = 361 and 180. Two sets of images are captured from two different surfaces. Specifically, Figure 5.2(a) and (b) are obtained on a surface perpendicular to the pipe axis at $z^+ = 0$, while (c) and (d) are on a plane at $\theta^+ = 0$.

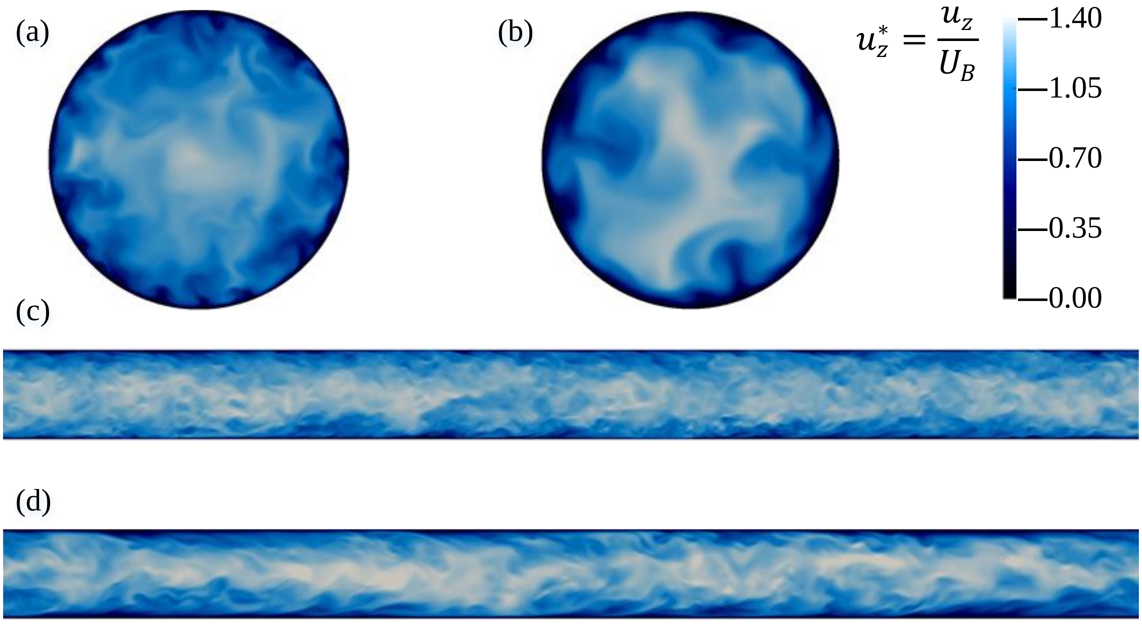

Figure 5.2 Isosurfaces of the normalized instantaneous streamwise velocity for (a) and (c) Re_τ = 361 and (b) and (d) Re_τ = 180.

A change in the character of the flow field with decreasing Reynolds number is visible in Figure 5.2. It is noticeable that more turbulent behaviour is found at Re_τ = 361, over a much wider range of length scales. More specifically, at the low Reynolds number (Figure 5.2(b)), large-scale bright blue coloured high-momentum regions and dark black low-momentum areas exist on the azimuthal direction, which have also been observed as having roughly mushroom shaped structures by Wu and Moin [290]. However, a more fine-grained structure with reduced apparent coherence is visible for the large Reynolds number case in Figure 5.2(a). The difference is also clear over the constant θ^+ plane shown in Figure 5.2(c) and (d), where the entire streamwise length of the pipe is presented. In Figure 5.2(d), the low-momentum wavy structures are inclined away from the wall towards the streamwise direction (from left to right) for the low Reynolds number case, while the same behaviour is less obvious for the high Reynolds number simulation in Figure 5.2(c). Consistency between both Reynolds numbers is found in the elongated high-speed wavy structures in the pipe central region. Additionally, the average distance between the near-wall low-speed streaks in the high Reynolds number case, seen Figure 5.2(a), is approximately one quarter of the pipe radius. For the low Reynolds number case in Figure 5.2(b), this space is observed to be approximately 50% of the radius. These spacing scales are in accordance with El Khoury et al. [293], where the distance was quantified to be around 100 wall units at $Re_\tau = 180$.

5.2.3 Averaged statistics

Validation of the velocity statistics is carried out by comparing with the results from El Khoury et al. [293]. The averaged statistics are obtained from fully-developed conditions by averaging until gathered values are independent of time. The averaging routine has already been introduced in Chapter 3. Here, time- and space-averaged results normalized by the shear, at $Re_\tau = 180$ and 361, are reproduced in Figure 5.3 and Figure 5.4, respectively. Good agreement is found in both the mean streamwise velocity, the normal turbulent stresses and the Reynolds shear stress for both Reynolds numbers. Even at $Re_\tau = 361$, where the mesh resolution is lower than that of El Khoury et al. [293], results are in good agreement with their DNS.

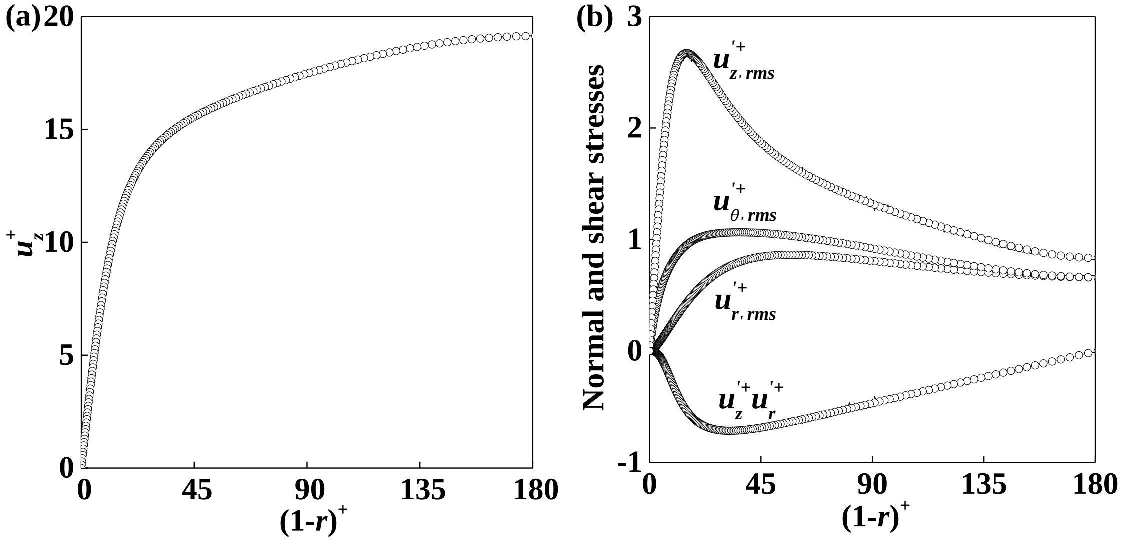

Figure 5.3 Comparison of single-phase fluid at Re_τ = 180 (—) with predictions of El Khoury et al. [293] (○). (a) Mean streamwise fluid velocity (u_z^+); (b) non-dimensional radial ($u'^+_{r,rms}$), azimuthal ($u'^+_{\theta,rms}$) and streamwise ($u'^+_{z,rms}$) rms of velocity fluctuations and shear stress ($u'^+_z u'^+_r$).

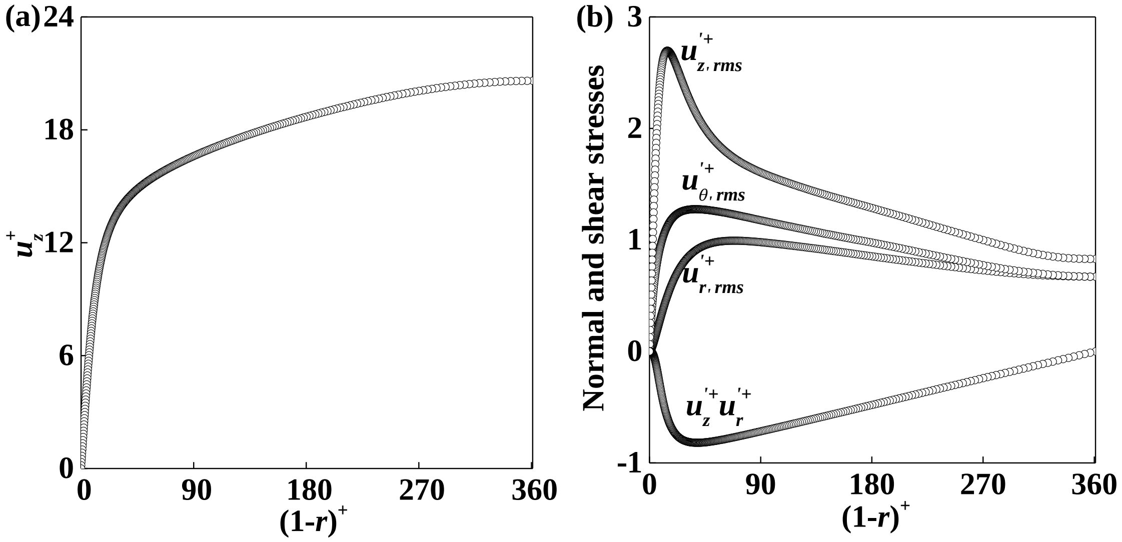

Figure 5.4 Comparison of single-phase fluid at Re_τ = 361 (—) with predictions of El Khoury et al. [293] (○). (a) Mean streamwise fluid velocity (u_z^+); (b) non-dimensional radial ($u'^+_{r,rms}$), azimuthal ($u'^+_{\theta,rms}$) and streamwise ($u'^+_{z,rms}$) rms of velocity fluctuations and shear stress ($u'^+_z u'^+_r$).

5.3 Two-phase pipe flows with one-way coupling

In this section, DNS of the bubbly flows was performed by injecting microbubbles of diameter d_b = 110 μm under the one-way coupling assumption. Both upward and downward pipe flows at $Re_\tau = 361$ are considered. The pipe diameter is set as 0.04 m. Correspondingly, a total of 90,192 bubbles were injected starting from the fully developed single-phase flow solution. This number of bubbles corresponds to a void fraction of 0.01%, which is low enough to keep the system dilute, and for bubble-bubble interactions to be neglected. The density of the air bubbles and the surface tension at the water/air interface are maintained from Chapter 4. In the Lagrangian tracker, microbubbles are again considered as non-deformable spheres subject to gravity, drag, added mass, pressure gradient and lift forces. The bubbles were injected with a random spatial distribution, with the initial bubble velocities matching those of the fluid at the bubble centre. When a bubble reached a periodic boundary, it was re-injected at the coupled boundary with the same velocity, to maintain a constant average void fraction value of the bubble phase.

The simulation results for downward and upward channel flows are presented in Sections 5.3.1 and 5.3.2, including the mean velocity and normal and shear stresses of the fluid and the bubbles, the bubble forces and the bubble concentration profiles.

5.3.1 Downflow at $Re_\tau = 361$ with $d_b = 110$ µm

The bubble distribution is analysed first. The averaged microbubble number density profile in the pipe normalised by the initial concentration ($c_0 = N_b / V$, with V the volume of the pipe domain), and the time evolution of this instantaneous number density in the viscous sub-layer, are plotted in Figure 5.5. These results were obtained by dividing the pipe uniformly into 120 wall-parallel cylindrical slices, in which the number of bubbles was counted and the bubble concentration in each slice computed as $c = N_{b,i} / V_i$, where $i = 1, \ldots, 120$. In Figure 5.5(a), the normalised microbubble number density profile at the final time-step is presented. It is expected that, due to the lift force, bubbles in downflow preferentially travel towards the pipe core region and the bubble density becomes lower in the near-wall region. Therefore, one extra case without the lift force was added to Figure 5.5(a) to demonstrate its impact in promoting bubble migration away from the wall. This is further emphasized by the decrease of the concentration of the microbubbles in the viscous sub-layer, as shown in Figure 5.5(b), where the values reaches an equilibrium condition after around $t^+ = 1100$. From the distribution profiles in Figure 5.5(a), it is also evident how, away from the pipe wall ($(1\text{-}r)^+ > 20$), the bubbles are nearly uniformly distributed no matter if the lift force is considered or not.

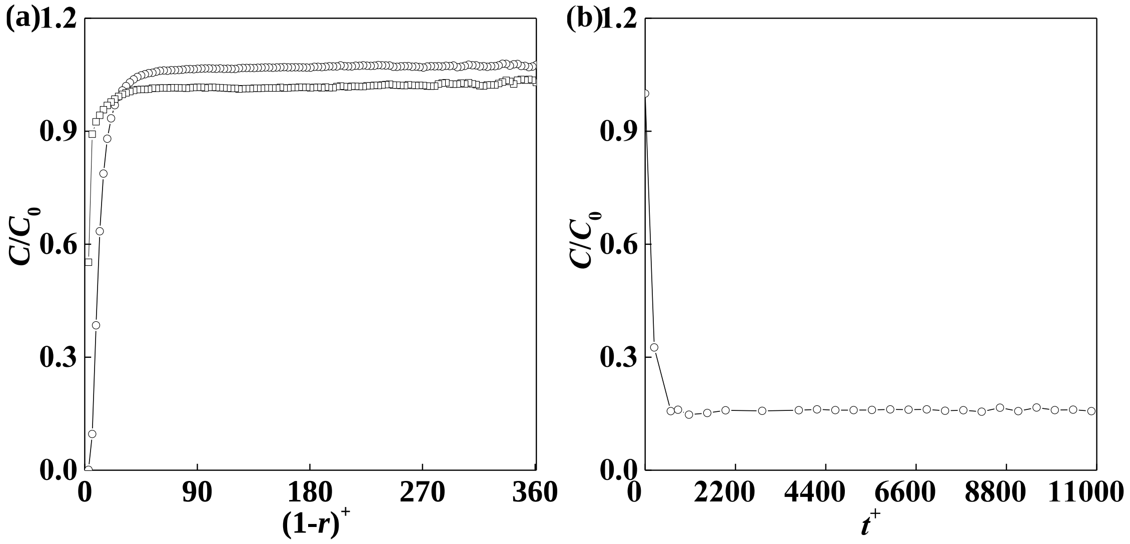

Figure 5.5 Microbubble number density profiles normalised by the initial bubble concentration in DNS of one-way coupled downflow at Re_τ = 361 with d_b = 110 μm. (a) Mean normalised microbubbles distribution profile; (b) time evolution profile of normalised microbubbles number density in viscous sub-layer ($(1 - r)^+ \leq 5$). Symbols: □ cases without lift force; ○ cases with lift force.

Once the flow reached a fully-developed state, namely at t^+ = 1,600 (here $t^+ = 4Re_\tau^2/ Re_b\times t^*$), the instantaneous velocity field was averaged until fluid and bubble velocity statistics that were independent of time were obtained. In Figure 5.6(a), the bubble mean streamwise velocity is plotted and compared with the fluid velocity. Necessarily, the bubbles have no influence on the fluid motion, and it is easily seen that the bubbles move slightly slower than the fluid. Figure 5.6(b) provides bubble normal and shear stresses, which are decreased with respect to those of the fluid in Figure 5.4(b). In Figure 5.6(b), the very near-wall region ($(1\text{-}r)^+ \leq 3$) is not shown given that the very low number of bubbles in this region made averaging meaningless.

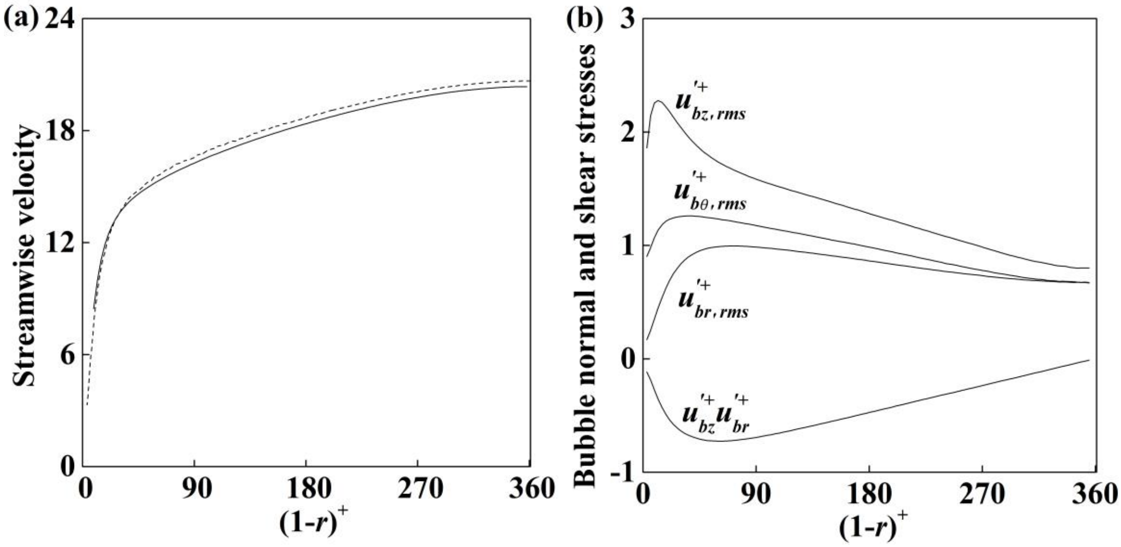

Figure 5.6 Comparison of bubble statistics (—) with fluid results (---) in DNS of one-way coupled downflow at Re_τ = 361 with d_b = 110 μm. (a) Non-dimensional mean streamwise fluid velocity (u_z^+) and microbubble velocity (u_{bz}^+); (b) non-dimensional radial ($u'^+_{br,rms}$), azimuthal ($u'^+_{b\theta,rms}$) and streamwise ($u'^+_{bz,rms}$) rms of microbubble velocity fluctuations and shear stress ($u'^+_{bz}u'^+_{br}$).

A visual impression of the instantaneous bubble distribution in the pipe domain at the final time step is presented, with contour levels of the bubble non-dimensional streamwise velocity, in

Figure 5.7. Note that the three-dimensional drawing of bubble size is not scaled to the pipe dimensions. Due to the lift force, more bubbles are found in the pipe core. As a result, only a small amount of bubbles having low velocity were observed in the wall area, where the bubble velocity u_{bz}^* is less than 0.5.

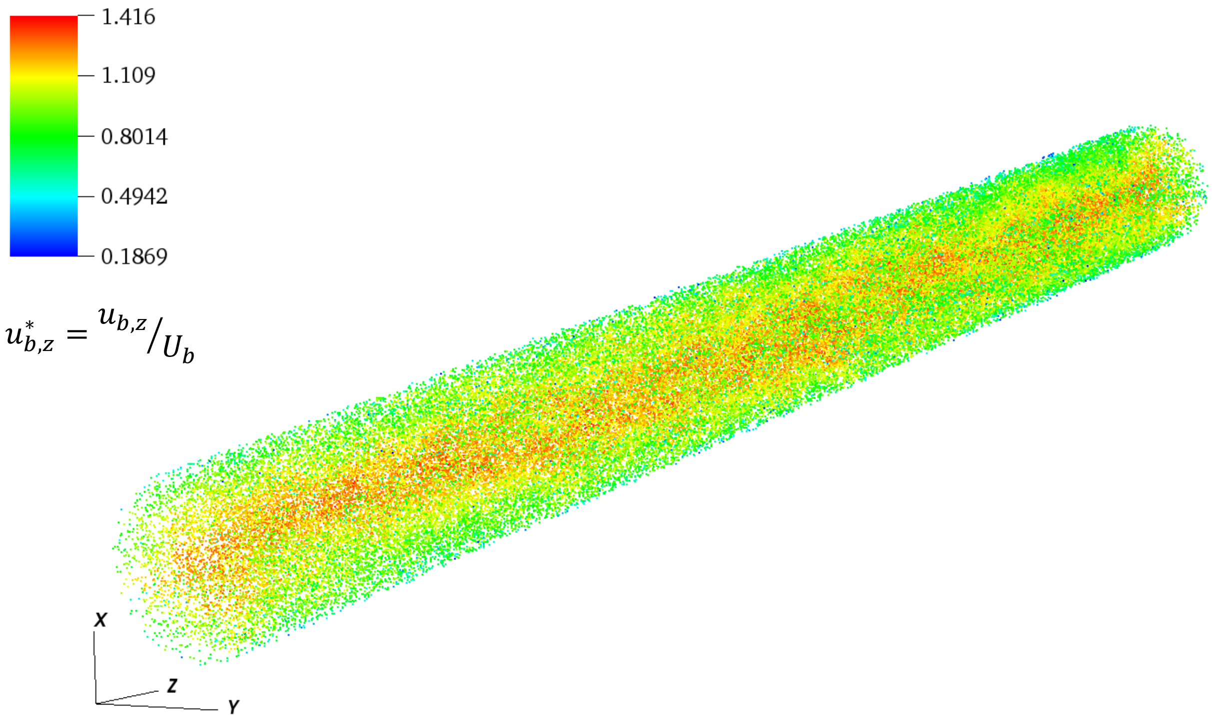

Figure 5.7 Instantaneous bubble distribution with contour levels of bubble non-dimensional streamwise velocity in the whole pipe for the one-way coupled downflow with lift force at $Re_\tau = 361$ with $d_b = 110$ µm.

A reason for the preferential bubble distribution in Figure 5.5 can be found in the averaged force components acting on the bubbles in the streamwise and wall-normal directions, which are presented as a function of the normalised radial distance $(1 - r)^+$ in Figure 5.8, which allows an assessment of the effect of the lift force. Figure 5.8(a) and (c) were derived taking the effect of the lift force into account and show the mean force components in the streamwise and radial directions, respectively. The same is done in Figure 5.8(b) and (d) with the lift force being neglected. The comparison of Figure 5.8(a) and (b) demonstrates that the lift force is not dominant in the streamwise direction, as would be expected, although it is observed that the drag and the gravity/buoyancy forces are balanced. Clearly, being a downflow, the gravity/buoyancy force on the bubbles has a negative sign. Furthermore, Figure 5.8(c) shows that the sign of lift force is negative (towards pipe core), and higher in the wall region ($(1 - r)^+ \leq 90$). This better explains the nearly bubble free region close to the wall in Figure 5.5(a). This observation is quantitatively similar with that of the channel flow considered in Section 4.2.2.1, where a bubble free region was found for $y^+ \leq 45$. Consistency is also found in a similar amount of bubbles (≈ 25%) in the near-wall region relative to those in the whole domain. This follows from the universality in the near-wall region of the velocity profile in channel and pipe flows [282-284]. In contrast, the case without the lift force does not exhibit any obvious force towards the pipe centre, except for the pressure gradient which is slightly higher than the rest of the forces and balanced by the drag force in the very near-wall region. This is the reason for the much smaller decrease in the near-wall bubble distribution in Figure 5.5(a).

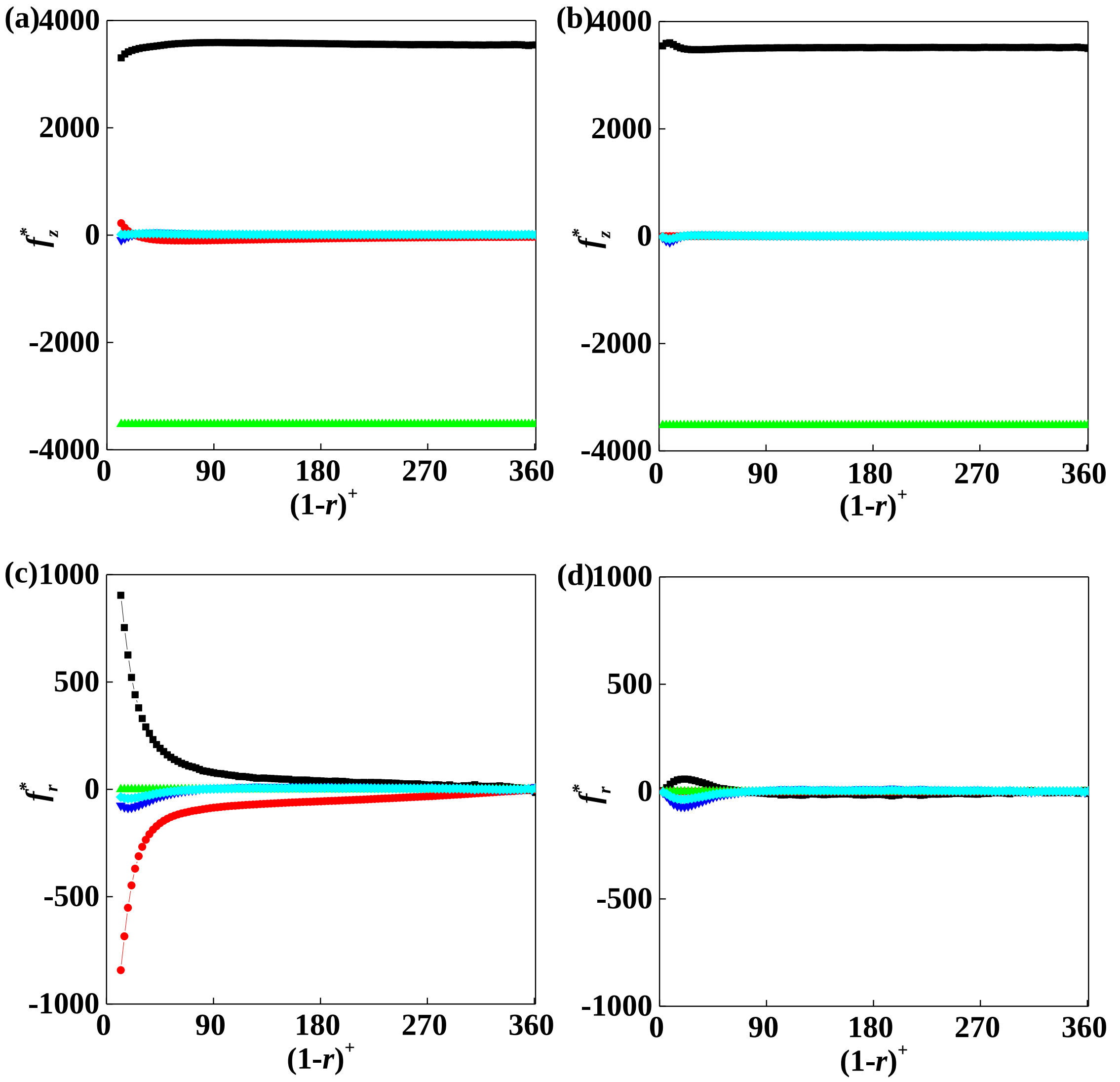

Figure 5.8 Forces acting on the bubbles in DNS of one-way coupled downflow at Re_τ = 361 with d_b = 110 μm. (a) Streamwise and (c) radial components of the forces acting on the bubbles with lift force; (b) streamwise and (d) radial components of the forces acting on the bubbles without lift force. Symbols: ■ drag force; ● lift force; ▲ gravity/buoyancy; ▼ pressure gradient force; ♦ virtual mass force.

5.3.2 Upflow at Re_τ = 361 with d_b = 110 μm

The one-way coupled simulation for the upflow was performed similarly, and the results are presented in this section. The mean normalised microbubble distribution profile is plotted in Figure 5.9(a), together with a case without the lift force. It can be easily seen that there is a dramatic increase of the bubble density towards the wall under the action of the lift force. After the wall peak, the distribution slightly decreases before reaching a uniform value away from the wall. Figure 5.9(b) gives the time evolution of the microbubble concentration in the viscous sub-layer, where it increases until it reaches a nearly uniform value.

In addition, a comparison between the bubble densities in downflow (Figure 5.5(a)) and upflow (in Figure 5.9(a)) without the lift force can also be made. It can be concluded that the bubbles distribute in nearly the same way, with $c / c_0 < 1$ in the near-wall region and uniform in the rest of the domain.

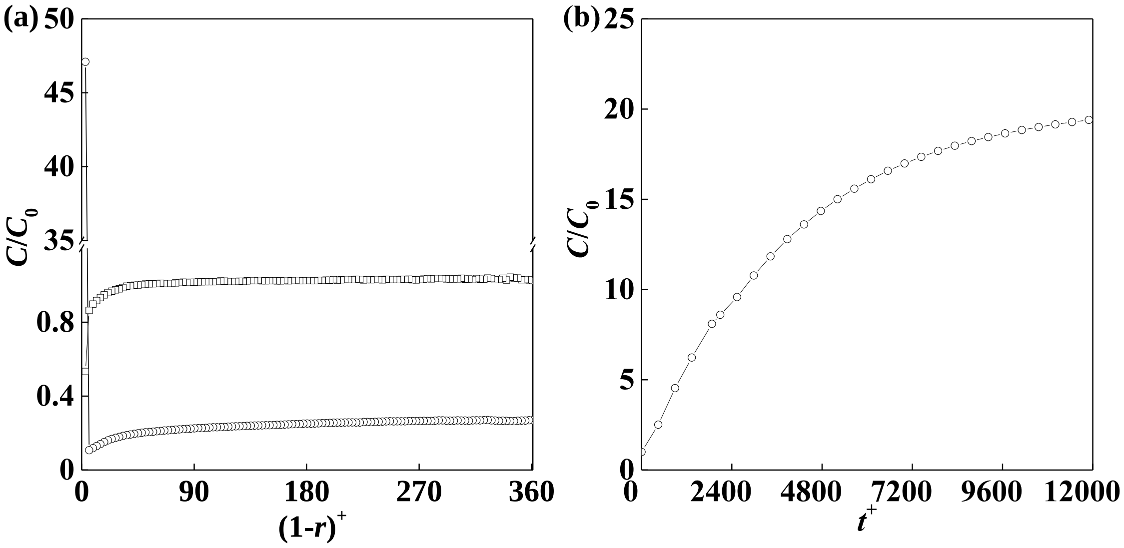

Figure 5.9 Microbubble number density profiles normalised by the initial bubble concentration in DNS of one-way coupled upflow at Re_τ = 361 with d_b = 110 μm. (a) Mean normalised microbubbles distribution profile; (b) time evolution profile of normalised microbubbles number density in viscous sub-layer ($(1 - r)^+ \leq 5$). Symbols: □ cases without lift force; ○ cases with lift force.

Mean bubble statistics for the upflow with d_b = 110 μm bubbles are presented in Figure 5.10, with the averaging started at t^+ = 1500. It is necessarily the case that the averaged quantities and turbulence intensities of the carrier phase are not altered by the bubbles under the one-way coupling assumption. Considering the difference between averaged statistics of the bubbles and the fluid, a comparison is made in Figure 5.10(a) where the mean bubble and fluid velocities are plotted. Due to the impact of buoyancy, bubbles in upflow travel faster than the carrier phase. In Figure 10(b), the turbulence quantities are the same as those found in the single-phase flow.

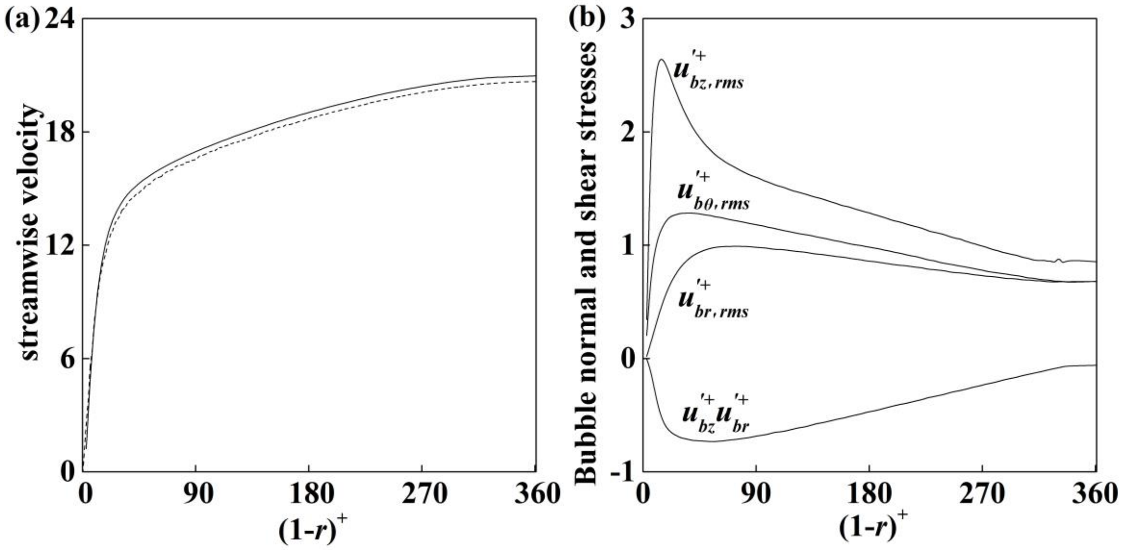

Figure 5.10 Comparison of bubble velocity statistics (—) with fluid results (---) in DNS of one-way coupled upflow at Re_τ = 361 with d_b = 110 μm. (a) Non-dimensional mean streamwise fluid velocity (u_z^+) and microbubble velocity (u_{bz}^+); (b) non-dimensional radial ($u_{br,rms}'^+$), azimuthal ($u_{b\theta,rms}'^+$) and streamwise ($u_{bz,rms}'^+$) rms of microbubbles velocity fluctuations and shear stress ($u_{bz}'^+ u_{br}'^+$).

The instantaneous bubble distribution in the upward pipe flow with contours of the bubble velocity is shown in Figure 5.11. It can be immediately seen that more bubbles are located in the wall region and travel with a low velocity. In this region, elongated streaks of bubbles are visible. This is due to the quasi-streamwise vortices in the near-wall region, which generate relatively lower streamwise fluid velocity regions, or low speed streaks, such that the bubbles travel to these regions because of their higher velocity than that of the fluid. This bubble clustering is in accordance with the channel flows in Section 4.2.2.4.

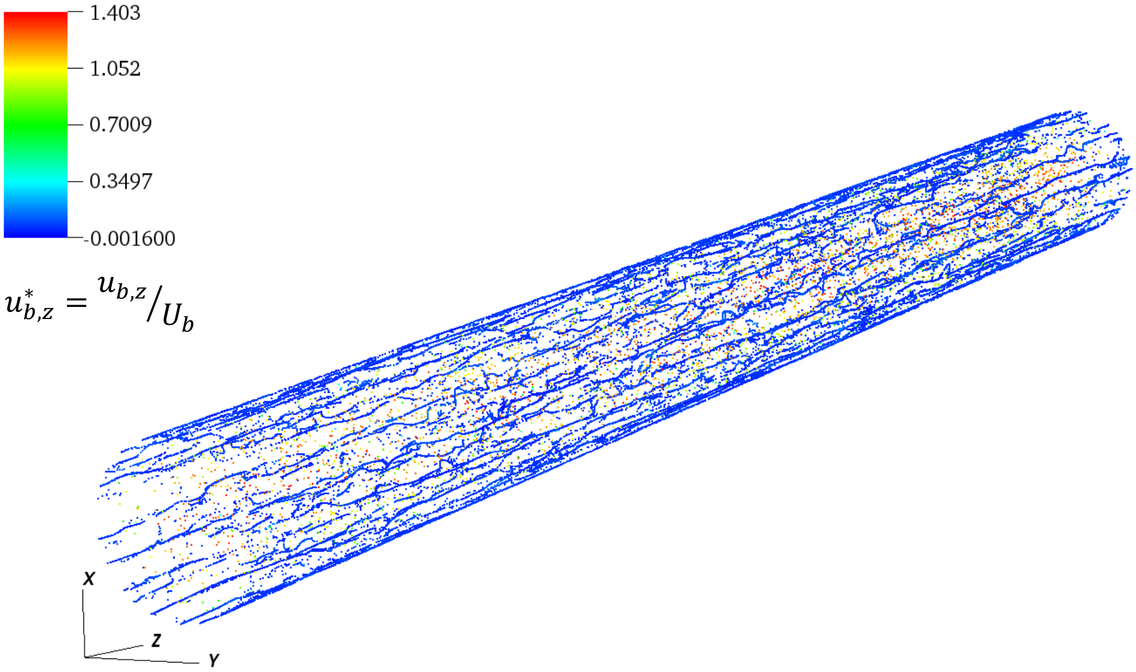

Figure 5.11 Instantaneous bubble distribution with contour levels of the bubble non-dimensional streamwise velocity in the whole pipe for the one-way coupled upflow with lift force at $Re_\tau = 361$ with $d_b = 110$ µm.

It is known that the wall peak in the bubble concentration is due to the effect of the lift force [156, 303, 304]. The mean forces acting on the bubbles are again analysed by switching the lift force on or off. The various components of the bubble forces are plotted in Figure 5.12 in a similar way to that in Section 5.3.1. Figure 5.12(a) and (b) confirm the two dominant forces acting on the bubbles in the axial direction, i.e. the drag force and gravity/buoyancy. In this direction, the sign of gravity/buoyancy is seen to be positive which is balanced with drag force. In the radial direction, the same conclusion can be drawn in that that the absolute value of the lift force increases towards the wall which move the bubbles towards the near-wall region. This dominant region of the lift force exists in $(1\text{-}r)^+ \leq 45$, leading to a dramatic increase of the bubble concentration in the very near-wall region (see Figure 5.9(a)). Other forces are similar to the downflow case, as are the results with the lift force turned off.

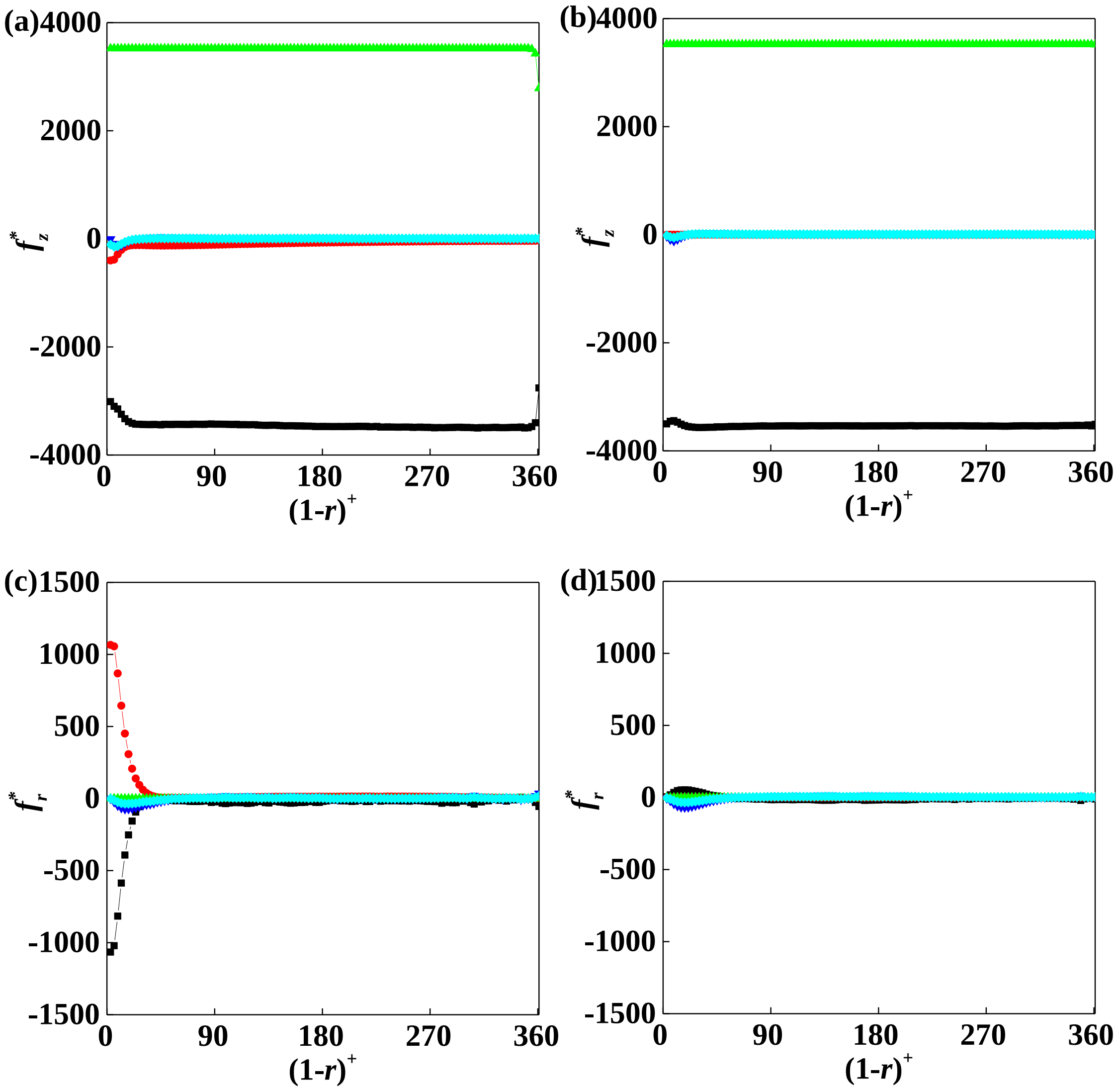

Figure 5.12 Forces acting on the bubbles in DNS of one-way coupled upflow at $Re_\tau = 361$ with $d_b = 110$ μm. (a) Streamwise and (c) radial components of the forces in the simulation with lift force; (b) streamwise and (d) radial components of the forces in the simulation without lift force. Symbols: ■ drag force; ● lift force; ▲ gravity/buoyancy; ▼ pressure gradient force; ♦ virtual mass force.

5.4 Two-phase pipe flows with two-way coupling

In this section, the DNS of both the downward and upward two-phase pipe flows at $Re_\tau = 361$ with microbubbles of diameter $d_b = 110$ μm are considered under the two-way coupling assumption. The void fraction is still kept at 0.01%, corresponding to a total of 90,192 bubbles in the flow. The two-way coupling simulations were started from fully developed one-way coupling cases. In the two-way coupling mechanism, described in Section 3.2.2, the coupling terms are computed and distributed via a Gaussian function, depending on the bubble size and the Eulerian numerical grid resolution. The distribution is therefore case independent. For example, when the bubble diameter is of the order of the spatial resolution, the effect of the bubble is spread over the surrounding grid points, rather than a single grid point, particularly close to wall boundaries. To reduce computational time, however, the assumption is made that each bubble only has a significant effect inside the same spectral element.

Consideration is again given to results for the bubble velocity statistics, the bubble number density profile and the forces acting on the bubbles for both downward and upward pipe flows. Comparisons between two-way and one-way coupling are made where appropriate.

5.4.1 Downflow at $Re_\tau = 361$ with $d_b = 110$ µm

Given that the simulations are started from one-way coupled cases, the concentration profile (Figure5.13(a)) and the time evolution of the microbubble density in the viscous sub-layer (Figure5.13(b)) are already close to their fully-developed values at the beginning ($t^+ = 0$) of the simulations. The results of Figure 5.13(b) show that two-way coupling, at a void fraction 0.01%, does not change the bubble distribution in the viscous sub-layer, which remains nearly bubble free ($c / c_0 \approx 0.15$). This lack of change is also true for the rest of the pipe domain, where an almost uniform bubble distribution is found in Figure 5.13(a).

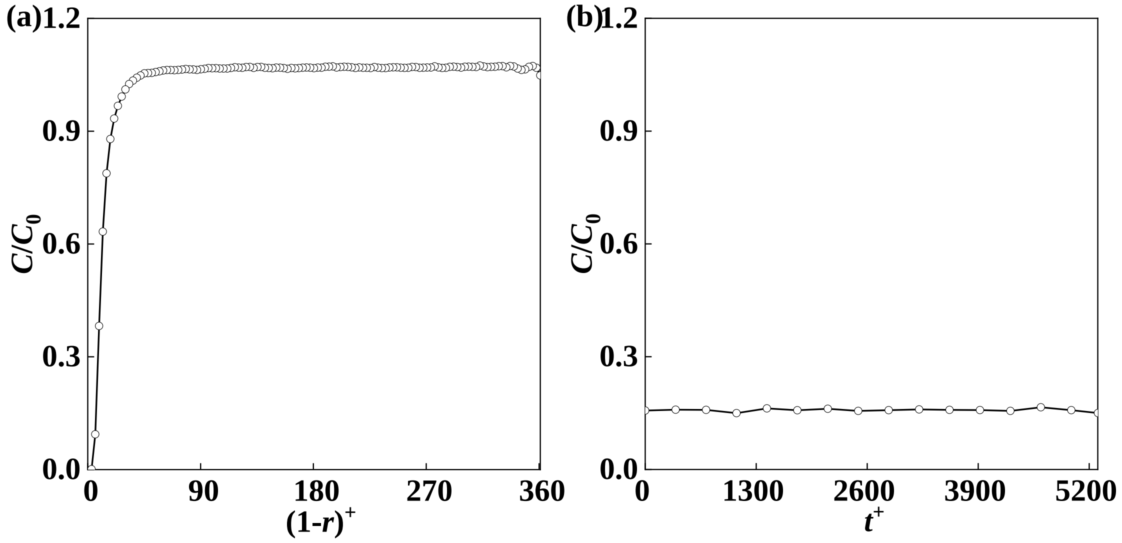

Figure 5.13 Microbubble number density profiles normalised by the initial bubble concentration in DNS of two-way coupled downflow at $Re_\tau = 361$ with $d_b = 110$ µm. (a)

Mean normalised microbubble distribution profile in the whole pipe; (b) time evolution profile of the normalised microbubble number density in the viscous sub-layer ($(1 - r)^+ \leq 5$).

Averaging of the instantaneous flow field was started at $t^+ = 200$ and ended at $t^+ = 5{,}300$ in Figure 5.13(b). Similar averaging was used to derive the fluid velocity statistics which are compared with the single-phase predictions in Figure 5.14. The two-way coupled streamwise velocity (Figure 5.14(a)) is immediately seen to be decreased in the two-way coupled simulation with respect to the single-phase flow. This decrease is, however, observed to be very slight, and limited to the pipe core region ($(1 - r)^+ \geq 200$). However, this slight decrease of the mean streamwise velocity gives a higher streamwise rms of the velocity fluctuation in the same region ($(1 - r)^+ \geq 200$), which is shown in Figure 5.14(b). The radial and azimuthal rms of the velocity fluctuations and the shear stress are consistent with single-phase flow results.

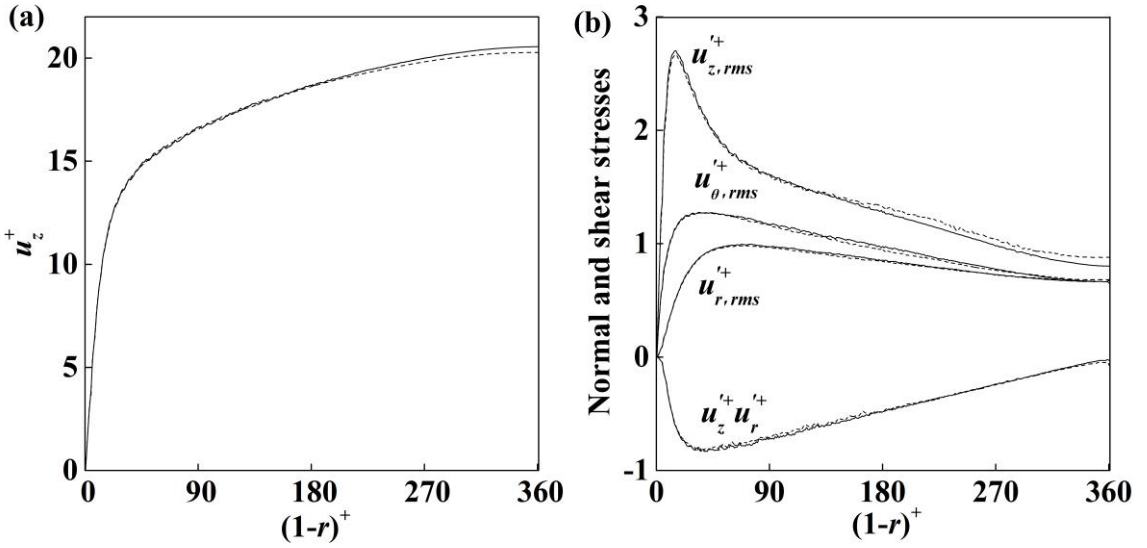

Figure 5.14 Comparison of fluid statistics in DNS of two-way coupled downflow at $Re_\tau = 361$ with $d_b = 110$ μm (---) with single-phase results (—). (a) Non-dimensional mean streamwise fluid velocity (u_z^+); (b) non-dimensional radial ($u'^+_{r,rms}$), azimuthal ($u'^+_{\theta,rms}$) and streamwise ($u'^+_{z,rms}$) rms of velocity fluctuations and shear stress ($u'^+_z u'^+_r$).

The bubble mean velocity and normal and shear stress profiles are presented in Figure 5.15. The bubble mean streamwise velocity is found to be lower than the fluid, as expected, in Figure 5.15(a). Also, the bubbles velocity fluctuations are observed to be lower than the fluid turbulence intensities in Figure 5.15(b), compared with the fluid predictions in Figure 5.14(b). Again, in near-wall region, the normalised microbubble number density is very low and averages in this region are not included in Figure 5.15(b). Compared to the bubble-free region (c / $c_0 \leq 0.1\%$) under one-way coupling, which in Figure 5.5(a) is in the region $(1 - r)^+ \leq 3$, a wider range ($(1 - r)^+ \leq 6$) is found in the two-way coupled simulation, leading to a larger zone where predictions are not available in Figure 5.15(b).

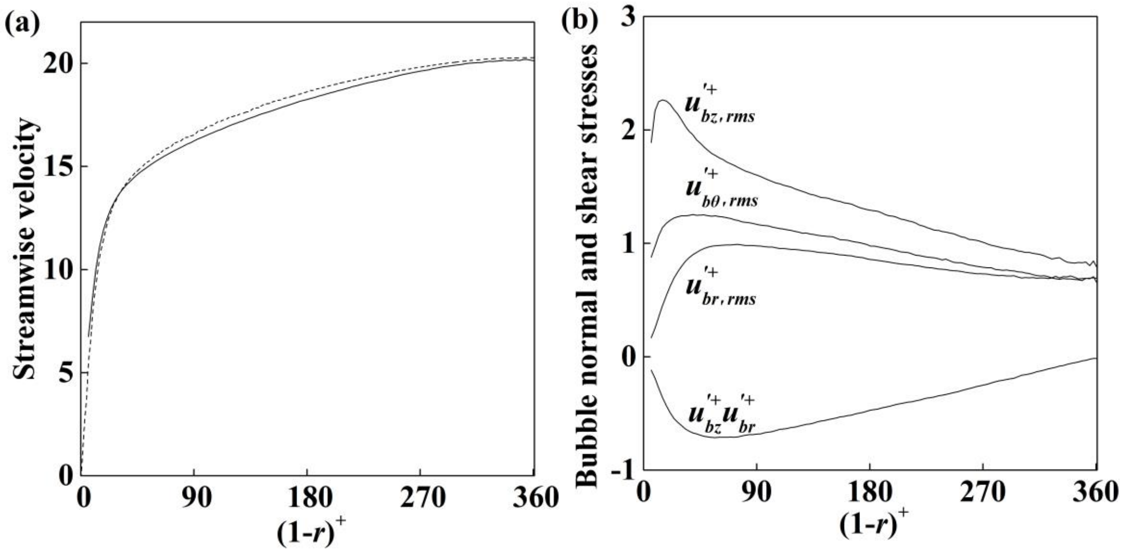

Figure 5.15 Comparison of bubble statistics (—) with fluid results (···) in DNS of two-way coupled downflow at Re_τ = 361 with d_b = 110 μm. (a) Non-dimensional mean streamwise fluid velocity (u_z^+) and bubble velocity (u_{bz}^+); (b) non-dimensional radial ($u'^+_{br,rms}$), azimuthal ($u'^+_{b\theta,rms}$) and streamwise ($u'^+_{bz,rms}$) rms of microbubbles velocity fluctuations and shear stress ($u'^+_{bz}u'^+_{br}$).

Forces acting on the bubbles are essentially equal to those found under one-way coupling, as presented in Figure 5.16, including the lift force. Results in Figure 5.16(a) confirm that gravity/buoyancy are perfectly balanced by the drag force in the streamwise direction. A negative lift force is found in the radial direction which is balanced by the drag force. This negative lift force drifts the bubbles away from the wall causing the core-peaked distribution profile.

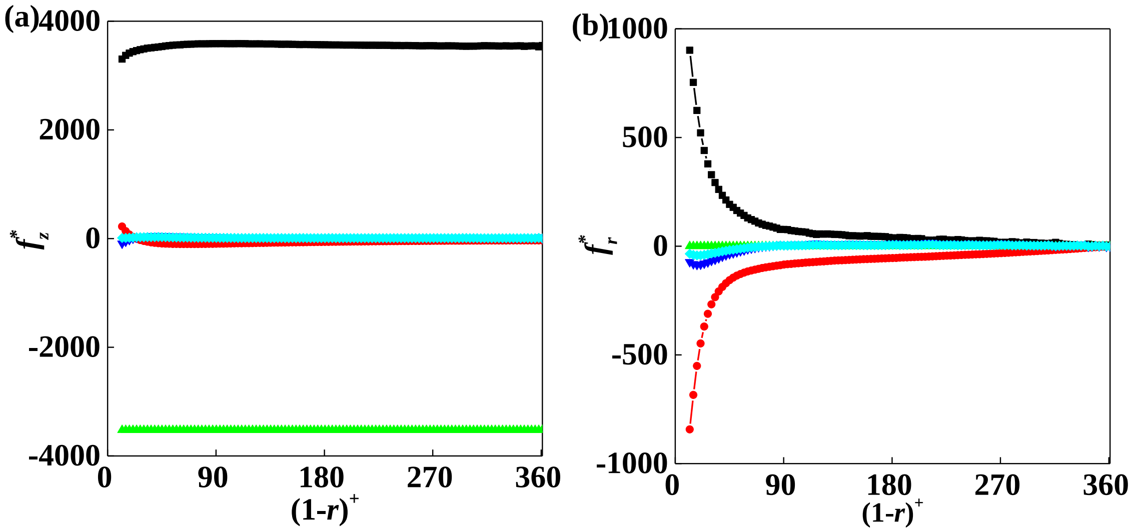

Figure 5.16 (a) Streamwise and (b) radial components of the forces acting on the bubbles in DNS of two-way coupled downflow at $Re_\tau = 361$ with $d_b = 110$ µm. Symbols: ■ drag force; ● lift force; ▲ gravity/buoyancy; ▼ pressure gradient force; ♦ virtual mass force.

5.4.2 Upflow at $Re_\tau = 361$ with $d_b = 110$ µm

The upflow simulation was again started from the fully developed one-way coupled case, where a peak in the bubble concentration was found near the pipe wall (Figure 5.9(a)). The mean bubble concentration is shown in Figure 5.17(a), and the time evolution of the concentration in the viscous sub-layer during the simulation was again monitored, the results of which are given in Figure 5.17(b). Here, $t^+ = 0$ represents the starting point from the fully developed one-way coupled upflow case. A slight increase of bubble concentration in the viscous sub-layer is found with time in Figure 5.17(b), which leads to a higher averaged normalised bubble concentration in the region closest to the wall in Figure 5.17(a) when compared to Figure 5.9(a), while the concertation is slightly lower ($c / c_0 < 0.05$) in the rest of pipe domain, such the large majority of the bubbles are found in the near-wall area.

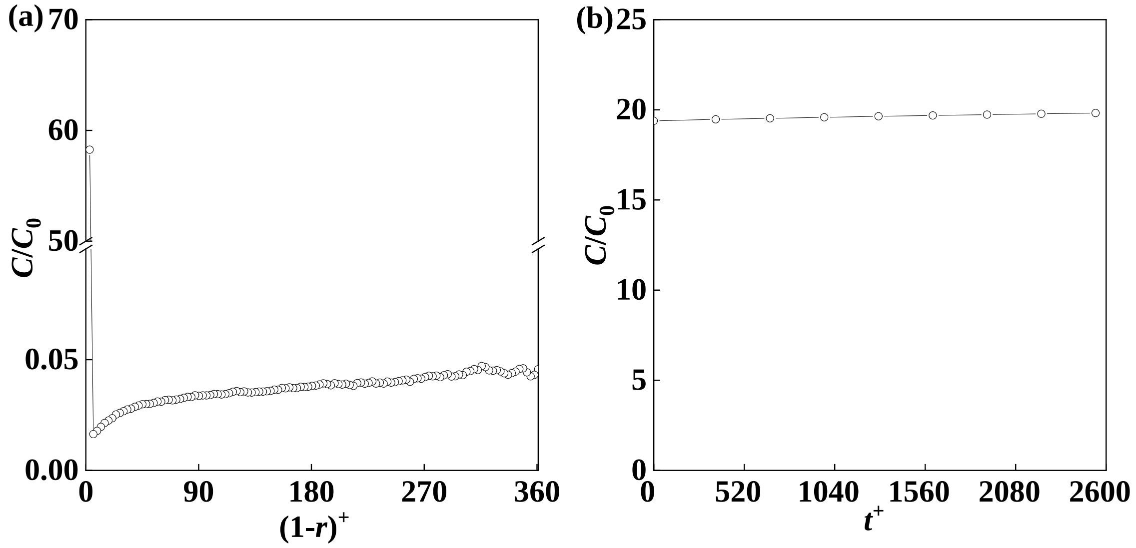

Figure 5.17 Microbubble number density profiles normalised by the initial bubble concentration in DNS of two-way coupled upflow at Re_τ = 361 with d_b = 110 μm. (a) Mean normalised microbubble distribution profile in the whole pipe; (b) time evolution of normalised microbubble number density in the viscous sub-layer ($(1 - r)^+ \leq 5$).

The averaging of the fluid and bubble velocity was done from time t^+ = 1,000, after which c / c_0 in the viscous sub-layer is nearly uniform, until the end of the simulation. The comparison between single-phase and two-way coupled predictions is presented in Figure 5.18. Clearly, at this low void fraction of 0.01%, the mean streamwise velocity and normal and shear stresses are not changed. Therefore, the differences between both the fluid and the bubble statistics under one-way and two-way coupling are limited, given that the bubble size is relatively small, and the bubbly flow dilute.

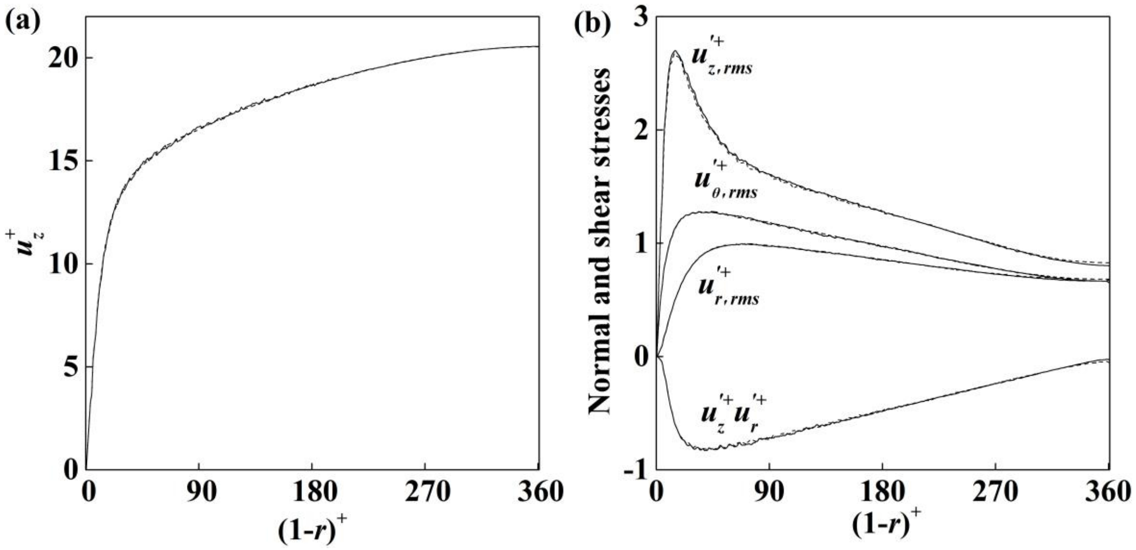

Figure 5.18 Comparison of fluid statistics in DNS of two-way coupled upflow at Re_τ = 361 with d_b = 110 μm (---) with single-phase results (—). (a) Non-dimensional mean streamwise fluid velocity (u_z^+); (b) non-dimensional radial ($u'^+_{r,rms}$), azimuthal ($u'^+_{\theta,rms}$) and streamwise ($u'^+_{z,rms}$) rms of velocity fluctuations and shear stress ($u'^+_z u'^+_r$).

The same results for the bubble phase are plotted in Figure 5.19, including the streamwise bubble mean velocity in Figure 5.19(a) and the bubble normal and shear stresses in Figure 5.19(b). Because of buoyancy, the bubble velocity (in Figure 5.19(a)) is higher than the fluid velocity. This increase is much higher away from the pipe wall, while the two velocities are nearly equal in the pipe wall region. However, in the pipe core region, compared with one-way coupled results, a reduction of nearly 56% in the number of bubbles was found in the first 18 slices of central region due to the effects of the lift force. The small bubble sample makes the averaging of bubble statistics in this region less accurate. Thus, the plot from $(1 - r)^+ > 306$ to the pipe centreline is absent in Figure 5.19(a). The same is the case for the bubble normal and shear stresses plotted in Figure 5.19(b), which were similarly impacted by the lack of bubbles in the central pipe region.

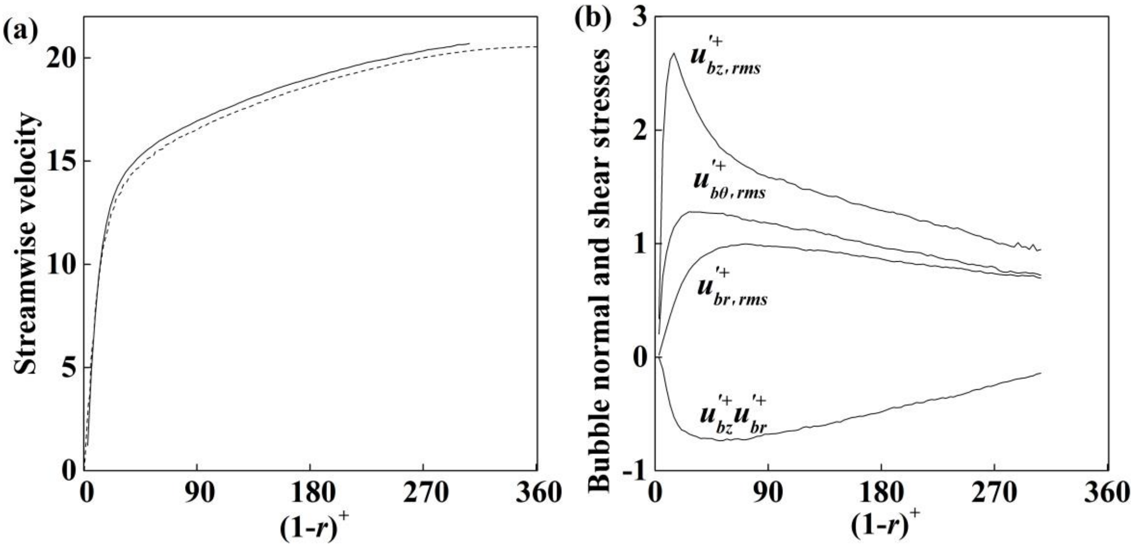

Figure 5.19 Comparison of bubble statistics (—) with fluid results (···) in DNS of two-way coupled upflow at Re_τ = 361 with d_b = 110 μm. (a) Non-dimensional mean streamwise fluid velocity (u_z^+) and bubble velocity (u_{bz}^+); (b) non-dimensional radial ($u'^+_{br,rms}$), azimuthal ($u'^+_{b\theta,rms}$) and streamwise ($u'^+_{bz,rms}$) rms of microbubbles velocity fluctuations and shear stress ($u'^+_{bz}u'^+_{br}$).

Lastly, the forces acting on the bubbles in the streamwise and radial directions are shown in Figure 5.20(a) and (b). Results in the pipe core region are absent in Figure 5.20 for the reasons noted above. Results in the two directions confirm those found in one-way coupling. Therefore, in the streamwise direction, the drag and buoyancy/gravity are well balanced. A positive lift force is observed in the radial direction, which pushes bubbles towards the pipe wall. From Figure 5.20(b), lift force remains high until a distance of $(1-r)^+ \leq 45$, in agreement with the one-way coupled results shown in Figure 5.12(b).

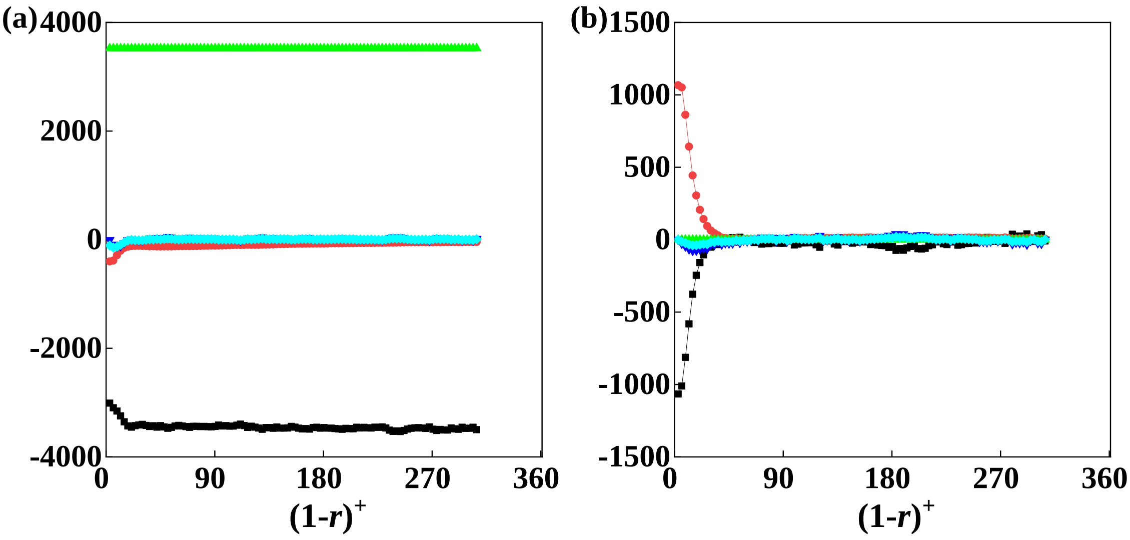

Figure 5.20 (a) Streamwise and (b) radial components of the forces acting on the bubbles in DNS of two-way coupled upflow at $Re_\tau = 361$ with $d_b = 110$ μm. Symbols: ■ drag force; ● lift force; ▲ gravity and buoyancy; ▼ pressure gradient force; ♦ virtual mass force.

5.5 Two-phase pipe flows with four-way coupling and coalescence

In this section, the DNS of two-phase pipe flows at $Re_\tau = 361$ with microbubbles of diameter $d_b = 110$ μm is extended to four-coupling with bubble coalescence considered. Both simulations of downward and upward flows were performed, starting from the initial random injection of microbubbles in the fully developed single-phase pipe flows, with special attention paid on avoiding bubbles overlapping at the beginning of the simulations. As bubble collision is the main consideration in this section, a higher void fraction of 0.10% was considered, to obtain quantitatively significant numbers of collisions and coalescences. The methodology adopted to detect bubble collision and evaluate coalescence occurrence was identical to that described in Chapter 4, with only binary collisions considered and bubble rotation neglected. Coalescence occurrence was predicted using the film drainage model. Downward flow results are presented in Section 5.5.1 and upward flow in Section 5.5.2.

5.5.1 Downflow at $Re_\tau = 361$ with $d_b = 110$ µm

The first simulation made was a downflow at $Re_\tau = 361$ with $d_b = 110$ µm bubbles. Given that the void fraction was set to 0.01% in the work described in the previous section, a four-way coupled simulation at this low void fraction was performed first, and the time evolution of the number of bubble collisions is plotted in Figure 5.21(a). At this low void fraction, the number of collisions increases slowly with time and after $t^+ \approx 400$ only $O(10^3)$ collisions were observed up to $t^+ = 490$, with the total number only slightly increasing beyond that point. To obtain a number of collisions high enough for significant numbers of agglomerations to occur, and to permit quantitative analysis, the void fraction was increased to 0.10%. The time evolution of the bubble collisions for this case is also plotted in Figure 5.21(a). It can be noted in Figure 5.21(a) that the number of bubble collisions increases immediately after bubble injection and increases to $O(10^4)$ in a very short time. With time, the number of bubbles is reduced by coalescence events, and the rate of increase of collisions then slows down significantly. The time evolution of bubbles of different sizes under this high void fraction is given in Figure 5.21(b). The size of bubble used here means that original bubble with diameter $d_b = 110$ µm has size 1. When bubble coalescence occurs, the new bubble volume equals the sum of the volumes of the collided bubbles, generating bubbles of larger sizes shown in Figure 5.21(b). From Figure 5.21(b), the simulation was stopped when the number of bubbles of size four was over $O(10^3)$, after which the number of collisions increases very slowly and very large bubbles, not consistent with the point bubble assumption of the Lagrangian tracker, would have been generated. Thus, a total of 60,532 collisions were collected and the analysis of these collisions is presented below.

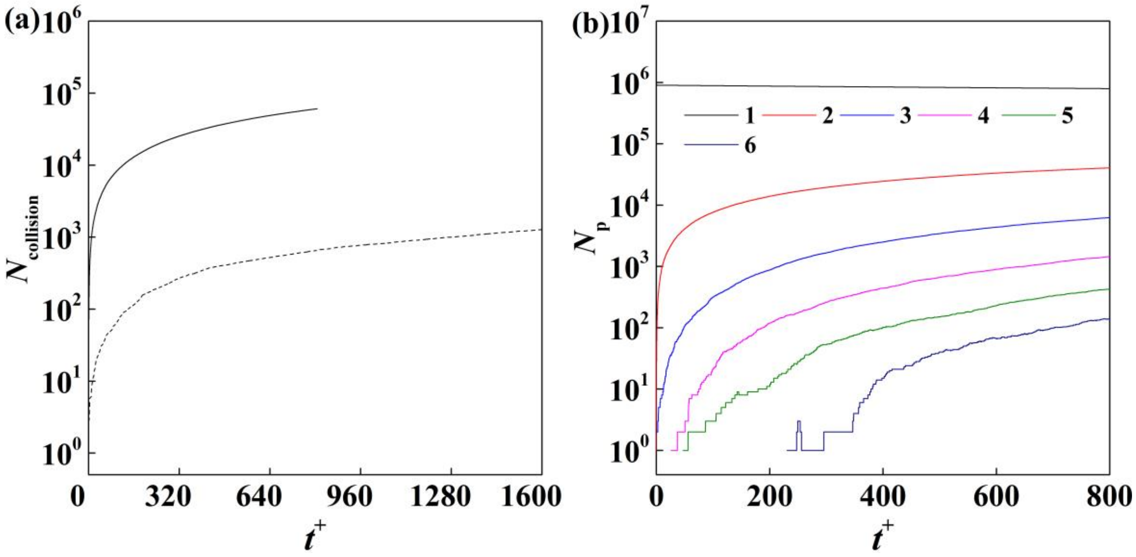

Figure 5.21 (a) Number of bubble collisions at void fraction of 0.01% (---) and 0.10% (—); (b) number of bubbles of different sizes as a function of the dimensionless time (by shear) in downflow at $Re_\tau = 361$ with $d_b = 110$ μm bubbles and void fraction 0.10%.

As the pipe flow statistics are functions of the radial coordinate, the collision statistics are presented in the same way. To obtain the spatial behaviour of the bubble collisions, the pipe geometry was uniformly divided into 10 parallel cylindrical slices in the radial direction. The limits of each slice were given by its radial coordinates. The number of collisions and coalescences, velocities and positions of each binary collision and collision angles were collected in each slice. Considering that the bubble size was very small compared with the slice limits, and a collision between two bubbles belonging to two different slices would be rather rare, it is reasonable in these cases to allocate the collision to the slice where the centre of one of the bubbles was located. Distribution in the radial direction of collision and coalescence events is presented in Figure 5.22. Because each slice has the same radial distance range, it also has a different volume. Hence, Figure 5.22 is obtained by normalising the numbers of collisions and coalescences with the volume of each slice. In pipe downflow, as discussed before, the microbubble migration is towards the pipe core region under the effect of the lift force, so that the microbubble concentration density is a minimum in the vicinity of the pipe wall. However, it can be seen from Figure 5.22 that more collisions are found in the first slice from the wall, where the highest levels of turbulence and the largest velocity gradients exist which promote bubble collision. Towards the core region, the number of collisions decreases until half the radial distance from the wall and then increases further because of the higher bubble concentration density in the core region.

Recall that the bubble coalescence efficiency is defined as the ratio between the number of coalescences and collisions. Each collision event is judged with the film drainage model, using the contact time model of Sommerfeld et al. [71] and the film drainage time model of Prince and Blanch [68]. Figure 5.22 confirms that every collision leads to a coalescence, which means the coalescence efficiency is 100%. Similarly to as was found in the results of Chapter 3, therefore, bubble collision parameters such as the relative collision velocity and angle are crucial in determining the coalescence efficiency, and these are discussed below.

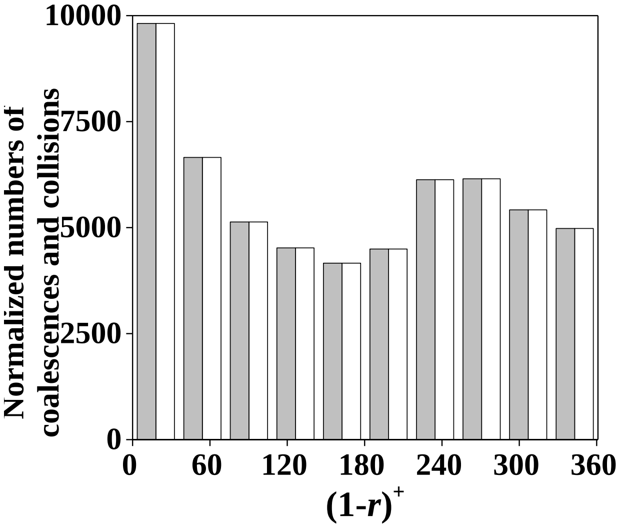

Figure 5.22 Normalised numbers of bubble collisions (□) and coalescences (■) in the radial direction in downflow at $Re_\tau = 361$ with $d_b = 110$ μm bubbles.

Figure 5.23 plots the relative bubble collision velocities in the four well-defined regions in which a downward turbulent flow in a pipe can be defined based on the velocity and turbulence behaviour, namely the viscous sub-layer ($(1-r)^+ < 5$), the buffer region ($5 < (1-r)^+ < 30$), the log-law region ($30 < (1-r)^+ < 100$) and the bulk flow region ($(1-r)^+ > 100$). The same is done for collision angles in Figure 5.24. Recall that, the relative collision velocity and the collision angle for two bubbles *i* and *j* are defined as:

$$u_{br,rel} = \left|u_{br,i} - u_{br,j}\right|, u_{b\theta,rel} = \left|u_{b\theta,i} - u_{b\theta,j}\right|, u_{bz,rel} = \left|u_{bz,i} - u_{bz,j}\right| \tag{5.1}$$

$$\theta_c = cos^{-1}\left[\frac{\boldsymbol{u}_{b,rel} \cdot \boldsymbol{x}_{b,rel}}{\left|\boldsymbol{u}_{b,rel}\right|\left|\boldsymbol{x}_{b,rel}\right|}\right] \tag{5.2}$$

In Figure 5.23, the relative collision velocities in the azimuthal and streamwise directions are all found to be highest in the viscous sub-layer, where the largest mean velocity gradients, but the lowest turbulence levels, exist. The radial relative collision velocity has a similar small range through the pipe. This follows from the fact that the bubble velocity fluctuations in the radial direction are minimal. The largest relative collision velocities in the viscous sub-layer cause the highest collision angles in Figure 5.24(a).

Away from the pipe wall, the streamwise relative collision velocity decreases towards the pipe core. The same is true for the radial and azimuthal components, although they both show a marginal increase in the log-law region. All three components are seen to be lowest in the bulk flow region, where the rms of the bubble velocity fluctuations are smallest. This is also reflected in the bubble collision angles, which are smallest in the pipe core. From Figure 5.24, the range of collision angles never exceeds 10°. Although bubbles collide with the largest relative velocity in the viscous sub-layer, they still collide with a very small angle, which means they will experience a long contact time. This long contact time determines the bubble coalescence efficiency being 100%.

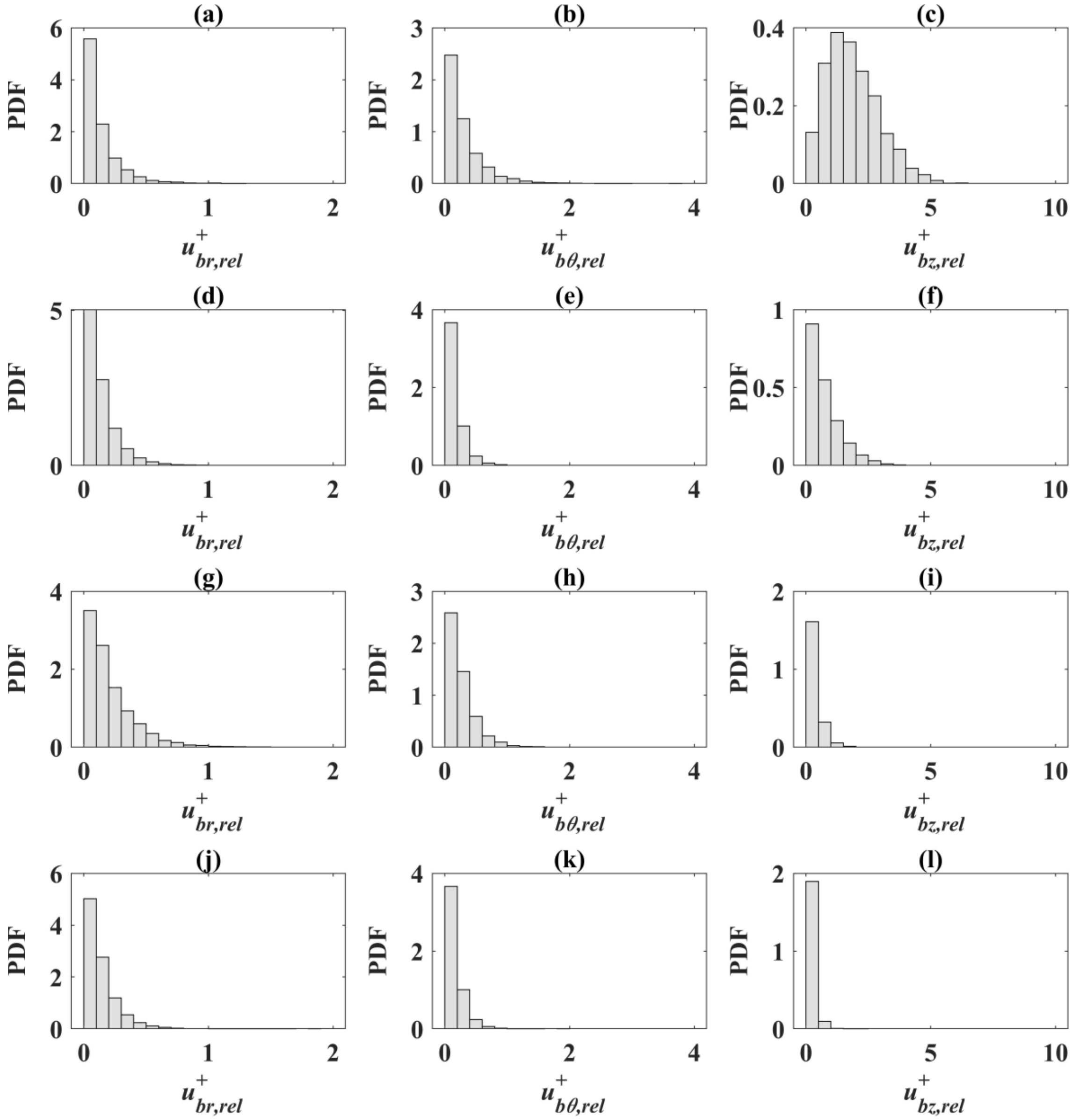

Figure 5.23 PDF of relative bubble collision velocities in radial ($u^+_{br,rel}$), azimuthal ($u^+_{b\theta,rel}$) and streamwise ($u^+_{bz,rel}$) direction and different regions of the pipe in downflow at Re_τ = 361 with d_b = 110 μm bubbles. (a), (b) and (c) Viscous sub-layer; (d), (e) and (f) buffer region; (g), (h) and (i) log-law region; (j), (k) and (l) bulk region.

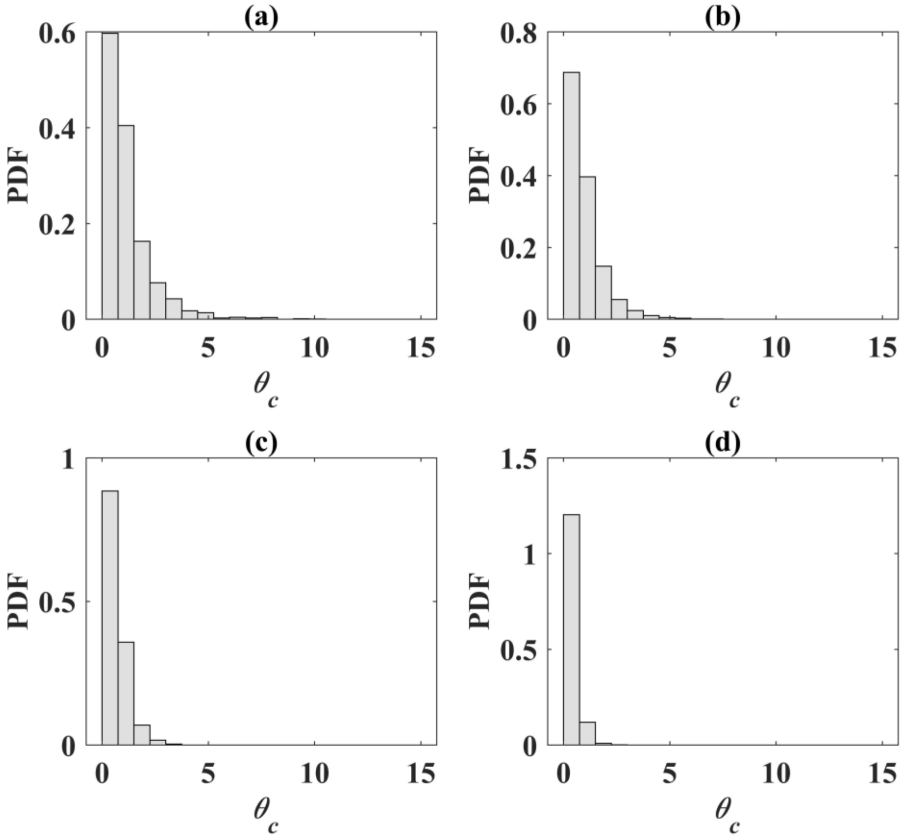

Figure 5.24 PDF of bubble collision angles in different regions of the pipe in downflow at $Re_\tau = 361$ with $d_b = 110$ µm bubbles. (a) Viscous sub-layer; (b) buffer region; (c) log-law region; (d) bulk region.

5.5.2 Upflow at $Re_\tau = 361$ with $d_b = 110$ µm

The case of upflow at $Re_\tau = 361$ with $d_b = 110$ µm bubbles is now discussed. The four-way coupled simulation with a void fraction of 0.01% was firstly performed and the number of bubble collisions as a function of the dimensionless time is presented in Figure 5.25(a). As before, only $O(10^3)$ collisions were obtained until $t^+ = 390$. For this reason, the void fraction was again increased to 0.10%. The number of bubble collisions at this higher void fraction is also given in Figure 5.25(a). A much higher increase in the number of bubble collisions is observed immediately after injection of the bubbles, although the occurrence of collisions and coalescences reduces the bubble number density and makes the rate of increase of the collision frequency decrease with time. The corresponding bubble sizes evolution is shown in Figure 5.25(b). Only six sizes of bubbles are presented. Although larger bubbles were observed to be formed in the flow, they are not included in Figure 5.25(b) because of their very small number density. The simulation was stopped when the number of quadruple bubbles exceeded $O(10^3)$, after which it is assumed that collisions happen with low frequency and too large bubbles are formed. As noticed in Figure 5.25(b), at the final time $t^+ = 726$, bubbles with one, two and three sizes represent the large majority. Overall, a total of 52,304 collisions were recorded.

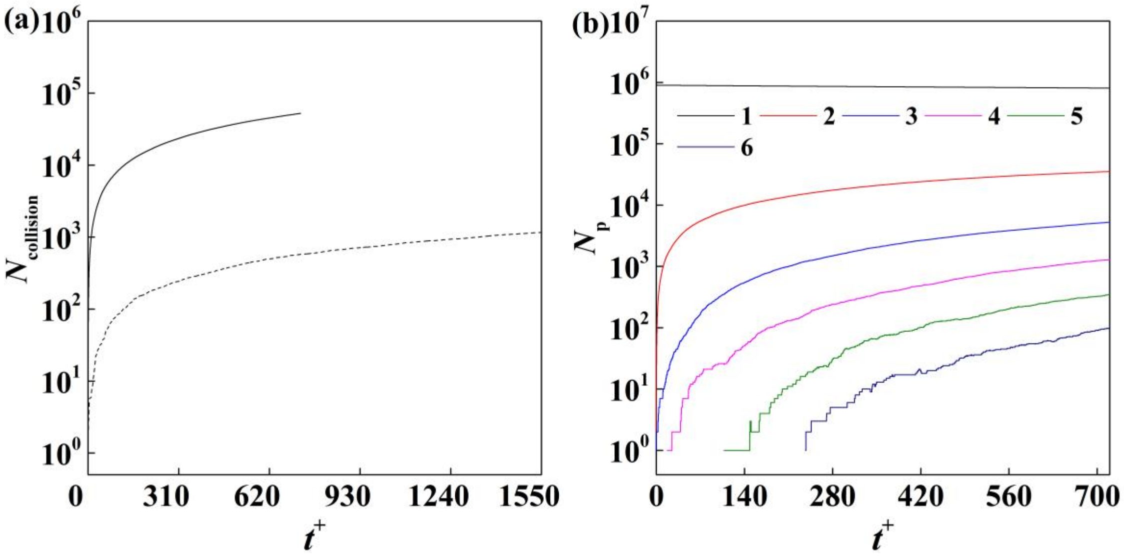

Figure 5.25 (a) Number of bubble collisions at void fraction of 0.01% (---) and 0.10% (—); (b) number of bubbles of different sizes as a function of the dimensionless time (by shear) in upflow at $Re_\tau = 361$ with $d_b = 110$ μm bubbles and void fraction 0.10%.

The normalised numbers of bubble collisions and coalescences are plotted as a function of the radial coordinate in Figure 5.26. This is again obtained by counting events in 10 radial parallel cylindrical slices and normalising by the volume of each slice. Obviously, in Figure 5.26, many more collisions are observed in the very near-wall region compared to in the rest of the flow. As discussed in Section 5.5.1, this is the region with the highest levels of turbulence and with the largest velocity gradients. Moreover, compared with the downflow case in Figure 5.22, the bubble number density is higher near the wall because of the action of the lift force. Towards the pipe core, the collision events are seen to decrease greatly and maintain an almost uniform profile across the rest of entire pipe. All collisions are found to result in coalescences, as shown in Figure 5.26 by the 100% coalescence efficiency.

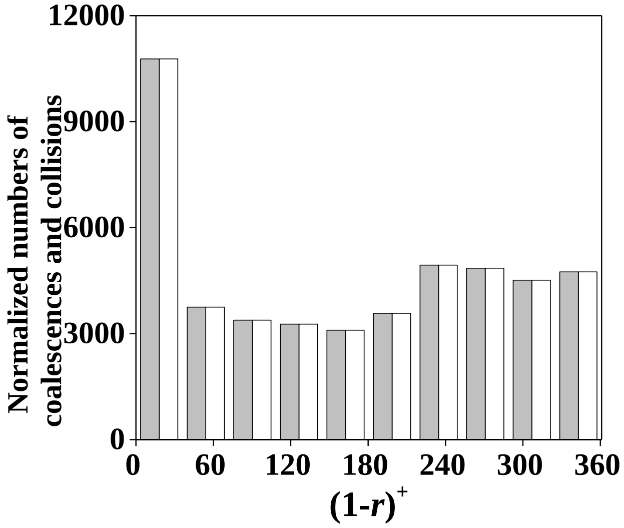

Figure 5.26 Normalised numbers of bubble collisions (□) and coalescences (■) in the radial direction in upflow at Re_τ = 361 with d_b = 110 µm bubbles.

The relative bubble collision velocity components in the four regions of the pipe are presented in Figure 5.27. The trends of the streamwise and azimuthal relative collision velocities have similar shapes with respect to those in downflow in Figure 5.23, and are again largest in the viscous sub-layer, where the largest mean velocity gradients and the lowest turbulence levels are found. Due to high bubble collision numbers in the viscous sub-layer, more coalescences events happen. The magnitude of the streamwise relative velocities is therefore increased in upflow, being almost two times larger than for downflow in Figure 5.23(c). However, the relative collision velocities in the other two directions are almost equal with respect to downflow. The largest magnitude of streamwise relative collision velocity occurring in the viscous sub-layer corresponds to the widest range of collision angles in Figure 5.28, where the collision angle distribution is plotted in the same four regions. The radial relative velocity is smallest in the viscous sub-layer (Figure 5.27(a)). However, it has a very low value in the entire pipe and is therefore not expected to impact bubble collision behaviour. Therefore, the viscous sub-layer remains the most important region for bubble collision and the streamwise component dominates the relative collision velocity.

Towards the pipe centre, the streamwise collision velocity decreases sharply and has a minimum in the bulk region as the velocities of collided bubbles are more correlated. While the bubble velocity fluctuations in the other two directions are limited, a small decreasing variation is seen for both, although an enhancement in the log-law region is apparent. In a similar way, the collision angles decrease away from the wall. The highest collision angle in upflow is found to be ≈ 30°, significantly higher with respect to downflow. This is likely because a higher bubble density exists in the wall region in upflow and microbubbles tend to flow with and be correlated to the fluid flow. Therefore, due to the velocity gradients in this region, larger collision angles are found.

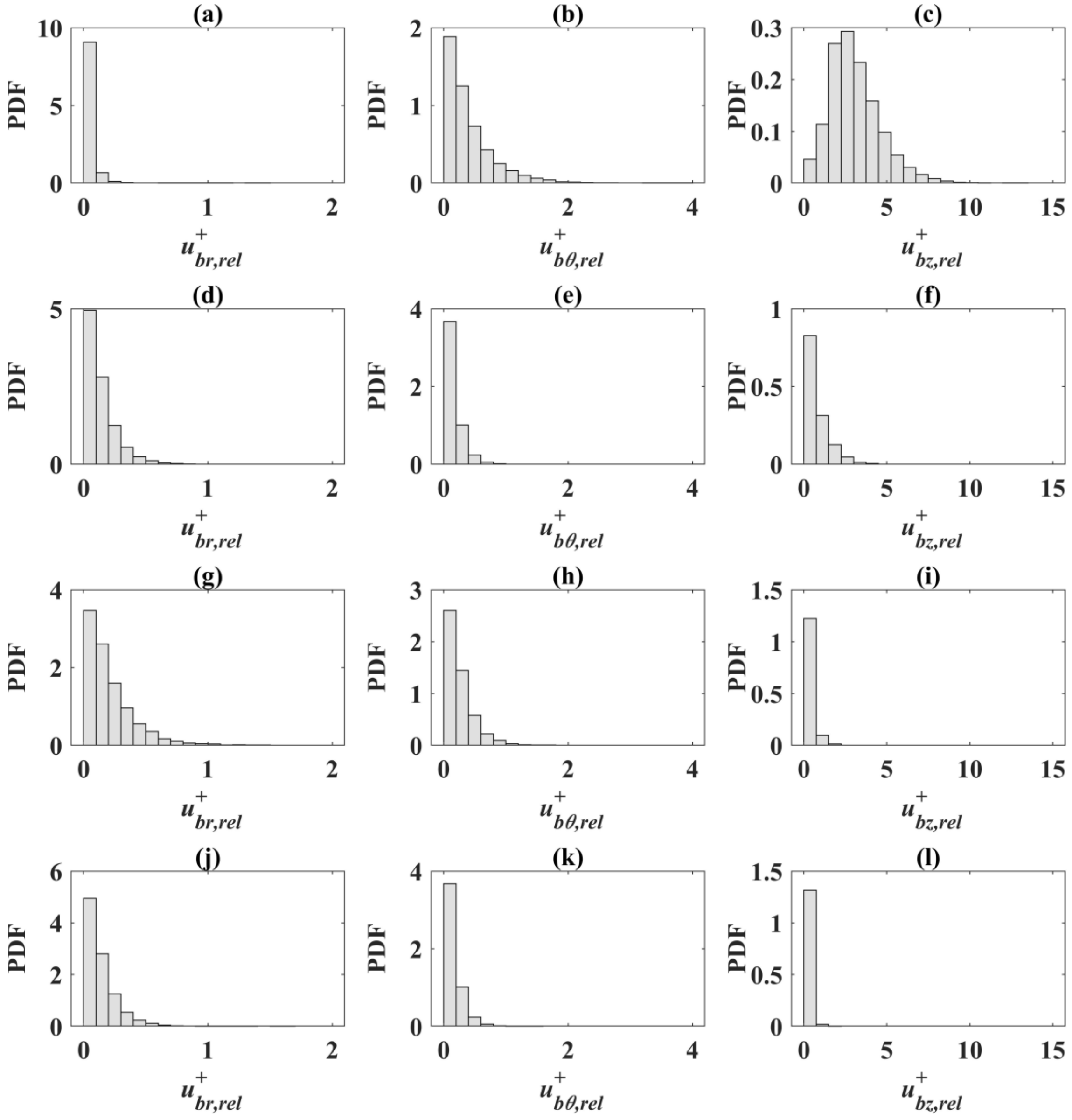

Figure 5.27 PDF of relative bubble collision velocities in radial ($u^+_{br,rel}$), azimuthal ($u^+_{b\theta,rel}$) and streamwise ($u^+_{bz,rel}$) direction and different regions of the pipe in upflow at Re_τ = 361 with d_b = 110 μm bubbles. (a), (b) and (c) Viscous sub-layer; (d), (e) and (f) buffer region; (g), (h) and (i) log-law region; (j), (k) and (l) bulk region.

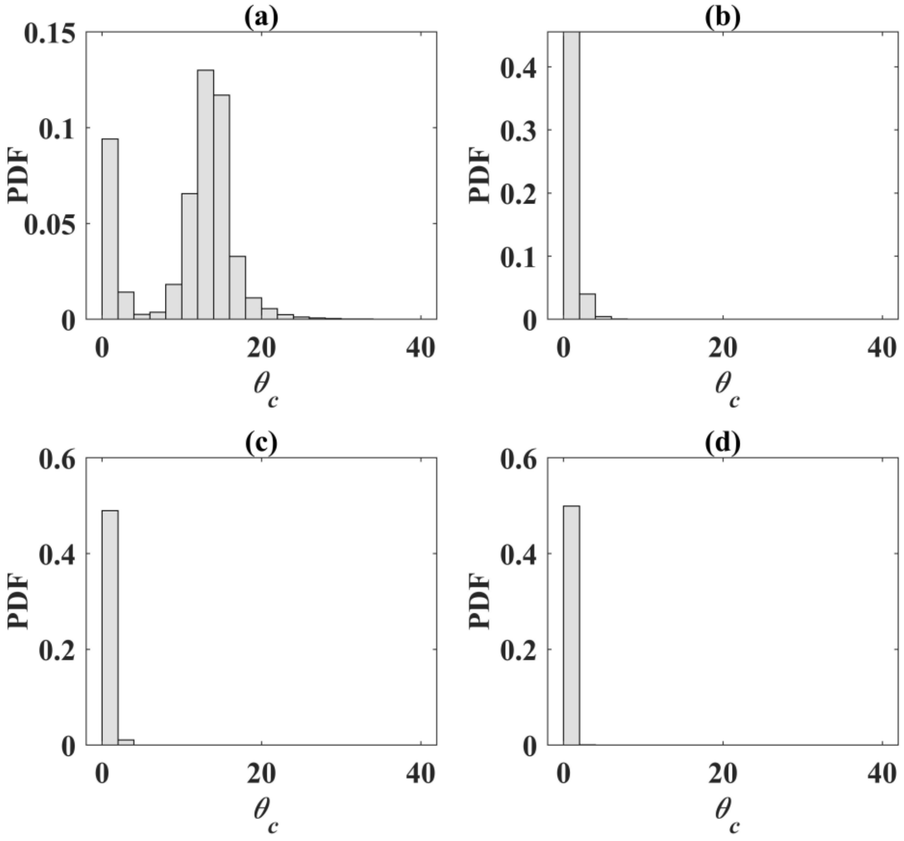

Figure 5.28 PDF of bubble collision angles in different regions of the pipe in upflow at Re_τ = 361 with d_b = 110 μm bubbles. (a) Viscous sub-layer; (b) buffer region; (c) log-law region; (d) bulk region.

5.6 Summary and conclusions

In this chapter, one-way, two-way and four-way (including the effect of bubble coalescence) coupled DNS-based computations of turbulent bubbly pipe flows have been performed. Both upward and downward flow directions were considered. The microbubbles were treated in a Lagrangian way, under the effect of pressure gradient, gravity/buoyancy, drag, virtual added-mass and lift forces. A deterministic hard sphere collision model was used to compute the bubble-bubble collision process, with coalescence evaluated using a film drainage model using two characteristic timescales, namely the bubble contact time and the film drainage time. Confidence in the model accuracy and capability was established by validating the predicted single-phase pipe flow at two Reynolds numbers. One-way coupled results clearly demonstrated that bubbles have different preferential distributions in upflow and downflow and these are mainly governed by the lift force. The effect on the fluid by the bubbles was also examined using the two-way coupled mechanism. However, no obvious difference was observed in upflow. The limited change is mainly due to the fact that the bubble size considered was very small, and the system studied was very dilute.

The four-way coupled model results provide a quantitative description of microbubble dynamics and clarifies the mechanisms of bubble collision and coalescence, driven by the continuous fluid flow field. More collision events are found in the viscous sub-layer of both downflow and upflow cases, due to the action of the large velocity gradients in the region. The maximum bubble collision angle, equal to around 30°, was found in the viscous sub-layer in upflow. However, bubbles tend to generally collide with low collision angles. Additionally, they also collide with small relative velocities. This means that the bubbles correlate with the fluid flow. Under this circumstance, it is more likely that colliding bubbles coalesce.

Chapter 6 DNS of Bubbly Channel Flows with Interface Tracking Approach

6.1 Introduction

In previous chapters, non-deformable, spherical microbubbles were studied using the Lagrangian particle tracking approach. Lagrangian particle tracking, however, is only applicable when bubbles are small enough to be treated as point particles. For large bubbles, this assumption is no longer valid since the forces acting on a bubble can no longer be approximated as acting at a single point. In most practical engineering flows the bubbles are frequently sufficiently large, i.e. with diameters of a few millimetres, to be deformed by the flow. The fact that bubbles are deformable leads to dramatic differences when compared with non-deformable bubbles. For example, bubble deformability and change of shape can reverse the sign of the lift force leading to a different bubble lateral distribution in wall bounded flows [90]. Additionally, the drag characteristics of deformed bubbles will differ from those of their spherical equivalents. Also, deformable bubbles with the same void fraction as spherical bubbles can introduced more turbulence kinetic energy into the flow [90]. Thus, understanding how bubbles transport and deform in turbulent flows is valuable and necessary to the prediction of actual bubble behaviour, with such understanding also beneficial to improvements in the accuracy of simple Lagrangian point-particle based approaches. With the rapid development of high performance computing facilities, DNS coupled with interface tracking methods can now be used to shed light on the mechanics of turbulent flows with deformable bubbles, as described in Chapter 2. At the present time, however, computer run time restrictions mean that it is not feasible to use DNS to simulate large-scale industrial processes using the interface tracking techniques needed to simulate bubble deformation. However, and as noted, the understanding generated by the application of such approaches to simple systems cannot only be used to develop more accurate and realistic closure relations for use with Lagrangian particle tracking approaches to account for the most important phenomena prevailing at all length and time scales for implementation in more pragmatic modelling approaches, but also develop understanding of the dispersion of larger bubbles that cannot be realistically simulated using Lagrangian particle tracking approach. Therefore, in this chapter, consideration is given to the DNS of turbulent channel flow with deformable bubbles simulated using the volume of fluid (VOF) method. The objective of the work reported is to consider how the deformation of bubbles affects their lateral movement, drag coefficient, bubble-induced turbulence and bubble swarm behaviour. A brief literature review of previous work relevant to the present chapter is given below.

The lateral distribution of bubbles in wall bounded flows is altered by bubble deformability. The DNS simulations of Bolotnov et al. [101] showed that in an upward channel flow, a large bubble with an equivalent diameter of 5 mm takes on a cap-like shape after fully developing and stays in the channel centre from where it was released. In contrast, small bubbles with a diameter of 0.9 mm move towards the wall. This bubble distribution transition can be explained in terms of the Eötvös number (*Eo*) which is a measure of the importance of gravitational forces compared to surface tension forces. Consequently, a high Eötvös number means that bubbles are highly deformable. In the same flow, Dabiri et al. [100] also used a front tracking technique with DNS and concluded that a critical *Eo* exists below which the bubble's deformability has little effect on bubble motion so that bubbles concentrate near the channel walls, while for higher *Eo* values the bubbles concentrate in the central regions of the channel core.

Furthermore, understanding of the forces acting on bubbles is critical to predicting bubble distribution, and the terminal shape and velocity of the bubbles. One force of major importance is the drag force, i.e. the resistance force caused by the motion of the bubble through a liquid. As discussed in Chapter 4, for rising bubbles at steady-state, the drag force is balanced by the buoyancy force and determines the relative velocity between the bubble and the continuous phase fluid flow. As a result, the drag force plays a dominant role in determining gas phase residence time, bubble rise velocity, momentum transfer to the liquid phase and bubble clustering phenomenon. Therefore, an accurate closure for the drag coefficient (C_D) is essential. Many factors can affect the drag coefficient, such as bubble size, bubble shape, physical properties and even the purity of the carrier phase [93]. For spherical bubbles in pure liquid, the works of Hadamard [313] and Rybcszynski [314] have given correlations for low bubble Reynolds number ($Re_B \ll 1$, $Re_B =$

$|u_f - u_b|d_b/\nu$), as shown in Eq. (6.1). For high bubble Reynolds numbers ($Re_B \gg 1$), Moore [315] estimated it using Eq. (6.2).

$$C_{\mathrm{D}} = \frac{16}{Re_B} \tag{6.1}$$

$$C_{\mathrm{D}} = \frac{48}{Re_B}\left(1 - 2.21 Re_B^{-0.5}\right) \tag{6.2}$$

For deformable bubbles in pure liquid, the closure of Tomiyama et al. [316] is widely used and described as below. They used demineralized water rather than ultra-purified water, which leads to a higher estimation [317] of the drag coefficient.

$$C_{\mathrm{D}} = \max\left[\min\left[\frac{16}{Re_B}\left(1 + 0.15 Re_B^{0.687}\right), \frac{48}{Re_B}\right], \frac{8}{3}\frac{Eo}{Eo + 4}\right] \tag{6.3}$$

Experimental investigations of bubbly flows are difficult to perform, and it is impossible to isolate the influence of a single parameter on bubble behaviour. DNS can overcome this problem and has already provided some insights. For example, Dijkhuizen et al. [93] used a front tracking method and gave the drag correlation for a single rising bubble as:

$$C_{\mathrm{D}} = \sqrt{[C_{\mathrm{D}}(Re_B)]^2 + [C_{\mathrm{D}}(Eo)]^2} \tag{6.4}$$

$$C_{\mathrm{D}}(Re_B) = \frac{16}{Re_B}\left(1 + \frac{2}{1 + \frac{16}{Re_B} + \frac{3.315}{\sqrt{Re_B}}}\right) \tag{6.5}$$

$$C_{\mathrm{D}}(Eo) = \frac{4Eo}{Eo + 9.5} \tag{6.6}$$

The study was further developed by Roghair et al. [106] in a mono-disperse bubble swarm who gave the drag coefficient as a function of the local gas fraction α and the Eo number:

$$\frac{C_{\mathrm{D}}}{C_{\mathrm{D},\infty}(1 - \alpha)} = 1 + \left(\frac{18}{Eo}\right)\alpha \tag{6.7}$$

This drag coefficient model was validated in an Eulerian-Lagrangian framework [107] where good predictions with respect to experimental results were obtained [108]. More noteworthy studies were performed by Feng and Bolotnov [318, 319]. They used a proportional-integral-derivative bubble controller to fix an isolated bubble and reported the drag coefficient within a Re_B of 900 flow as:

$$C_{\mathrm{D}} = \min\left[\frac{16}{Re_B}\left(1 + 0.15Re_B^{0.687}\right), \frac{48}{Re_B}\left(1 + 3 \times 10^{-10}Re_B^{3.3189}\right)\right] \quad (6.8)$$

Another important issue is understanding the effect of bubbles on the fluid phase, and in particular on the turbulence field within it, commonly referred to as bubble-induced turbulence (BIT). In bubbly flow, the bubble-generated vorticity is normally proportional to the local bubble interface curvature and, accordingly, deformable bubbles produce more turbulent vorticity than spherical bubbles. As a result, the mechanism for BIT by deformable bubbles is more complex. Previous experiments [170, 320] mainly estimated the overall net change in turbulence levels for bubble flows. However, details of how single deformable bubbles contribute to the fluid turbulence is rather limited. DNS with interface tracking methods can control any parameter, e.g. the surface tension, and gives a way to evaluate in detail the impact of a bubble of the continuum turbulence field. For example, Feng and Bolotnov [116] employed a level set method to fix the bubble position and evaluated BIT by estimating the turbulent field around different sizes of deformable bubbles. It was found that the carrier liquid phase experiences a transition from turbulence reduction to turbulence enhancement due to bubble deformation. In addition, the results of parametric studies showed that bubbles with higher deformability introduce more turbulence behind the bubble. This is consistent with previous studies [101] where the influence of a large deformable bubble on the surrounding liquid was found to be greater than that of a dispersed bubbly flow with a few nearly spherical bubbles and a similar void fraction from the turbulence kinetic energy profile. More recently, Feng et al. [321] used a front tracking method to simulate deformable bubbles in a vertical channel flow. The DNS results were processed by evaluating the coefficients commonly used in BIT models within Reynolds-averaged Navier-Stokes modelling approaches, i.e. in relation to the k-ε and explicit algebraic stress models. However, the channel domain size ($\pi\delta \times 2\delta \times \pi/2\delta$) and liquid/gas mass density ratio (10) used in their study are rather limited. In addition, the DNS of clean deformable bubbles is rarely seen in the literature.

Multiple deformable bubbles namely bubble swarms, present dramatically different features from spherical bubble swarms in turbulent flow, including the void fraction distribution, bubble-fluid interaction and bubble clustering phenomena, which are not feasible to investigate by means of the Lagrangian particle tracking method. For example, Bunner and Tryggvason [89], Santarelli and Fröhlich [115], and Cifani et al. [322] suggest nearly spherical bubbles tend to form horizontally aligned clusters. However, the dynamic interaction of two deformable bubbles is changed by wake effects. As a result, deformable bubbles prefer to align vertically [90, 182], and the trailing bubble moves in the wake of the leading bubble and is attracted towards it. One physical explanation found in pseudo-turbulence by Martínez-Mercado [182] is the inversion of the lift force acting on bubbles that causes them to drift to the downflow side of a vortex in the bubble wake region. Another possible reason, as described in Martínez-Mercado [182], is the pressure reduction present in the bubble wake region, whereas small and spherical bubbles have smaller wakes leading to the horizontal alignment. Therefore, further investigations are desirable to understand highly deformable bubble clustering in a turbulent flow.

Therefore, in this chapter, direct numerical simulations of bubbly channel flow with deformable bubbles are studied. Of interest is the clean bubble in water. The rest of the chapter is organized in the following manner. Firstly, a model validation of a single-phase channel flow is given in Section 6.2. This is obtained by comparing first and second order flow statistics with validated data. Then, the two-phase bubbly flow is simulated where the carrier and dispersed phases are considered incompressible and immiscible. Two kinds of bubbly flow cases are performed, i.e. the single bubble case, and multiple bubble case. The single bubble case study includes a bubble motion and trajectory study in Section 6.3.1, bubble drag coefficient estimation in Section 6.3.2, and bubble induced turbulence (BIT) evaluation in Section 6.3.3. The multiple bubbles case study is presented in Section 6.4. Finally, concluding remarks are given in Section 6.5.

6.2 Model validation

In this section, the validation of a single-phase flow in a vertical channel is presented. The shear Reynolds number is selected as $Re_\tau = 150$. The domain size is larger than used in most DNS papers with the same Reynolds number [321, 323], and is set as $4\pi\delta \times 2\delta \times 2\pi\delta$ which is same as used in previous chapters. More details of the methodology can be found in Section 3.3.

6.2.1 Computational details

A vertical upward channel flow is simulated and driven by a fixed pressure gradient to meet the target Reynolds number. Periodic conditions were assumed in both the streamwise and spanwise directions. The non-slip condition was imposed at the walls. As noted in Section 3.3.2, the governing equations were discretized by means of the finite volume method which casts the computational domain into small finite control volumes with a stationary structured mesh and discretizes the momentum and continuity equations in all grid cells. The computational geometry is discretised on a three-dimensional Cartesian grid. Specifically, the staggered grids along the streamwise (x) and spanwise (z) directions are uniformly spaced, while the grid was refined in the wall-normal (y) direction using a hyperbolic tangent profile [222]. In order to capture the bubble interface, a refined grid resolution is required. This is due to several issues such as the solution of the volume fraction field needing good computational resolution, with flow in the channel centre also requiring reasonable grid refinement. According to [216], at least 15 grid points per bubble diameter is required to resolve the shape of a bubble as it deforms. So, in this chapter, the channel is divided into 512 × 256 × 256 elements ($N_x \times N_y \times N_z$) corresponding to a total of 33.5 M cells. As a result, the grid spacings in streamwise and spanwise directions are $\Delta x^+ = \Delta z^+ = 3.68$. The maximum grid spacing in the wall-normal direction, located in the channel centre, is $\Delta y^+_c = 1.85$. The present computational grid resolution is provided and compared with those of other studies in the literature [259, 321, 323] using the same flow Reynolds number in Table 6.1.

In terms of the mesh arrangement, and in order to capture the smallest length scale of turbulence, the Kolmogorov length scale should be evaluated using $\eta = (\nu / \varepsilon)^{1/4}$. However, calculation of the turbulence kinetic energy dissipation rate ε is complex and requires accurate statistics. For wall-bounded flows, η can be estimated as below [324]:

$$\eta = (k\, y^+)^{\frac{1}{4}} \tag{6.9}$$

where k is the von Karman constant ($k \approx 0.41$), and y^+ is the distance from the closest wall in wall units. Accordingly, the Kolmogorov length scale η for the present channel flow at $Re_\tau = 150$ is 2.80 wall units. As is generally understood, the grid spacing in DNS should be of the same order of magnitude as η. In present study, the largest spacing in the wall-normal direction is 1.85 wall units which is smaller than η. Although the spacings in streamwise and spanwise directions are larger than η, they are still of the same order of magnitude and comparable with those of other literature studies, as listed in Table 6.1. On the other hand, higher resolution requires more computational effort. Therefore, the current mesh resolution is selected and, when compared to other studies, regarded as acceptable for the present DNS study.

Table 6.1 Computational grid resolution of DNS and literature studies.

References	$L_x \times L_y \times L_z$	$N_x \times N_y \times N_z$	Δx^+	Δz^+	Δy^+_c
Iwamoto et al. [323]	$2.5\pi\delta \times 2\delta \times \pi\delta$	64 × 97 × 64	18.4	7.36	4.91
Molin et al. [259]	$4\pi\delta \times 2\delta \times 2\pi\delta$	128 × 129 × 128	14.7	7.4	3.7
Feng et al. [321]	$\pi\delta \times 2\delta \times 0.5\pi\delta$	384 × 256 × 192	1.23	1.23	1.51
Present DNS	$4\pi\delta \times 2\delta \times 2\pi\delta$	512 × 256 × 256	3.68	3.68	1.85

6.2.2 Mean statistics

The single-phase flow was driven by a constant pressure gradient in the streamwise direction by varying the flow rate. Firstly, a parabolic profile with a cosine perturbation wave on the initial velocity was introduced. Then, the average wall shear stress ($\tau_w = \rho_f u_\tau^2$) was monitored until a statistically steady turbulent single-phase flow was achieved, indicated by a non-dimensional wall shear stress with a value of 1 being achieved. Figure 6.1 plots the non-dimensional wall shear stress profile as a function of computational time (solid line) which is compared with unity value (dash line). It can be seen that the non-dimensional overall averaged wall shear stress over the whole channel achieved a unity value at a time t^+ of around 50, before which it is lower than required because of oscillations of the flow statistics during the transition from laminar to turbulent flow and as a steady state mean velocity profile is established.

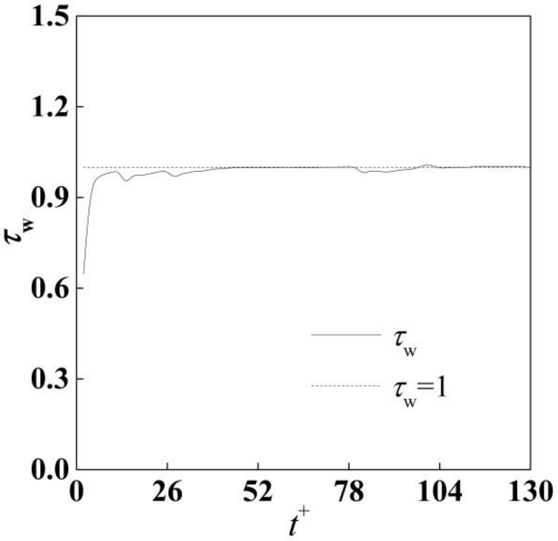

Figure 6.1 The wall shear versus computational time for single-phase channel flow.

In order to further ensure that the single-phase flow had converged to a steady solution, predictions of the mean streamwise velocity, rms of velocity fluctuations and shear stress are compared with the results given in Chapter 4, obtained using the Nek5000 DNS code. The mean statistics for the fluid phase were computed by employing the volume fraction averaging method as:

$$< q > = \frac{\overline{(1-f)\cdot q}}{\overline{(1-f)}} \tag{6.10}$$

where (1 – *f*) refers to fluid phase volume fraction and q is a quantity of interest. The overbar ($^{-}$) denotes the average over time and homogenous directions. Accordingly, the rms of the fluid velocity fluctuations can be obtained as:

$$\mathrm{rms}(q') = \sqrt{\frac{\overline{(1-f)\cdot q^2}}{\overline{(1-f)}} - \left(\frac{\overline{(1-f)\cdot q}}{\overline{(1-f)}}\right)^2} \tag{6.11}$$

For the single-phase flow, *f* is replaced by unity. Note that the averaging in this chapter generate profiles on the 256 wall-normal grid space centres, which does not follow the method used in Chapters 4 and 5.

Figure 6.2(a) gives the streamwise mean velocity profile over the channel half width, together with that of the single-phase results of Chapter 4. A similar comparison of normal and shear stresses is provided in Figure 6.2(b). These averaged data were obtained from $t^+ = 50$ to $t^+ = 130$ and non-dimensionalized by the shear velocity. In Figure 6.2(a), good consistency of the streamwise velocity is found in the channel wall area ($y^+ < 30$). The velocity away from the channel wall, however, is somewhat higher than expected, with a maximum relative discrepancy of approximately 2.9%. This is consistent with the work of the TBFsolver developers [325] where an discrepancy of 3% was found. Unfortunately, the developers did not give any explanation for this small relative error, although in the present case this is likely due to the differing numerical resolutions used for the Nek5000 and TBFsolver runs. Full agreement is found for the normal and shear stresses in Figure 6.2(b). Given the consistent agreement of the first and second order statistics, confidence in the current mesh arrangement is sufficient to allow use of this solution for the two-phase flow study. The instantaneous streamwise velocity in the single-phase flow at the final timestep is presented in Figure 6.3, and this was selected as the initial condition for the two-phase flow simulations.

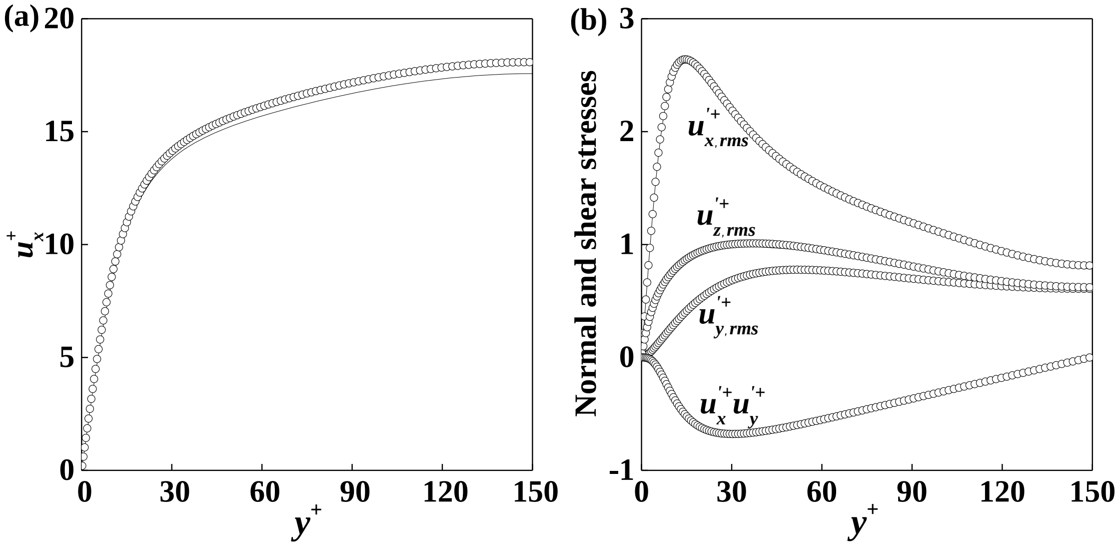

Figure 6.2 Comparison of single-phase fluid results in current DNS at $Re_\tau = 150$ (○) with results obtained using Nek5000 (—). (a) Non-dimensional mean streamwise fluid velocity (u_x^+), and (b) non-dimensional wall-normal ($u'^+_{y,rms}$), spanwise ($u'^+_{z,rms}$) and streamwise ($u'^+_{x,rms}$) root mean square (rms) of velocity fluctuations and shear stress ($u'^+_x u'^+_y$).

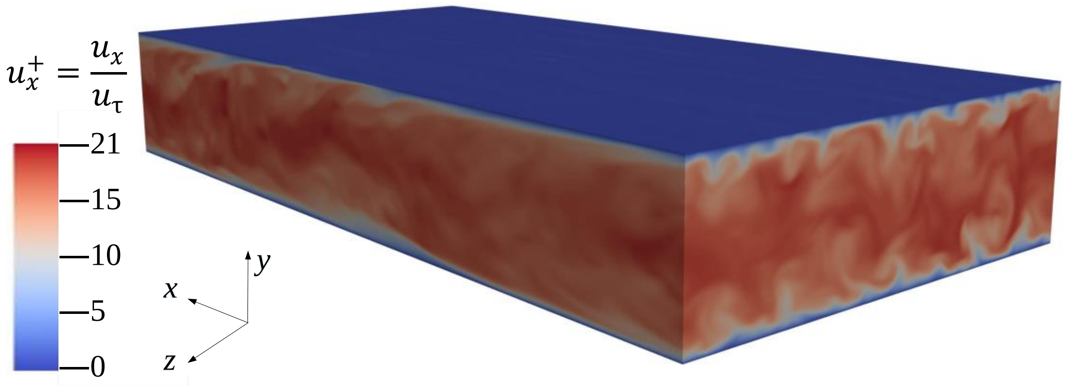

Figure 6.3 Pseudo-colours of instantaneous axial velocity normalized by the shear velocity.

6.3 Single bubble case study

Based on the previously validated single-phase flow, the single bubble case studies are described in this section. The numerical procedure employs a VOF method coupled with an accurate bubble curvature computation using the generalised height function method. Firstly, the characteristic parameters of the two-phase flows are discussed. The DNS cases described in the present chapter were carried out using non-dimensional parameters. Specifically, the non-dimensional density of the fluid at room temperature is 1 (996.5 kg

m^{-3} in dimensional units). The non-dimensional channel half width is 1 and the non-dimensional dynamic viscosity is 0.00667, leading to the shear Reynolds number of 150 based on channel half width. The density ratio between carrier and gas phases is 100, corresponding to 9.965 kg m^{-3} for the density of the gas phase. It should be noted that, in order to ensure the accurate resolution of bubble interfaces, the non-dimensional bubble diameter in all cases was set to 1/5th of the whole channel width, giving at least 15 grid points in every direction across the bubble diameter. This was achieved for differing bubble diameters by changing the channel half width for each case. The bubble deformability is characterized by the Morton number and the Eötvös number, with the bubbles chosen having corresponding diameters of 1mm, 4mm and 8mm. According to Grace's diagram [261], the shape of these bubbles varies from nearly spherical to ellipsoidal and wobbling, as shown in Figure 6.4. For the present fluid, the Morton number is constant. The physical quantities for all simulations are summarized in Table 6.2.

Table 6.2 Characteristic parameters of single bubble cases.

Parameters	Notation	Case I	Case II	Case III
Fluid density	ρ_f / kg m^{-3}	996.5	996.5	996.5
	ρ_f^*	1	1	1
Fluid dynamic viscosity	$\mu_f \times 10^{-3}$ / kg (m s)$^{-1}$	1	1	1
	μ_f^*	0.00667	0.00667	0.00667
Bubble density	ρ_b / kg m^{-3}	9.965	9.965	9.965
	ρ_b^*	0.01	0.01	0.01
Number of bubbles	N_b	1	1	1
Bubble diameter	d_b / mm	1	4	8
	d_b^*	0.4	0.4	0.4
Half channel width	$H/2$ / mm	2.5	10	20
	δ^*	1	1	1
Fluid shear velocity	u_τ, m s^{-1}	0.06	0.015	0.0075
	u_τ^*	1	1	1
Log Morton number	$Log\ Mo$	-10.87	-10.87	-10.87
Eötvös number	Eo	0.13	2.14	8.56

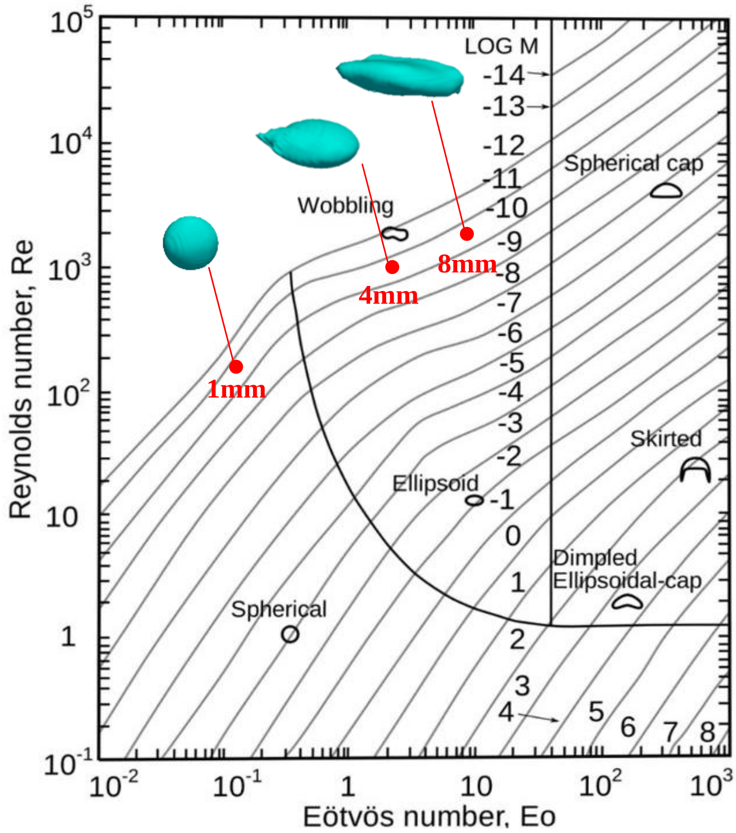

Figure 6.4 Studied bubble size range in current work in the diagram of Grace [261].

A single bubble was injected as an initially spherical gas bubble released from rest. All simulations in this section were driven by a fixed pressure gradient. The volume fraction field was initialized in the computational domain with values of 0 and 1 for the liquid and gas phases, respectively. The numerical simulations were performed over a sufficiently long time period to allow the bubble to develop to a steady state terminal shape and velocity. The bubble lateral movement, bubble shape, bubble drag coefficient as well as bubble-induced turbulence evaluation are investigated below.

6.3.1 Bubble trajectory

In this section, an overall impression of the trajectory of the different sizes of bubbles is first presented. Figure 6.5, Figure 6.6 and Figure 6.7 show the shape evolution, trajectory and lateral bubble movement for bubbles with diameters of 1 mm, 4 mm and 8 mm, respectively. These figures show the bubble/water interface (identified as the surface where the volume fraction $f = 0.5$) at six successive instants in time. The time interval was adjusted to allow the bubbles to flow one pass-through the channel for 1 mm and 4 mm bubbles, and 2 pass-throughs for the 8 mm bubble. In each snapshot, the left and right boundaries are the non-slip channel walls. The fluid flows from the bottom to the top of the channel in upflow, with periodic conditions applied. The figures are plotted together with contour levels of the two-dimensional fluid instantaneous streamwise velocity field cross the channel.

In Figure 6.5, a 1 mm bubble is injected with a spherical shape and released from the channel centre, after which it starts to flow with the carrier fluid. It is seen that the bubble moves to the channel wall and reaches the wall after approximately 3/4 of one pass through the channel, after which it remains at or close to the wall and does not move back towards the channel centre. In addition, during its movement, it remains spherical until it touches the channel wall where, under the effect of high vorticity near the wall, the bubble shape changes a little, but overall it exhibits a close to spherical shape, as expected from Grace’s diagram [261].

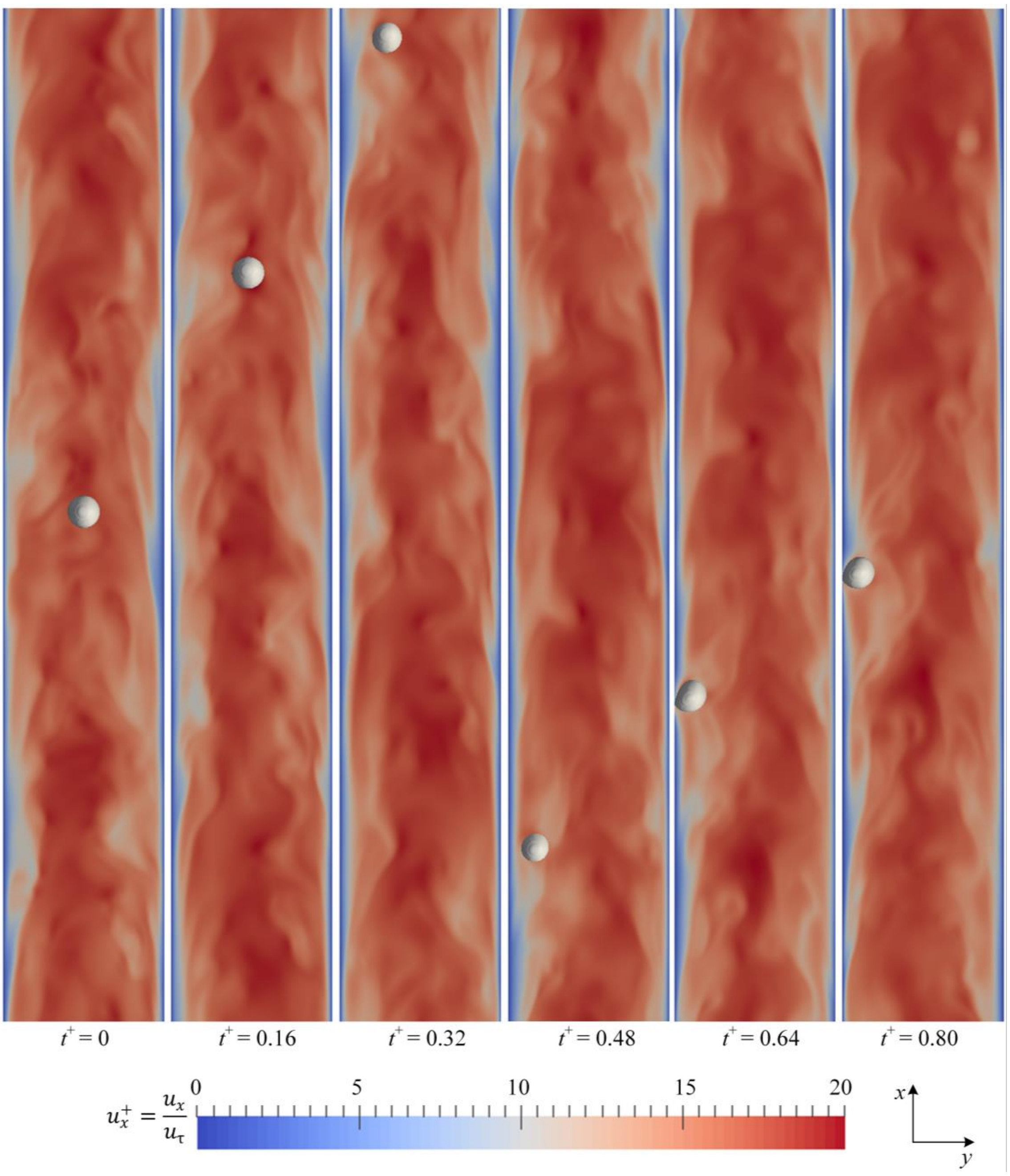

Figure 6.5 Time evolution of a 1 mm bubble in the channel identified by the volume fraction contour $f = 0.5$.

A similar lateral movement is observed for the 4 mm bubble in Figure 6.6, where a spherical bubble is again released at the channel centre. The bubble considered in Figure 6.6 is characterized by a higher deformability. As a result, its motion is different from that of the 1 mm bubble. It can be noted that once the bubble is released at the channel centre it starts to deform very quickly, varying in the shape from spherical to a wobbling ellipsoid. The bubble again moves towards the channel wall with time, and eventually it touches the wall. It is also clear in Figure 6.6 that the local structure of the carrier phase velocity field is affected by the bubble motion and deformation as the bubble rises in the channel, introducing a higher level of turbulence in the bubble wake region that is not observed for the 1 mm bubble. However, due to the low overall void fraction in the flow domain, the rest of the channel remains approximately the same as the single-phase flow. In addition, the bubble-induced turbulence decreases when the bubble touches the wall. This is simply because of the lower velocities and turbulence levels in the wall region. The effects of bubble-induced turbulence are discussed thoroughly in Section 6.3.3. Also, when the bubble touches the wall, its terminal shape remains ellipsoidal and wobbling with the time.

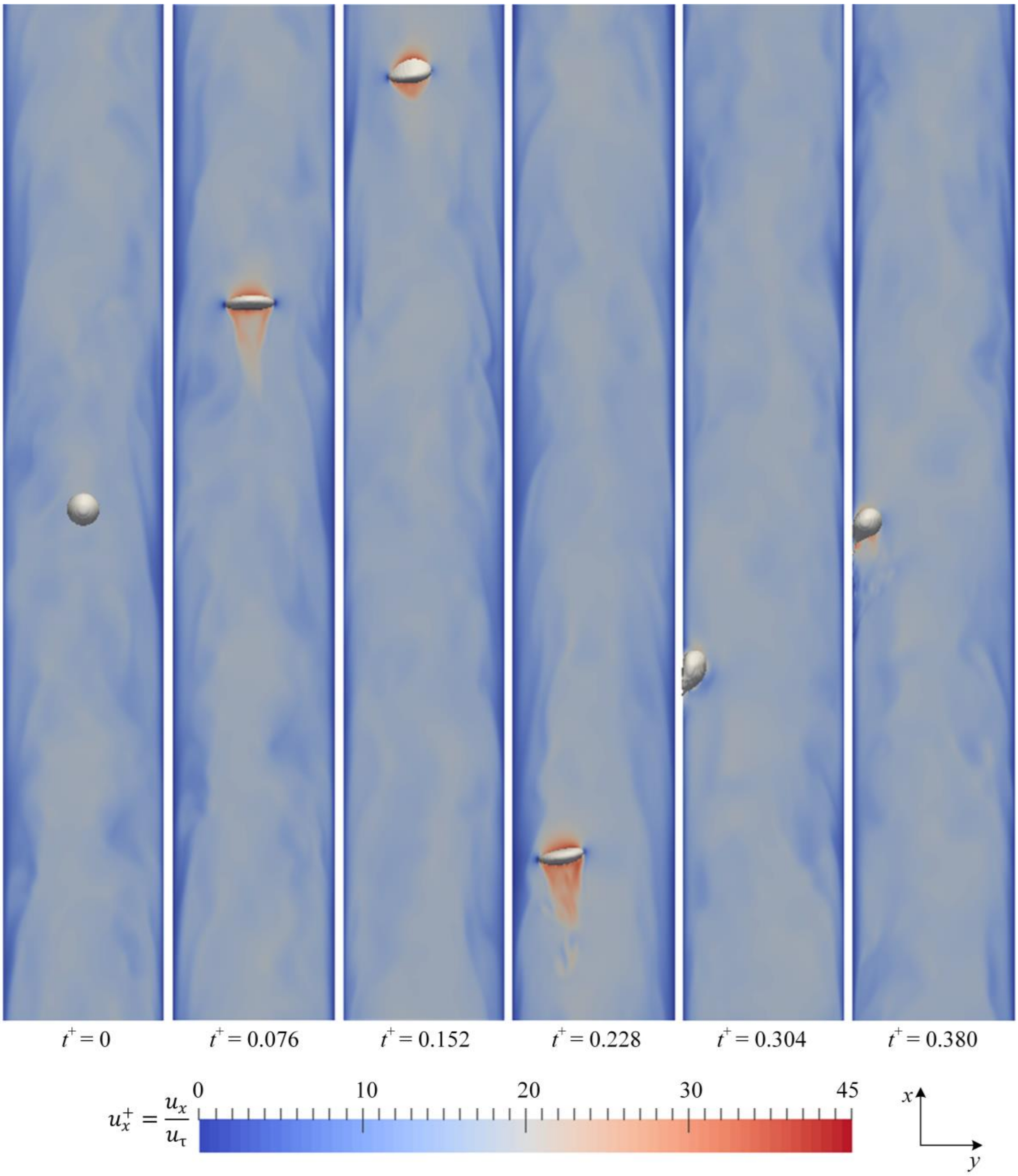

Figure 6.6 Time evolution of a 4 mm bubble in the channel identified by the volume fraction contour $f = 0.5$.

The last case is the 8 mm bubble with a very high *Eo* which translates into a very high bubble deformability. As can be seen in Figure 6.7, this highly deformable bubble again changes shape rapidly with its motion restricted to the middle part of channel. The overall lateral movement is minimal, in contrast to the motion of the 1 mm and 4 mm bubbles. This is due to the fact that the bubble size and its increase in deformability changes the direction of the lift force acting on the bubble [100] when compared to the two previous cases. Here it is important to note that in Lagrangian particle tracking, the reversal of the lift force acting on large deformable bubbles can be related to the pressure gradient lift force or the Weber number [326]. Although such approaches can reasonably simulate some simple cases such as laminar shear flows or turbulent flows with low bubble Reynolds numbers, it relies on the accurate determination of the lift force model. However, the reversal of the lift force is still poorly understood and modelled in more complicated turbulent flows. In contrast, with the interface tracking approach, the bubble/water interfaces are resolved explicitly which avoids all the possible modelling uncertainties and allows a better understanding of deformable bubbles in turbulent flows.

As also observed in Figure 6.7, the bubble is released from rest at the beginning of the simulation, after which it flows twice through the channel within the time period of $t^+ = 0 \sim 0.5$. This rapid motion follows from the fact that the fluid flows faster in the middle regions of the channel and the increased influence of buoyancy for this large bubble, leading to a higher bubble velocity than in the case of the smaller bubbles. Another observation is the significant influence of the bubble on the surrounding fluid flow where the level of turbulence is increased dramatically. Although the void fraction is low, and hence the overall impact on the flow field is low, the bubble-induced turbulence is seen to be more significant than in the case of the 4 mm bubble, extending to large distances behind it and also laterally within the flow. More details of BIT quantities are discussed in Section 6.3.3. Due to the high bubble velocity, two passes through in the channel were monitored in order to capture the bubble terminal shape. However, from the results of Figure 6.7, it can be concluded that the 8 mm bubble takes only up to $t^+ = 0.1$ to attain its expected steady state shape, after which it starts wobbling.

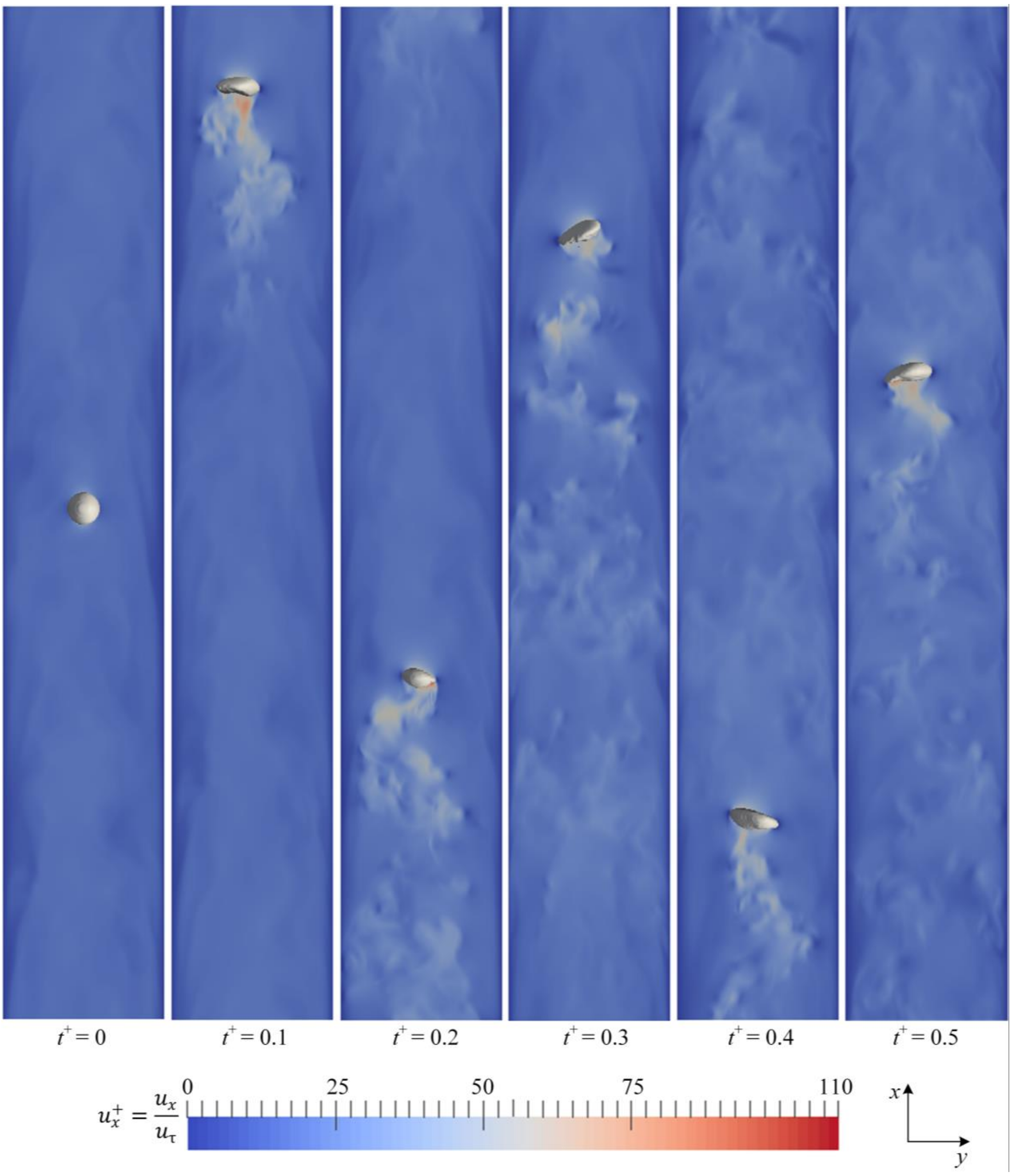

Figure 6.7 Time evolution of an 8 mm bubble in the channel identified by the volume fraction contour $f = 0.5$.

As discussed above, bubble deformability controls the lateral movement of a bubble. In the case of the 1 mm and 4 mm bubbles in the upward channel flow, the bubbles drift towards the channel wall under the action of the lateral lift force [113] and at some point touch the channel wall. Of particular interest is understanding the bubble motion near the vertical wall since both the wall effect and the bubble wake instability will have an effect on any instability in the rising bubble's trajectory [327]. Therefore, in the present study, the bubble shape and motion were captured for both these smaller bubble cases. Both bubbles were originally placed in the same position in the single-phase channel flow, as previously described. Once they rise relative to the flow, they drift towards the channel wall. The TBFsolver code simulates bubble-wall interaction based on a contact angle model by Afkhami and Bussmann[328]. As noted by Cifani [325], a zero-gradient of the volume fraction field at the wall results in the bubbles sticking to the wall. Accordingly, the contact angle model solves the problem of how the bubble interface adjacent to the wall should be reconstructed. Specifically, a contact angle of 180 degrees is employed indicating that the interface normal and the wall normal point directly towards each other. The code developers validated this approach using bubble-wall bouncing events in [325] by means of this method. Therefore, particular interest here is paid on the bubble motion close to the wall. Figure 6.8 shows the bubble shape and motion in the x-y plane as they move closer to the channel wall before eventually touching the wall. The bubble interface in Figure 6.8 was similarly identified by the volume fraction contour $f = 0.5$. Every subplot of each case in Figure 6.8 was made at an equal time interval. Note that the results are plotted in the x-y plane only because the present flow conditions did not give any instability of the bubble path in the three-dimension which made bubble movement in other planes negligible.

In the case of the 4 mm bubble, as shown on the left of Figure 6.8, the shear-induced lift force acts towards the lower fluid velocity side from the higher velocity side. The initial shape of the bubble is seen to be an oblate ellipsoid at the top of Figure 6.8. While approaching to the wall, the shape becomes more deformed and more slanted in the vertical direction as it touches the wall. However, the 1 mm bubble maintains its near-spherical shape and only deforms slightly when it collides with the wall, as seen on the right of Figure 6.8. This is simply because the 1 mm bubble has a low deformability ($Eo = 0.13$) and holds its shape in low Reynolds number regions of the flow.

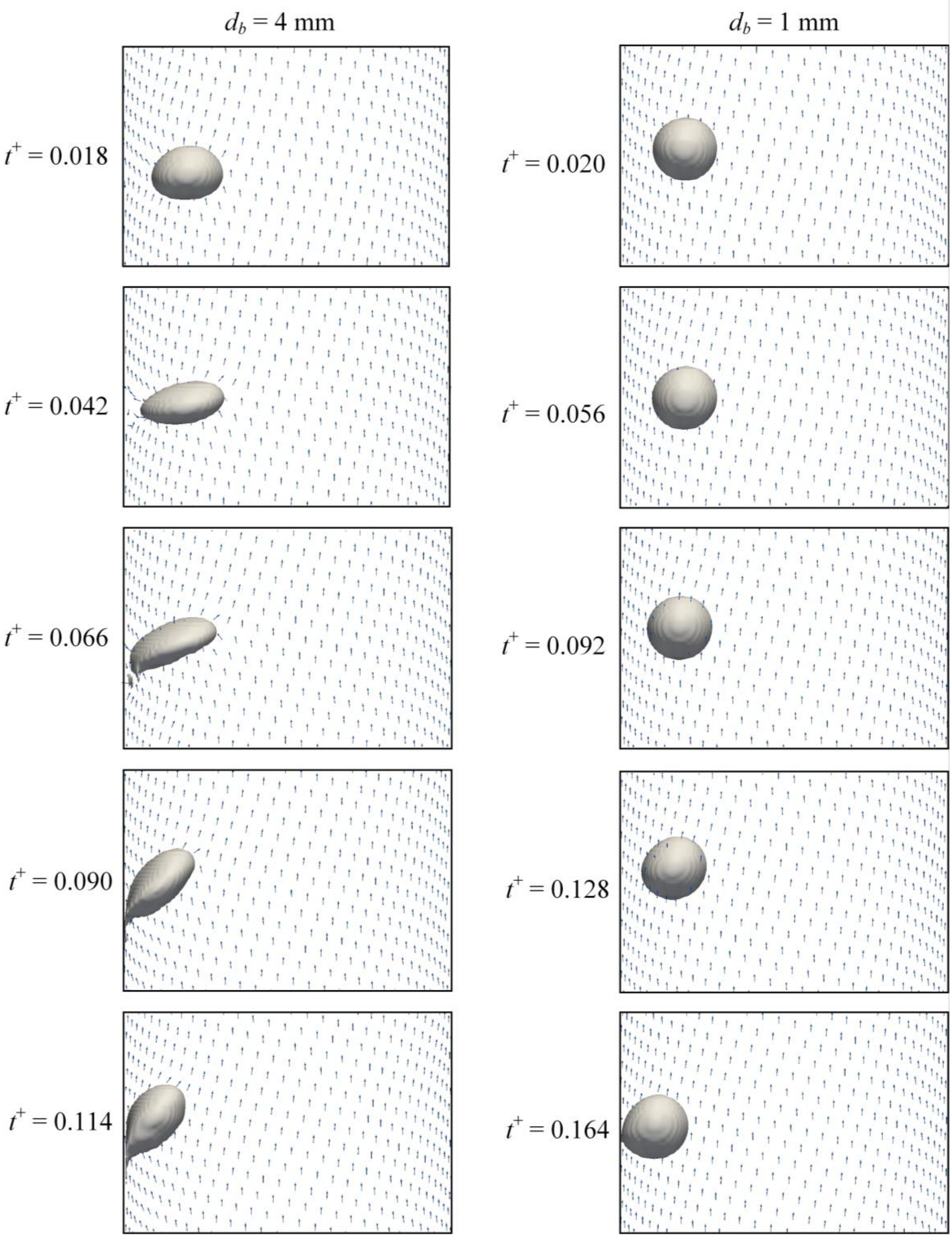

Figure 6.8 Time evolution of bubble shape and motion for bubbles of d_b = 4 mm (left) and d_b = 1 mm (right) with fluid velocity vectors.

Interestingly, a thin film of fluid is observed between the bubble and the wall after contact with the solid surface, this being particularly the case for the 4 mm bubble. This thin film creates a lubrication force that acts to move the bubble away from the wall [329], with this force being found to increase as the film becomes thinner [329]. Therefore, after the bubble collides with the wall, it may slide along the wall, bounce repeatedly off the wall, or move away from the wall [327]. To examine the bubble's behaviour after collision with the wall, the trajectories of the two bubbles considered are plotted in Figure 6.9 based on the computed bubble centre. For the case of the 1 mm bubble, Figure 6.9 shows that the bubble touches the wall later than the 4 mm bubble. The non-dimensional bubble diameter $y^* \approx 0.2$ for this case. It can be seen that after the collision, the centre of the 1 mm bubble varies in its location as it bounces off the wall, with that variation being over a relatively short distance of approximately ¼ of the bubble's radius. Eventually, however, the bubble achieves an equilibrium as the distance it bounces off the wall decays with time. This means that the 1 mm bubble effectively slides along the wall immediately after the collision. This can be attributed to the vorticial structure behind a spherical bubble which is stabilized in close proximity to the wall both at a low and high Re_B [330], making the bubble effectively slide on the non-slip wall.

A similar trend is observed for the 4 mm bubble, although deformation of the shape of the bubble contributes significantly to the oscillatory motion of its trajectory. In Figure 6.9, the 4 mm diameter bubble collides with wall at $t^+ \approx 2$ with its centre being at $y^* \approx 0.16$. As noted in Figure 6.8, the bubble is significantly deformed after contact with the wall, after which the bubble's centre moves away from the solid surface. The furthest distance from the wall that the bubble travels is around $y^* \approx 0.22$ which is approximately equal to the radius of an equivalent spherical bubble. The 4 mm bubble therefore also slides parallel to the wall as its centre maintains an approximately constant, although oscillating, distance from the surface. The surface energy of a deformable bubble results in a significant effect on the bubble's oscillation amplitude, whether the bubble is in a high-Re_B or a low-Re_B regime [331], as observed in this case.

On the other hand, recall that in the Lagrangian tracking routine, a fully elastic collision model without friction is applied. In this way, only the sign of the wall-normal direction velocity will be changed after bubble collision with the wall, whereas the other velocity components remain unchanged. However, this behaviour of bouncing after every collision with the wall is not always physically accurate. Further detailed study of bubble movement close to a wall is required in order to improve Lagrangian treatments of bubble motion, with current approaches requiring extension to handle more complex bubble-wall interactions.

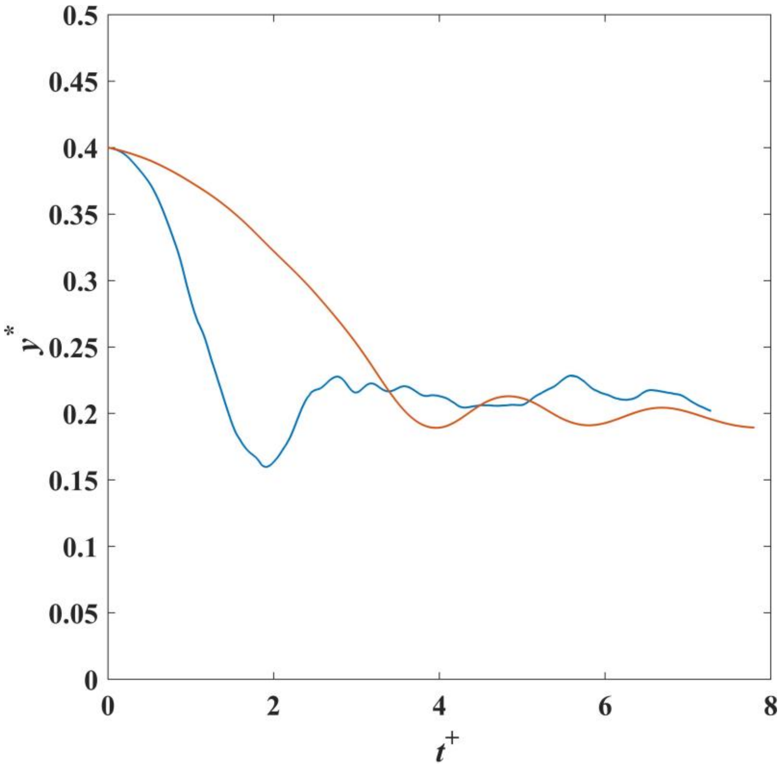

Figure 6.9 Time evolution of the distance between bubble centre and wall for bubbles of d_b = 1 mm (—) and d_b = 4 mm (—).

6.3.2 Drag coefficient and bubble shape

In this section, the simulations are used to estimate the drag coefficient and bubble shape. Recall that the drag force is the resistance force caused by the motion of the bubble through a liquid. This is usually taken as:

$$\overrightarrow{F_D} = -\frac{1}{2} C_{\mathrm{D}} A \rho_f \left|\overrightarrow{u_g} - \overrightarrow{u_f}\right| \left(\overrightarrow{u_g} - \overrightarrow{u_f}\right) \tag{6.12}$$

where A is the projected area of the bubble. The drag coefficient C_{D} can be derived from a steady state force balance in the streamwise direction, yielding a practical closure. However, the complex physics encountered due to interactions between a bubble and a solid surface in a turbulent flow, affected by the wall distance and any surface contamination [93], make drag coefficient estimation extremely difficult in the wall area [279]. Only a few studies in the literature have reported drag force determinations in such regions, which normally need very well-controlled conditions to be successful. For example, Feng and Bolotnov [319] used a proportional-integral-derivative bubble controller to fix an isolated bubble in different positions away from the wall and balance the forces acting on the bubble in every direction. Their results demonstrated that as the bubble moves towards the wall, the drag force increases. However, they limited their studies to bubbles in a laminar shear flow. In turbulent flow, the calculation is more complex, and studies in the literature are rarely seen. Despite this, Feng and Bolotnov [318] employed the same method as in [319], allowing drag and gravity/buoyancy forces to act on the bubble. However, in the present study, it is more difficult to evaluate the drag force since the bubble is moving within the flow field. For the current single bubble case studies, the 1 mm and 4 mm bubbles travel towards the wall, while the 8 mm bubble, although wobbling, remains in the middle part of the channel domain. Therefore, the focus of this section is on drag coefficient estimation for the 8 mm bubble only.

A wobbling bubble in turbulent flow exhibits a chaotic path with varying bubble velocities. For rectilinearly rising bubbles, the balance of the drag and gravity/buoyancy forces in the streamwise direction (x) can be expressed as:

$$\left(\overrightarrow{F_D} + \overrightarrow{F_G}\right)_x = 0$$
$$-\frac{1}{2}C_{\mathrm{D}}A\rho_f\left|u_g - u_f\right|\left(u_g - u_f\right) + \frac{\pi}{6}d_{eq}^3\left(\rho_f - \rho_b\right)g = 0 \tag{6.13}$$

where the projected area A can be calculated from the equivalent diameter d_{eq} [93] as:

$$d_{eq} = \sqrt[3]{d_x d_y d_z} \tag{6.14}$$

where d_x, d_y and d_z are the bubble diameter in x, y and z directions, respectively. As a result, the drag coefficient can be derived as:

$$C_{\mathrm{D}} = \frac{4d_{eq}\left(\rho_f - \rho_b\right)g}{3\rho_f\left(u_g - u_f\right)^2} \tag{6.15}$$

Due to the wobbling of a bubble in the channel, the bubble shape may exhibit different path- and/or shape-instabilities, and the averaging of Eq. (6.15) is essential to obtain the drag coefficient. Basically, there are two ways to do this time averaging. One can take advantage of the mean of $(u_g - u_f)^2$ by either averaging $(u_g - u_f)$ or $(u_g - u_f)^2$ over all time steps. Using this method, the difference in averaging $(u_g - u_f)$ or $(u_g - u_f)^2$ was found to be very small (< 0.5%) [93]. Alternatively, C_{D} can be averaged from all computed instantaneous C_{D} for each time step, and this is employed in presented study. Literature results using both methods have shown only minor differences [332].

The aspect ratio (E) of the bubble is a crucial parameter used to characterize the bubble shape. The expression for E is given by:

$$E = \frac{d_v}{d_h} = \frac{d_x}{\sqrt{d_y d_z}} \tag{6.16}$$

where d_v and d_h are the lengths of the vertical and horizontal axes.

A spherical 8 mm diameter air bubble was introduced into a single-phase flow at time zero and placed horizontally in the centre and vertically at the bottom of the computational domain. Note that the effect of the initial bubble shape, e.g. a sphere or an ellipsoid, is not examined in the present study as it has been found to have no effect on the final bubble shape [93]. Figure 6.10(a), (b) and (c) plot the time evolution of the bubble's centroid in the streamwise (x), wall-normal (y) and spanwise (z) directions starting from $x_b^* = 0.3$, $y_b^* = 1$ and $z_b^* = \pi$. The bubble was injected with the same velocity as the fluid, so that the instantaneous slip velocity of the bubble was zero at the start of the simulation. After injection, the bubble is pushed by the upward flow and, due to buoyancy, eventually travels faster than the surrounding fluid. As seen in Figure 6.10(d), the slip velocity, i.e. the bubble velocity minus the fluid velocity, increases rapidly and, in a very short time, achieves a steady-state terminal velocity at around $t^+ = 0.1$ ($t = 0.266$ s). After $\Delta t^+ = 0.23$, the bubble has traversed one channel length. Due to the periodic condition in the streamwise direction, the bubble was then placed back at the bottom of the channel, as indicated in Figure 6.10(a). To allow a sufficient time interval for averaging, the bubble was allowed to pass four times through the channel, taking a total time $\Delta t^+ = 0.936$. During this time period, the bubble's path is also described using the bubble positions in the y and z directions, as plotted in Figure 6.10(b) and (c). It is found the oscillations in the z direction are much smaller than in the y direction. Therefore, this only slight zigzagging of the bubble in the channel central region fulfils the above rectilinear trajectory assumption used in Eq. (6.15).

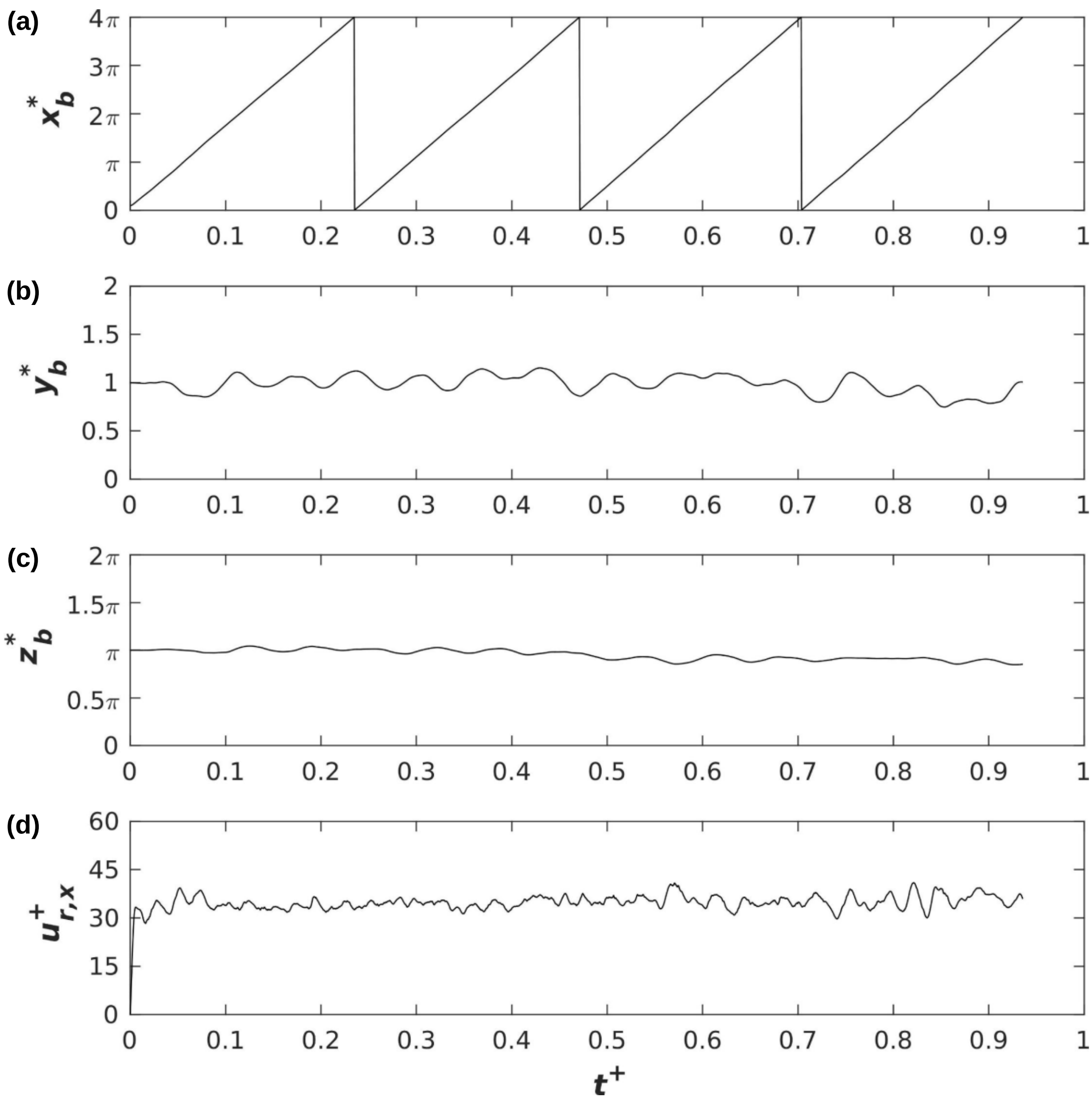

Figure 6.10 Time evolution of 8mm bubble position (a - c) and slip velocity (d).

Figure 6.11(a), (b) and (c) show plots of the bubble volume, drag coefficient and aspect ratio, respectively, versus time in this same time period. The instantaneous bubble volume is observed to be decreasing with the time in Figure 6.11(a). This small volume loss is often encountered in VOF advection because of small overshoots or undershoots during the advection steps [246]. The influence of this volume loss on the estimation of the drag coefficient and aspect ratio needs to be considered. In Figure 6.11(b), the predicted drag coefficient versus time is plotted, with values whose magnitude is much larger than the average, caused by the low slip velocity at the beginning of the simulation, excluded. It is seen that after a small time period (Δt = 0.266 s) as the bubble achieves its terminal velocity, the bubble reaches a steady-state shape (Figure 6.11 (c)) and drag force, although with periodic fluctuations about the mean. Following this initial period, the bubble starts wobbling in the channel, and averaging of the drag coefficient and aspect ratio began until the end of four passes through the channel by the bubble. It is clear that the predicted drag coefficient does decrease slightly with time due to the bubble's volume loss, although the decrease is small, with no equivalent decrease noted in the bubble aspect ratio. As a consequence, the mean drag coefficient was determined as noted and for the 8mm bubble in water was found to be 1.92, with the mean aspect ratio 0.44. Also, the mean equivalent diameter of the 8 mm bubble was calculated as 10.03 mm. From Figure 6.10(b), the average non-dimensional streamwise terminal velocity can be calculated as 34.88, corresponding to 0.262 m s^{-1}. Accordingly, the mean bubble Reynolds number is 2616. Zhou et al. [333] summarized existing drag coefficient correlations in the literature for a wide range of conditions. However, correlations that cover an 8 mm diameter air bubble in water with a bubble Reynolds number greater than 2500 are limited. The only applicable correlations are by Tomiyama et al. [316] and Dijkhuizen et al. [93], which are compared with the present result in Table 6.3. It is found that the present drag coefficient is slightly higher than these literature correlations. Interestingly, the result from Dijkhuizen et al. [93] is found to be slightly higher than that from Tomiyama et al. [316]. Dijkhuizen et al. [93] proposed the correlation of Eq. (6.4) for air bubbles in water which generally predicts values lower than Tomiyama et al. [316]. However, the experiments considered in [93] were limited to $Re_B \ll 1600$. For the present high Re_B, Dijkhuizen et al. [10] failed to compare their predictions with those of Tomiyama et al. [8]. As a result, in this study at least, a higher drag coefficient is found using the correlation of Dijkhuizen et al. [93]. The relative error between the present drag coefficient value and those from the correlations of Dijkhuizen et al. [93] and Tomiyama et al. [316] is 1.0 % and 5.4 %, respectively.

Table 6.3 Comparison of drag coefficient between present work and literature correlations.

Reference	Drag coefficient
Tomiyama et al. [316]	1.82
Dijkhuizen et al. [93]	1.90
Present DNS	1.92

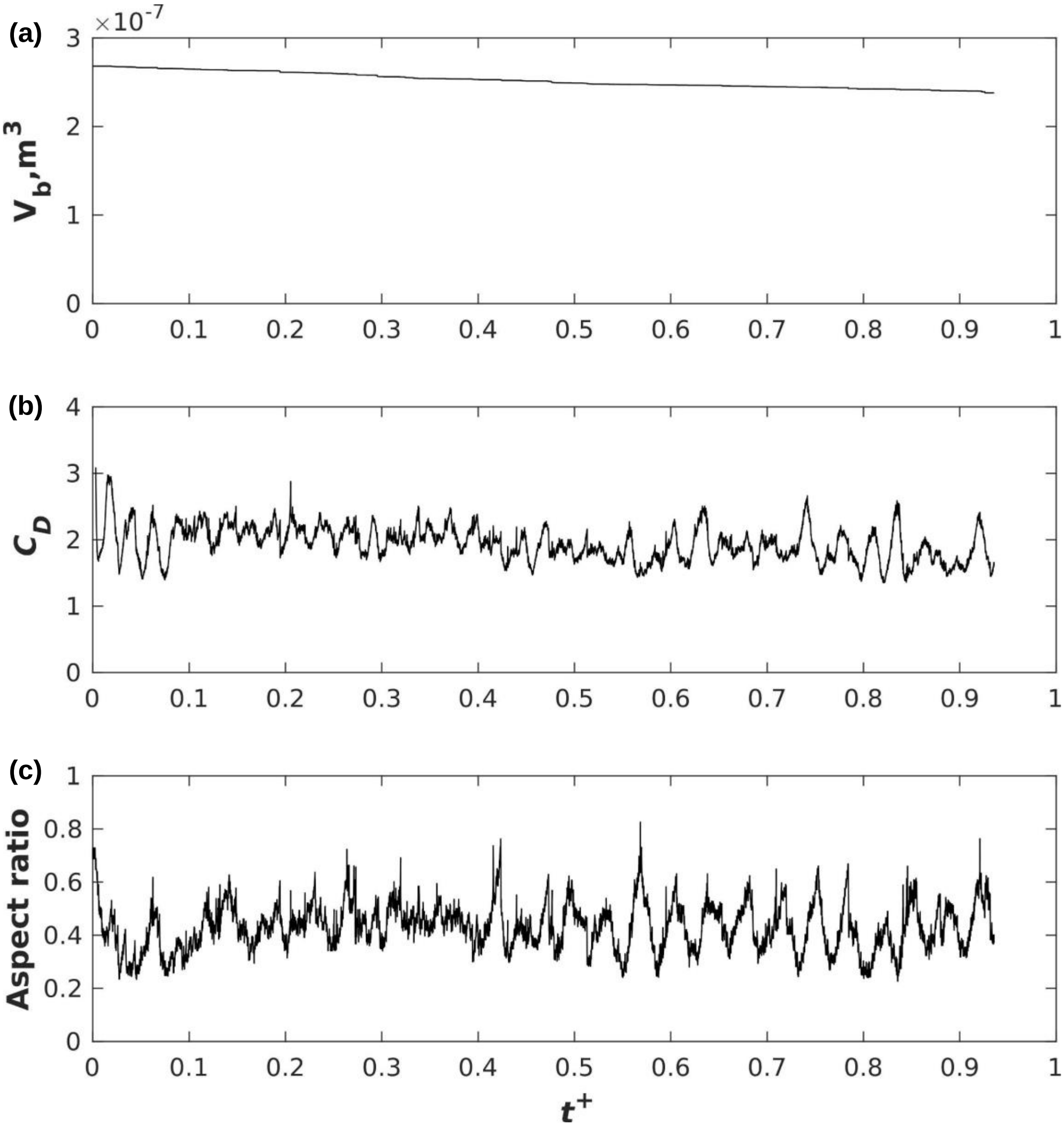

Figure 6.11 Time evolution of (a) bubble volume, (b) drag coefficient and (c) aspect ratio.

During the bubble's four passes through the channel, the volume loss was around 11 %. To check the influence of this volume loss on the predicted drag coefficient, the averaging process was repeated up to $t^+ = 0.4$ during which time a reduced volume loss of 5 % occurred. After calculation, the average drag coefficient has a value of 2.08 which has a relative error of 9.7 % with the correlation of Dijkhuizen et al. [93], and 14.43 % with that of Tomiyama et al. [316]. In contrast, this reduced volume does not significantly change the predicted mean aspect ratio (0.45) or the mean equivalent diameter (10.36 mm).

For both averaging approaches noted above, a slight overestimation of the drag coefficient is observed relative to accepted correlations. This small difference is likely caused by an overestimation of the equivalent bubble diameter. In the present study, the predicted aspect ratio (about 0.44) is slightly lower than that (about 0.56) of Dijkhuizen et al. [93]. In Eq. (6.16), therefore, a smaller equivalent bubble diameter in the vertical direction is produced and larger diameters are found in the other two directions. The discrepancy in the bubble shape aspect ratio suggests further investigation is desirable of the grid dependency of the equivalent bubble diameter and therefore the predicted drag coefficient. Despite this error, it can be concluded that the method implemented in this study is reasonably accurate, and provides a reliable method for drag coefficient determination. Further studies for different bubble diameters and locations in a channel would be useful in helping to improve the Lagrangian point tracking model, although the bubble volume loss produced by the VOF approach needs to be addressed.

6.3.3 Bubble-induced turbulence

As is widely known, the presence of a deformable bubble in a fluid flow introduces additional turbulent eddies and enhances turbulence in the bubble wake region, i.e. bubble-induced turbulence (BIT) occurs. Therefore, in this section, the results of a BIT analysis of the simulations are discussed in terms of time-averaged phase velocities and the rms of the fluctuating velocities, in addition to the turbulence kinetic energy (TKE). The results were obtained using the predictions described in Section 6.3.1. More specifically, the analysis of three simulations of 1 mm, 4 mm and 8 mm diameter bubbles in a vertical channel upflow are presented. Recall that the bubble distribution observed earlier is that the small bubbles (d_b = 1 mm or 4 mm) slide along the channel wall whilst the large bubble (d_b = 8 mm) rises in the channel centre region. During the simulations, the large bubble firstly achieves a terminal shape, i.e. a quasi-steady state form, after which the simulation was continued to give sufficient information to allow the derivation of time-averaged statistics. The small bubble cases were originally injected in the channel centre after which they migrate to the wall. Therefore, time-averaging is started once they have moved to the wall.

6.3.3.1 Case I: d_b = 8 mm

The first case is the simulation of an 8 mm bubble in the upward channel flow. Figure 6.12 shows the average void fraction (α) profile (black solid line) versus the non-dimensional cross-channel coordinate. The void fraction was averaged over planes parallel to the channel walls for the time interval $\Delta t^+ = 1$ after the bubble achieves its steady state shape. It is seen the void fraction varies over a region that is approximately twice the bubble diameter over which the bubble wobbles, with the peak of the void fraction very close to the channel centre. Due to only one bubble being in the domain, zero void fraction is observed towards the wall area where the bubble does not travel. In Figure 6.12, the quantities describing the turbulent flow include the non-dimensional streamwise ($u'^{+}_{x,rms}$), wall-normal ($u'^{+}_{y,rms}$) and spanwise ($u'^{+}_{z,rms}$) rms of the velocity fluctuations, the shear stress ($u'^{+}_{x}u'^{+}_{y}$), the turbulence kinetic energy (k) and streamwise velocity for both the bubbly flow (red dashed line) and single-phase flow (red solid line). The velocity and void fraction averaging were performed in a consistent way with Eqs. (6.10) and (6.11). During this averaging time period, the bubble travels three passes through in the channel.

Generally, in Figure 6.12(a), the rms of the streamwise velocity fluctuations is enhanced in the bubbly flow when compared with the single-phase flow, as expected in upflow with a deformable bubble [99]. The trend in the bubbly flow values near the channel walls is qualitatively similar to the single-phase case, but higher peak fluctuations are found in the bubbly flow. In the channel centre region where the bubble is present, however, the velocity fluctuations are dramatically increased by the bubble. This induced enhancement is also observed in the wall-normal (see Figure 6.12(b)) and spanwise (see Figure 6.12(c)) directions, in these cases with the peak being in the channel centre. At the centre of the channel, the rms velocities in the streamwise direction are significantly higher than for the wall-normal and spanwise components, with the latter being almost the same. The streamwise rms is therefore approximately 1.6 - 1.7 times larger than the other two components which reflects anisotropy in the bubbly flow [321]. It is also interesting to note that the presence of a highly deformable bubble means that peak turbulence levels are not necessarily encountered near the walls, as they do for the single-phase flow.

Due to the wobbling pathway of the deformable bubble in the channel centre and the short averaging time employed, the axis of symmetry of the void fraction profile is slightly shifted from the channel centre ($y^* = 0$) to the left in the plots. Note that the present results were not derived in line with other literature studies (e.g. [99]) which forced such profiles to be symmetric on the left and right hand sides of the channel. This results in an asymmetry in all the rms velocity plots with more enhanced in regions towards the left channel wall, this being especially the case for the streamwise rms in Figure 6.12(a). For the shear stress plot in Figure 6.12(d), a linear variation across the middle of the channel is seen for both single- and multi-phase cases. However, a greater slope in this region is observed in the bubbly flow. For the bubbly flow, the deformable bubble travels in the channel centre region resulting in a lighter mixture. Therefore, a stronger driving force is required in the channel centre than in the wall area. Because of the change in turbulent stresses which must balance the driving force, as a result, the slope of the shear stress in the channel centre is higher than for the single-phase case.

In Figure 6.12(e), it is found the large bubble significantly alters the turbulence kinetic energy profile compared with the single-phase case, and the enhancement in the kinetic energy occurs almost everywhere across the channel. This can be explained by the presence of turbulent fluctuations in the bubble wake, as seen in Figure 6.7. The bubble therefore generates turbulence not only directly behind its location but also in regions where the bubble never travels due to the expanding wake. Interestingly, the profile of the TKE is enhanced more by the presence of the bubble in the channel centre than in the study by Bolotnov et al. [101]. However, due to the very small void fraction associated with only one relatively small bubble in the channel, the streamwise velocity is not obviously altered in Figure 6.12(f).

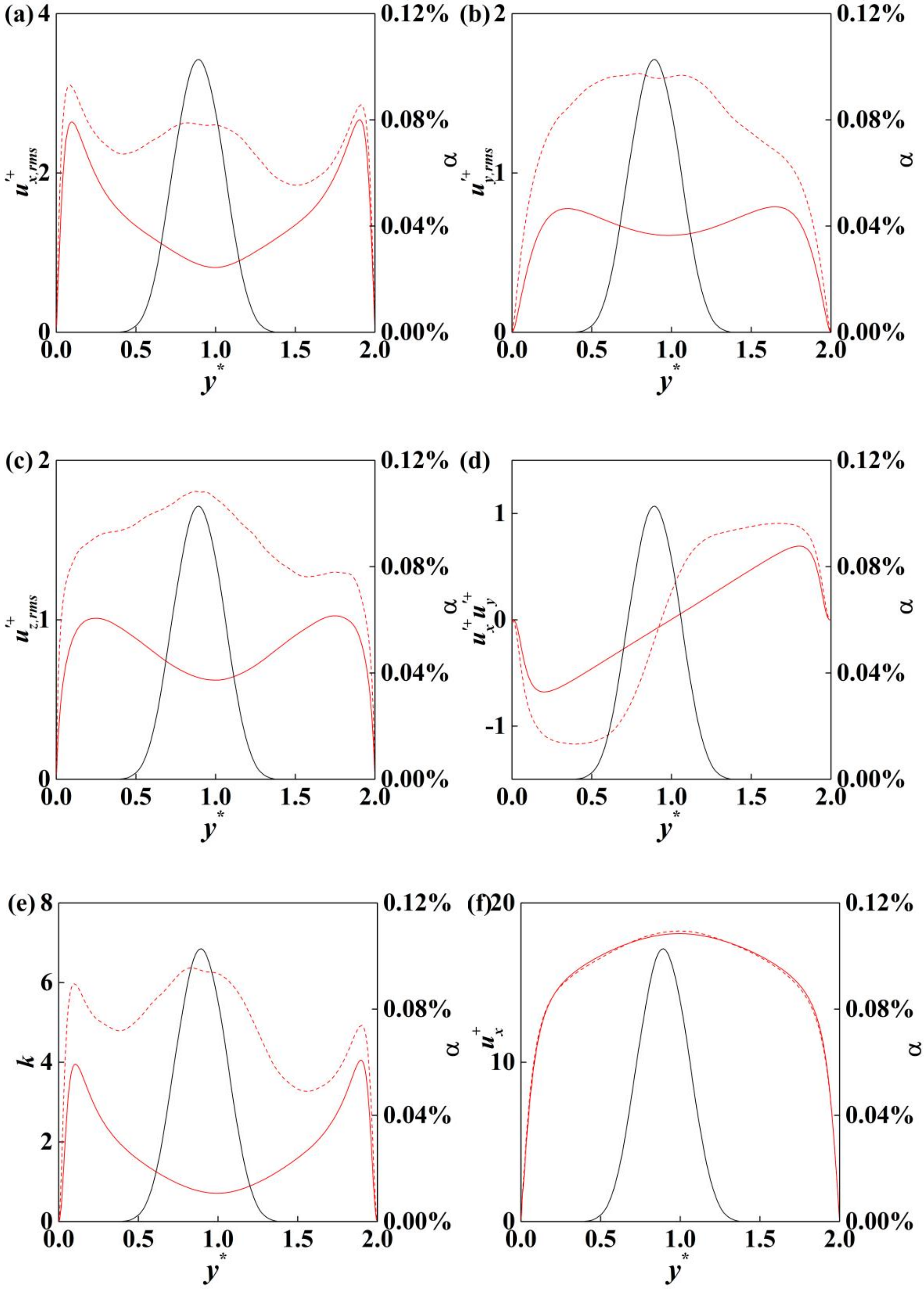

Figure 6.12 Comparison of continuous phase results in DNS of upflow at Re_τ = 150 with one bubble of d_b = 8 mm. Multi-phase (---) and single-phase (—) normal and shear stresses, turbulence kinetic energy, and streamwise velocity and (—) void fraction. (a) Non-dimensional streamwise ($u'^{+}_{x,rms}$) rms of velocity fluctuations, (b) non-dimensional

wall-normal ($u'^{+}_{y,rms}$) rms of velocity fluctuations, (c) non-dimensional spanwise ($u'^{+}_{z,rms}$) rms of velocity fluctuations, (d) shear stress ($u'^{+}_{x}u'^{+}_{y}$),(e) turbulence kinetic energy and (f) non-dimensional streamwise velocity (u^{+}_{x}).

As noted in Figure 6.7, the 8 mm bubble generates a significant effect on the fluid flow and its turbulence over a large portion of the computational domain. Therefore, it is meaningful to perform an additional study to address the influence of a single bubble in the channel on the fluid in its wake region. To this end, an analysis was performed along five lines in the wall-normal direction at different distances behind the bubble and the average quantities were captured and compared with single-phase quantities to evaluate the bubble-induced turbulence. Specifically, five lines behind the 8 mm bubble with distances from the notional bubble centre of 2 d_b, 4 d_b, 6 d_b, 8 d_b and 10 d_b (where d_b = 8 mm) were considered. The position of these lines was automatically adjusted in the wake region as the bubble rose in the channel, maintaining their fixed distance from the bubble centre. Fluid flow quantities, such as the fluid mean velocity, the rms of the velocity fluctuations and the shear stress, were recorded along each line at every timestep and averaged over a time interval. The averaging time interval is consistent with Figure 6.12 to avoid further volume loss.

Figure 6.13 plots the mean streamwise fluid velocity versus the wall-normal coordinate for all lines and compares them with the single-phase case. Due to the short averaging time period, the fluid velocity profiles are not as smooth as for the single-phase, especially for the first three locations behind the bubble which are significantly affected by the lack of averaging. However, it is clear that compared with the case without the bubble, the first location at a distance of 2 d_b from the bubble centre shows a large increase in the streamwise mean velocity, with this enhancement being reduced as the distance behind the bubble increases. In the far field region, the influence of the bubble is reduced to be almost the same along the lines at 8 d_b and 10 d_b, although even at these locations it is still significant compared with the single-phase flow.

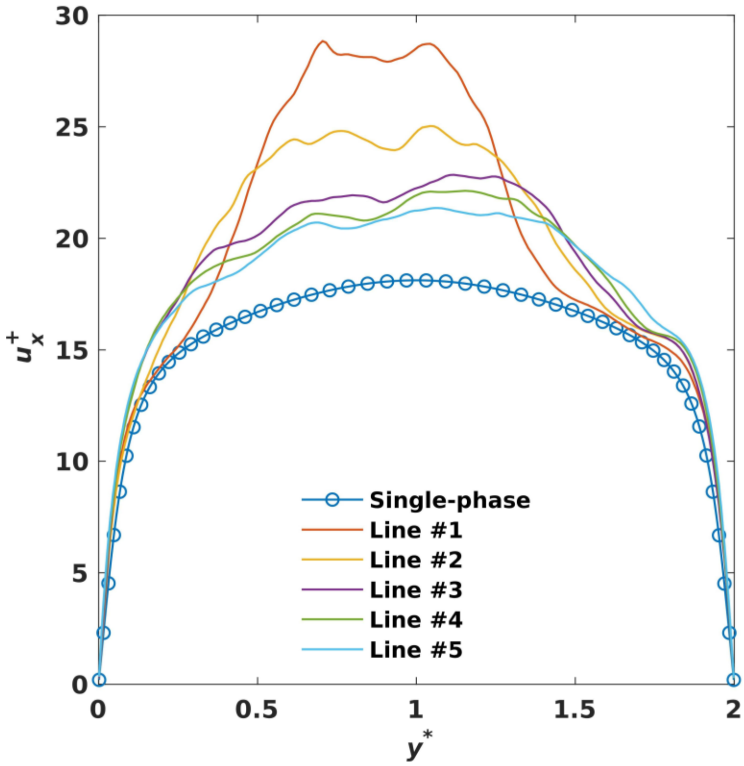

Figure 6.13 Comparison of mean streamwise fluid velocity (u_x^+) for single-phase flow and at locations behind the d_b = 8 mm bubble, with distances to the bubble centre of 2 d_b (Line #1), 4 d_b (Line #2), 6 d_b (Line #3), 8 d_b (Line #4) and 10 d_b (Line #5).

This enhancement is also found for the normal and shear stresses behind the bubble, as presented in Figure 6.14. Figure 6.14(a) givens the rms of streamwise fluid velocity fluctuations. It is seen that the bubble introduces additional fluctuations along all lines in the bubble wake region which again reduce with increasing distance from the bubble centre. In line with results for the mean velocity, at the two locations furthest from the bubble centre (i.e. Lines #4 and #5), nearly the same increase is found in this normal stress, and it might be expected that the shape and magnitude of results at these two locations would overlap after a sufficiently long averaging time. These comments also apply to results in the wall-normal and spanwise directions, shown in Figure 6.14(b) and (c), with significant enhancement observed along the first three lines behind the bubble. A similar trend is also observed for the shear stress in Figure 6.14(d). Therefore, it can be concluded that the effect of an 8 mm bubble on the fluid turbulence has a transition regime in the wake region within a length corresponding to approximately 8 d_b from the bubble centre.

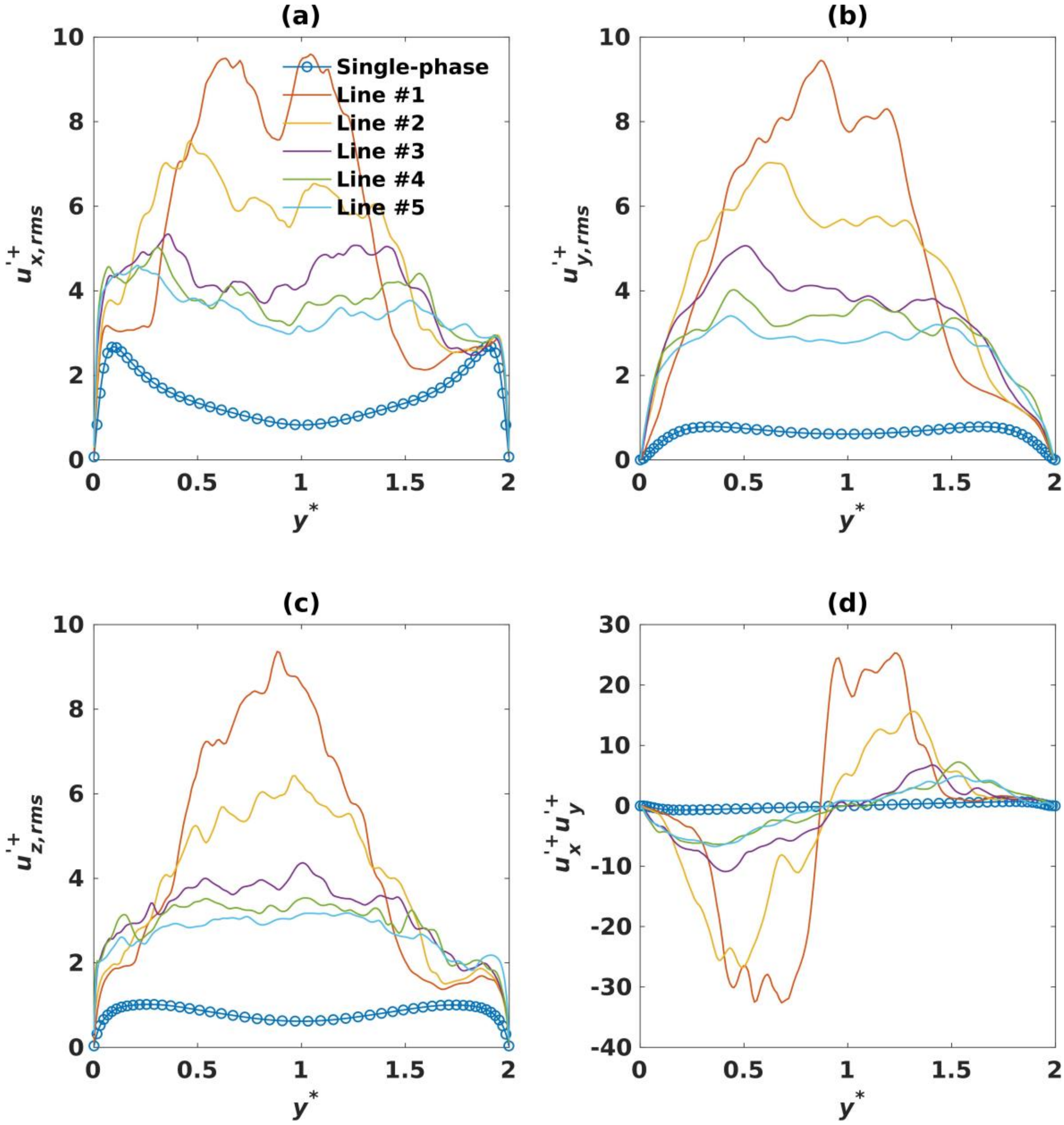

Figure 6.14 Comparison of normal and shear stresses for single-phase flow and at locations behind the d_b = 8 mm bubble, with distances to the bubble centre of 2 d_b (Line #1), 4 d_b (Line #2), 6 d_b (Line #3), 8 d_b (Line #4) and 10 d_b (Line #5). (a) Non-dimensional rms of streamwise velocity fluctuations ($u'^{+}_{x,rms}$), (b) non-dimensional rms of wall-normal velocity fluctuations ($u'^{+}_{y,rms}$), (c) non-dimensional rms of spanwise velocity fluctuations ($u'^{+}_{z,rms}$) and (d) shear stress ($u'^{+}_{x}u'^{+}_{y}$).

6.3.3.2 Case II: d_b = 4 mm

Compared with the 8 mm bubble, the 4 mm bubble exhibits less deformability. The simulation results were analysed and are plotted in the same way as for the 8 mm bubble in Figure 6.15. The average void fraction profile across the channel shows that, for this spheroidal bubble, the range of the profile extends over a region of about 1.2 bubble diameters in the vicinity of the bubble which is sliding along the left channel wall. In each subplot of Figure 6.15, the streamwise, wall-normal and spanwise rms of velocity fluctuations, the shear stress and TKE for this case, with and without the bubble present, are shown. Generally, the bubble-induced turbulence decreases as the bubble becomes less deformable. Compared with the 8 mm bubble, the enhancement of the rms of fluctuating velocities and the shear stress is obviously seen to decrease in Figure 6.15. More specifically, the rms of velocity fluctuations in all directions, see Figure 6.15(a), (b) and (c), are enhanced in the wall region where the bubble is present, while the profiles over the rest of the domain remain consistent with single-phase predictions, although some slight differences with the latter are apparent, most likely due to the short averaging time period. That said, the TKE profile of the bubbly flow in Figure 6.15(e) is clearly higher in the wall region than that of the single-phase as it is computed from the rms velocities in all directions. However, in Figure 6.15(d) and (f), there is no obvious difference between the patterns of shear stress and streamwise velocity with and without the bubble. Therefore, it can be concluded that the presence of a 4 mm bubble has an impact on the carrier phase, but only slight.

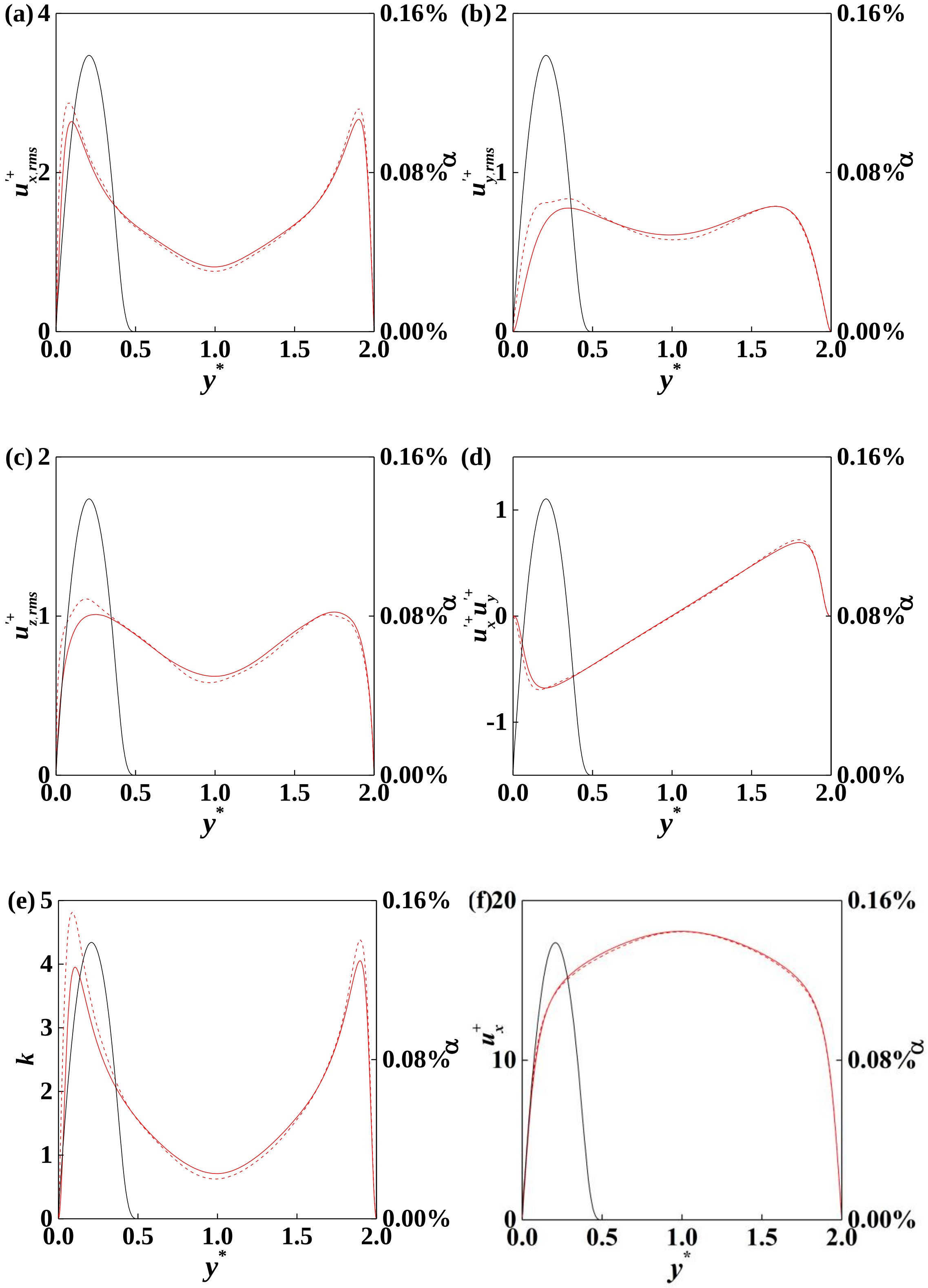

Figure 6.15 Comparison of continuous phase results in DNS of upflow at Re_τ = 150 with one bubble of d_b = 4 mm. Multi-phase (---) and single-phase (—) normal and shear stresses, turbulence kinetic energy, and streamwise velocity and (—) void fraction. (a) Non-dimensional streamwise ($u'^{+}_{x,rms}$) rms of velocity fluctuations, (b) non-dimensional

wall-normal ($u'^{+}_{y,rms}$) rms of velocity fluctuations, (c) non-dimensional spanwise ($u'^{+}_{z,rms}$) rms of velocity fluctuations, (d) shear stress ($u'^{+}_{x}u'^{+}_{y}$), (e) turbulence kinetic energy and (f) streamwise velocity (u^{+}_{x}).

6.3.3.3 Case III: d_b = 1 mm

For the case with a 1 mm bubble, the results are presented in the same way in Figure 6.16. For this nearly spherical bubble, the lateral void fraction distribution shows a thickness of one bubble diameter at the left wall and this is slightly less than for the 4 mm bubble case. However, the profiles of the rms of velocity fluctuations in all directions, the shear stress and the TKE in Figure 6.16 show clearly that no significant effect is found on the continuous phase by the 1 mm bubble in the present channel domain, with any differences with the single-phase results only small and again likely due to the short averaging time period employed.

Considering the results obtained for all bubble sizes, it can again be concluded that the method implemented in this study provides a useful means for evaluating bubble-induced turbulence in bubbly flows. Further studies for different bubble diameters and locations in a channel would be useful, and clearly longer averaging times need to be used to increase the reliability of the results.

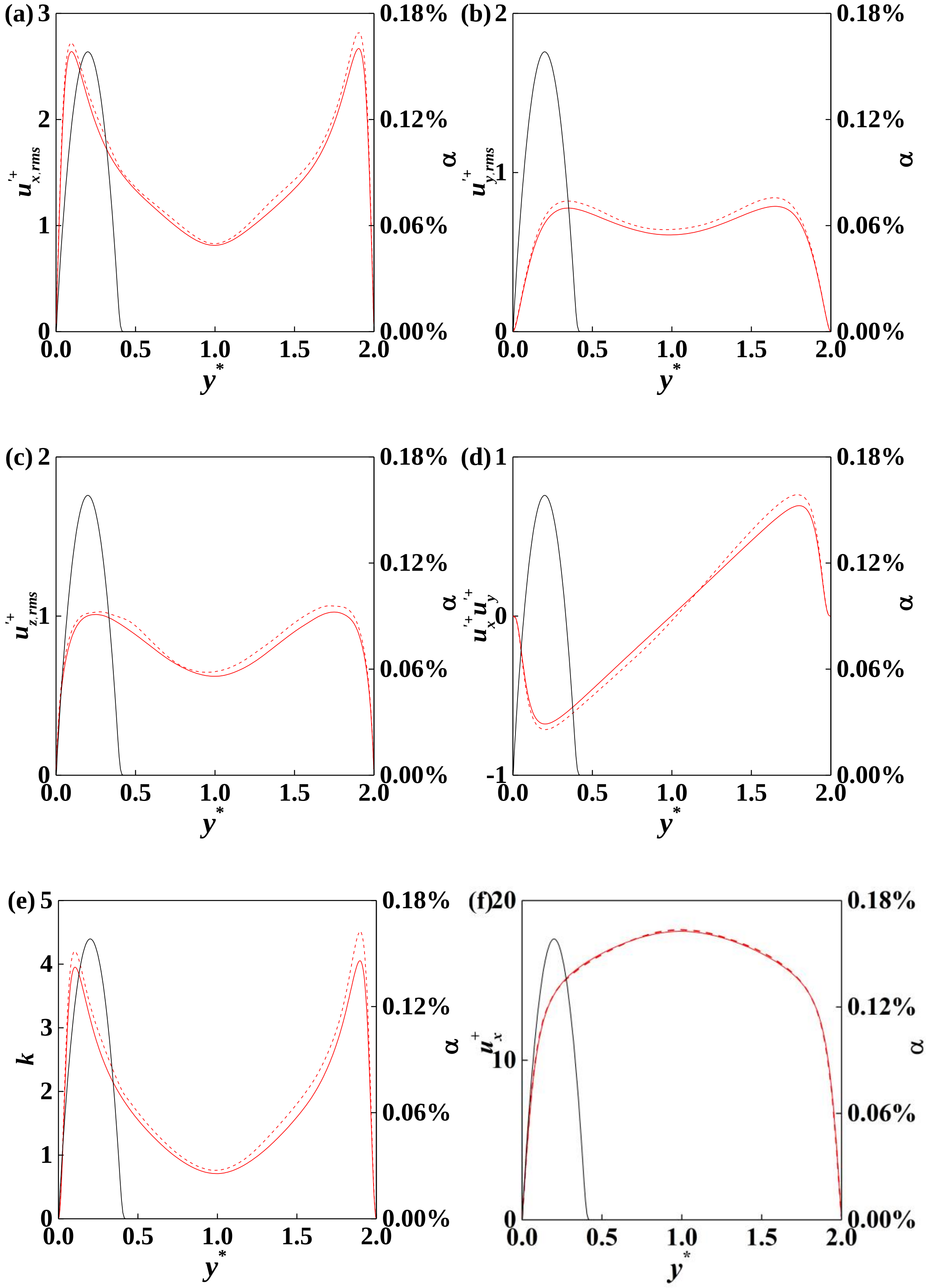

Figure 6.16 Comparison of continuous phase results in DNS of upflow at Re_τ = 150 with one bubble of d_b = 1 mm. Multi-phase (---) and single-phase (—) normal and shear stresses, turbulence kinetic energy, and streamwise velocity and (—) void fraction. (a) Non-dimensional streamwise ($u'^{+}_{x,rms}$) rms of velocity fluctuations, (b) non-dimensional

wall-normal ($u'^{+}_{y,rms}$) rms of velocity fluctuations, (c) non-dimensional spanwise ($u'^{+}_{z,rms}$) rms of velocity fluctuations, (d) shear stress ($u'^{+}_{x}u'^{+}_{y}$), (e) turbulence kinetic energy and (f) streamwise velocity (u^{+}_{x}).

6.4 Multiple bubbles case study

In this section, the results of a simulation of deformable bubble swarms are discussed. The focus of the present study is on the bubble-liquid interaction and bubble clustering. The characteristic parameters of the two-phase flow are introduced first. The simulation was carried out in the same channel with the same Reynolds number as in previous sections. The characteristic parameters of the two phases were consistent with those of Section 6.3 in Table 6.2. The bubble size of interest is d_b = 4 mm which as noted in Section 6.3.1 drifts towards the wall in upflow. The reason for the choice of this bubble size, on the one hand, is due to its higher bubble deformability than the studies [115, 322] of bubble clustering in the literature. For example, Santarelli and Fröhlich [115] simulated nearly spherical bubbles in a channel flow with a realistic value of *Eo* = 0.3 for 1 mm bubbles in contaminated water, and even more recently, Cifani et al. [322] performed bubble swarms of nearly spherical/ellipsoidal bubbles with *Eo* = 0.67. On the other hand, a 4 mm diameter bubble is close to the critical bubble diameter which causes changes in bubble lateral motion in air-water upflows (5 - 6 mm in Liu [334], and 4.5 mm in Lu and Tryggvason [99]). Therefore, it is worth investigating the dynamics of such turbulent bubbly flows. Due to the specific bubble lateral movement pattern of 4 mm bubbles, a downflow was employed in the present study so that a sufficient number of bubble-bubble interactions in the core region of the flow could be recorded. Therefore, gravity was switched to point downwards aligning with the streamwise flow direction and the bubbles flow relative to the fluid. A multiple-marker method was employed to avoid bubble coalescence as described in Chapter 3. Two simulations of bubbly flows were performed on the same steady state single-phase flow field. The main difference was the number of bubbles in each case which were selected as 240 and 480, corresponding to a void fraction α = 5.1% and 10.2%, respectively. These will be referred in the text below as dilute and dense swarms, respectively. The simulations reported in this section were performed with a constant flow rate to maintain consistency with other literature studies [98, 115, 322]. For this purpose, the instantaneous pressure gradient along the channel was adjusted at every time step. The initial spherical bubbles were randomly injected into the well-developed single-phase flow, after which they flow with the fluid and gradually deform until they reach a statistical steady state. The time- and space-averaged statistics, such as void fraction distribution and streamwise velocity for the fluid phase were computed using Eqs. (6.10) and (6.11). The bubble clustering and preferential alignment were analysed by evaluating the bubble pair correlation function.

6.4.1 Fluid and bubble phase characteristics

For the dilute swarm with void fraction 5.1%, the time evolution of each bubble's centroid in the streamwise (*x*), wall-normal (*y*) and spanwise (*z*) directions is plotted in Figure 6.17 versus time after injection. Due to the periodic condition in the streamwise and spanwise directions, the bubbles were then placed back into the channel on exiting those boundaries, as indicated by some vertical lines in Figure 6.17(a) and (c). It can be seen that the bubbles move significantly in the spanwise and wall-normal directions whilst travelling with the flow. The same plot is made for the dense swarm with void fraction 10.2% in Figure 6.18. In the wall-normal direction, few bubbles are observed near both walls in both swarms. It should be noted that the 4 mm bubbles in downflow travel very slowly in the streamwise direction, as indicated by t^+ values in Figure 6.17(a) and Figure 6.18(a). For example, the simulation of the dilute bubble swarm was performed over a run time of 384 hours to progress 1,148,432 time steps using 64 processes on ARC4, a high perform computing facility at the University of Leeds. Several passes of the bubbles through the channel would have taken several months to compute.

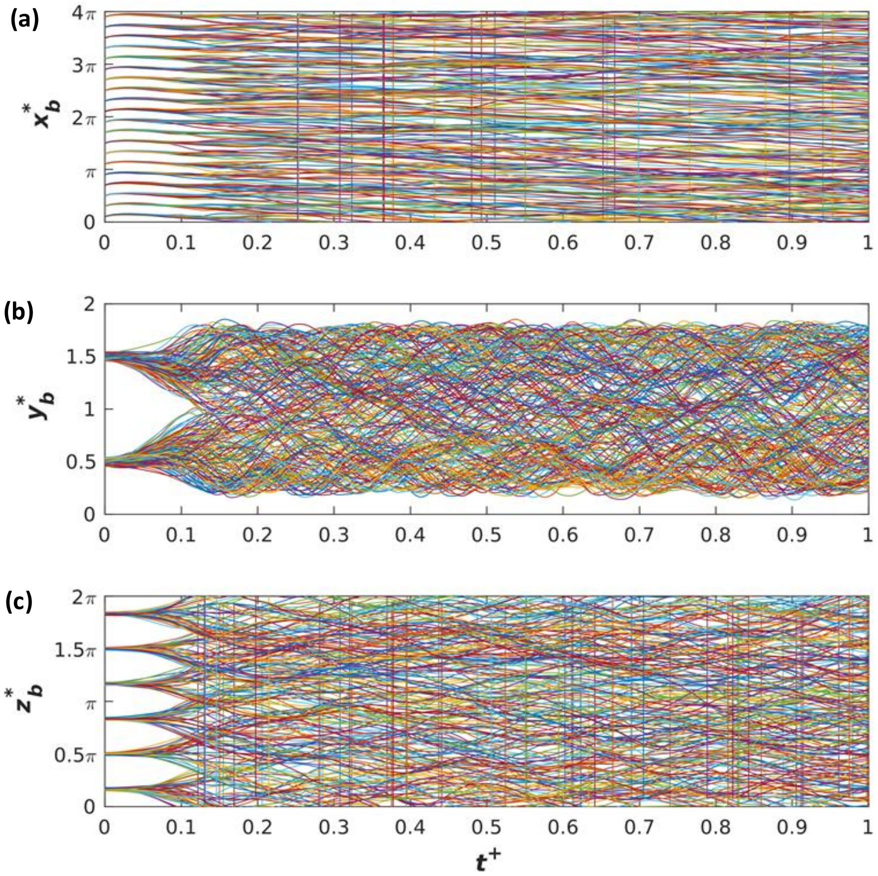

Figure 6.17 Time evolution of bubble positions in a dilute swarm with void fraction 5.1%. (a) Streamwise; (b) wall-normal; and (c) spanwise directions.

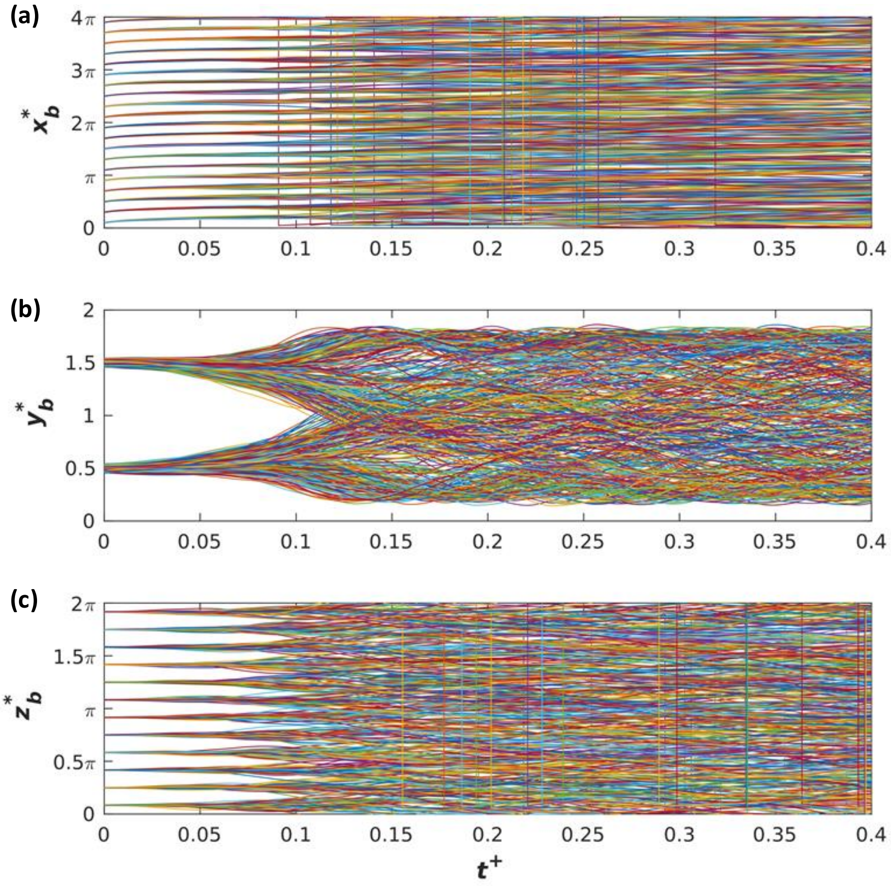

Figure 6.18 Time evolution of bubble positions in a dense swarm with void fraction 10.2%. (a) Streamwise; (b) wall-normal; and (c) spanwise directions.

To quantify the distribution of the bubble phase and the fluid statistics, the mean void fraction and mean liquid streamwise velocity profiles across the wall-normal coordinate were averaged. The time interval for the dilute swarm was taken from the time $t^+ = 0.25$ until the end of simulation at $t^+ = 1.0$, and $\Delta t^+ = 0.15 – 0.4$ was used for dense swarm. In Figure 6.19(a), the averaged results for the void fraction profiles for both swarms are plotted across the wall-normal coordinate. Generally, the bubbles in both swarms are seen preferentially rising in the core region of the channel ($\sim 0.3 \leq y^* \leq \sim 1.8$). Although the plot has not been forced to average over the left and the right hand sides of the channel as in some literature studies (e.g. [99]), symmetric profiles are observed for both cases. In the channel centre region ($0.6 \leq y^* \leq 1.4$), the void fraction is nearly constant in both swarms and this feature is consistent with literature channel studies of downflow with less deformable bubbles [95, 96, 322]. Approaching the walls, a peak in the void fraction is seen, this being most clearly observable in the higher void fraction case. The characteristic peak is observed not only in the DNS works of less deformable bubbly flows by Lu and

Tryggvason [95] with α = 6%, and by Cifani et al. [322] with α = 10%, but also in experiments [152]. This is most likely due to the high void fraction in the domain [152]. In the very near-wall region, the void fraction decreases until it reduces to zero at the wall. In the present work, however, a nearly bubble-free near-wall region is not observed. Under the present circumstance of higher bubble deformability than in other literature studies [95, 322], some bubbles migrate to the walls first but then they move back towards the central channel region, although the latter was a very slow process. The transitional motion of the bubbles to hydrostatic equilibrium therefore precludes bubble-free region in the present study.

In Figure 6.19(b), averaged results for the non-dimensional continuous phase streamwise velocity for both cases are plotted in the same way, and compared with the single-phase case. Unlike the velocity profile in the single-phase flow, the mean velocity of the bubbly flows generally shows a uniform distribution in the channel centre region where the mean shear becomes nearly zero at equilibrium [95]. Due to the effect of bubbles in the centre region, a reduction of the velocity magnitude is observed, this being most obvious for the dense swarm. Away from the centre and towards the walls, a peak in the fluid velocity is observed in both near-wall regions as the presence of the bubbles there results in higher gradients in the fluid. However, after the transitional motion of the bubbles to a steady-state, the peak in the fluid velocity profile is expected to be lower. This was confirmed at later simulation times (not shown).

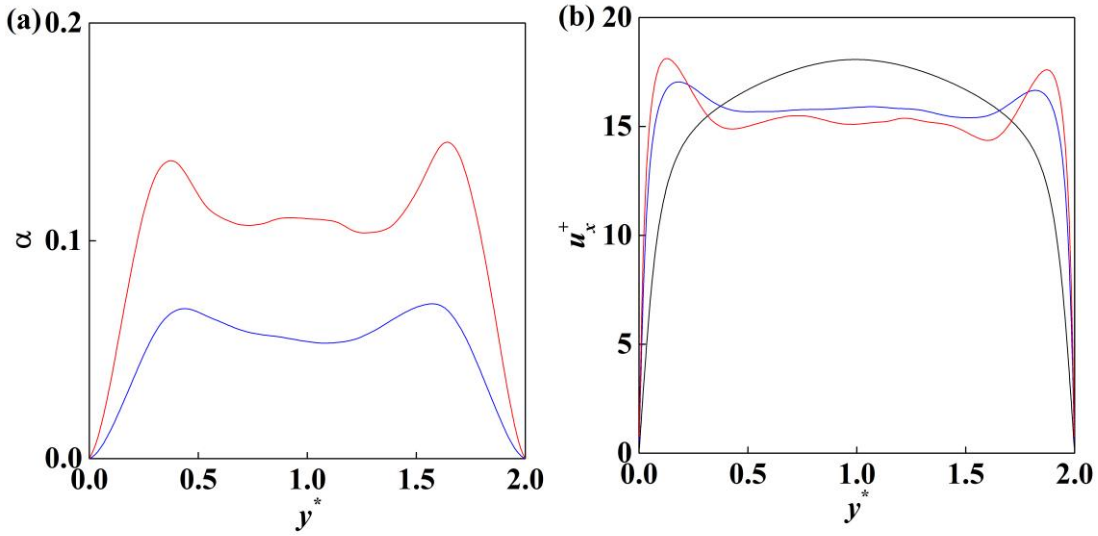

Figure 6.19 Void fraction profile (a) and continuous phase mean velocity (b) for dilute (—) and dense (—) swarms, and single-phase flow (—).

6.4.2 Bubble clustering and distribution

To quantify bubble clustering and bubble-bubble interaction, a widely employed pair correlation function $G(r)$ [89, 115, 182, 322] was used to obtain the probability of distances between two bubbles and is expressed as:

$$G(r) = \frac{V}{N_b(N_b - 1)}\left[\sum_{i=1}^{N_b} \sum_{j=1, i\neq j}^{N_b} \delta(\boldsymbol{r} - \boldsymbol{r}_{ij})\right] \tag{6.17}$$

where V is the volume of the channel, and N_b is the number of bubbles. The vector $\boldsymbol{r}_{ij}$ linking the centres of neighbouring bubbles i and j is defined with a magnitude r_{ij} and an orientation angle θ with respect to the streamwise direction in Figure 6.20.

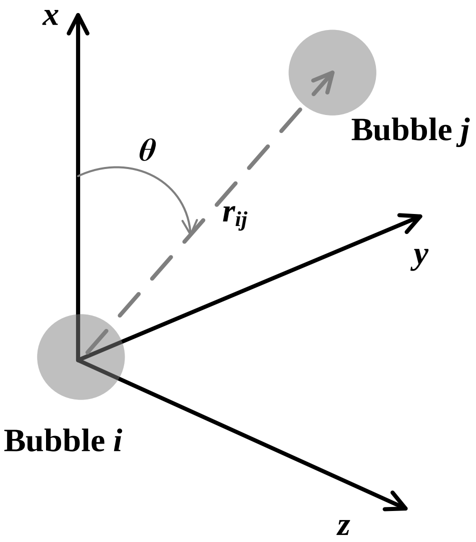

Figure 6.20 Illustration of vector $\boldsymbol{r}_{ij}$ with magnitude r_{ij} and orientation θ between bubbles i and j [182].

The radial pair probability function $G(r)$ is the integral of $G(r)$ over thin shells of step width Δr and radius r. The maximum r in the present study was specified as the channel width. For a random bubble distribution in the channel $G(r)$ is 1. Due to the difference of sampling shells used between studies [115, 322] and [89, 182], however, a lack of bubbles exists in those sample volumes whose boundaries meet the wall. As a result, $G(r)$ of a random distribution decreases from 1 as r increases. For spherical bubbles without coalescence, $G(r)$ is completely zero if $r < 2\ r_b$. Because of the bubble deformability in the present study, $G(r)$ will be larger than 0 within $r < 2\ r_b$ if bubble interaction happens.

To obtain an averaged bubbles pair correlation, 500 samples were taken in the averaging intervals as discussed in Section 6.4.1. The pair correlation functions $G(r)$ for both cases are presented in Figure 6.21 as a function of the radius non-dimensionalised by the spherical bubble radius r_b = 2 mm. The probability increases with the void fraction so that a higher peak for the dense swarm is found in Figure 6.21. In present study, the bubbles are deformable and ellipsoidal in shape. Therefore, the probability is found to be $G(r) > 0$ for $r < 2\ r_b$, as expected. For both flow cases, it is clearly seen that the peak of bubble the pair probability lies around bubbles with a distance of 2.4 r_b. This is qualitatively visible from the instantaneous bubble distributions in Figure 6.22.

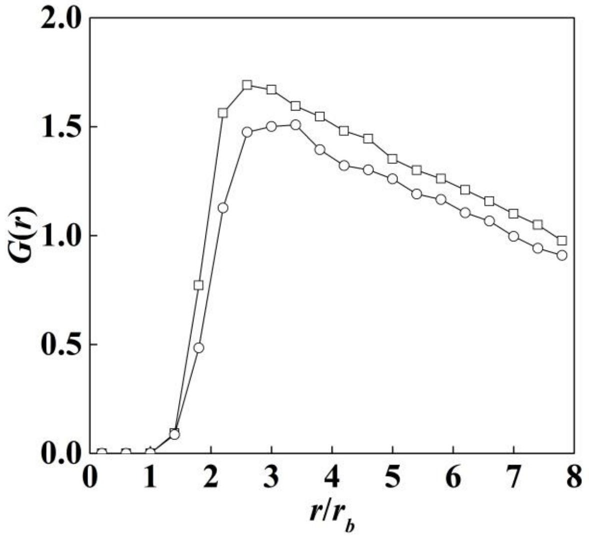

Figure 6.21 Bubble pair probability $G(r)$ profiles as a function of radius of dilute (○) and dense (□) swarms.

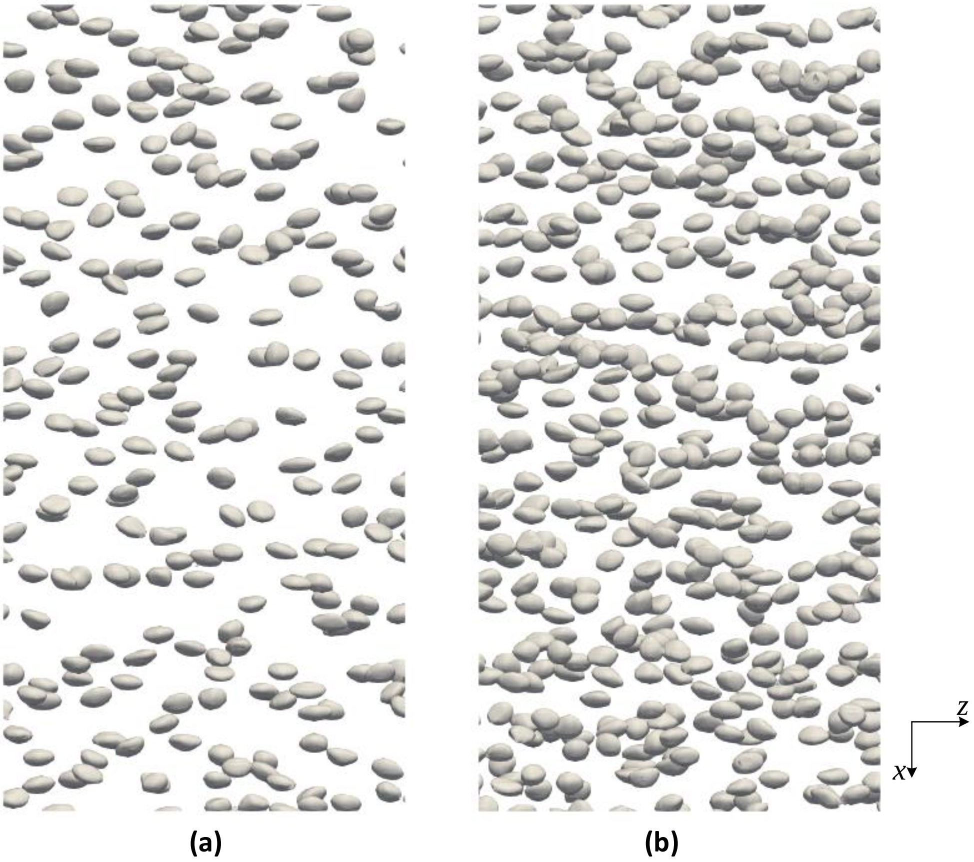

Figure 6.22 Instantaneous bubble distribution: (a) dilute swarm; and (b) dense swarm.

To examine the orientation of the bubble pair clustering, the PDF of orientation angles θ is calculated at six bubble pair distances, namely $r = 2.2\ r_b$, $2.6\ r_b$, $3\ r_b$, $4\ r_b$, $5\ r_b$ and $6\ r_b$, and is shown in Figure 6.23 for the dilute swarm and in Figure 6.24 for the dense swarm. A value of $\theta = 0$ and π means that the bubble pair is vertically clustered, and a value of $\theta = \pi / 2$ translates into a horizontal bubble pair. In the dilute bubble swarm, the two regions $r = 2.2\ r_b$ and $2.6\ r_b$ as shown in Figure 6.21 have the most likely bubble pair clustering. For these two distances, as seen in Figure 6.23(a) and (b), the peak of the orientation angles develops at $\theta = \pi / 2$. This horizontal alignment is also clearly seen in the instantaneous bubble distribution in Figure 6.22.

By increasing the distance, the peak of probability of $\theta = \pi / 2$ weakens until a more uniform distribution occurs at $r = 6\ r_b$ in Figure 6.23(f). The enhanced probability distribution is even more pronounced in the dense swarm as shown in Figure 6.24. The peak occurs at $\theta = \pi / 2$ at $r = 2.2\ r_b$ and $2.6\ r_b$. At a further distance of $r = 6\ r_b$, a more uniform distribution is again observed.

The results discussed in this section, provide a description of the effect of deformable bubble swarms on the fluid flow, as well as the bubble clustering phenomena, predicted by means of an interface tracking simulation. Clearly the current results form a foundation towards the eventual prediction of bubble coalescence. In the bubble coalescence process, contact and collision are the premise of coalescence. The collision is usually caused by the relative velocity between two colliding bubbles. One of the bubble collision induced coalescence mechanisms is the bubble wake interaction, and it can be directly considered if $\theta = 0$ or π (bubbles are vertically aligned) in the present model. On the other hand, the relative collision velocity can be quantified if $r < 2\ r_b$ depending on the relative motions of the colliding bubbles. Therefore, the relative velocity can be studied together with the bubble swarm and bubble shape effect. This should be addressed in future work, although physical modelling of coalescence needs to be incorporated into the simulations before such studies can proceed.

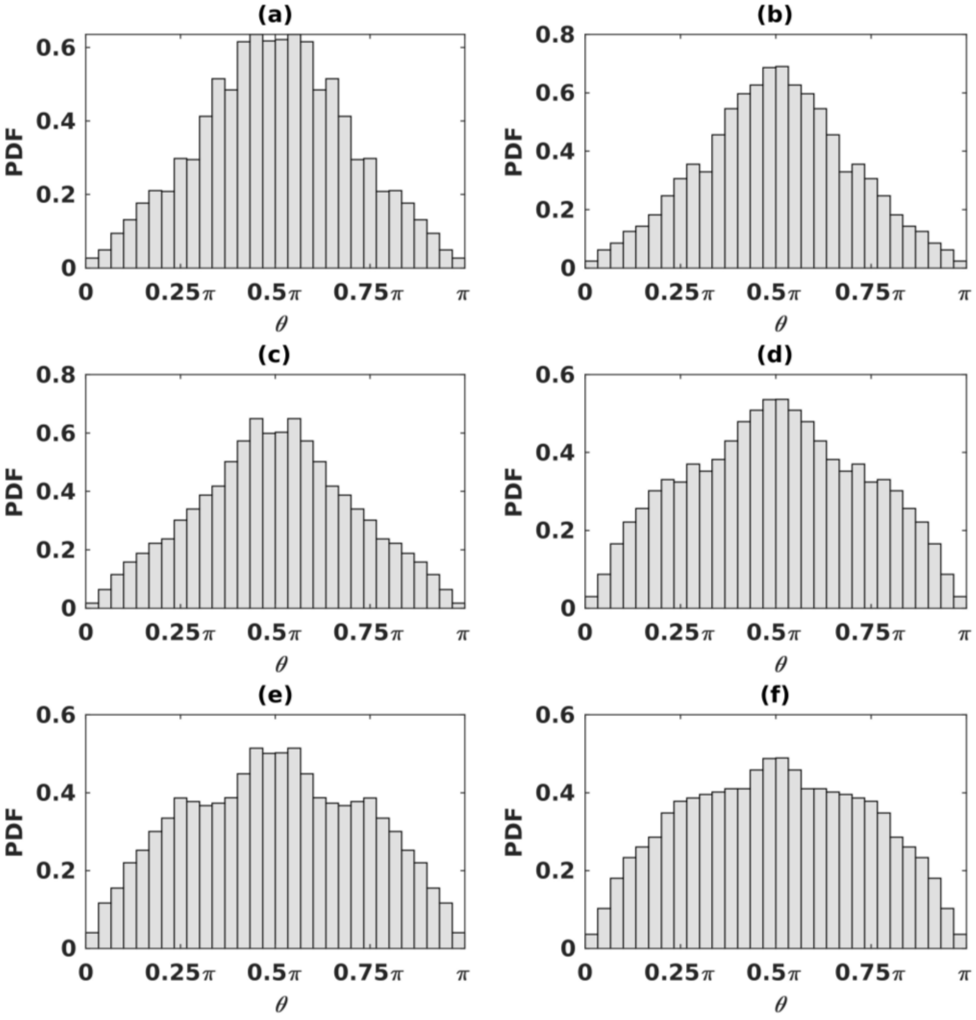

Figure 6.23 PDF of the orientation angles of bubble clustering in dilute swarm at different bubble-pair distances: (a) r = 2.2 r_b; (b) r = 2.6 r_b; (c) r = 3 r_b; (d) r = 4 r_b; (e) r = 5 r_b; and (f) r = 6 r_b.

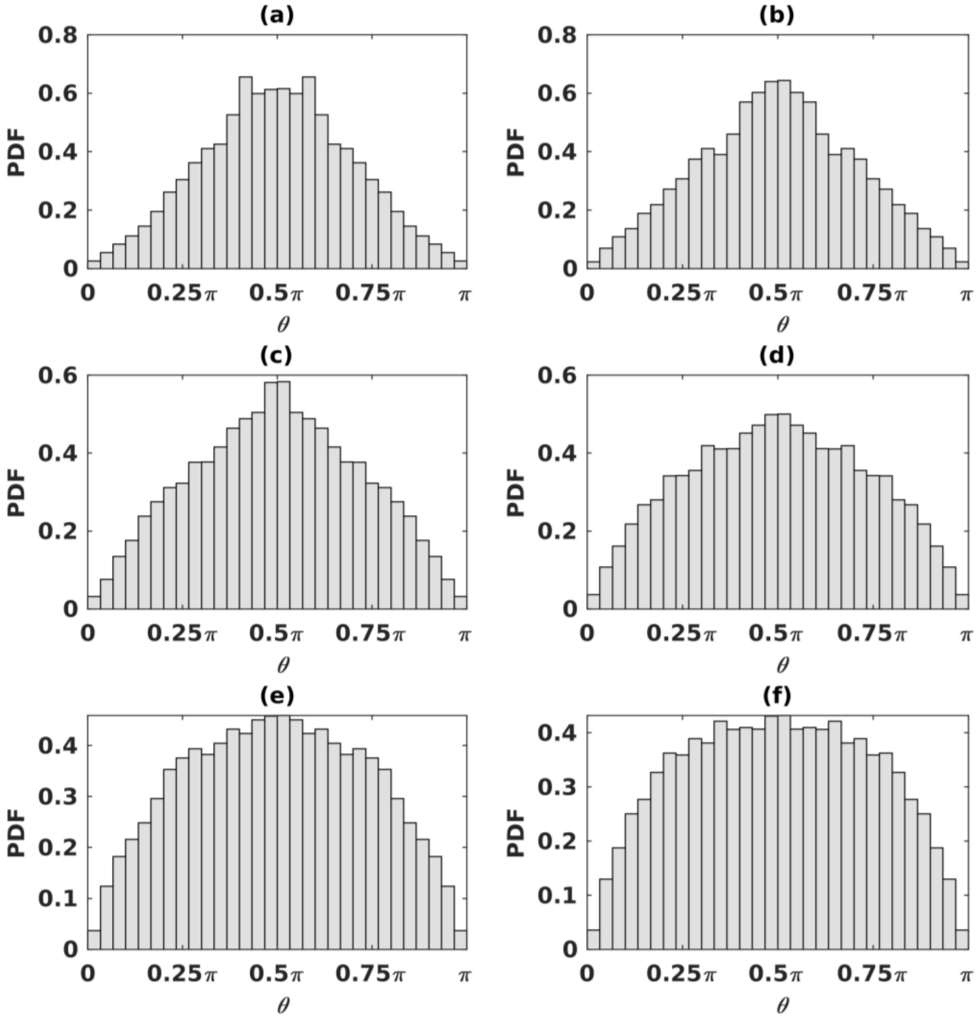

Figure 6.24 PDF of the orientation angles of bubble clustering in dense swarm at different bubble-pair distances: (a) $r = 2.2\ r_b$; (b) $r = 2.6\ r_b$; (c) $r = 3\ r_b$; (d) $r = 4\ r_b$; (e) $r = 5\ r_b$; and (f) $r = 6\ r_b$.

6.5 Summary and conclusions

The investigation performed in this chapter concerned the DNS of turbulent bubbly channel flows with large and deformable bubbles. A high mass density ratio closer to real air bubbles in water was investigated by means of DNS coupled with the VOF method. The simulation of single-phase channel flow was validated with previous DNS results obtained using Nek5000 in Chapter 4, with good agreement found. The DNS of single bubble cases demonstrated the effect of bubble size on the bubble lateral movement in a vertical channel upflow, such that 8 mm bubble was found to wobble in the channel centre while 1 mm and 4 mm bubbles travelled to the wall under the effect of the lift force. The bubble shape and bubble wake were also well captured. A method of estimating bubble drag coefficient was proposed and applied to the 8 mm bubble case. Bubble-induced turbulence was evaluated in terms of time-averaged phase velocities, the rms of the fluctuating velocities and the TKE. The BIT of an 8 mm bubble shows the most significant effect on the fluid flow among all bubble sizes, and its turbulence alters a large portion of the computational domain. Special attention was paid to evaluating the change on five lines behind the 8 mm bubble. Results show that the most significant enhancement as along a line a distance of 2 d_b behind the bubble centre.

Multiple deformable bubbles with two void fractions were simulated in channel downflows. In both bubble swarms, a nearly uniform void fraction was observed in the channel central region while peaks were observed approaching the walls. The effect of the deformable bubbles on the fluid phase was investigated in terms of the streamwise fluid velocity which was seen to be suppressed and uniform in the channel centre but was enhanced approaching the walls. Bubble positions were used to study the bubble clustering and distribution in the turbulent channel flow. The evaluation of the bubble pair correlation function $G(r)$ demonstrated that a pair of bubbles preferentially clusters within $2.2\ r_b < r < 2.6\ r_b$. This characteristic feature was confirmed by increasing the void fraction. The PDF of the orientation angles clearly gave a horizontal alignment at the distances of $r = 2.2\ r_b$ and $2.6\ r_b$.

The successful application of the VOF method in this chapter demonstrates the dramatically different bubble behaviour and bubble-fluid interactions compared to those discussed in previous chapters. The database from these simulations provides information on the fluid turbulence statistics, complex bubble shapes, the drag coefficient of deformed bubbles, bubble-induced turbulence and bubble clustering in bubble swarms. The results shed light on the dynamics of deformable bubbles which is of value in improving physical understanding of the complex mechanisms involved in many practical applications, such as the reactive processes in bubble columns, which strongly rely on the parameters of bubble shape and drag forces. In addition, the results are also useful as a basis for the implementation of interface effects and generally improving the level of detail that can be accommodated in Lagrangian tracking techniques that could be used to further improve their accuracy. The extension of the present interface tracking model to larger scales should be performed to allow comparison of the same scenarios considered above with the multi-fluid model, and provide important input to the development of closure relations for turbulent bubbly flows.

Chapter 7 Conclusions and Future Work

In this last chapter, the conclusions drawn in previous chapters are summarized in Section 7.1, and some suggestions for future work are presented in Section 7.2.

7.1 Conclusions

The work carried out in the present study used direct numerical simulation (DNS) to numerically model bubbly flows, helping to address key aspects of physical phenomena underpinning such bubbly flows. For this purpose, a literature review of existing applications of DNS to, and experimental studies of, bubbly flows in different geometries was first performed to cover previous work relevant to the present study. The methodology employed was based on Eulerian-Lagrangian tracking and volume of fluid approaches which were applied to microbubble flows and deformable bubble flows, respectively.

In the first results chapter, as a first step, the fluid phase in the channel governed by Navier-Stokes equations was predicted by employing the Nek5000 code, and a Lagrangian particle/bubble tracking (LPT) framework was developed and interfaced with the Nek5000 environment to model the transport of the dispersed microbubbles which were assumed to be non-deformable and spherical. DNS of turbulent upward and downward flows of microbubbles in a channel was performed under one-way and two-way coupling between the bubbles and the fluid. Confidence in the accuracy and validity of the overall model was established by validating against single-phase, one-way and two-way coupled two-phase fully developed channel flow results on the literature. The one-way coupled model gives a general impression of microbubble distributions in downward and upward channel flows. In downflow, the microbubbles tend to travel in the channel centre region, while they are pushed to the wall clustering in vortices and low-speed streaks under the effect of the lift force. The effect of microbubbles on the fluid turbulence intensity was examined under two-way coupling, this being enhanced or suppressed in upflow or downflow, respectively. The success of this first step provided a strong foundation for later works. In the next step, the LPT model was extended to a four-way coupled channel flow with bubble collision and coalescence considered. A binary deterministic hard sphere collision model was applied to compute the bubble-bubble collision process. The four-way coupled model provided a quantitative description of microbubble dynamics and clarified the mechanisms of bubble collision and coalescence driven by the continuous fluid flow field. At the levels of turbulence investigated, collisions mainly occur on quasi-rectilinear bubble trajectories. Therefore, the angle of collision between bubbles is usually very small and the relative approach velocity between two colliding bubbles is generally low. These low-energy collisions favour use of the film drainage coalescence model over the energy model, although the contradictory predictions obtained from these two approaches warrants further investigation. To the best knowledge of the author, the pattern of bubble collisions observed in present simulation is rarely reported in literature.

In the second results chapter, the Eulerian-Lagrangian method was extended to simulating straight, circular cross-section microbubble pipe flows given that the pipe geometry is more practically relevant than a plane channel from an engineering viewpoint. One-way, two-way and four-way (including the effect of bubble coalescence) coupled DNS-based computations of turbulent bubbly downward and upward pipe flows were performed. The DNS results for fully developed single-phase pipe flows were successfully verified by validating first- and second-order fluid statistics against existing literature DNS databases. In one-way coupled DNS, results clearly demonstrated that bubbles have different preferential distributions in upflow and downflow and these are mainly governed by the lift force. Two-way coupled simulation was used to examine the effect on the fluid flow by the bubbles. In the very near pipe wall region, when the bubble diameter is of the order of the spatial resolution of the numerical solver, a Gaussian function treatment was proposed to deal with the effects of a bubble by spreading its influence over the surrounding grid points rather than a single grid point. In the present study, however, no obvious difference due to the effect of the bubbles on the fluid was observed in upflow. The lack of change is mainly due to the fact that the bubble size considered was very small, and the system studied was very dilute. In the four-way coupled model, a similar analysis of bubble collision and coalescence was made, and results provide a quantitative description of microbubble dynamics and clarify the mechanisms of bubble collision and coalescence, driven by the continuous fluid flow field. More collision events were found in the viscous sub-layer region of both downflow and upflow cases, due to the action of the large velocity gradients in this region. The maximum bubble collision angle, equal to around 30°, was found in the viscous sub-layer in upflow. However, bubbles tend to generally collide with low collision angles. Additionally, they also collide with small relative velocities. This means that the bubbles correlate with the fluid flow. Under this circumstance, it is more likely that colliding bubbles coalesce.

In the last results chapter, bubbly channel flows with large and deformable bubbles were numerically studied by means of the VOF approach with accurate bubble curvature computation using the generalised height function method. The DNS of a single-phase channel flow at a Reynolds number $Re_\tau = 150$ and with the same geometry size used in previous chapters was performed and validated against the results obtained with Nek5000. Confidence in the computations was gained given the consistent agreement of the first and second order statistics of the fluid phase. Based on the fully developed single-phase channel flow, two-phase bubbly flows were simulated with a high mass density ratio closer to real air bubbles in water. In the single bubble cases considered, DNS of bubbly flows with three bubble sizes of 1 mm, 4 mm and 8 mm was performed and results were used to address bubble lateral movement, bubble shape, bubble drag coefficient as well as the evaluation of bubble-induced turbulence. In turbulent a bubbly upward channel flow, the 1 mm and 4 mm bubbles were pushed to the wall region, while the 8 mm bubble wobbled but remaining in the channel centre under the effect of the lift force. A method of estimating the bubble drag coefficient was proposed and applied to the 8 mm bubble. During the bubble's rise in the channel, the bubble shape and bubble wake were also captured. Due to the deformability, the 1 mm bubble remained nearly spherical approaching the wall, whilst the 4 mm bubble deformed to be a nearly ellipsoid after injection. The 8 mm bubbles with highest deformability amongst all the bubble sizes wobbled in the channel. The wake effect on the carrier phase, namely bubble-induced turbulence, was evaluated for each bubble size in terms of time-averaged phase velocities, the rms of the fluctuating velocities and the TKE. The BIT of the 8 mm bubble showed the most significant effect on the fluid flow among all the bubble sizes, and the turbulence generated by it altered a large portion of the flow in the computational domain. Special attention was paid to evaluating this change on five lines behind the 8 mm bubble. Results show the most significant enhancement to be on a line at a distance of 2 d_b behind the bubble centre. To further investigate the study of deformable bubble dynamics, DNS of multiple deformable bubbles in channel downflows with two void fractions (α = 5.1% and 10.2%) was carried out. Results for the bubble phase demonstrated that in both bubble swarms, a nearly uniform void fraction was observed in the central channel region while peaks were seen approaching the walls. The streamwise fluid velocity was suppressed by the effect of the deformable bubbles and showed a largely uniform profile in the channel centre region which was enhanced approaching the walls. Bubble clustering and orientation was analysed in terms of the Lagrangian bubble positions. The evaluation of the bubble pair correlation function $G(r)$ demonstrated that a pair of bubbles in the dilute bubble swarm preferentially clusters within $2.2\ r_b < r < 2.6\ r_b$. This characteristic feature was further confirmed in the dense bubble swarm with a higher void fraction. The PDF of the orientation angles clearly demonstrated a horizontal alignment of the bubbles at distances of $r = 2.2\ r_b$ and $2.6\ r_b$.

The aforementioned DNS-based work presented in this thesis has been proven to be of value in gaining a better understanding of the phenomena involved in bubbly flows down to the smallest scales, and has provided useful insights into such flows. Confidence in the predictions is sufficient to permit the use of these techniques to explore bubble dynamics in related industrial applications. The Lagrangian particle tracking technique used in the present study has been proven to be a powerful tool when the bubble size is smaller than that of the numerical solution grid cell size. In particular, the results for four-way coupled DNS of microbubble flows discussed and clarified the mechanisms of bubble collision and coalescence. On the other hand, following increasing the bubble size, the interface tracking approach was employed to extend applicability with respect to larger bubbles that cannot be treated using point tracking approach. On the other hand, the present interface tracking simulations, resolving all bubble details, provided fundamental information that elucidates and captures the physics of deformable bubbly flows, such as bubble interfacial force closures, bubble-induced turbulence, bubbles clustering and preferential orientations during bubble interactions. With increasing computer power, the interface tracking method will become of increasing importance for the production of reference data that is of value in refining, and improving the accuracy of, the Lagrangian particle tracking framework. The interface tracking method can also be extended to larger scales to give a comparison of the same scenarios with the multi-fluid model, and provides important knowledge on closure relations to turbulent bubbly flows.

7.2 Future work

Based on the results and conclusions that have emerged from the work reported in this thesis, the following suggestions can be made for further investigation and improvement.

- The Eulerian-Lagrangian method was successfully used to understand the microbubble dynamics under four-way coupling with coalescence. The extension of the present LPT model to turbulent flows at higher Reynolds numbers is desirable.

- In the present LPT framework, bubble breakup was neglected because of the small bubble sizes and the low Reynolds numbers considered, with such bubbles having previously been demonstrated to be incapable of breaking up. However, in extending the work to highly turbulent flows, the breakup process will become more important and will contribute in determining the bubble size distribution. Breakup models should therefore be incorporated and tested within the predictive framework described.

- The contradictory predictions of microbubble coalescence efficiency obtained from the film drainage and the energy model warrant further investigation by means of the VOF method which can account for all relevant physical mechanisms including inertia, viscous effect and bubble deformability. Such applications of VOF should be used to refine the simple coalescence models tested in this work with the aim of improving their accuracy.

- In the present LPT framework, a fully elastic collision model without friction was applied. In this approach, only the sign of the wall-normal direction velocity is changed after bubble collisions with a wall, whereas the other velocity components remain unchanged. However, this behaviour of bouncing after every collision with the wall is not always physically accurate. The treatment of bubble-wall interaction in the VOF model is based on a contact angle approach to solve the problem of how the bubble interface adjacent to the wall should be reconstructed. Specifically, a contact angle of 180 degrees is employed indicating that the interface normal and the wall normal point directly towards each other. Although the model works well in the present DNS of turbulent bubbly channel flows, further extension and detailed study to examine the influence of contact angle in the VOF model should be performed to consider more complex bubble-wall interactions which would be beneficial in improving Lagrangian treatments of bubble motion.

- In the present VOF model, the discrepancy in the bubble shape aspect ratio suggests further investigation is desirable of the grid dependency of the equivalent bubble diameter and therefore the predicted drag coefficient. Additionally, further studies for different bubble diameters and locations in a channel would be useful in helping to improve the Lagrangian point tracking model, although the bubble volume loss produced by the VOF approach needs to be addressed.

- In the present simulations of bubble swarms with 4 mm bubbles in downflow, the bubbles travel very slowly in the streamwise direction. Further extended computations are desirable to obtain a steady state, with bubbles travelling several passes through the channel so that the effect of the bubbles on the fluid phase, such as evaluations of the rms of velocity fluctuations and shear stress, can be sufficiently quantified.

- The present DNS-based analysis suffers from the lack of an extensive validation against experimental data. This is because experiments with reliable and detailed data, to the best knowledge of the author, are lacking in the literature. Therefore, to validate the DNS-based models discussed in this thesis, another key aspect for future work is the experimental measurement of single bubbles and bubble swarms in turbulent flows across a wide range of void fractions. Such information would not only be of value for validation purposes, but would provide insights into bubble dynamics of value in improving all engineering approaches to bubbly flow prediction.

Bibliography

1. Balachandar, S. and Eaton, J.K. Turbulent dispersed multiphase flow. *Annual Review of Fluid Mechanics.* 2010, **42**(1), pp.111-133.

2. Mudde, R.F. Gravity-driven bubbly flows. *Annual Review of Fluid Mechanics.* 2005, **37**(1), pp.393-423.

3. Salman, W., Gavriilidis, A. and Angeli, P. On the formation of Taylor bubbles in small tubes. *Chemical Engineering Science.* 2006, **61**(20), pp.6653-6666.

4. Shao, N., Gavriilidis, A. and Angeli, P. Effect of inlet conditions on taylor bubble length in microchannels. *Heat Transfer Engineering.* 2011, **32**(13-14), pp.1117-1125.

5. Abdulmouti, H. Bubbly two-phase flow: Part I- characteristics, structures, behaviors and flow patterns. *American Journal of Fluid Dynamics.* 2014, **4**(4), pp.194-240.

6. Todreas, N.E. and Kazimi, M.S. *Nuclear systems volume I: Thermal hydraulic fundamentals.* Boca Raton: CRC press, 2011.

7. Glasstone, S. and Sesonske, A. *Nuclear reactor engineering: Reactor systems engineering.* 4th ed. Boston: Springe, 1994.

8. Lau, Y.M., Deen, N.G. and Kuipers, J.A.M. Development of an image measurement technique for size distribution in dense bubbly flows. *Chemical Engineering Science.* 2013, **94**, pp.20-29.

9. Shah, Y.T., Kelkar, B.G., Godbole, S.P. and Deckwer, W.D. Design parameters estimations for bubble column reactors. *AIChE Journal.* 1982, **28**(3), pp.353-379.

10. Rollbusch, P., Bothe, M., Becker, M., Ludwig, M., Grünewald, M., Schlüter, M. and Franke, R. Bubble columns operated under industrially relevant conditions –

Current understanding of design parameters. *Chemical Engineering Science*. 2015, **126**, pp.660-678.

11. Muroyama, K., Imai, K., Oka, Y. and Hayashi, J.i. Mass transfer properties in a bubble column associated with micro-bubble dispersions. *Chemical Engineering Science*. 2013, **100**, pp.464-473.

12. Guo, K., Wang, J. and Wang, T. Hydrodynamics of a bubble column with phase change. *Chemical Engineering Science*. 2017, **157**, pp.107-115.

13. Krishna, R., Ellenberger, J. and Sie, S.T. Reactor development for conversion of natural gas to liquid fuels: A scale-up strategy relying on hydrodynamic analogies. *Chemical Engineering Science*. 1996, **51**(10), pp.2041-2050.

14. Magnaudet, J. and Eames, I. The motion of high-Reynolds-number bubbles in inhomogeneous flows. *Annual Review of Fluid Mechanics*. 2000, **32**(1), pp.659-708.

15. Elghobashi, S. On predicting particle-laden turbulent flows. *Applied Scientific Research*. 1994, **52**(4), pp.309-329.

16. Clift, R., Grace, J.R. and Weber, M.E. *Bubbles, drops, and particles*. New York: Academic Press, 1978.

17. Lu, J., Muradoglu, M. and Tryggvason, G. Effect of insoluble surfactant on turbulent bubbly flows in vertical channels. *International Journal of Multiphase Flow*. 2017, **95**, pp.135-143.

18. Eames, I., Takagi, S., Ogasawara, T. and Matsumoto, Y. The effects of surfactant on the multiscale structure of bubbly flows. *Philosophical Transactions of the Royal Society A: Mathematical, Physical and Engineering Sciences*. 2008, **366**(1873), pp.2117-2129.

19. Laborde-Boutet, C., Larachi, F., Dromard, N., Delsart, O. and Schweich, D. CFD simulation of bubble column flows: Investigations on turbulence models in RANS approach. *Chemical Engineering Science*. 2009, **64**(21), pp.4399-4413.

20. Colombo, M. and Fairweather, M. Multiphase turbulence in bubbly flows: RANS simulations. *International Journal of Multiphase Flow*. 2015, **77**, pp.222-243.

21. Tryggvason, G. and Lu, J. Direct numerical simulations of bubbly flows. *Mechanical Engineering Reviews.* 2015, **2**(2), pp.15-00220.

22. Tryggvason, G., Thomas, S., Lu, J. and Aboulhasanzadeh, B. Multiscale issues in DNS of multiphase flows. *Acta Mathematica Scientia.* 2010, **30**(2), pp.551-562.

23. Prosperetti, A. and Tryggvason, G. *Computational methods for multiphase flow.* Cambridge: Cambridge University Press, 2009.

24. Tryggvason, G., Esmaeeli, A., Lu, J. and Biswas, S. Direct numerical simulations of gas/liquid multiphase flows. *Fluid Dynamics Research.* 2006, **38**(9), pp.660-681.

25. Tryggvason, G., Dabiri, S., Aboulhasanzadeh, B. and Lu, J. Multiscale considerations in direct numerical simulations of multiphase flows. *Physics of Fluids.* 2013, **25**(3), p.031302.

26. Tryggvason, G., Scardovelli, R. and Zaleski, S. *Direct numerical simulations of gas-liquid multiphase flows.* Cambridge: Cambridge University Press, 2011.

27. Joshi, J.B., Nandakumar, K., Evans, G.M., Pareek, V.K., Gumulya, M.M., Sathe, M.J. and Khanwale, M.A. Bubble generated turbulence and direct numerical simulations. *Chemical Engineering Science.* 2017, **157**, pp.26-75.

28. Elghobashi, S. Direct numerical simulation of turbulent flows laden with droplets or bubbles. *Annual Review of Fluid Mechanics.* 2019, **51**(1), pp.217-244.

29. Ryskin, G. and Leal, L.G. Numerical solution of free-boundary problems in fluid mechanics. Part 2. Buoyancy-driven motion of a gas bubble through a quiescent liquid. *Journal of Fluid Mechanics.* 1984, **148**, pp.19-35.

30. Taeibi-Rahni, M., Loth, E. and Tryggvason, G. Flow modulation of a planar free shear layer with large bubbles-direct numerical simulations. *International Journal of Multiphase Flow.* 1994, **20**(6), pp.1109-1128.

31. Smereka, P. On the motion of bubbles in a periodic box. *Journal of Fluid Mechanics.* 1993, **254**, pp.79-112.

32. Druzhinin, O. and Elghobashi, S. Direct numerical simulation of a three-dimensional spatially developing bubble-laden mixing layer with two-way coupling. *Journal of Fluid Mechanics.* 2001, **429**, pp.23-61.

33. Antal, S.P., Lahey Jr, R.T. and Flaherty, J.E. Analysis of phase distribution in fully developed laminar bubbly two-phase flow. *International Journal of Multiphase Flow.* 1991, **17**(5), pp.635-652.

34. Lopez de Bertodano, M., Lahey Jr, R.T. and Jones, O.C. Phase distribution in bubbly two-phase flow in vertical ducts. *International Journal of Multiphase Flow.* 1994, **20**(5), pp.805-818.

35. Pan, Y., Dudukovic, M.P. and Chang, M. Dynamic simulation of bubbly flow in bubble columns. *Chemical Engineering Science.* 1999, **54**(13-14), pp.2481-2489.

36. Druzhinin, O.A. and Elghobashi, S. Direct numerical simulations of bubble-laden turbulent flows using the two-fluid formulation. *Physics of Fluids.* 1998, **10**(3), pp.685-697.

37. Zhou, L., Li, R. and Du, R. Numerical simulation of the effect of void fraction and inlet velocity on two-phase turbulence in bubble-liquid flows. *Acta Mechanica Sinica.* 2006, **22**(5), pp.425-432.

38. Ferrante, A. and Elghobashi, S. On the accuracy of the two-fluid formulation in direct numerical simulation of bubble-laden turbulent boundary layers. *Physics of Fluids.* 2007, **19**(4), p.045105.

39. Ferrante, A. and Elghobashi, S. Reynolds number effect on drag reduction in a microbubble-laden spatially developing turbulent boundary layer. *Journal of Fluid Mechanics.* 2005, **543**, pp.93-106.

40. Ferrante, A. and Elghobashi, S. On the physical mechanisms of drag reduction in a spatially developing turbulent boundary layer laden with microbubbles. *Journal of Fluid Mechanics.* 2004, **503**, pp.345-355.

41. Liao, Y., Ma, T., Liu, L., Ziegenhein, T., Krepper, E. and Lucas, D. Eulerian modelling of turbulent bubbly flow based on a baseline closure concept. *Nuclear Engineering and Design.* 2018, **337**, pp.450-459.

42. Ma, T., Santarelli, C., Ziegenhein, T., Lucas, D. and Fröhlich, J. Direct numerical simulation-based Reynolds-averaged closure for bubble-induced turbulence. *Physical Review Fluids.* 2017, **2**(3), p.034301.

43. Colombo, M. and Fairweather, M. Influence of multiphase turbulence modelling on interfacial momentum transfer in two-fluid Eulerian-Eulerian CFD models of bubbly flows. *Chemical Engineering Science.* 2019, **195**, pp.968-984.

44. Dhotre, M.T., Deen, N.G., Niceno, B., Khan, Z. and Joshi, J.B. Large eddy simulation for dispersed bubbly flows: A review. *International Journal of Chemical Engineering.* 2013, **2013**, pp.1-22.

45. Trapp, J.A. and Mortensen, G.A. A discrete particle model for bubble-slug two-phase flows. *Journal of Computational Physics.* 1993, **107**(2), pp.367-377.

46. Lapin, A. and Lübbert, A. Numerical simulation of the dynamics of two-phase gas-liquid flows in bubble columns. *Chemical Engineering Science.* 1994, **49**(21), pp.3661-3674.

47. Devanathan, N., Dudukovic, M.P., Lapin, A. and Lübbert, A. Chaotic flow in bubble column reactors. *Chemical Engineering Science.* 1995, **50**(16), pp.2661-2667.

48. Delnoij, E., Lammers, F.A., Kuipers, J.A.M. and van Swaaij, W.P.M. Dynamic simulation of dispersed gas-liquid two-phase flow using a discrete bubble model. *Chemical Engineering Science.* 1997, **52**(9), pp.1429-1458.

49. Laín, S., Bröder, D., Sommerfeld, M. and Göz, M.F. Modelling hydrodynamics and turbulence in a bubble column using the Euler-Lagrange procedure. *International Journal of Multiphase Flow.* 2002, **28**(8), pp.1381-1407.

50. Lain, S., Bröder, D. and Sommerfeld, M. Experimental and numerical studies of the hydrodynamics in a bubble column. *Chemical Engineering Science.* 1999, **54**(21), pp.4913-4920.

51. Ekambara, K., Dhotre, M.T. and Joshi, J.B. CFD simulations of bubble column reactors: 1D, 2D and 3D approach. *Chemical Engineering Science.* 2005, **60**(23), pp.6733-6746.

52. Hibiki, T. and Ishii, M. Lift force in bubbly flow systems. *Chemical Engineering Science.* 2007, **62**(22), pp.6457-6474.

53. Mazzitelli, I.M., Lohse, D. and Toschi, F. On the relevance of the lift force in bubbly turbulence. *Journal of Fluid Mechanics.* 2003, **488**, pp.283-313.

54. Mazzitelli, I.M., Lohse, D. and Toschi, F. The effect of microbubbles on developed turbulence. *Physics of Fluids.* 2002, **15**(1), pp.L5-L8.

55. Giusti, A., Lucci, F. and Soldati, A. Influence of the lift force in direct numerical simulation of upward/downward turbulent channel flow laden with surfactant contaminated microbubbles. *Chemical Engineering Science.* 2005, **60**(22), pp.6176-6187.

56. Pang, M., Wei, J. and Yu, B. Numerical study of bubbly upflows in a vertical channel using the Euler-Lagrange two-way model. *Chemical Engineering Science.* 2010, **65**(23), pp.6215-6228.

57. Wang, L.-P. and Maxey, M.R. The motion of microbubbles in a forced isotropic and homogeneous turbulence. *Applied Scientific Research.* 1993, **51**(1), pp.291-296.

58. Spelt, P.D.M. and Biesheuvel, A. On the motion of gas bubbles in homogeneous isotropic turbulence. *Journal of Fluid Mechanics.* 1997, **336**, pp.221-244.

59. Snyder, M.R., Knio, O.M., Katz, J. and Le Maître, O.P. Statistical analysis of small bubble dynamics in isotropic turbulence. *Physics of Fluids.* 2007, **19**(6), p.065108.

60. Okawa, T., Kataoka, I. and Mori, M. Numerical simulation of lateral phase distribution in turbulent upward bubbly two-phase flows. *Nuclear Engineering and Design.* 2002, **213**(2), pp.183-197.

61. Cencini, M., Bec, J., Biferale, L., Boffetta, G., Celani, A., Lanotte, A.S., Musacchio, S. and Toschi, F. Dynamics and statistics of heavy particles in turbulent flows. *Journal of Turbulence.* 2006, **7**, p.N36.

62. Calzavarini, E., Berg, T.H.v.d., Toschi, F. and Lohse, D. Quantifying microbubble clustering in turbulent flow from single-point measurements. *Physics of Fluids.* 2008, **20**(4), p.040702.

63. Shams, E., Finn, J. and Apte, S.V. A numerical scheme for Euler-Lagrange simulation of bubbly flows in complex systems. *International Journal for Numerical Methods in Fluids.* 2011, **67**(12), pp.1865-1898.

64. Molin, D., Marchioli, C. and Soldati, A. Turbulence modulation and microbubble dynamics in vertical channel flow. *International Journal of Multiphase Flow.* 2012, **42**, pp.80-95.

65. Liu, N., Cheng, B., Que, X. and Lu, X. Direct numerical simulations of turbulent channel flows with consideration of the buoyancy effect of the bubble phase. *Journal of Hydrodynamics.* 2011, **23**(3), pp.282-288.

66. Sungkorn, R., Derksen, J.J. and Khinast, J.G. Modeling of turbulent gas-liquid bubbly flows using stochastic Lagrangian model and lattice-Boltzmann scheme. *Chemical Engineering Science.* 2011, **66**(12), pp.2745-2757.

67. Sungkorn;, R., Derksen;, J.J. and Khinast, J.G. Euler-Lagrange modeling of a gas-liquid stirred reactor with consideration of bubble breakage and coalescence. *AIChE Journal.* 2012, **58**(5), pp.1356-1370.

68. Prince, M.J. and Blanch, H.W. Bubble coalescence and break-up in air-sparged bubble columns. *AIChE Journal.* 1990, **36**(10), pp.1485-1499.

69. Luo, H. *Coalescence, breakup and liquid circulation in bubble column reactors*. Ph.D. thesis, The Norwegian Institute of Technology, 1993.

70. Darmana, D., Deen, N.G. and Kuipers, J.A.M. Parallelization of an Euler-Lagrange model using mixed domain decomposition and a mirror domain technique: Application to dispersed gas-liquid two-phase flow. *Journal of Computational Physics.* 2006, **220**(1), pp.216-248.

71. Sommerfeld, M., Bourloutski, E. and Bröder, D. Euler/Lagrange calculations of bubbly flows with consideration of bubble coalescence. *The Canadian Journal of Chemical Engineering.* 2003, **81**(3-4), pp.508-518.

72. Lau, Y.M., Bai, W., Deen, N.G. and Kuipers, J.A.M. Numerical study of bubble break-up in bubbly flows using a deterministic Euler-Lagrange framework. *Chemical Engineering Science.* 2014, **108**, pp.9-22.

73. Martínez-Bazán, C., Montañés, J.L. and Lasheras, J.C. On the breakup of an air bubble injected into a fully developed turbulent flow. Part 1. Breakup frequency. *Journal of Fluid Mechanics.* 1999, **401**, pp.157-182.

74. Martínez-Bazán, C., Montañés, J.L. and Lasheras, J.C. On the breakup of an air bubble injected into a fully developed turbulent flow. Part 2. Size PDF of the resulting daughter bubbles. *Journal of Fluid Mechanics.* 1999, **401**, pp.183-207.

75. Xu, J.I.N., Maxey, M.R. and Karniadakis, G.E. Numerical simulation of turbulent drag reduction using micro-bubbles. *Journal of Fluid Mechanics.* 2002, **468**, pp.271-281.

76. Pang, M.J., Wei, J.J. and Yu, B. Numerical study on modulation of microbubbles on turbulence frictional drag in a horizontal channel. *Ocean Engineering.* 2014, **81**, pp.58-68.

77. Hirt, C.W. and Nichols, B.D. Volume of fluid (VOF) method for the dynamics of free boundaries. *Journal of Computational Physics.* 1981, **39**(1), pp.201-225.

78. Osher, S. and Sethian, J.A. Fronts propagating with curvature-dependent speed: Algorithms based on Hamilton-Jacobi formulations. *Journal of Computational Physics.* 1988, **79**(1), pp.12-49.

79. Osher, S. and Fedkiw, R.P. Level set methods: An overview and some recent results. *Journal of Computational Physics.* 2001, **169**(2), pp.463-502.

80. Unverdi, S.O. and Tryggvason, G. A front-tracking method for viscous, incompressible, multi-fluid flows. *Journal of Computational Physics.* 1992, **100**(1), pp.25-37.

81. Esmaeeli, A. and Tryggvason, G. Direct numerical simulations of bubbly flows Part 2. Moderate Reynolds number arrays. *Journal of Fluid Mechanics.* 1999, **385**, pp.325-358.

82. Bunner, B. and Tryggvason, G. Dynamics of homogeneous bubbly flows Part 2. Velocity fluctuations. *Journal of Fluid Mechanics.* 2002, **466**, pp.53-84.

83. Tryggvason, G., Bunner, B., Esmaeeli, A., Juric, D., Al-Rawahi, N., Tauber, W., Han, J., Nas, S. and Jan, Y.J. A front-tracking method for the computations of multiphase flow. *Journal of Computational Physics.* 2001, **169**(2), pp.708-759.

84. Hua, J. and Lou, J. Numerical simulation of bubble rising in viscous liquid. *Journal of Computational Physics.* 2007, **222**(2), pp.769-795.

85. Hua, J., Stene, J.F. and Lin, P. Numerical simulation of 3D bubbles rising in viscous liquids using a front tracking method. *Journal of Computational Physics.* 2008, **227**(6), pp.3358-3382.

86. Dijkhuizen, W., van den Hengel, E.I.V., Deen, N.G., van Sint Annaland, M. and Kuipers, J.A.M. Numerical investigation of closures for interface forces acting on single air-bubbles in water using Volume of Fluid and Front Tracking models. *Chemical Engineering Science.* 2005, **60**(22), pp.6169-6175.

87. Aboulhasanzadeh, B., Thomas, S., Taeibi-Rahni, M. and Tryggvason, G. Multiscale computations of mass transfer from buoyant bubbles. *Chemical Engineering Science.* 2012, **75**, pp.456-467.

88. Esmaeeli, A. and Tryggvason, G. Direct numerical simulations of bubbly flows. Part 1. Low Reynolds number arrays. *Journal of Fluid Mechanics.* 1998, **377**, pp.313-345.

89. Bunner, B. and Tryggvason, G. Dynamics of homogeneous bubbly flows Part 1. Rise velocity and microstructure of the bubbles. *Journal of Fluid Mechanics.* 2002, **466**, pp.17-52.

90. Bunner, B. and Tryggvason, G. Effect of bubble deformation on the properties of bubbly flows. *Journal of Fluid Mechanics.* 2003, **495**, pp.77-118.

91. Esmaeeli, A. and Tryggvason, G. A direct numerical simulation study of the buoyant rise of bubbles at O(100) Reynolds number. *Physics of Fluids.* 2005, **17**(9), p.093303.

92. Lu, J., Biswas, S. and Tryggvason, G. A DNS study of laminar bubbly flows in a vertical channel. *International Journal of Multiphase Flow.* 2006, **32**(6), pp.643-660.

93. Dijkhuizen, W., Roghair, I., Van Sint Annaland, M. and Kuipers, J.A.M. DNS of gas bubbles behaviour using an improved 3D front tracking model-Drag force on isolated bubbles and comparison with experiments. *Chemical Engineering Science.* 2010, **65**(4), pp.1415-1426.

94. van Sint Annaland, M., Dijkhuizen, W., Deen, N.G. and Kuipers, J.A.M. Numerical simulation of behavior of gas bubbles using a 3-D front-tracking method. *AIChE Journal.* 2006, **52**(1), pp.99-110.

95. Lu, J. and Tryggvason, G. Numerical study of turbulent bubbly downflows in a vertical channel. *Physics of Fluids.* 2006, **18**(10), p.103302.

96. Lu, J. and Tryggvason, G. Effect of bubble size in turbulent bubbly downflow in a vertical channel. *Chemical Engineering Science.* 2007, **62**(11), pp.3008-3018.

97. Lu, J. and Tryggvason, G. Dynamics of nearly spherical bubbles in a turbulent channel upflow. *Journal of Fluid Mechanics.* 2013, **732**, pp.166-189.

98. Santarelli, C. and Fröhlich, J. Direct numerical simulations of spherical bubbles in vertical turbulent channel flow. Influence of bubble size and bidispersity. *International Journal of Multiphase Flow.* 2016, **81**, pp.27-45.

99. Lu, J. and Tryggvason, G. Effect of bubble deformability in turbulent bubbly upflow in a vertical channel. *Physics of Fluids.* 2008, **20**(4), p.040701.

100. Dabiri, S., Lu, J. and Tryggvason, G. Transition between regimes of a vertical channel bubbly upflow due to bubble deformability. *Physics of Fluids.* 2013, **25**(10), p.102110.

101. Bolotnov, I.A., Jansen, K.E., Drew, D.A., Oberai, A.A., Lahey, R.T., Jr. and Podowski, M.Z. Detached direct numerical simulations of turbulent two-phase bubbly channel flow. *International Journal of Multiphase Flow.* 2011, **37**(6), pp.647-659.

102. Tagawa, Y., Roghair, I., Prakash, V.N., van Sint Annaland, M., Kuipers, H., Sun, C. and Lohse, D. The clustering morphology of freely rising deformable bubbles. *Journal of Fluid Mechanics.* 2013, **721**, p.R2.

103. Grace, J.R. Shapes and velocities of bubbles rising in infinite liquids. *Transactions of the Institution of Chemical Engineers.* 1973, **51**(2), pp.116-120.

104. Deen, N.G., van Sint Annaland, M. and Kuipers, J.A.M. Multi-scale modeling of dispersed gas-liquid two-phase flow. *Chemical Engineering Science.* 2004, **59**(8-9), pp.1853-1861.

105. Roghair, I., Van Sint Annaland, M. and Kuipers, H.J.A.M. Drag force and clustering in bubble swarms. *AIChE Journal.* 2013, **59**(5), pp.1791-1800.

106. Roghair, I., Lau, Y.M., Deen, N.G., Slagter, H.M., Baltussen, M.W., Van Sint Annaland, M. and Kuipers, J.A.M. On the drag force of bubbles in bubble swarms at intermediate and high Reynolds numbers. *Chemical Engineering Science.* 2011, **66**(14), pp.3204-3211.

107. Lau, Y.M., Roghair, I., Deen, N.G., van Sint Annaland, M. and Kuipers, J.A.M. Numerical investigation of the drag closure for bubbles in bubble swarms. *Chemical Engineering Science.* 2011, **66**(14), pp.3309-3316.

108. Deen, N.G., Hjertager, B.H. and Solberg, T. Comparison of PIV and LDA measurement methods applied to the gas-liquid flow in a bubble column. In: *10th International symposium on applications of laser techniques to fluid mechanics, 10-13 July 2000, Lisbon, Portugal*. 2000.

109. Roghair, I., Baltussen, M.W., Van Sint Annaland, M. and Kuipers, J.A.M. Direct numerical simulations of the drag force of bi-disperse bubble swarms. *Chemical Engineering Science.* 2013, **95**, pp.48-53.

110. Legendre, D. and Magnaudet, J. The lift force on a spherical bubble in a viscous linear shear flow. *Journal of Fluid Mechanics.* 1998, **368**, pp.81-126.

111. Bothe, D., Schmidtke, M. and Warnecke, H.-J. VOF-simulation of the lift force for single bubbles in a simple shear flow. *Chemical Engineering & Technology.* 2006, **29**(9), pp.1048-1053.

112. Auton, T.R. The lift force on a spherical body in a rotational flow. *Journal of Fluid Mechanics.* 2006, **183**, pp.199-218.

113. Adoua, R., Legendre, D. and Magnaudet, J. Reversal of the lift force on an oblate bubble in a weakly viscous linear shear flow. *Journal of Fluid Mechanics.* 2009, **628**, pp.23-41.

114. Dijkhuizen, W., van Sint Annaland, M. and Kuipers, J.A.M. Numerical and experimental investigation of the lift force on single bubbles. *Chemical Engineering Science.* 2010, **65**(3), pp.1274-1287.

115. Santarelli, C. and Fröhlich, J. Direct Numerical Simulations of spherical bubbles in vertical turbulent channel flow. *International Journal of Multiphase Flow.* 2015, **75**, pp.174-193.

116. Feng, J. and Bolotnov, I.A. Evaluation of bubble-induced turbulence using direct numerical simulation. *International Journal of Multiphase Flow.* 2017, **93**, pp.92-107.

117. Tsuji, Y., Tanaka, T. and Ishida, T. Lagrangian numerical simulation of plug flow of cohesionless particles in a horizontal pipe. *Powder Technology.* 1992, **71**(3), pp.239-250.

118. Breuer, M. and Alletto, M. Efficient simulation of particle-laden turbulent flows with high mass loadings using LES. *International Journal of Heat and Fluid Flow.* 2012, **35**, pp.2-12.

119. Sommerfeld, M. Validation of a stochastic Lagrangian modelling approach for inter-particle collisions in homogeneous isotropic turbulence. *International Journal of Multiphase Flow.* 2001, **27**(10), pp.1829-1858.

120. Crowe, C., Schwarzkopf, J., Sommerfeld, M. and Tsuji, Y. *Multiphase flows with droplets and particles.* 2nd ed. Boca Raton: CRC Press, 2011.

121. Chesters, A.K. Modelling of coalescence processes in fluid-liquid dispersions: a review of current understanding. *Chemical Engineering Research and Design.* 1991, **69**(A4), pp.259-270.

122. Liao, Y. and Lucas, D. A literature review on mechanisms and models for the coalescence process of fluid particles. *Chemical Engineering Science.* 2010, **65**(10), pp.2851-2864.

123. Shinnar, R. and Church, J.M. Statistical theories of turbulence in predicting particle size in agitated dispersions. *Industrial & Engineering Chemistry.* 1960, **52**(3), pp.253-256.

124. Oolman, T.O. and Blanch, H.W. Bubble coalescence in stagnant liquids. *Chemical Engineering Communications.* 1986, **43**(4-6), pp.237-261.

125. Kamp, A.M., Chesters, A.K., Colin, C. and Fabre, J. Bubble coalescence in turbulent flows: A mechanistic model for turbulence-induced coalescence applied

to microgravity bubbly pipe flow. *International Journal of Multiphase Flow.* 2001, **27**(8), pp.1363-1396.

126. Chesters, A.K. and Hofman, G. Bubble coalescence in pure liquids. In: van Wijngaarden, L. ed. *Mechanics and Physics of Bubbles in Liquids, 15-19 June 1981, Pasadena, California*. Dordrecht: Springer, 1982, pp.353-361.

127. Hoppe, F. and Breuer, M. A deterministic and viable coalescence model for Euler-Lagrange simulations of turbulent microbubble-laden flows. *International Journal of Multiphase Flow.* 2018, **99**, pp.213-230.

128. Xue, J., Chen, F., Yang, N. and Ge, W. Eulerian-Lagrangian simulation of bubble coalescence in bubbly flow using the spring-dashpot model. *Chinese Journal of Chemical Engineering.* 2017, **25**(3), pp.249-256.

129. Asiagbe, K.S., Fairweather, M., Njobuenwu, D.O. and Colombo, M. Large eddy simulation of microbubble transport in a turbulent horizontal channel flow. *International Journal of Multiphase Flow.* 2017, **94**, pp.80-93.

130. Witz, C., Treffer, D., Hardiman, T. and Khinast, J. Local gas holdup simulation and validation of industrial-scale aerated bioreactors. *Chemical Engineering Science.* 2016, **152**, pp.636-648.

131. Jain, D., Kuipers, J.A.M. and Deen, N.G. Numerical modeling of carbon dioxide chemisorption in sodium hydroxide solution in a micro-structured bubble column. *Chemical Engineering Science.* 2015, **137**, pp.685-696.

132. Jain, D., Kuipers, J.A.M. and Deen, N.G. Numerical study of coalescence and breakup in a bubble column using a hybrid volume of fluid and discrete bubble model approach. *Chemical Engineering Science.* 2014, **119**, pp.134-146.

133. Mackay, G.D.M. and Mason, S.G. The gravity approach and coalescence of fluid drops at liquid interfaces. *The Canadian Journal of Chemical Engineering.* 1963, **41**(5), pp.203-212.

134. Chesters, A.K. The applicability of dynamic-similarity criteria to isothermal, liquid-gas, two-phase flows without mass transfer. *International Journal of Multiphase Flow.* 1975, **2**(2), pp.191-212.

135. Howarth, W.J. Coalescence of drops in a turbulent flow field. *Chemical Engineering Science.* 1964, **19**(1), pp.33-38.

136. Howarth, W.J. Measurement of coalescence frequency in an agitated tank. *AIChE Journal.* 1967, **13**(5), pp.1007-1013.

137. Sovová, H. Breakage and coalescence of drops in a batch stirred vessel-II comparison of model and experiments. *Chemical Engineering Science.* 1981, **36**(9), pp.1567-1573.

138. Simon, M. *Koaleszenz von tropfen und tropfenschwärmen*. Ph.D. thesis, TU Kaiserslautern, 2004.

139. Lehr, F., Millies, M. and Mewes, D. Bubble-size distributions and flow fields in bubble columns. *AIChE Journal.* 2002, **48**(11), pp.2426-2443.

140. Serizawa, A., Kataoka, I. and Michiyoshi, I. Turbulence structure of air-water bubbly flow-I. measuring techniques. *International Journal of Multiphase Flow.* 1975, **2**(3), pp.221-233.

141. Serizawa, A., Kataoka, I. and Michiyoshi, I. Turbulence structure of air-water bubbly flow-II. local properties. *International Journal of Multiphase Flow.* 1975, **2**(3), pp.235-246.

142. Serizawa, A., Kataoka, I. and Michiyoshi, I. Turbulence structure of air-water bubbly flow-III. transport properties. *International Journal of Multiphase Flow.* 1975, **2**(3), pp.247-259.

143. Sato, Y. and Sekoguchi, K. Liquid velocity distribution in two-phase bubble flow. *International Journal of Multiphase Flow.* 1975, **2**(1), pp.79-95.

144. Theofanous, T. and Sullivan, J. Turbulence in two-phase dispersed flows. *Journal of Fluid Mechanics.* 1982, **116**, pp.343-362.

145. Van Der Welle, R. Void fraction, bubble velocity and bubble size in two-phase flow. *International Journal of Multiphase Flow.* 1985, **11**(3), pp.317-345.

146. Wang, S.K., Lee, S.J., Jones, O.C. and Lahey, R.T. 3-D turbulence structure and phase distribution measurements in bubbly two-phase flows. *International Journal of Multiphase Flow.* 1987, **13**(3), pp.327-343.

147. Hesketh, R.P., Etchells, A.W. and Russell, T.W.F. Experimental observations of bubble breakage in turbulent flow. *Industrial & Engineering Chemistry Research.* 1991, **30**(5), pp.835-841.

148. Liu, T.J. and Bankoff, S.G. Structure of air-water bubbly flow in a vertical pipe-I. Liquid mean velocity and turbulence measurements. *International Journal of Heat and Mass Transfer.* 1993, **36**(4), pp.1049-1060.

149. Liu, T.J. and Bankoff, S.G. Structure of air-water bubbly flow in a vertical pipe-II. Void fraction, bubble velocity and bubble size distribution. *International Journal of Heat and Mass Transfer.* 1993, **36**(4), pp.1061-1072.

150. Ohnuki, A. and Akimoto, H. An experimental study on developing air-water two-phase flow along a large vertical pipe: Effect of air injection method. *International Journal of Multiphase Flow.* 1996, **22**(6), pp.1143-1154.

151. Nakoryakov, V.E., Kashinsky, O.N., Randin, V.V. and Timkin, L.S. Gas-liquid bubbly flow in vertical pipes. *Journal of Fluids Engineering.* 1996, **118**(2), pp.377-382.

152. Kashinsky, O.N. and Randin, V.V. Downward bubbly gas-liquid flow in a vertical pipe. *International Journal of Multiphase Flow.* 1999, **25**(1), pp.109-138.

153. Yoneda, K., Yasuo, A. and Okawa, T. Flow structure and bubble characteristics of steam-water two-phase flow in a large-diameter pipe. *Nuclear Engineering and Design.* 2002, **217**(3), pp.267-281.

154. Guet, S., Ooms, G., Oliemans, R.V.A. and Mudde, R.F. Bubble injector effect on the gaslift efficiency. *AIChE Journal.* 2003, **49**(9), pp.2242-2252.

155. Guet, S., Ooms, G., Oliemans, R.V.A. and Mudde, R.F. Bubble size effect on low liquid input drift-flux parameters. *Chemical Engineering Science.* 2004, **59**(16), pp.3315-3329.

156. Fujiwara, A., Minato, D. and Hishida, K. Effect of bubble diameter on modification of turbulence in an upward pipe flow. *International Journal of Heat and Fluid Flow.* 2004, **25**(3), pp.481-488.

157. Shen, X., Mishima, K. and Nakamura, H. Two-phase phase distribution in a vertical large diameter pipe. *International Journal of Heat and Mass Transfer.* 2005, **48**(1), pp.211-225.

158. Descamps, M.N., Oliemans, R.V.A., Ooms, G. and Mudde, R.F. Air-water flow in a vertical pipe: experimental study of air bubbles in the vicinity of the wall. *Experiments in Fluids.* 2008, **45**(2), pp.357-370.

159. Shawkat, M.E., Ching, C.Y. and Shoukri, M. On the liquid turbulence energy spectra in two-phase bubbly flow in a large diameter vertical pipe. *International Journal of Multiphase Flow.* 2007, **33**(3), pp.300-316.

160. Shawkat, M.E., Ching, C.Y. and Shoukri, M. Bubble and liquid turbulence characteristics of bubbly flow in a large diameter vertical pipe. *International Journal of Multiphase Flow.* 2008, **34**(8), pp.767-785.

161. Nakagawa, M., Koyasu, M., Tanaka, T., Sato, Y. and Hishida, K. Transport mechanisms of turbulent kinetic energy in upward bubbly pipe flow. In: *14th international symposium on application of laser techniques to fluid mechanics, Lisbon, Portugal*. 2008.

162. Shawkat, M.E. and Ching, C.Y. Liquid turbulence kinetic energy budget of co-current bubbly flow in a large diameter vertical pipe. *Journal of Fluids Engineering.* 2011, **133**(9), pp.091303-091303-091314.

163. Lelouvetel, J., Nakagawa, M., Sato, Y. and Hishida, K. Effect of bubbles on turbulent kinetic energy transport in downward flow measured by time-resolved PTV. *Experiments in Fluids.* 2011, **50**(4), pp.813-823.

164. Smith, T.R., Schlegel, J.P., Hibiki, T. and Ishii, M. Two-phase flow structure in large diameter pipes. *International Journal of Heat and Fluid Flow.* 2012, **33**(1), pp.156-167.

165. Lelouvetel, J., Tanaka, T., Sato, Y. and Hishida, K. Transport mechanisms of the turbulent energy cascade in upward/downward bubbly flows. *Journal of Fluid Mechanics.* 2014, **741**, pp.514-542.

166. Ohnuki, A. and Akimoto, H. Experimental study on transition of flow pattern and phase distribution in upward air-water two-phase flow along a large vertical pipe. *International Journal of Multiphase Flow.* 2000, **26**(3), pp.367-386.

167. Mendez-Diaz, S., Zenit, R., Chiva, S., Muñoz-Cobo, J.L. and Martinez-Martinez, S. A criterion for the transition from wall to core peak gas volume fraction distributions in bubbly flows. *International Journal of Multiphase Flow.* 2012, **43**, pp.56-61.

168. Kataoka, I. Local instant formulation of two-phase flow. *International Journal of Multiphase Flow.* 1986, **12**(5), pp.745-758.

169. Kataoka, I. and Serizawa, A. Basic equations of turbulence in gas-liquid two-phase flow. *International Journal of Multiphase Flow.* 1989, **15**(5), pp.843-855.

170. Lance, M. and Bataille, J. Turbulence in the liquid phase of a uniform bubbly air-water flow. *Journal of Fluid Mechanics.* 1991, **222**, pp.95-118.

171. Lunde, K. and Perkins, R.J. Shape Oscillations of Rising Bubbles. *Applied Scientific Research.* 1997, **58**(1), pp.387-408.

172. Deshpande, N.S., Prasad, C.V., Kulkarni, A.A. and Joshi, J.B. Hydrodynamic characterization of dispersed two-phase flows by laser doppler velocimeter. *Chemical Engineering Research and Design.* 2000, **78**(6), pp.903-910.

173. Murai, Y., Song, X.-q., Takagi, T., Ishikawa, M.-a., Yamamoto, F. and Ohta, J. Inverse energy cascade structure of turbulence in a bubbly flow : PIV measurment and results. *JSME International Journal Series B.* 2000, **43**(2), pp.188-196.

174. Ellingsen, K. and Risso, F. On the rise of an ellipsoidal bubble in water: oscillatory paths and liquid-induced velocity. *Journal of Fluid Mechanics.* 2001, **440**, pp.235-268.

175. So, S., Morikita, H., Takagi, S. and Matsumoto, Y. Laser Doppler velocimetry measurement of turbulent bubbly channel flow. *Experiments in Fluids.* 2002, **33**(1), pp.135-142.

176. Wu, M. and Gharib, M. Experimental studies on the shape and path of small air bubbles rising in clean water. *Physics of Fluids.* 2002, **14**(7), pp.L49-L52.

177. Zenit, R., Tsang, Y.H., Koch, D.L. and Sangani, A.S. Shear flow of a suspension of bubbles rising in an inclined channel. *Journal of Fluid Mechanics.* 2004, **515**, pp.261-292.

178. Rensen, J., Luther, S. and Lohse, D. The effect of bubbles on developed turbulence. *Journal of Fluid Mechanics.* 2005, **538**, pp.153-187.

179. Luther, S., Rensen, J., van den Berg, T.H. and Lohse, D. Data analysis for hot-film anemometry in turbulent bubbly flow. *Experimental Thermal and Fluid Science.* 2005, **29**(7), pp.821-826.

180. Martínez-Mercado, J., Palacios-Morales, C.A. and Zenit, R. Measurement of pseudoturbulence intensity in monodispersed bubbly liquids for $10 < Re < 500$. *Physics of Fluids.* 2007, **19**(10), p.103302.

181. Riboux, G., Risso, F. and Legendre, D. Experimental characterization of the agitation generated by bubbles rising at high Reynolds number. *Journal of Fluid Mechanics.* 2010, **643**, pp.509-539.

182. Martínez-Mercado, J., Chehata Gómez, D., Van Gils, D., Sun, C. and Lohse, D. On bubble clustering and energy spectra in pseudo-turbulence. *Journal of Fluid Mechanics.* 2010, **650**, pp.287-306.

183. Bouche, E., Roig, V., Risso, F. and Billet, A.-M. Homogeneous swarm of high-Reynolds-number bubbles rising within a thin gap. Part 1. Bubble dynamics. *Journal of Fluid Mechanics.* 2012, **704**, pp.211-231.

184. Bouche, E., Cazin, S., Roig, V. and Risso, F. Mixing in a swarm of bubbles rising in a confined cell measured by mean of PLIF with two different dyes. *Experiments in Fluids.* 2013, **54**(6), pp.1-9.

185. Sathe, M., Joshi, J. and Evans, G. Characterization of turbulence in rectangular bubble column. *Chemical Engineering Science.* 2013, **100**, pp.52-68.

186. Mendez-Diaz, S., Serrano-García, J.C., Zenit, R. and Hernández-Cordero, J.A. Power spectral distributions of pseudo-turbulent bubbly flows. *Physics of Fluids.* 2013, **25**(4), p.043303.

187. Bouche, E., Roig, V., Risso, F. and Billet, A.-M. Homogeneous swarm of high-Reynolds-number bubbles rising within a thin gap. Part 2. Liquid dynamics. *Journal of Fluid Mechanics.* 2014, **758**, pp.508-521.

188. Liu, T.-J. Investigation of the wall shear stress in vertical bubbly flow under different bubble size conditions. *International Journal of Multiphase Flow.* 1997, **23**(6), pp.1085-1109.

189. Esmaeeli, A. and Tryggvason, G. An inverse energy cascade in two-dimensional low Reynolds number bubbly flows. *Journal of Fluid Mechanics.* 1996, **314**, pp.315-330.

190. Moin, P. and Mahesh, K. Direct numerical simulation: A tool in turbulence research. *Annual Review of Fluid Mechanics.* 1998, **30**(1), pp.539-578.

191. Roelofs, F. and Shams, A. 6 - CFD—Introduction. In: Roelofs, F. ed. *Thermal Hydraulics Aspects of Liquid Metal Cooled Nuclear Reactors*. Woodhead Publishing, 2019, pp.213-218.

192. Kim, J.J. *Investigation of separation and reattachment of a turbulent shear layer: flow over a backward-facing step*. Ph.D thesis, Stanford University, 1978.

193. Schlatter, P., Örlü, R., Li, Q., Brethouwer, G., Fransson, J.H.M., Johansson, A.V., Alfredsson, P.H. and Henningson, D.S. Turbulent boundary layers up to Re_θ = 2500 studied through simulation and experiment. *Physics of Fluids.* 2009, **21**(5), p.051702.

194. Yeung, P.K., Donzis, D.A. and Sreenivasan, K.R. Dissipation, enstrophy and pressure statistics in turbulence simulations at high Reynolds numbers. *Journal of Fluid Mechanics.* 2012, **700**, pp.5-15.

195. Sillero, J.A., Jiménez, J. and Moser, R.D. One-point statistics for turbulent wall-bounded flows at Reynolds numbers up to $\delta^+ \approx 2000$. *Physics of Fluids.* 2013, **25**(10), p.105102.

196. Laizet, S., Nedić, J. and Vassilicos, C. Influence of the spatial resolution on fine-scale features in DNS of turbulence generated by a single square grid. *International Journal of Computational Fluid Dynamics.* 2015, **29**(3-5), pp.286-302.

197. Orzag, S. Comparison of pseudospectral and spectral approximations. *Stud. Appl. Math.* 1972, **51**, pp.253-259.

198. Patera, A.T. A spectral element method for fluid dynamics: Laminar flow in a channel expansion. *Journal of Computational Physics.* 1984, **54**(3), pp.468-488.

199. Fischer, P., Kruse, J., Mullen, J., Tufo, H., Lottes, J. and Kerkemeier, S. *Nek5000: Open source spectral element CFD solver.* [Online]. 2008. [Accessed 25 Oct 2016]. Available from: https://nek5000.mcs.anl.gov

200. Ohlsson, J., Schlatter, P., Fischer, P.F. and Henningson, D.S. Direct numerical simulation of separated flow in a three-dimensional diffuser. *Journal of Fluid Mechanics.* 2010, **650**, pp.307-318.

201. Giannakopoulos, G.K., Frouzakis, C.E., Boulouchos, K., Fischer, P.F. and Tomboulides, A.G. Direct numerical simulation of the flow in the intake pipe of an internal combustion engine. *International Journal of Heat and Fluid Flow.* 2017, **68**, pp.257-268.

202. Hosseini, S.M., Vinuesa, R., Schlatter, P., Hanifi, A. and Henningson, D.S. Direct numerical simulation of the flow around a wing section at moderate Reynolds number. *International Journal of Heat and Fluid Flow.* 2016, **61**, pp.117-128.

203. Mortimer, L.F., Njobuenwu, D.O. and Fairweather, M. Near-wall dynamics of inertial particles in dilute turbulent channel flows. *Physics of Fluids.* 2019, **31**(6), p.063302.

204. Sardina, G., Schlatter, P., Brandt, L., Picano, F. and Casciola, C.M. Wall accumulation and spatial localization in particle-laden wall flows. *Journal of Fluid Mechanics.* 2012, **699**, pp.50-78.

205. Maday, Y. and Patera, A.T. *Spectral element methods for the incompressible Navier-Stokes equations.* New York: American Society of Mechanical Engineer, 1989.

206. Deville, M.O., Fischer, P.F., Fischer, P.F. and Mund, E. *High-order methods for incompressible fluid flow.* Cambridge: Cambridge University Press, 2002.

207. Naumann, Z. and Schiller, L. A drag coefficient correlation. *Z Ver Deutsch Ing.* 1935, **77**, pp.318-323.

208. Brennen, C.E. *A review of added mass and fluid inertial forces.* Port Hueneme, California: Naval Civil Engineering Laboratory, 1982.

209. Maxey, M.R. and Riley, J.J. Equation of motion for a small rigid sphere in a nonuniform flow. *Physics of Fluids.* 1983, **26**(4), pp.883-889.

210. Noorani, A., Sardina, G., Brandt, L. and Schlatter, P. Particle transport in turbulent curved pipe flow. *Journal of Fluid Mechanics.* 2016, **793**, pp.248-279.

211. Noorani, A., Peplinski, A. and Schlatter, P. *Informal introduction to program structure of spectral interpolation in nek5000.* [Online]. Stockholm: KTH Royal Institute of Technology, 2015. [Accessed 1 May 2019]. Available from: https://www.kth.se/social/group/simex/page/publications-3/

212. Watanabe, T. and Gotoh, T. On the smoothing of point force in the two-way coupling simulation of polymer-laden turbulent flow. *Journal of Physics: Conference Series.* 2018, **1035**, p.012010.

213. Fraga, B., Stoesser, T., Lai, C.C.K. and Socolofsky, S.A. A LES-based Eulerian-Lagrangian approach to predict the dynamics of bubble plumes. *Ocean Modelling.* 2016, **97**, pp.27-36.

214. Yamamoto, Y., Potthoff, M., Tanaka, T., Kajishima, T. and Tsuji, Y. Large-eddy simulation of turbulent gas-particle flow in a vertical channel: Effect of considering inter-particle collisions. *Journal of Fluid Mechanics.* 2001, **442**, pp.303-334.

215. Breuer, M. and Almohammed, N. Modeling and simulation of particle agglomeration in turbulent flows using a hard-sphere model with deterministic collision detection and enhanced structure models. *International Journal of Multiphase Flow.* 2015, **73**, pp.171-206.

216. Cifani, P., Kuerten, J.G.M. and Geurts, B.J. Highly scalable DNS solver for turbulent bubble-laden channel flow. *Computers & Fluids.* 2018, **172**, pp.67-83.

217. Cifani, P., Michalek, W.R., Priems, G.J.M., Kuerten, J.G.M., van der Geld, C.W.M. and Geurts, B.J. A comparison between the surface compression method and an interface reconstruction method for the VOF approach. *Computers & Fluids.* 2016, **136**, pp.421-435.

218. Pathak, A. and Raessi, M. A three-dimensional volume-of-fluid method for reconstructing and advecting three-material interfaces forming contact lines. *Journal of Computational Physics.* 2016, **307**, pp.550-573.

219. Udaykumar, H.S., Mittal, R. and Rampunggoon, P. Interface tracking finite volume method for complex solid–fluid interactions on fixed meshes. *Communications in Numerical Methods in Engineering.* 2002, **18**(2), pp.89-97.

220. Ferziger, J.H. and Perić, M. *Computational methods for fluid dynamics.* 3rd ed. Heidelberg: Springer, 2002.

221. Lorinczi, P., Burns, A.D., Lesnic, D., Fisher, Q.J., Crook, A.J., Grattoni, C. and Rybalcenko, K. Modelling of gas flow in shale using a finite volume method. *Applied Mathematical Modelling.* 2017, **49**, pp.394-414.

222. Vreman, A.W. The projection method for the incompressible Navier-Stokes equations: The pressure near a no-slip wall. *Journal of Computational Physics.* 2014, **263**, pp.353-374.

223. Meier, H.F., Alves, J.J.N. and Mori, M. Comparison between staggered and collocated grids in the finite-volume method performance for single and multi-phase flows. *Computers & Chemical Engineering.* 1999, **23**(3), pp.247-262.

224. Rhie, C.M. and Chow, W.L. Numerical study of the turbulent flow past an airfoil with trailing edge separation. *AIAA Journal.* 1983, **21**(11), pp.1525-1532.

225. Verstappen, R.W.C.P. and Veldman, A.E.P. Symmetry-preserving discretization of turbulent flow. *Journal of Computational Physics.* 2003, **187**(1), pp.343-368.

226. Lei, Z. and Qiu, C. A stochastic variational formulation for nonlinear dynamic analysis of structure. *Computer Methods in Applied Mechanics and Engineering.* 2000, **190**(5), pp.597-608.

227. Denner, F. and van Wachem, B.G.M. Numerical time-step restrictions as a result of capillary waves. *Journal of Computational Physics.* 2015, **285**, pp.24-40.

228. Wesseling, P. *Principles of computational fluid dynamics.* Heidelberg: Springer, 2001.

229. Lee, M.J., Oh, B.D. and Kim, Y.B. Canonical fractional-step methods and consistent boundary conditions for the incompressible Navier-Stokes equations. *Journal of Computational Physics.* 2001, **168**(1), pp.73-100.

230. Capuano, F., Coppola, G., Rández, L. and de Luca, L. Explicit Runge-Kutta schemes for incompressible flow with improved energy-conservation properties. *Journal of Computational Physics.* 2017, **328**, pp.86-94.

231. Mohan Rai, M. and Moin, P. Direct simulations of turbulent flow using finite-difference schemes. *Journal of Computational Physics.* 1991, **96**(1), pp.15-53.

232. Chorin, A.J. Numerical solution of the Navier-Stokes equations. *Mathematics of computation.* 1968, **22**(104), pp.745-762.

233. Dong, S. and Shen, J. A time-stepping scheme involving constant coefficient matrices for phase-field simulations of two-phase incompressible flows with large density ratios. *Journal of Computational Physics.* 2012, **231**(17), pp.5788-5804.

234. Dodd, M.S. and Ferrante, A. A fast pressure-correction method for incompressible two-fluid flows. *Journal of Computational Physics.* 2014, **273**, pp.416-434.

235. Brackbill, J.U., Kothe, D.B. and Zemach, C. A continuum method for modeling surface tension. *Journal of Computational Physics.* 1992, **100**(2), pp.335-354.

236. Francois, M.M., Cummins, S.J., Dendy, E.D., Kothe, D.B., Sicilian, J.M. and Williams, M.W. A balanced-force algorithm for continuous and sharp interfacial surface tension models within a volume tracking framework. *Journal of Computational Physics.* 2006, **213**(1), pp.141-173.

237. Meier, M., Yadigaroglu, G. and Smith, B.L. A novel technique for including surface tension in PLIC-VOF methods. *European Journal of Mechanics - B/Fluids.* 2002, **21**(1), pp.61-73.

238. Cummins, S.J., Francois, M.M. and Kothe, D.B. Estimating curvature from volume fractions. *Computers & Structures.* 2005, **83**(6), pp.425-434.

239. Popinet, S. An accurate adaptive solver for surface-tension-driven interfacial flows. *Journal of Computational Physics.* 2009, **228**(16), pp.5838-5866.

240. Coyajee, E. and Boersma, B.J. Numerical simulation of drop impact on a liquid-liquid interface with a multiple marker front-capturing method. *Journal of Computational Physics.* 2009, **228**(12), pp.4444-4467.

241. Kwakkel, M., Breugem, W.-P. and Boersma, B.J. An efficient multiple marker front-capturing method for two-phase flows. *Computers & Fluids.* 2012, **63**, pp.47-56.

242. Kwakkel, M., Breugem, W.-P. and Boersma, B.J. Extension of a CLSVOF method for droplet-laden flows with a coalescence/breakup model. *Journal of Computational Physics.* 2013, **253**, pp.166-188.

243. Scardovelli, R. and Zaleski, S. Direct numerical simulation of free-surface and interfacial flow. *Annual Review of Fluid Mechanics.* 1999, **31**(1), pp.567-603.

244. Fuster, D., Bagué, A., Boeck, T., Le Moyne, L., Leboissetier, A., Popinet, S., Ray, P., Scardovelli, R. and Zaleski, S. Simulation of primary atomization with an octree adaptive mesh refinement and VOF method. *International Journal of Multiphase Flow.* 2009, **35**(6), pp.550-565.

245. Aulisa, E., Manservisi, S., Scardovelli, R. and Zaleski, S. Interface reconstruction with least-squares fit and split advection in three-dimensional Cartesian geometry. *Journal of Computational Physics.* 2007, **225**(2), pp.2301-2319.

246. Rider, W.J. and Kothe, D.B. Reconstructing Volume Tracking. *Journal of Computational Physics.* 1998, **141**(2), pp.112-152.

247. Deutsch, S. and Castano, J. Microbubble skin friction reduction on an axisymmetric body. *The Physics of Fluids.* 1986, **29**(11), pp.3590-3597.

248. Madavan, N.K., Deutsch, S. and Merkle, C.L. Reduction of turbulent skin friction by microbubbles. *The Physics of Fluids.* 1984, **27**(2), pp.356-363.

249. Pal, S., Merkle, C.L. and Deutsch, S. Bubble characteristics and trajectories in a microbubble boundary layer. *The Physics of Fluids.* 1988, **31**(4), pp.744-751.

250. Worden, R.M. and Bredwell, M.D. Mass-transfer properties of microbubbles. 2. Analysis using a dynamic model. *Biotechnology Progress.* 1998, **14**(1), pp.39-46.

251. Maxey, M.R., Chang, E.J. and Wang, L.P. Simulation of interactions between microbubbles and turbulent Flows. *Applied Mechanics Reviews.* 1994, **47**(6S), pp.S70-S74.

252. Lu, J., Corvalan, C.M., Chew, Y.M.J. and Huang, J.-Y. Coalescence of small bubbles with surfactants. *Chemical Engineering Science.* 2019, **196**, pp.493-500.

253. Asiagbe, K.S., Fairweather, M., Njobuenwu, D.O. and Colombo, M. Large eddy simulation of microbubble dispersion and flow field modulation in vertical channel flows. *AIChE Journal.* 2019, **65**(4), pp.1325-1339.

254. Shinnar, R. On the behaviour of liquid dispersions in mixing vessels. *Journal of Fluid Mechanics.* 1961, **10**(2), pp.259-275.

255. Chen, R., Yu, H., Zhu, L., Patil, R.M. and Lee, T. Spatial and temporal scaling of unequal microbubble coalescence. *AIChE Journal.* 2017, **63**(4), pp.1441-1450.

256. Takagi, S. and Matsumoto, Y. Surfactant effects on bubble motion and bubbly flows. *Annual Review of Fluid Mechanics.* 2011, **43**(1), pp.615-636.

257. Moser, R.D., Kim, J. and Mansour, N.N. Direct numerical simulation of turbulent channel flow up to $Re_\tau = 590$. *Physics of Fluids.* 1999, **11**(4), pp.943-945.

258. Tryggvason, G., Ma, M. and Lu, J. DNS-Assisted modeling of bubbly flows in vertical channels. *Nuclear Science and Engineering.* 2016, **184**(3), pp.312-320.

259. Marchioli, C., Picciotto, M. and Soldati, A. Particle dispersion and wall-dependent turbulent flow scales: implications for local equilibrium models. *Journal of Turbulence.* 2006, **7**, p.N60.

260. Wen, L.H., Ismail, A.B., Menon, P.M., Saththasivam, J., Thu, K. and Choon, N.K. Case studies of microbubbles in wastewater treatment. *Desalination and Water Treatment.* 2011, **30**(1-3), pp.10-16.

261. Grace, J. Shapes and velocities of single drops and bubbles moving freely through immiscible liquids. *Chemical Engineering Research and Design.* 1976, **54**, pp.167-173.

262. Elghobashi, S. and Truesdell, G.C. Direct simulation of particle dispersion in a decaying isotropic turbulence. *Journal of Fluid Mechanics.* 1992, **242**, pp.655-700.

263. Kulkarni, A.A. Lift force on bubbles in a bubble column reactor: Experimental analysis. *Chemical Engineering Science.* 2008, **63**(6), pp.1710-1723.

264. Harleman, M.J.W., Delfos, R., Terwisga, T.J.C.v. and Westerweel, J. Dispersion of bubbles in fully developed channel flow. *Journal of Physics: Conference Series.* 2011, **318**(5), p.052007.

265. Thomas, N., Auton, T., Sene, K. and Hunt, J. Entrapment and transport of bubbles by transient large eddies in multiphase turbulent shear flows. In: *International conference on the physical modelling of multi-phase flow, 19-21 April 1983, Coventry*. BHRA, 1983, pp.169-184.

266. Ounis, H., Ahmadi, G. and McLaughlin, J.B. Dispersion and deposition of Brownian particles from point sources in a simulated turbulent channel flow. *Journal of Colloid and Interface Science.* 1991, **147**(1), pp.233-250.

267. Chen, M. and McLaughlin, J.B. A new correlation for the aerosol deposition rate in vertical ducts. *Journal of Colloid and Interface Science.* 1995, **169**(2), pp.437-455.

268. Coulaloglou, C.A. and Tavlarides, L.L. Description of interaction processes in agitated liquid-liquid dispersions. *Chemical Engineering Science.* 1977, **32**(11), pp.1289-1297.

269. Svendsen, H.F. and Luo, H. Modeling of approach processes for equal or unequal sized fluid particles. *The Canadian Journal of Chemical Engineering.* 1996, **74**(3), pp.321-330.

270. Gong, S., Han, L. and Luo, H.a. A novel multiscale theoretical model for droplet coalescence induced by turbulence in the framework of entire energy spectrum. *Chemical Engineering Science.* 2018, **176**, pp.377-399.

271. Kirkpatrick, R.D. and Lockett, M.J. The influence of approach velocity on bubble coalescence. *Chemical Engineering Science.* 1974, **29**(12), pp.2363-2373.

272. Jain, D., Lau, Y.M., Kuipers, J.A.M. and Deen, N.G. Discrete bubble modeling for a micro-structured bubble column. *Chemical Engineering Science.* 2013, **100**, pp.496-505.

273. Tsouris, C. and Tavlarides, L.L. Breakage and coalescence models for drops in turbulent dispersions. *AIChE Journal.* 1994, **40**(3), pp.395-406.

274. Eskin, D., Leonenko, Y. and Vinogradov, O. Theoretical estimates of air bubble behavior in dense pipeline slurry flows. *Chemical Engineering and Processing: Process Intensification.* 2004, **43**(6), pp.727-737.

275. Doubliez, L. The drainage and rupture of a non-foaming liquid film formed upon bubble impact with a free surface. *International Journal of Multiphase Flow.* 1991, **17**(6), pp.783-803.

276. Pope, S.B. *Turbulent flows.* Cambridge: Cambridge University Press, 2000.

277. Andrade, J.R., Martins, R.S., Mompean, G., Thais, L. and Gatski, T.B. Analyzing the spectral energy cascade in turbulent channel flow. *Physics of Fluids.* 2018, **30**(6), p.065110.

278. Kurose, R. and Komori, S. Drag and lift forces on a rotating sphere in a linear shear flow. *Journal of Fluid Mechanics.* 1999, **384**, pp.183-206.

279. Takemura, F. and Magnaudet, J. The transverse force on clean and contaminated bubbles rising near a vertical wall at moderate Reynolds number. *Journal of Fluid Mechanics.* 2003, **495**, pp.235-253.

280. Asiagbe, K.S., Fairweather, M., Njobuenwu, D.O. and Colombo, M. Microbubbles coalescence during transport in vertical channel flows. In: Friedl, A. et al. eds. *Computer Aided Chemical Engineering*. Elsevier, 2018, pp.79-84.

281. Kaftori, D., Hetsroni, G. and Banerjee, S. Particle behavior in the turbulent boundary layer. I. Motion, deposition, and entrainment. *Physics of Fluids.* 1995, **7**(5), pp.1095-1106.

282. Monty, J.P., Hutchins, N., Ng, H.C.H., Marusic, I. and Chong, M.S. A comparison of turbulent pipe, channel and boundary layer flows. *Journal of Fluid Mechanics.* 2009, **632**, pp.431-442.

283. Khoury, G.K.E., Schlatter, P., Brethouwer, G. and Johansson, A.V. Turbulent pipe flow: Statistics, *Re*-dependence, structures and similarities with channel and boundary layer flows. *Journal of Physics: Conference Series.* 2014, **506**, p.012010.

284. Heinz, S. On mean flow universality of turbulent wall flows. I. High Reynolds number flow analysis. *Journal of Turbulence.* 2019, **19**(11-12), pp.929-958.

285. Patel, V.C. and Head, M.R. Some observations on skin friction and velocity profiles in fully developed pipe and channel flows. *Journal of Fluid Mechanics.* 1969, **38**(1), pp.181-201.

286. Huffman, G.D. and Bradshaw, P. A note on von Kármán's constant in low Reynolds number turbulent flows. *Journal of Fluid Mechanics.* 1972, **53**(1), pp.45-60.

287. Jiménez, J. Cascades in wall-bounded turbulence. *Annual Review of Fluid Mechanics.* 2012, **44**(1), pp.27-45.

288. Jacob, B., Olivieri, A., Miozzi, M., Campana, E.F. and Piva, R. Drag reduction by microbubbles in a turbulent boundary layer. *Physics of Fluids.* 2010, **22**(11), p.115104.

289. Eggels, J.G.M., Unger, F., Weiss, M.H., Westerweel, J., Adrian, R.J., Friedrich, R. and Nieuwstadt, F.T.M. Fully developed turbulent pipe flow: a comparison between direct numerical simulation and experiment. *Journal of Fluid Mechanics.* 1994, **268**, pp.175-210.

290. Wu, X. and Moin, P. A direct numerical simulation study on the mean velocity characteristics in turbulent pipe flow. *Journal of Fluid Mechanics.* 2008, **608**, pp.81-112.

291. Ahn, J., Lee, J.H., Lee, J., Kang, J.-h. and Sung, H.J. Direct numerical simulation of a $30R$ long turbulent pipe flow at $Re_\tau = 3008$. *Physics of Fluids.* 2015, **27**(6), p.065110.

292. Kim, K.C. and Adrian, R.J. Very large-scale motion in the outer layer. *Physics of Fluids.* 1999, **11**(2), pp.417-422.

293. El Khoury, G.K., Schlatter, P., Noorani, A., Fischer, P.F., Brethouwer, G. and Johansson, A.V. Direct numerical simulation of turbulent pipe flow at moderately high Reynolds numbers. *Flow, Turbulence and Combustion.* 2013, **91**(3), pp.475-495.

294. Orlandi, P. and Fatica, M. Direct simulations of turbulent flow in a pipe rotating about its axis. *Journal of Fluid Mechanics.* 1997, **343**, pp.43-72.

295. Wagner, C., Hüttl, T.J. and Friedrich, R. Low-Reynolds-number effects derived from direct numerical simulations of turbulent pipe flow. *Computers & Fluids.* 2001, **30**(5), pp.581-590.

296. Chin, C., Ooi, A.S.H., Marusic, I. and Blackburn, H.M. The influence of pipe length on turbulence statistics computed from direct numerical simulation data. *Physics of Fluids.* 2010, **22**(11), p.115107.

297. Wu, X., Baltzer, J.R. and Adrian, R.J. Direct numerical simulation of a 30R long turbulent pipe flow at $R^+ = 685$: large- and very large-scale motions. *Journal of Fluid Mechanics.* 2012, **698**, pp.235-281.

298. Klewicki, J., Chin, C., Blackburn, H.M., Ooi, A. and Marusic, I. Emergence of the four layer dynamical regime in turbulent pipe flow. *Physics of Fluids.* 2012, **24**(4), p.045107.

299. Lee, J.H. and Sung, H.J. Comparison of very-large-scale motions of turbulent pipe and boundary layer simulations. *Physics of Fluids.* 2013, **25**(4), p.045103.

300. Chin, C., Monty, J.P. and Ooi, A. Reynolds number effects in DNS of pipe flow and comparison with channels and boundary layers. *International Journal of Heat and Fluid Flow.* 2014, **45**, pp.33-40.

301. Feldmann, D., Bauer, C. and Wagner, C. Computational domain length and Reynolds number effects on large-scale coherent motions in turbulent pipe flow. *Journal of Turbulence.* 2018, **19**(3), pp.274-295.

302. Kim, J., Moin, P. and Moser, R. Turbulence statistics in fully developed channel flow at low Reynolds number. *Journal of Fluid Mechanics.* 1987, **177**, pp.133-166.

303. Lote, D.A., Vinod, V. and Patwardhan, A.W. Computational fluid dynamics simulations of the air-water two-phase vertically upward bubbly flow in pipes. *Industrial & Engineering Chemistry Research.* 2018, **57**(31), pp.10609-10627.

304. Tomiyama, A. Struggle with computational bubble dynamics. *Multiphase Science and Technology.* 1998, **10**(4), pp.369-405.

305. Lahey, R.T., Lopez de Bertodano, M. and Jones, O.C. Phase distribution in complex geometry conduits. *Nuclear Engineering and Design.* 1993, **141**(1), pp.177-201.

306. Hibiki, T., Goda, H., Kim, S., Ishii, M. and Uhle, J. Structure of vertical downward bubbly flow. *International Journal of Heat and Mass Transfer.* 2004, **47**(8), pp.1847-1862.

307. Colin, C., Fabre, J. and Kamp, A. Turbulent bubbly flow in pipe under gravity and microgravity conditions. *Journal of Fluid Mechanics.* 2012, **711**, pp.469-515.

308. Nouri, N.M., Yekani Motlagh, S., Navidbakhsh, M., Dalilhaghi, M. and Moltani, A.A. Bubble effect on pressure drop reduction in upward pipe flow. *Experimental Thermal and Fluid Science.* 2013, **44**, pp.592-598.

309. Abdulbari, H.A., Yunus, R.M., Abdurahman, N.H. and Charles, A. Going against the flow-A review of non-additive means of drag reduction. *Journal of Industrial and Engineering Chemistry.* 2013, **19**(1), pp.27-36.

310. Shatat, M.M.E., Yanase, S., Takami, T. and Hyakutake, T. Drag reduction effects of micro-bubbles in straight and helical pipes. *Journal of Fluid Science and Technology.* 2009, **4**(1), pp.156-167.

311. Yonemoto, Y., Yanagisawa, H., Kawara, Z. and Kunugi, T. Coalescence of microbubble. *Journal of JSEM.* 2008, **8**(1), pp.38-44.

312. Antoranz, A., Gonzalo, A., Flores, O. and García-Villalba, M. Numerical simulation of heat transfer in a pipe with non-homogeneous thermal boundary conditions. *International Journal of Heat and Fluid Flow.* 2015, **55**, pp.45-51.

313. Hadamard, J. Mouvement permanent lent d'une sphère liquid et visqueuse dans un liquide visqueux. *CR Hebd. Seances Acad. Sci. Paris.* 1911, **152**, pp.1735-1738.

314. Rybczynski, W. Uber die fortschreitende Bewegung einer flussigen Kugel in einem zahen Medium. *Bull. Acad. Sci. Cracovie A.* 1911, **1**, pp.40-46.

315. Moore, D.W. The boundary layer on a spherical gas bubble. *Journal of Fluid Mechanics.* 1962, **16**(2), pp.161-176.

316. Tomiyama, A., Kataoka, I., Zun, I. and Sakaguchi, T. Drag coefficients of single bubbles under normal and micro gravity conditions. *JSME International Journal Series B Fluids and Thermal Engineering.* 1998, **41**(2), pp.472-479.

317. Veldhuis, C. *Leonardo's paradox: Path and shape instabilities of particles and bubbles*. Ph.D thesis, University of Twente, 2007.

318. Feng, J. and Bolotnov, I.A. Interfacial force study on a single bubble in laminar and turbulent flows. *Nuclear Engineering and Design.* 2017, **313**, pp.345-360.

319. Feng, J. and Bolotnov, I.A. Effect of the wall presence on the bubble interfacial forces in a shear flow field. *International Journal of Multiphase Flow.* 2018, **99**, pp.73-85.

320. Hibiki, T., Hogsett, S. and Ishii, M. Local measurement of interfacial area, interfacial velocity and liquid turbulence in two-phase flow. *Nuclear Engineering and Design.* 1998, **184**(2), pp.287-304.

321. Feng, X., Yang, C., Mao, Z.-S., Lu, J. and Tryggvason, G. Bubble induced turbulence model improved by direct numerical simulation of bubbly flow. *Chemical Engineering Journal.* 2019, **377**, p.120001.

322. Cifani, P., Kuerten, J.G.M. and Geurts, B.J. Flow and bubble statistics of turbulent bubble-laden downflow channel. *International Journal of Multiphase Flow.* 2020, **126**, p.103244.

323. Iwamoto, K., Suzuki, Y. and Kasagi, N. Reynolds number effect on wall turbulence: toward effective feedback control. *International Journal of Heat and Fluid Flow.* 2002, **23**(5), pp.678-689.

324. Tiselj, I., Stalio, E., Angeli, D. and Oder, J. 6.1.1 - Direct numerical simulations for liquid metal applications. In: Roelofs, F. ed. *Thermal Hydraulics Aspects of Liquid Metal Cooled Nuclear Reactors*. Woodhead Publishing, 2019, pp.219-244.

325. Cifani, P. *DNS of turbulent bubble-laden channel flows*. Ph.D thesis, University of Twente, 2017.

326. du Cluzeau, A., Bois, G., Toutant, A. and Martinez, J.M. On bubble forces in turbulent channel flows from direct numerical simulations. *Journal of Fluid Mechanics.* 2019, **882**, p.A27.

327. de Vries, A.W.G., Biesheuvel, A. and van Wijngaarden, L. Notes on the path and wake of a gas bubble rising in pure water. *International Journal of Multiphase Flow.* 2002, **28**(11), pp.1823-1835.

328. Afkhami, S. and Bussmann, M. Height functions for applying contact angles to 3D VOF simulations. *International Journal for Numerical Methods in Fluids.* 2009, **61**(8), pp.827-847.

329. Dabiri, S. and Bhuvankar, P. Scaling law for bubbles rising near vertical walls. *Physics of Fluids.* 2016, **28**(6), p.062101.

330. Tsutsui, T. Flow around a sphere in a plane turbulent boundary layer. *Journal of Wind Engineering and Industrial Aerodynamics.* 2008, **96**(6), pp.779-792.

331. Jeong, H. and Park, H. Near-wall rising behaviour of a deformable bubble at high Reynolds number. *Journal of Fluid Mechanics.* 2015, **771**, pp.564-594.

332. Roghair, I., Dijkhuizen, W., van Sint Annaland, M. and Kuipers, J. Front Tracking simulations on liquid-liquid systems; an investigation of the drag force on droplets. In: *6th International conference on computation fluid dynamics in the oil & gas, metallurgical and process industries, 10-12 June 2008, Trondheim, Norway*. 2008.

333. Zhou, Y., Zhao, C. and Bo, H. Analyses and modified models for bubble shape and drag coefficient covering a wide range of working conditions. *International Journal of Multiphase Flow.* 2020, **127**, p.103265.

334. Liu, T.J. Bubble size and entrance length effects on void development in a vertical channel. *International Journal of Multiphase Flow.* 1993, **19**(1), pp.99-113.